

International Studies in

SCIENCE *and* MATHEMATICS

EDITORS

PROF. DR. ALPARSLAN DAYANGAÇ

PROF. HASAN AKGÜL

June 2025

Genel Yayın Yönetmeni / Editor in Chief • Eda Altunel

Kapak & İç Tasarım / Cover & Interior Design • Serüven Yayınevi

Birinci Basım / First Edition • © Haziran 2025

ISBN • 978-625-5897-29-9

© copyright

Bu kitabın yayın hakkı Serüven Yayınevi'ne aittir.

Kaynak gösterilmeden alıntı yapılamaz, izin almadan hiçbir yolla çoğaltılamaz. The right to publish this book belongs to Serüven Publishing. Citation can not be shown without the source, reproduced in any way without permission.

Serüven Yayınevi / Serüven Publishing

Türkiye Adres / Turkey Address: Kızılay Mah. Fevzi Çakmak 1. Sokak

Ümit Apt No: 22/A Çankaya/ANKARA

Telefon / Phone: 05437675765

web: www.seruenyayinevi.com

e-mail: seruenyayinevi@gmail.com

Baskı & Cilt / Printing & Volume

Sertifika / Certificate No: 42488

INTERNATIONAL STUDIES
in
SCIENCE *and*
MATHEMATICS

EDITORS

PROF. DR. ALPARSLAN DAYANGAÇ
PROF. HASAN AKGÜL

CONTENTS

Chapter 1

SYNTHESIS AND THERAPEUTIC IMPORTANCE OF THIAZOLE DERIVATIVES

Nurcan BERBER —1

Chapter 2

POSSIBLE THEORIES FOR THE BEGINNING OF THE UNIVERSE

E.Nihal ERCAN —15

Chapter 3

ROBUST 3^k FACTORIAL DESIGN WHEN THE UNDERLYING DISTRIBUTION IS SKEW-NORMAL

Özgün KARATEPE, Birdal ŞENOĞLU —27

Chapter 4

ESTIMATING THE PARAMETERS OF LONG-TAILED SYMMETRIC DISTRIBUTION USING METAHEURISTIC ALGORITHMS

Adil KILIÇ, Gamze GÜVEN, Birdal ŞENOĞLU —51

Chapter 5

TESTING BLOCKS FOR QUASI-METRIC VALIDATION IN FINITE TOPOLOGIES

Bünyamin YILDIZ —67

Chapter 6

TYPES OF CONVERGENCE IN LATTICES AND THEIR INTERRELATIONSHIPS

Büşra Zümre DOĞRU —83

Chapter 7

ON POINTWISE CONVERGENCE OF M-SINGULAR INTEGRAL OPERATORS INVOLVING FINITE SUM

GÜMRAH UYSAL —99

Chapter 8

EFFECT OF METAL OXIDE TYPE AND PARTICLE SIZE ON OPTICAL AND STRUCTURAL BEHAVIOR OF PS/METAL OXIDE NANOCOMPOSITE FILMS

M. Selin SUNAY, Abdelhamid ELAISSARI —113

Chapter 9

AN INVESTIGATION OF TOTALLY UMBILICAL SEMI-INVARIANT SUBMANIFOLDS IN LOCALLY DECOMPOSABLE GOLDEN RIEMANNIAN MANIFOLDS

Mustafa GÖK —141

Chapter 10

MATERIAL INNOVATIONS DRIVING THE FUTURE OF LIGHT-CHARGED SUPERCAPACITORS

*Melisa ÖĞRETİCİ, Kibar ARAS,
Sinem ORTABOY SEZER —153*

Chapter 11

GENETICS OF *DROSOPHILA MELANOGASTER*

Aylin YILMAZ ÇETINKAYA —185

Chapter 1

SYNTHESIS AND THERAPEUTIC IMPORTANCE OF THIAZOLE DERIVATIVES

Nurcan BERBER¹

¹ Vocational School of Health Services, Çanakkale Onsekiz Mart University, Terzioğlu Campus, 17100, Çanakkale / TURKEY, nberber@comu.edu.tr <https://orcid.org/0000-0002-1595-585X>

1. Introduction

Thiazole is five-membered heterocyclic compound containing both sulfur and nitrogen atoms at positions 1 and 3 of the ring, is found in important natural compounds like thiamine (vitamin B1), penicillin, and carboxylase, as well as in numerous synthetic drugs, dyes, and industrial chemicals [1-4]. First described by Hantzsch and Weber in 1887, its structure confirmed by Popp in 1889. With the molecular formula C_3H_3NS , the thiazole ring exhibits aromatic character due to a conjugated π -electron system, similar to that of benzene. This aromaticity, provided by the delocalization of six π -electrons across the ring, contributes to the chemical stability of thiazole, Fig.1 [5-8].

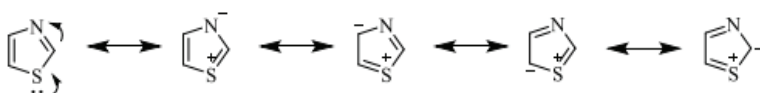


Figure 1. The resonance forms of thiazole

Thiazole exhibits mildly basic properties. The nitrogen atom's lone pair is involved in the aromatic π -system, which makes it a weak base. Nevertheless, the thiazole ring is relatively reactive toward electrophilic agents, allowing it to serve as a useful intermediate in various synthetic pathways. Electrophilic substitution reactions on the thiazole ring primarily occur at the C-2 and C-5 positions, where electron density is relatively high. The ring can also undergo nucleophilic or basic reactions, sometimes leading to ring-opening or structural modifications. This reactivity profile makes thiazole a versatile building block in organic synthesis [9-13].

2. Synthetic Methodology of Thiazoles

2.1. Hantzsch Synthesis

The Hantzsch thiazole synthesis is a classical organic reaction that forms thiazole rings by condensing α -haloketones with thioamides. This method, first reported by Arthur Rudolf Hantzsch in 1887, provides an efficient route to substituted thiazoles, which are five-membered heterocyclic compounds containing both sulfur and nitrogen atoms, Fig. 2 [14].

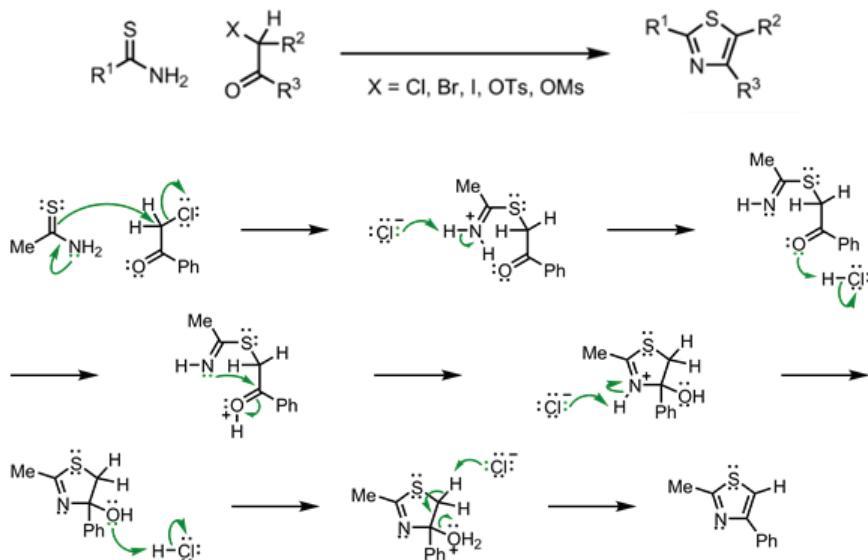
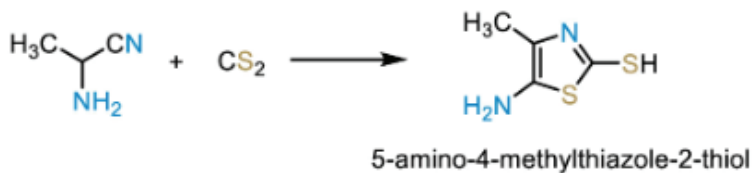


Figure 2. Synthesis of substituted 2-aminothiazoles with Hantzsch condensation

2.2. Cook–Heilbron Synthesis

In this synthesis, an α -aminonitriles/ α -aminoamides reacts with carbon disulfide to produce the thiazole ring, Fig.3 [15].



Figur 3. Cook-Heilbron thiazole synthesis

2.3. Robinson-Gabriel Synthesis

Gabriel synthesis is another way to synthesize thiazole compounds. In this reaction, 2,5-disubstituted thiazole derivatives are produced by treating acylamino-ketone with phosphorus pentasulfide, this technique focuses on the closure of the thiazole ring, Fig.4 [16].

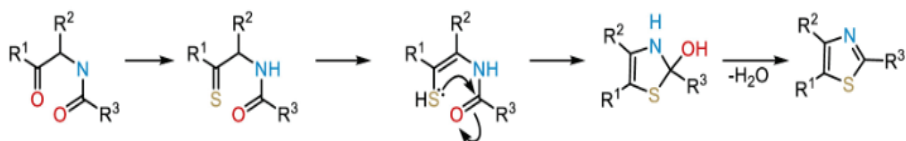
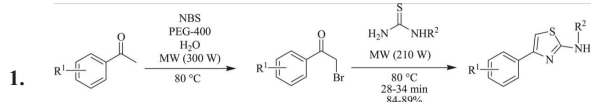
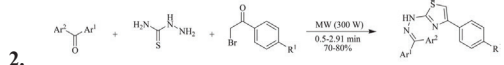


Figure 4. Gabriel's synthesis of 2,5-disubstituted 1,3-thiazoles

2.4. Microwave-assisted synthesis of thiazoles

Microwave-assisted organic synthesis (MAOS) has emerged as a powerful technique in modern synthetic chemistry, offering significant advantages over conventional thermal methods. In the context of thiazole synthesis, microwave irradiation enables rapid and uniform heating, which significantly shortens reaction times and improves energy efficiency. This approach often leads to higher product yields and improved purity, while also minimizing the formation of side products. Furthermore, it typically requires little to no solvent, contributing to the principles of green chemistry by reducing environmental impact. The enhanced reproducibility and operational simplicity of microwave-assisted methods also make them particularly attractive for the synthesis of heterocyclic compounds, including bioactive thiazole derivatives. Patel et al., in their review article, have highlighted various synthetic strategies for thiazole derivatives carried out under microwave-assisted conditions, in Table 1 [17].

Table 1. Synthesis of some thiazole derivatives using microwave irradiation

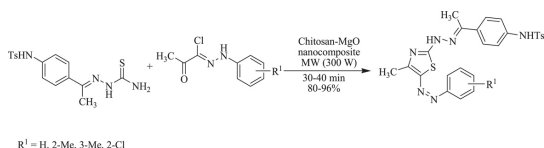
Synthesis Method	Source
<p>1. </p> <p>$R^1 = 4\text{-Me, H, 4-F, 4-Cl, 4-Br, 4-NO}_2, 4\text{-OMe, 2,4-Cl}_2$ $R^2 = \text{H, Me, Cl, 2-ClPh, 4-ClPh, 4-MePh, 4-MeOPh}$</p>	<p>Wagare, D. S., Netankar, P. D., Shaikh, M., Farooqui, M., & Durrani, A. (2017). Highly efficient microwave-assisted one-pot synthesis of 4-aryl-2-aminothiazoles in aqueous medium. <i>Environmental Chemistry Letters</i>, 15(3), 475-479.</p>
<p>2. </p> <p>$Ar^1 = 4\text{-ClPh, 4-FC}_6\text{H}_4, 4\text{-H}_2\text{NPh, 2-NH}_2\text{-4-NO}_2\text{Ph, 2-NH}_2\text{-5-ClPh}$ $Ar^2 = \text{Ph, 4-MePh}$ $R^1 = \text{OMe, Cl, NO}_2$</p>	<p>Karamthulla, S., Pal, S., Khan, M. N., & Choudhury, L. H. (2014). "On-water" synthesis of novel trisubstituted 1,3-thiazoles via microwave-assisted catalyst-free domino reactions. <i>RSC Advances</i>, 4(71), 37889-37899.</p>

3.



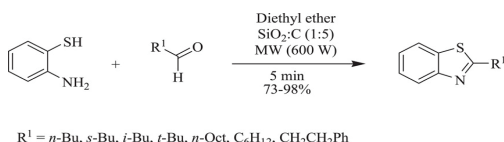
Chinnaraja, D., & Rajalakshmi, R. (2015). A facile, solvent and catalyst free, microwave assisted one pot synthesis of hydrazinyl thiazole derivatives. *Journal of Saudi Chemical Society*, 19(2), 200-206.

4.



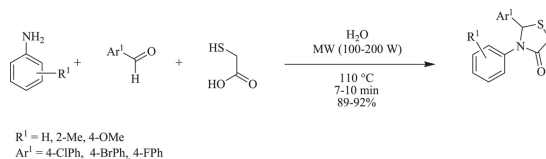
Riyadh, S. M., Khalil, K. D., & Aljuhani, A. (2018). Chitosan-MgO nanocomposite: One pot preparation and its utility as an ecofriendly biocatalyst in the synthesis of thiazoles and [1, 3, 4]thiadiazoles. *Nanomaterials*, 8(11), 928.

5.



Sakiyama, R., Aoyama, T., Akazawa, H., Kikuchi, N., Omura, K., Ohsaki, A., ... & Kodomari, M. (2018). Solvent-free synthesis of 2-alkylbenzothiazoles and bile acid derivatives containing benzothiazole ring by using active carbon/silica gel and microwave. *Journal of Oleo Science*, 67(10), 1209-1217.

6.



Shi, F., Li, C., Xia, M., Miao, K., Zhao, Y., Tu, S., ... & Ma, N. (2009). Green chemoselective synthesis of thiazolo [3, 2-a] pyridine derivatives and evaluation of their antioxidant and cytotoxic activities. *Bioorganic & medicinal chemistry letters*, 19(19), 5565-5568.

2.5. Ultrasound irradiated synthesis of thiazole derivatives

Ultrasound waves create cavitation (the formation and collapse of microbubbles) in a liquid medium. Produces local high temperature and pressure, increases the collision frequency of reactants and lowers the activation energy. This allows reactions to occur faster, more efficiently and more cleanly [18]. Patel et al., in their review article, have highlighted various synthetic strategies for thiazole derivatives carried out under ultrasound waves, in Table 2 [17].

Table 1. Synthesis of some thiazole derivatives using ultrasound irradiation

	Synthesis Method	Source
1.	<p>Ar¹ = Ph, 2-MePh, 4-PhPh, 3-NO₂Ph, 4-MeOPh, 4-ClPh, 2-BrPh, 3-BrPh, 4-BrPh, 3,4-(MeO)₂Ph, 2,4-Cl₂Ph.</p>	<p>Venzke, D., Flores, A. F., Quina, F. H., Pizzuti, L., & Pereira, C. M. (2011). Ultrasound promoted greener synthesis of 2-(3, 5-diaryl-4, 5-dihydro-1H-pyrazol-1-yl)-4-phenylthiazoles. <i>Ultrasonics sonochemistry</i>, 18(1), 370-374.</p>
2.	<p>R¹ = H, 4-OH, 4-Cl, 4-NO₂, 4-Me, 4-OMe, 4-NO₂</p>	<p>Sadjadi, S., & Sepehrian, H. (2011). Cu (OAc)₂/MCM-41: An efficient and solid acid catalyst for synthesis of 2-arylbenzothiazoles under ultrasound irradiation. <i>Ultrasonics sonochemistry</i>, 18(2), 480-483.</p>
3.	<p>R¹, R², R³ = H, Cl, OMe, OH, NO₂</p>	<p>Bouherrou, H., Saidoun, A., Abderrahmani, A., Abdellaziz, L., Rachedi, Y., Dumas, F., & Demenceau, A. (2017). Synthesis and biological evaluation of new substituted hantzsch thiazole derivatives from environmentally benign one-pot synthesis using silica supported tungstosilicic acid as reusable catalyst. <i>Molecules</i>, 22(5), 757.</p>
4.	<p>R¹ = </p>	<p>Shabaan, S. N., Baaiu, B. S., Abdel-Aziem, A., & Abdel-Aziz, M. S. (2021). Ultrasound-assisted green synthesis and antimicrobial assessment of 1, 3-thiazoles and 1, 3, 4-thiadiazines. <i>Green Chemistry Letters and Reviews</i>, 14(4), 679-688.</p>
5.	<p>Ar¹ = Ph, 4-OMePh R¹ = Ph, 3,4-(Cl)₂Ph, naphthyl, furanyl, 4-FPh, 2-OMePh, 4-MePh,</p>	<p>Shahbazi-Alavi, H., & Safaei-Ghomi, J. (2019). Nano-Fe₃O₄ attached to Crosslinked sulfonated polyacrylamide (Cross-PAA-SO₃H) as high performance catalyst for the synthesis of thiazoles under ultrasonic irradiations. <i>Nanochemistry Research</i>, 4(1), 55-63.</p>

3. Therapeutic Importance of Thiazole Derivatives

3.1. Anticancer Activity of Thiazole

The thiazole ring also stands out as an effective compound in cancer treatment due to the presence of sulfur and nitrogen atoms in its structure. Sulfur, exhibiting strong nucleophilic properties, allows certain thiazole derivatives to bind to target regions on DNA through sulfur atoms. The nitrogen atom, on the other hand, can form proton and hydrogen bonds, enabling tight interactions with DNA. These interactions disrupt DNA replication and inhibit the proliferation of cancer cells [19, 20]. For example, Alpelisib was clinically approved by the FDA on May 24, 2019, and is used in the treatment of metastatic breast cancer to inhibit the proliferation of cancer cells [21]. Dasatinib, on the other hand, was approved in 2006 and began to be used for the oral treatment of leukemia [22]. Some anticancer thiazole derivatives are given in Fig. 5.

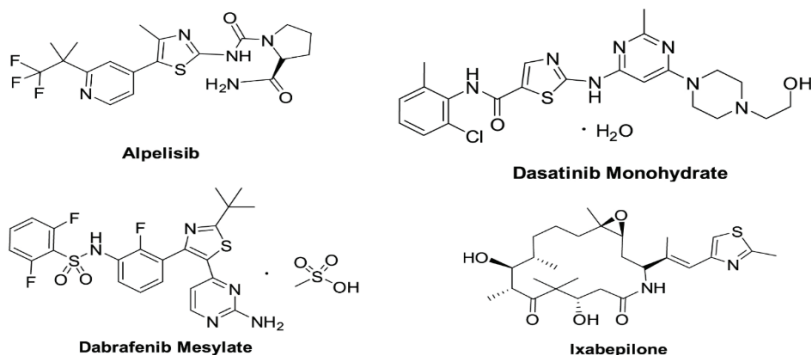


Figure 5. Structure of some thiazole derivative anticancer agents

3.2. Antibacterial activity of thiazole

Thiazole derivatives exert their antibacterial effects through various biochemical mechanisms. These effects may vary depending on their structural properties and the specific bacterial enzymes or cellular components they target. In general, thiazole derivatives exert their antibacterial effects: by inhibiting bacterial cell wall synthesis [23, 24]; by inhibiting bacterial DNA synthesis [25]; by targeting bacterial protein [26]; or inducing changes in the cell membrane that lead to bacterial cell death [27]. For example, Sulfathiazole, which contains a thiazole ring, competitively inhibits the bacterial dihydropteroate synthase enzyme, thereby blocking the folic acid synthesis pathway and indirectly inhibiting bacterial DNA synthesis [28]. On the other hand, Thiazomycin, a natural

thiazole derivative, binds to the ribosomal 50S subunit and inhibits protein synthesis; through this mechanism, it exhibits strong antibacterial activity, particularly against Gram-positive bacteria [29]. The chemical structures of these compounds are given in Fig.6.

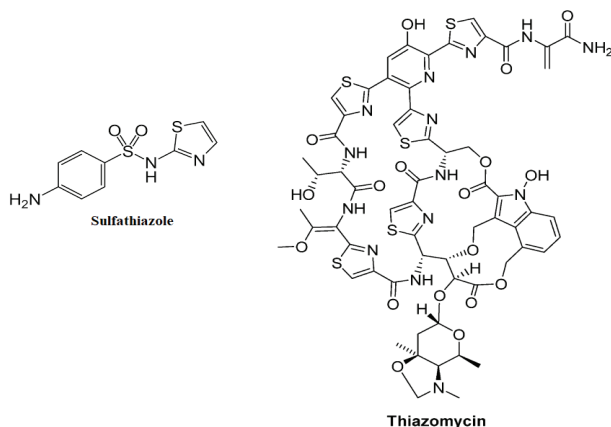


Figure 6. Chemical structure of Sulfathiazole and Thiazomycin

In addition, some representative examples of thiazole derivatives with antibacterial potential containing β -lactams are given in Fig. 7.

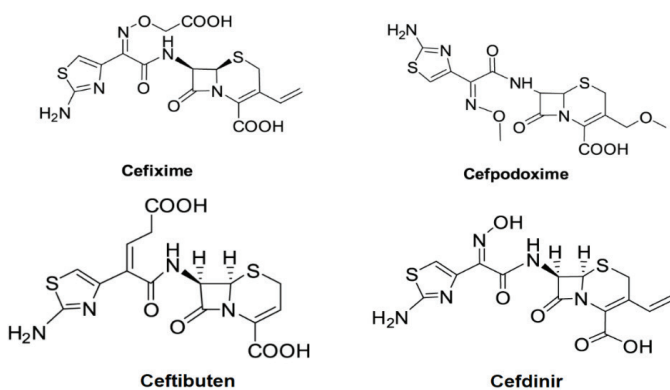


Figure 7. Structure of some β -lactam containing thiazole derivative antibacterial agents

3.3. Antivirus activity of thiazole

The antiviral effects of thiazole derivatives arise through various biochemical mechanisms. Some of these compounds inhibit viral replication by targeting viral RNA or DNA polymerase enzymes [30]. Other thiazole derivatives suppress viral proliferation by halting protein synthesis within the host cell [31]. Additionally, certain derivatives have been reported to exhibit antiviral activity by preventing viruses from entering host cells [32]. In this context, thiazole derivatives that have been synthesized are reported to inhibit a wide range of viruses, including influenza viruses, coronaviruses, herpesviruses, hepatitis B and C viruses, bovine viral diarrhea virus, chikungunya virus, and human immunodeficiency viruses (HIV) [33]. Some representative examples of thiazole derivatives with antivirus potential are given in Fig. 8.

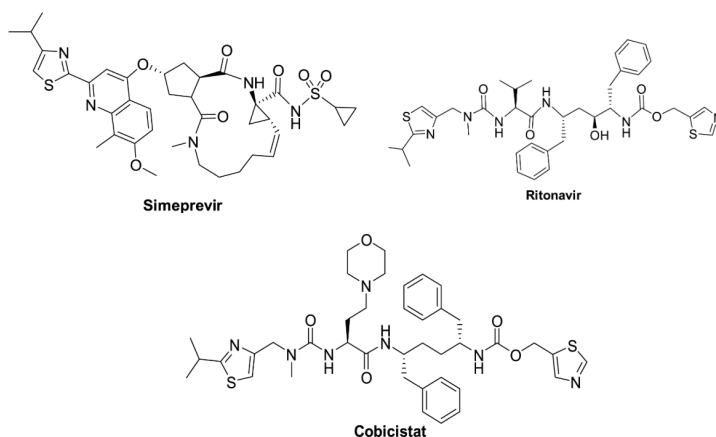


Figure 8. Structure of some thiazole derivative antivirus agents

3.4. Antifungal activity of thiazole

Fungal diseases are responsible for a higher global mortality rate than breast cancer or malaria [34]. Recent studies have shown that systemic infections caused by *Candida* species are the fourth most common cause of hospital-acquired bloodstream infections [35]. In Fig. 9 we see the structures of thiazole derivatives Isavuconazole, Fosravuconazole and Thiabendazole.

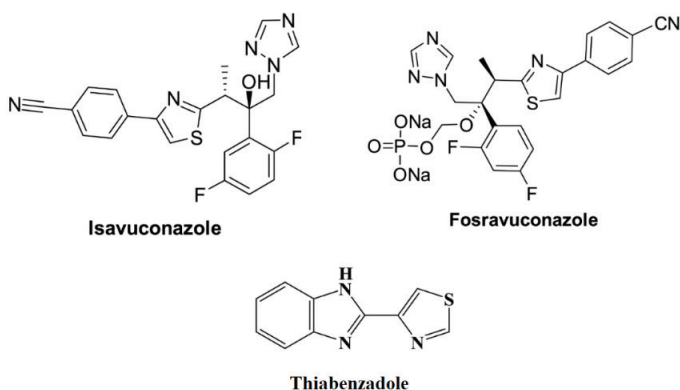


Figure 9. Structure of some thiazole derivative antivirus agents

3.5. Antiinflammatory activity of thiazole

Meloxicam is a well-known thiazole derivative nonsteroidal antiinflammatory drug used for the rheumatic and osteoarthritis diseases. It selectively inhibits the enzyme cyclooxygenase-2 (COX-2) [36]. Fentiazac is another thiazole derivative anti-inflammatory agent developed for use in joint and muscle pain[37]. The chemical structures of these compounds are given in Fig.10.

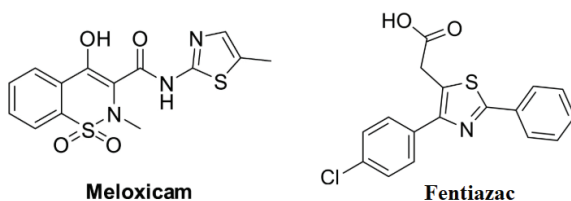


Figure 10. Chemical structure of Meloxicam and Fentiazac

4. Conclusion

In conclusion, thiazole derivatives stand out as an important class of heterocyclic compounds due to their versatile synthetic accessibility and broad spectrum of biological activities. In addition to classical methods such as the Hantzsch, Cook–Heilbron, and Gabriel syntheses, recent advances in microwave-assisted and ultrasound-promoted green methodologies have significantly enhanced the efficiency, yield, and eco-compatibility of thiazole synthesis. These alternative techniques offer shorter reaction times, higher selectivity, and reduced solvent consumption, thereby aligning well with the principles of green chemistry. Especially, green solvent-assisted syntheses using water, ethanol, and other benign media under irradiation conditions provide an environmentally friendly alternative to conventional organic solvents. The combined use of non-toxic solvents and energy-efficient technologies (such as microwave and ultrasound) not only minimizes environmental impact but also facilitates scalable and sustainable drug development processes.

Therapeutically, thiazole derivatives continue to demonstrate notable anticancer, antibacterial, antiviral, antifungal, and anti-inflammatory properties, with several FDA-approved examples already in clinical use. Their unique ability to interact with DNA, proteins, and enzymes at a molecular level renders them highly promising scaffolds for novel drug design. Overall, the integration of innovative synthetic methods with therapeutic targeting strategies will further enhance the relevance of thiazole derivatives in modern medicinal chemistry. Future research focusing on structure-activity relationship (SAR) studies, biocompatibility, and targeted delivery systems may pave the way for next-generation thiazole-based pharmaceuticals.

5. References

- 1- Siddiqui, N., Arshad, M.F., Ahsan, W., and Alam, M.S. (2009). Thiazoles: a valuable insight into the recent advances and biological activities. *Int. J. Pharm. Sci. Drug. Res.*, 1(3), 136-143.
- 2- Petrou, A., Fesatidou, M., & Geronikaki, A. (2021). Thiazole ring—A biologically active scaffold. *Molecules*, 26(11), 3166.
- 3- Schellack, G., Harirari, P., & Schellack, N. (2016). B-complex vitamin deficiency and supplementation. *SA Pharmaceutical Journal*, 83(4), 14-19.
- 4- Shindy, H. A. (2017). Fundamentals in the chemistry of cyanine dyes: A review. *Dyes and Pigments*, 145, 505-513.
- 5- Wu, Y.J. (2017). Five-membered ring systems: with N and S atom. *Prog. Heterocycl. Chem.*, 29, 315-336
- 6- Balaban, A. T., Oniciu, D. C., & Katritzky, A. R. (2004). Aromaticity as a cornerstone of heterocyclic chemistry. *Chemical reviews*, 104(5), 2777-2812.
- 7- Hantzsch, A., & Weber, J. H. (1887). Ueber verbindungen des thiazols (pyridins der thiophenreihe). *Berichte der deutschen chemischen Gesellschaft*, 20(2), 3118-3132.
- 8- Jo, J. W., Kim, S. S., & Jo, W. H. (2012). Synthesis of thieno [3, 4-d] thiazole-based conjugated polymers and HOMO level tuning for high VOC photovoltaic cell. *Organic Electronics*, 13(8), 1322-1328.
- 9- Newkome, G.R., & Hager, D.C. (1978). Chemistry of heterocyclic compounds. 27. An improved preparation of pyridyldiphenylphosphines. *The Journal of Organic Chemistry*, 43(5), 947-949.
- 10- Hu, Y., Li, C. Y., Wang, X. M., Yang, Y. H., & Zhu, H. L. (2014). 1, 3, 4-Thiadiazole: synthesis, reactions, and applications in medicinal, agricultural, and materials chemistry. *Chemical reviews*, 114(10), 5572-5610.
- 11- Radhakrishnan, R., & Sreejalekshmi, K. G. (2018). Computational design, synthesis, and structure property evaluation of 1, 3-thiazole-based color-tunable multi-heterocyclic small organic fluorophores as multifunctional molecular materials. *The Journal of Organic Chemistry*, 83(7), 3453-3466.
- 12- Habenicht, S. H., Siegmann, M., Kupfer, S., Kübel, J., Weiß, D., Cherek, D., ... & Beckert, R. (2015). And yet they glow: thiazole based push–pull fluorophores containing nitro groups and the influence of regioisomerism. *Methods and Applications in Fluorescence*, 3(2), 025005.
- 13- Murai, T., Hori, F., & Maruyama, T. (2011). Intramolecular cyclization of in situ generated adducts formed between thioamide dianions and thioformamides leading to generation of 5-amino-2-thiazolines and 5-aminothiazoles, and their fluorescence properties. *Organic Letters*, 13(7), 1718-1721.
- 14- Prakash, R., Kumar, A., Aggarwal, R., Prakash, O., & Singh, S. P. (2007). α , α -Dibromoketones: a superior alternative to α -bromoketones in Hantzsch

- thiazole synthesis. *Synthetic Communications*, 37(15), 2501-2505.
- 15- Kalinin, A. A., & Mamedov, V. A. (2004). Carbon Disulfide in Synthesis of Thiazolo [3, 4-a] quinoxalines Based on 3-(α -Chlorobenzyl) quinoxalin-2-(1H)-ones. *Chemistry of Heterocyclic Compounds*, 40(1).
 - 16- Mathew, B., Hobrath, J. V., Connelly, M. C., Guy, R. K., & Reynolds, R. C. (2018). Oxazole and thiazole analogs of sulindac for cancer prevention. *Future Medicinal Chemistry*, 10(7), 743-753.
 - 17- Patel, M., Bambharoliya, T., Shah, D., Patel, K., Patel, M., Shah, U., ... & Patel, A. (2024). Emerging green synthetic routes for thiazole and its derivatives: Current perspectives. *Archiv der Pharmazie*, 357(2), 2300420.
 - 18- Pagadala, R., Maddila, S., & Jonnalagadda, S. B. (2014). Eco-efficient ultrasonic responsive synthesis of pyrimidines/pyridines. *Ultrasonics sonochemistry*, 21(2), 472-477.
 - 19- Sahil, Kaur, K., Jaitak, V. 2022. "Thiazole and related heterocyclic systems as anticancer agents: A review on synthetic strategies, mechanisms of action and SAR studies". *Current Medicinal Chemistry*, 29, 29, 4958-5009.
 - 20- Ayati, A., Emami, S., Asadipour, A., Shafiee, A., Foroumadi, A. 2015. "Recent applications of 1, 3-thiazole core structure in the identification of new lead compounds and drug discovery". *European Journal of Medicinal Chemistry*, 97, 699-718.
 - 21- Alizadeh, S. R., Hashemi, S. M. 2021." Development and therapeutic potential of 2-aminothiazole derivatives in anticancer drug discovery". *Medicinal Chemistry Research*, 30, 771-806.
 - 22- Johnson, F. M., Agrawal, S., Burris, H., Rosen, L., Dhillon, N., Hong, D., Chiappori, A. A. 2010. "Phase 1 pharmacokinetic and drug-interaction study of dasatinib in patients with advanced solid tumors". *Cancer: Interdisciplinary International Journal of the American Cancer Society*, 116, 6, 1582-1591.
 - 23- Van, T. T. H., Nguyen, H. N. K., Smooker, P. M., & Coloe, P. J. (2012). The antibiotic resistance characteristics of non-typhoidal *Salmonella enterica* isolated from food-producing animals, retail meat and humans in South East Asia. *International Journal of Food Microbiology*, 154(3), 98-106.
 - 24- Watt, B., & Brown, F. V. (1982). In-vitro activity of cefotiam against bacteria of clinical interest. *Journal of Antimicrobial Chemotherapy*, 10(5), 391-395.
 - 25- Hussain, M., Qadri, T., Hussain, Z., Saeed, A., Channar, P. A., Shehzadi, S. A., ... & Malik, A. (2019). Synthesis, antibacterial activity and molecular docking study of vanillin derived 1, 4-disubstituted 1, 2, 3-triazoles as inhibitors of bacterial DNA synthesis. *Helvion*, 5(11).
 - 26- Sun, N., Lu, Y. J., Chan, F. Y., Du, R. L., Zheng, Y. Y., Zhang, K., ... & Wong, K. Y. (2017). A thiazole orange derivative targeting the bacterial protein FtsZ shows potent antibacterial activity. *Frontiers in microbiology*, 8, 855.
 - 27- Thakur, S., Sharma, R., Yadav, R., & Sardana, S. (2022). The potential of thiazole derivatives as antimicrobial agents. *Chemistry Proceedings*, 12(1),

- 36.
- 28- Martindale, C. (2009). *The complete drug reference* (Vol. 1). S. C. Sweetman (Ed.). London: Pharmaceutical press.
- 29- Bagley, M. C., Dale, J. W., Merritt, E. A., & Xiong, X. (2005). Thiopeptide antibiotics. *Chemical reviews*, 105(2), 685-714.
- 30- Spector, F. C., Liang, L., Giordano, H., Sivaraja, M., & Peterson, M. G. (1998). Inhibition of herpes simplex virus replication by a 2-amino thiazole via interactions with the helicase component of the UL5-UL8-UL52 complex. *Journal of virology*, 72(9), 6979-6987.
- 31- Lillsunde, K. E., Tomašič, T., Schult, P., Lohmann, V., Kikelj, D., & Tammela, P. (2019). Inhibition of Hepatitis C Replication by Targeting the Molecular Chaperone Hsp90: Synthesis and Biological Evaluation of 4, 5, 6, 7-Tetrahydrobenzo [1, 2-d] thiazole Derivatives. *ChemMedChem*, 14(3), 334-342.
- 32- Serban, G. (2020). Synthetic compounds with 2-amino-1, 3, 4-thiadiazole moiety against viral infections. *Molecules*, 25(4), 942.
- 33- Farghaly, T. A., Alsaedi, A. M., Alenazi, N. A., & Harras, M. F. (2022). Anti-viral activity of thiazole derivatives: an updated patent review. *Expert opinion on therapeutic patents*, 32(7), 791-815.
- 34- Qin, Y., Li, P., & Guo, Z. (2020). Cationic chitosan derivatives as potential antifungals: A review of structural optimization and applications. *Carbohydrate Polymers*, 236, 116002.
- 35- Sakagami, T., Kawano, T., Yamashita, K., Yamada, E., Fujino, N., Kaeriyama, M., ... & Mikamo, H. (2019). Antifungal susceptibility trend and analysis of resistance mechanism for *Candida* species isolated from bloodstream at a Japanese university hospital. *Journal of Infection and Chemotherapy*, 25(1), 34-40.
- 36- Del Tacca, M., Colucci, R., Fornai, M., & Blandizzi, C. (2002). Efficacy and tolerability of meloxicam, a COX-2 preferential nonsteroidal anti-inflammatory drug: A review. *Clinical drug investigation*, 22, 799-818.
- 37- Zhang, Z., Cao, P., Fang, M., Zou, T., Han, J., Duan, Y., ... & Li, Q. S. (2021). Design, synthesis, and SAR study of novel 4, 5-dihydropyrazole-Thiazole derivatives with anti-inflammatory activities for the treatment of sepsis. *European Journal of Medicinal Chemistry*, 225, 113743.

Chapter 2

POSSIBLE THEORIES FOR THE BEGINNING OF THE UNIVERSE

E.Nihal ERCAN¹

¹ Prof.Dr., Boğaziçi University, Physics Department

Studies and observations about the Universe originate back to very ancient eras. Assyro-Babylonians left the first documented records of systematic astronomical observations established in 1000 BCE [1]. Since then, learning about the Universe has been a curious subject. The first modern studies about the origin and evolution of the Universe started in the 20th century with the work of Edwin Hubble. Hubble's observations of distant galaxies revealed that the universe was expanding [17]. Four theories have emerged over the years, each providing different explanations for the beginning and evolution of the universe. These theories are the Steady State theory, the Pulsating theory, the Inflationary theory, and the Big Bang theory.

The Big Bang Theory

This theory is first based on the fact that galaxies are moving away from each other in all directions, for which a great force is needed. Georges Lemaitre, a Belgian priest, was the first to suggest this theory in the 1920s asserting the Universe arose from a single point [2]. The observations of Edwin Hubble corroborated this idea. He observed that galaxies rush away from the Earth in all directions. Moreover, with the discovery of cosmic microwave radiation by Arno Penzias and Robert Wilson in the 1960s, the Big Bang theory was verified since these microwaves are interpreted as the echoes of the Big Bang [2].

According to the theory, the Universe began around 13.7 billion years ago. The point mentioned above comprised of condensed infinitesimally small singularity, in other words infinitely dense and hot. From this point the explosion took place and the expansion was initiated, which is faster than the speed of light. Thereafter, the fundamental particles such as electrons, protons and neutrons formed. It was impossible to observe visible light on his "soup" of particles. However, over time free electrons and protons randomly met each other and formed neutral atoms. It allowed the constitution of visible light, which is estimated to happen 380,000 years after the Big Bang. It is called cosmic microwave background and discovered by accident [3].

In 1965, Arno Penzias and Robert Wilson were attempting to build a radio receiver; however, they caught very high temperatures, which they thought to be caused by pigeons. At the same time, a team at Princeton University led by Robert Dicke was also trying to find evidence for Cosmic Microwave Background, and they realized that this strange observation could be related to Cosmic Microwave Background, so they further investigated the situation, and together with Wilson and Penzias, published a paper about this observation being the discovery of Cosmic

Microwave Background[3]. After all, the discovery of the Cosmic Microwave Background is the strongest corroborative evidence of the Big Bang theory.

Another observation corroborating the Big Bang theory is the fact that galaxies and stars are observed from the Earth in a red-shifted manner [12]. It means that cosmic objects appear more reddish than they are when they are observed from the Earth, and it is caused by the 'Doppler Effect' [13]. Doppler Effect remarks that when an object moves away from the observer, the observed wavelength of either the sound or the electromagnetic wave becomes larger, and in the case of the electromagnetic wave, the appearance of the object shifts toward the red end of the spectrum. How much it is shifted is related to the relative velocity of the moving object. The higher the velocity the object has, the more red it appears [14]. In conclusion, the observation of the redshifted cosmic object from the Earth implies the fact that the universe is expanding [14]. Moreover, it is shown that this expansion is taking place in an accelerating way. In other words, the expansion rate of the universe is speeding up, the cause of which is still a mystery today [16].

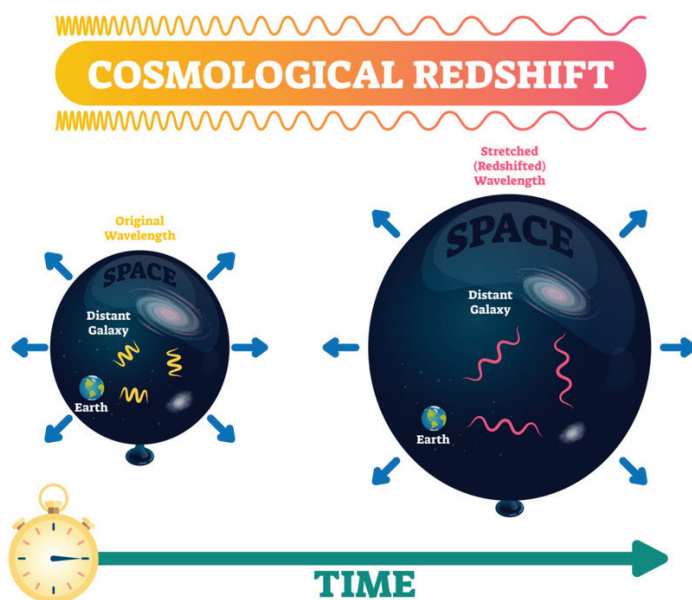


Figure 1: The figure shows how the expanding universe is related to the observation of red-shifted cosmic objects. Here we can see that as the universe expands, the appearance of the objects from the Earth shifts toward red. [15]

The Steady State Theory

The Steady State Theory was first proposed in 1948 by British astrophysicist Hermann Bondi, American mathematician Thomas Gold, and British mathematician Fred Hoyle [4]. They knew that the Universe constantly expands; however, they thought that the average density of matter is kept constant. That is why, they suggested that new matter is being continuously created so that new galaxies and stars can form. Thereby, it could explain how the Universe accomplish to keep uniformity on a large scale (not local). Moreover, according to the Steady State theory, there is neither the beginning nor the end of the universe in terms of time[4].

Back in time, the Steady State theory was the competitor theory against the Big Bang theory. Nonetheless, after the discovery of cosmic microwave background, the Steady State Theory was mostly falsified in that it had predicted that the density of the Universe does not change; on the other hand, the observation of cosmic microwave background states otherwise[4]. Also, The Steady State theory struggled to provide compelling evidence to substantiate its claims, particularly in explaining the observed abundance of light elements or the distribution of galaxies. Another big problem with the theory is that the continuous creation of matter violates the law of conservation of energy.

Not only the Steady State theory could not maintain its claims by pieces of evidence, but some discoveries contradict the premises of the steady state theory. As mentioned above, the Steady State theory anticipates a non-changing Universe on a large scale, so the general distribution of energy and matter in the Universe should be similar to what it was billions of years ago. However, it is shown that the formation of quasars was much more frequent billions of years ago[5]. It implies that the distribution of energy and matter has changed over time in the Universe, which is contradictory to a steady-state Universe.

The Pulsating Theory

The Pulsating Theory emerged as a contender to the prevailing Big Bang theory and is based on the Universe's cyclical nature. Although there is no definite originator of this theory to pinpoint, Albert Einstein, Richard Tolman, and Hermann Bondi, among others, can be counted as contributors [18, 19]. The theory suggests that the Universe cyclically undergoes expansion and contraction, resembling a cosmic heartbeat.

In terms of how the Universe begins, the Pulsation Theory considerably resembles the Big Bang theory. The Universe starts from a singularity and begins expanding. On the other hand, as opposed to the Big Bang

theory, the Pulsating Theory suggests a destination for the Universe, which is it is going to contract after a critical point in time that is referred to as 'the Big Crunch'[6]. During the Big Crunch, the Universe collapses inwards until it reaches the singularity point. It is important to note that the Pulsation Theory, unlike the Steady State theory, is consistent with the law of conservation of energy.

There are several challenges that the Pulsation Theory confronts. Firstly, the activity of the Big Crunch comes with the requirement of the violation of the second law of thermodynamics, which is in a closed system entropy never decreases [7]. Nonetheless, according to Pulsating Theory, the Universe is a closed system that undergoes expansions and collapses. Furthermore, it is shown that the Universe is expanding in a speeding-up manner; in other words, the Universe has an accelerating expansion activity [8]. However, a pulsating universe would be decelerating, so that it eventually stops and undergoes the Big Crunch. In addition to these falsifying arguments, since the theory suggests a cyclic universe, each of which would last billions of years, it is challenging to gather empirical data to confirm the theory, especially the Big Crunch. This is because if the Universe had undergone the Big Crunch before the Big Bang, then the Universe once reached singularity. It means that all the information from the Big Crunch disappeared in the singularity, so it is impossible to acquire evidence from the Big Crunch.

Inflationary Theory

The Inflationary Theory was first proposed in the early 1980s by American physicist Alan Guth and further developed by Andrei Linde, Paul Steinhardt, and others. It aimed to address several unanswered questions posed by the Big Bang Theory and provide an explanation for the universe's remarkable uniformity and structure [9]. The Inflationary Theory postulates that the universe experienced a brief and exponential expansion, often referred to as cosmic inflation, during its earliest moments. This expansion occurred within a fraction of a second (10^{-36} seconds[9]) after the Big Bang, causing the universe to grow exponentially larger by a factor of at least 10^{26} [10].

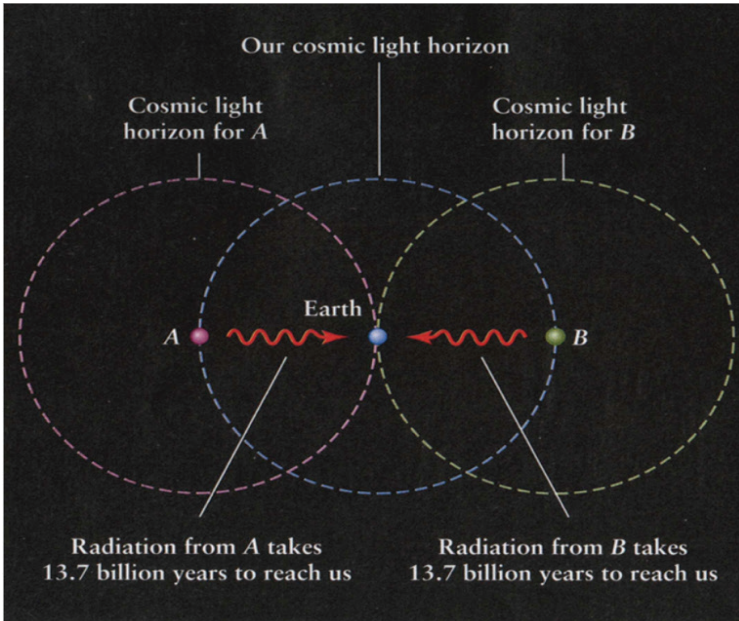


Figure 2: A demonstration showing that two photons (A and B) from separate horizons meet in another horizon. [10]

It is important to note that two points in separate cosmic horizons cannot communicate with each other since there is the limit as speed of light. In other words, there is no time for any photon emitted from cosmic horizon A to reach cosmic horizon B (see Figure 1). Instead, two photons emitted from these horizons separately can meet in the middle of another cosmic horizon, which is the Earth in the figure.

The cosmic microwave background radiation coming from different parts of the universe is observed to have the same temperature, suggesting they all originate from the beginning of the universe as if the Earth is the centre of the universe. However, it is valid for every point in the universe, though not every point in the universe may be the centre of the universe [10]. Then how can two photons, cosmic horizons of which cannot communicate with each other and released from the beginning of the universe reach one another? The answer is the Inflationary Theory. Because at the very beginning of the universe, the universe expands with an exponential, order of magnitude of 10^{26} [10], two photons released at the same time can be kept from different cosmic horizons. It means that at the very early times of the universe, cosmic horizons could form [10].

Because of the symmetry argument of classical physics, it would be expected for an early universe to expand in a perfectly symmetric way. However, cosmic inflation was so powerful that it could make quantum fluctuations influential. A normal 10^{-28} cm quantum fluctuation was enhanced to cosmological distances [10]. Thereby, it could provide uncertainty for the matter to locally behave. Together with the gravitational effects that became regionally denser due to quantum fluctuation's impact on matter, the variation from a perfect symmetry could be established. Consequently, the universe ended up locally heterogeneous but homogeneous/uniform in a larger scale [10]. This locally heterogeneous structure of the universe served as seeds for stars and galaxies to form.

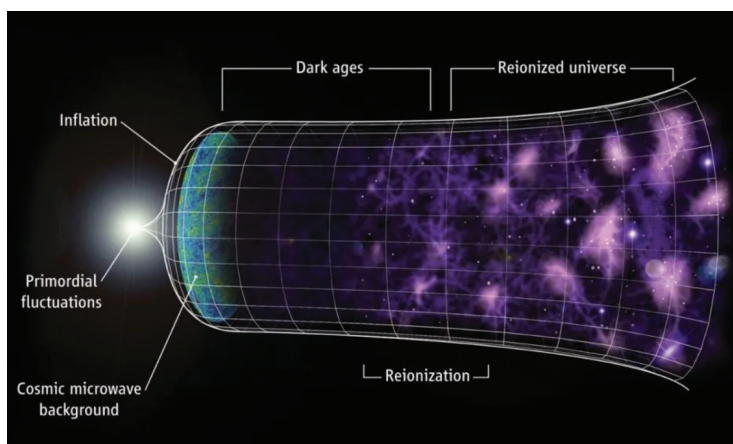


Figure 3: A demonstration of the evolution of the universe that has undergone cosmic inflation. As seen in the figure, it is possible to see a dramatic increase in the size of the universe at the beginning. It is important to note that proportions are fiction and are just meant to be demonstrative. [11]

Discussion & Conclusion

The quest to comprehend the mysteries of the universe has captivated human curiosity for centuries. Throughout history, scientists and cosmologists have proposed various theories to explain the origin, evolution, and fundamental nature of our vast cosmos. Four prominent cosmological theories that have shaped our understanding of the universe's inception and structure are the Big Bang Theory, the Steady State Theory, the Pulsating Theory, and the Inflationary Theory.

The Big Bang Theory, widely considered the foundation of modern cosmology, suggests that the universe originated from a singular explo-

sive event, approximately 13.8 billion years ago. This theory posits that the universe began as an infinitely hot, dense, and compact singularity, expanding rapidly and cooling over time [2]. Over time, the theory is corroborated by several observations and discoveries. Cosmic background microwave radiation carries traces from the very early ages of the universe, and it gives data from that time. Furthermore, the observation of redshifted cosmic objects proved the fact that the universe is expanding, which is one of the predictions of the Big Bang theory.

The Steady State theory was asserted as a main competitor to the Big Bang theory. It anticipated that time did not begin, and it won't end at a point. It is an everlasting concept. In order to balance the expansion of the universe, new matter is being continuously created so that steady density of the universe can be established. However, not only it could not maintain its premises with evidences, but also new observations like cosmic background microwave have mostly falsified the theory. Additionally, at the first place, the creation of new matter requires the violation of the law of the conservation of energy.

Pulsating theory emerged as an extended version of the Big Bang theory. It predicts the same scenario for the beginning of the universe with the Big Bang theory; on the other hand, it also claims that at a critical point in time, expansion of the universe will stop, and it will start to collapse inward, and it is referred as 'the Big Crunch'. Finally, this two event last forever in a cyclic manner one after another. There are two major problem with this theory. First, it violates the second law of thermodynamics, which is in a closed system entropy never decreases, because the Big Crunch requires decrease in entropy not locally but universally, which is impossible. Moreover, the theory claims that after the Big Crunch the universe again reaches the singularity; that's why practically, it impossible to collect empirical data from the previous cycle, and hence advocating the theory.

Inflationary theory could fill the blanks which the Big Bang theory left behind. How two separate photons carrying information from the very early stages of the Universe come from distinguished cosmic light horizons could be unveiled. The rate of expansion of the universe after the big explosion was so high that cosmic light horizons could form at the very early stages of the universe. Besides, how the perfect symmetry was not conserved was a big question. The inflation theory accomplished to answer this question, too. It advocates that the great expansion rate made the quantum fluctuation effective so that general symmetry could be preserved, though there could be some local heterogeneities, which is the characteristics of the universe that we observe today.

Today, the Steady State theory and Pulsating theory are not maintained because of a lack of evidence and the violation of some fundamental physical laws caused by their premises. The Big Bang theory and the Inflationary theory are the most prevailing theories that attempt to explain how the universe began and how it has been evolving. However, some questions are still waiting to be answered, some of which triggered the singularity to explode and expand in the first place, and what is the reason behind the accreting universe.

I would like to thank Mert Baysan, one of my undergraduate students, for his help in preparing this manuscript.

References

1. (2019). 'A HISTORY OF ASTROMETRY - PART I: MAPPING THE SKY FROM ANCIENT TO PRE-MODERN TIMES', Gaia. Available at: <https://sci.esa.int/web/gaia/-/53196-the-oldest-sky-maps#:~:text=The%20first%20documented%20records%20of,and%20recorded%20their%20periodic%20motions.>
2. Greshko, Micheal et al.(2017). 'ORIGINS OF THE UNIVERSE 101', National Geographic. Available at: <https://www.nationalgeographic.com/science/article/origins-of-the-universe>
3. May, Andrew et al.(2023), 'What is the Big Bang Theory?', space.com. Available at: <https://www.space.com/25126-big-bang-theory.html>
4. Britannica, T. Editors of Encyclopaedia (2022, March 29). *steady-state theory*. *Encyclopedia Britannica*. Available at: <https://www.britannica.com/science/steady-state-theory>
5. Fraknoi, Andrew, et al. 'Quasars as Probes of Evolution in the Universe', Astronomy, Chapter 27. Active Galaxies, Quasars, and Supermassive Black Holes, pressbooks. Available at: <https://pressbooks.online.ucf.edu/astronomybc/chapter/27-3-quasars-as-probes-of-evolution-in-the-universe/#:~:text=Quasars%20were%20much%20more%20common,accretion%20disk%20was%20more%20available.>
6. American Institute of Physics, NASA, NSF, U.S. Department of Energy, et al., Texas Symposium on Relativistic Astrophysics, 11th, Austin, TX, Dec. 12-17, 1982 New York Academy of Sciences, Annals (ISSN 0077-8923), vol. 422, 1984, p. 385-389. doi: 10.1111/j.1749-6632.1984.tb23407.x
7. Britannica, T. Editors of Encyclopaedia (2023, May 18). 'second law of thermodynamics'. *Encyclopedia Britannica*. Available at: <https://www.britannica.com/science/second-law-of-thermodynamics>
8. Kirshner, R.P. (2021, May). 'Accelerating universe'. *AccessScience*. doi: <https://doi.org/10.1036/1097-8542.800550>. Available at: <https://www.accessscience.com/content/article/a800550>
9. 'What is the Inflation Theory?', National Aeronautics and Space Administration. Available at: https://wmap.gsfc.nasa.gov/universe/bb_cosmo_infl.html
10. 'The Origins of the Universe: Inflation', The Stephen Hawking Centre of the Theoretical Cosmology. Available at: https://www.ctc.cam.ac.uk/outreach/origins/inflation_zero.php
11. Hossenfelder, Sabine(2017). 'Is the Inflationary Universe a Scientific Theory', forbes. Available at: <https://www.forbes.com/sites/startswithabang/2017/09/28/is-the-inflationary-universe-a-scientific-theory-not-anymore/?sh=739f19f3b45e>
12. Drayer, David(2017). 'How does a redshift give evidence to the Big Bang Theory?' Socratic Q&A. Available at: <https://socratic.org/questions/how-does-a-redshift-give-evidence-to-the-big-bang-theory>
13. Britannica, T. Editors of Encyclopaedia (2023, May 12). '*Doppler effect*', *Encyclopedia Britannica*. Available at: <https://www.britannica.com/science/doppler-effect>

com/science/Doppler-effect

14. Britannica, T. Editors of Encyclopaedia (2023, April 20). *redshift*. *Encyclopedia Britannica*. Available at: <https://www.britannica.com/science/redshift>
15. Millis, John P.(2018). ‘How Redshift Shows the Universe is Expanding’, Available at: <https://www.thoughtco.com/what-is-redshift-3072290>
16. Bahcal, Neta A.(2015), ‘Hubble’s Law of and the expanding universe’. 112 (11) 3173-3175, doi: <https://doi.org/10.1073/pnas.1424299112>
17. Britannica, T. Editors of Encyclopaedia (2021, June 1). ‘*expanding universe*’, *Encyclopedia Britannica*. Available at: <https://www.britannica.com/science/expanding-universe>
18. Assad, M.J.D., Romero(1992). ‘C. Eternal and pulsating universes in Einstein-Cartan space-time’. *Astrophys Space Sci* 191, 289–297. <https://doi.org/10.1007/BF00644776>
19. Tolman, Richard C. et al.(1929). ‘Experimental Demonstration of the Equivalence of a Mechanically Oscillated Electrostatic Charge to an Alternating Current’, *Phys. Rev.* **34**, 1075. doi: <https://doi.org/10.1103/PhysRev.34.1075>

Chapter 3

ROBUST 3^k FACTORIAL DESIGN WHEN THE UNDERLYING DISTRIBUTION IS SKEW-NORMAL

Özgün KARATEPE¹, Birdal ŞENOĞLU²

1 Ankara University, ORCID: 0000-0002-9179-7742, ozgunkaratepe@gmail.com

2 Prof. Dr., Ankara University, ORCID: 0000-0003-3707-2393, senoglu@science.
ankara.edu.tr

1 Introduction

Many experiments aim to investigate the main and interaction effects of two or more factors. Factorial designs examining the simultaneous effects of multiple factors on a response variable are the most efficient designs for such experiments in general. They provide an advantage to the experimenters in terms of time and cost and therefore are widely used in various fields such as engineering, marketing, health sciences, food industry, environmental sciences etc., (Fisher, 1935; Yates, 1937; Montgomery, 2007; Şenoğlu and Acıtaş, 2014).

Factorial design is defined as an experimental design in which each level of every factor appears with every level of all other factors, see Hicks (1982), Cox and Reid (2000), Kutner et al. (2004), Tabachnick and Fidell (2007), Onyiah (2008), Wu and Hamada (2009) and Montgomery (2017). Here, a factor is a controlled independent variable whose levels are determined by the experimenter.

There are special cases of factorial designs such as $2^k, 3^k, \dots$ etc., where k denotes the number of factors. In literature, most studies have focused on 2^k factorial designs in the context of parameter estimation and hypothesis testing. For example, Şenoğlu (2005, 2007) obtained robust estimators of the parameters in the 2^k factorial design using the modified maximum likelihood (MML) methodology proposed by Tiku (1967) and proposed test statistics based on these estimators for testing the main and interaction effects when the distributions of error terms are Weibull and generalized logistic, respectively. Şenoğlu et al. (2012) extends their results to the cases where the underlying distributions are short-tailed symmetric and long-tailed symmetric.

To the best of our knowledge, there is no study in the literature on 3^k factorial design in the context of robust estimation and hypothesis testing. In this study, we obtain the MML estimators of the model parameters and propose new tests for testing the main and interaction effects under the assumption that the distribution of error terms is Azzalini's skew-normal (SN), see Azzalini (1985). It should be noted that SN distribution is appropriate for analyzing data following unimodal empirical distribution while exhibiting a certain degree of skewness, a situation that is often encountered in practical applications, see Kim (2005). Therefore, it is extensively used to analyze real-life problems.

If the random variable Y has Azzalini's SN distribution, then it is denoted by $Y \sim SN(\mu, \sigma, \lambda)$. Probability density function (pdf) of SN distribution is given by

$$f(y) = \frac{2}{\sigma} \phi\left(\frac{y-\mu}{\sigma}\right) \Phi\left(\lambda \frac{y-\mu}{\sigma}\right), \quad y, \lambda, \mu \in \mathbb{R}; \quad \sigma \in \mathbb{R}^+. \quad (1)$$

Here, μ , σ and λ are the location, scale and skewness parameters, respectively. Also, ϕ and Φ denote the pdf and cumulative distribution function (cdf) of standard normal distribution, respectively.

Mean, variance, skewness (γ_1) and kurtosis (γ_2) of the random variable Y having standard SN($\mu = 0, \sigma = 1, \lambda$) distribution are given by

$$E(Y) = \sqrt{\frac{2}{\pi}} \left(\frac{\lambda}{\sqrt{1+\lambda^2}} \right), \quad V(Y) = 1 - \frac{2}{\pi} \left(\frac{\lambda}{\sqrt{1+\lambda^2}} \right)^2, \quad \gamma_1 = \frac{1}{2} (4 - \pi) \text{sign}(\lambda) \left(\frac{\lambda^2}{\frac{\pi}{2} + \left(\frac{\pi}{2} - 1\right)\lambda^2} \right)^{3/2}$$

and

$$\gamma_2 = 2(\pi - 3) \left(\frac{\lambda^2}{\frac{\pi}{2} + \left(\frac{\pi}{2} - 1\right)\lambda^2} \right)^2,$$

respectively. See Table 1 for the skewness and kurtosis values of the SN distribution for some selected values of λ .

Table 1: Skewness and kurtosis values of the SN distribution for some selected values of λ .

λ	-10	-3	0	3	10
γ_1	-0.96	-0.67	0.00	0.67	0.96
γ_2	3.82	3.51	3.00	3.51	3.82

It is clear from Table 1 that SN distribution can be symmetric or skewed depending on the value of parameter λ . Plots of the SN density function for different values of λ are shown in Figure 1.

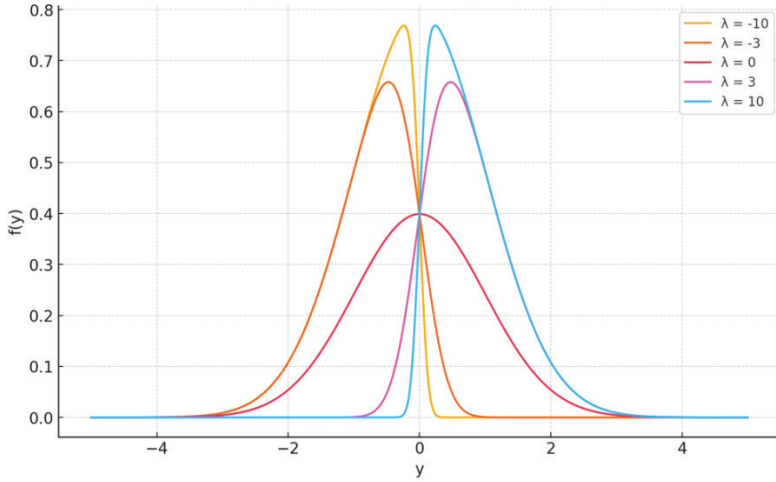


Figure 1: Plots of the SN density function for different values of λ .

It can be seen from Figure 1 and Table 1 that SN distribution reduces to the well-known standard normal distribution when the skewness parameter λ is equal to zero.

The rest of the paper is organized as follows. In Section 2, 3^k factorial design model is defined. In Section 3, MML estimators of the model parameters are obtained. In Section 4, new tests are proposed based on MML estimators for testing the main effects and interaction effects. In Section 5, performances of the MML estimators and proposed tests are compared with the corresponding LS estimators and the tests based on them, respectively, via Monte Carlo simulation study. A simulated data set is analyzed for illustrative purposes in Section 6. The results for the 3^k factorial design are given in Section 7. Finally, concluding remarks are given.

2 The 3^k Factorial Design

It is known that 3^2 and 3^3 factorial designs are the most commonly used special cases of 3^k factorial designs. The 3^2 factorial design is equivalent to a two-way ANOVA model when $i, j = 1, 2, 3$, therefore the results corresponding to the 3^2 factorial design are not given in this study for the sake of brevity, see Çelik (2012) in the context of two-way ANOVA when the distribution of error terms is SN. In this section, we just give the results corresponding to 3^3 factorial design. Obviously, the results obtained in the rest of the paper can easily be extended to the $3^4, 3^5, \dots$ factorial designs.

The mathematical model of 3^3 factorial design with three factors called as A, B and C , each having three levels, is given by

$$y_{ijkl} = \mu + \tau_i + \gamma_j + (\tau\gamma)_{ij} + \delta_k + (\tau\delta)_{ik} + (\gamma\delta)_{jk} + (\tau\gamma\delta)_{ijk} + \varepsilon_{ijkl}, \quad (2)$$

$$i, j, k = 1, 2, 3; l = 1, 2, \dots, n$$

where μ is the overall mean, τ_i, γ_j and δ_k are the effects of the i th level of factor A , j th level of factor B and k th level of factor C , respectively. Also, $(\tau\gamma)_{ij}, (\tau\delta)_{ik}$ and $(\gamma\delta)_{jk}$ are the effects of the two-factor interactions between τ_i and γ_j, τ_i and δ_k, γ_j and δ_k , respectively. $(\tau\gamma\delta)_{ijk}$ is the effect of three-factor interaction between τ_i, γ_j and δ_k . ε_{ijkl} denotes the independent and identically distributed SN error terms. This model is a fixed effect model with the following constraints

$$\sum_{i=1}^3 \tau_i = 0, \sum_{j=1}^3 \gamma_j = 0, \sum_{k=1}^3 \delta_k = 0, \sum_{i=1}^3 (\tau\gamma)_{ij} = 0, \sum_{j=1}^3 (\tau\gamma)_{ij} = 0,$$

$$\sum_{i=1}^3 (\tau\delta)_{ik} = 0, \sum_{k=1}^3 (\tau\delta)_{ik} = 0, \sum_{j=1}^3 (\gamma\delta)_{jk} = 0, \sum_{k=1}^3 (\gamma\delta)_{jk} = 0,$$

$$\sum_{i=1}^3 (\tau\gamma\delta)_{ijk} = 0, \sum_{j=1}^3 (\tau\gamma\delta)_{ijk}, \sum_{k=1}^3 (\tau\gamma\delta)_{ijk}.$$

Pictorial representation of the 3^3 factorial design is given below.

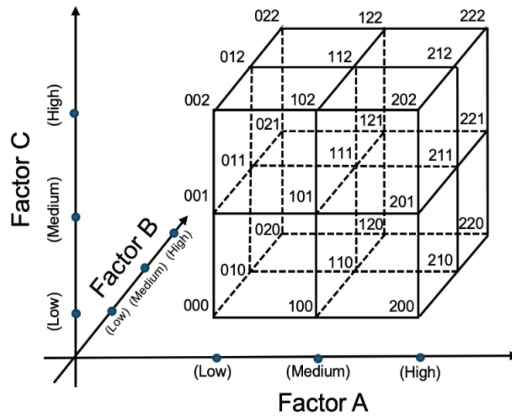


Figure 2: Pictorial representation of the 3^3 factorial design.

Here, it is obvious that there are $3^3=27$ treatment combinations.

3 MML Estimators

In this section, MML estimators of the model parameters in (2) are obtained when the underlying distribution is SN.

Likelihood (L) and log-likelihood ($\ln L$) functions are given by

$$L = \prod_{i=1}^3 \prod_{j=1}^3 \prod_{k=1}^3 \prod_{l=1}^n \frac{2}{\sigma \sqrt{2\pi}} e^{-\frac{1}{2} z_{ijkl}^2} \Phi(\lambda z_{ijkl}) \quad (3)$$

and

$$\begin{aligned} \ln L = N \ln \left(\frac{2}{\sigma} \right) - \frac{N}{2} \ln(2\pi) - \frac{1}{2} \sum_{i=1}^3 \sum_{j=1}^3 \sum_{k=1}^3 \sum_{l=1}^n z_{ijkl}^2 \\ + \sum_{i=1}^3 \sum_{j=1}^3 \sum_{k=1}^3 \sum_{l=1}^n \ln \left(\Phi(\lambda z_{ijkl}) \right), \end{aligned} \quad (4)$$

respectively. Here, $z_{ijkl} = \frac{y_{ijkl} - \mu - \tau_i - \gamma_j - (\tau\gamma)_{ij} - \delta_k - (\tau\delta)_{ik} - (\gamma\delta)_{jk} - (\tau\gamma\delta)_{ijk}}{\sigma}$,
 $N = 3^3 n$ and n is the number of replicates.

The partial derivatives of $\ln L$ function with respect to the parameters of interest give the following likelihood equations

$$\frac{\partial \ln L}{\partial \mu} = \frac{1}{\sigma} \sum_{i=1}^3 \sum_{j=1}^3 \sum_{k=1}^3 \sum_{l=1}^n z_{ijkl} - \frac{\lambda}{\sigma} \sum_{i=1}^3 \sum_{j=1}^3 \sum_{k=1}^3 \sum_{l=1}^n \frac{\phi(\lambda z_{ijkl})}{\Phi(\lambda z_{ijkl})} = 0,$$

$$\frac{\partial \ln L}{\partial \tau_i} = \frac{1}{\sigma} \sum_{j=1}^3 \sum_{k=1}^3 \sum_{l=1}^n z_{ijkl} - \frac{\lambda}{\sigma} \sum_{j=1}^3 \sum_{k=1}^3 \sum_{l=1}^n \frac{\phi(\lambda z_{ijkl})}{\Phi(\lambda z_{ijkl})} = 0,$$

$$\frac{\partial \ln L}{\partial \gamma_j} = \frac{1}{\sigma} \sum_{i=1}^3 \sum_{k=1}^3 \sum_{l=1}^n z_{ijkl} - \frac{\lambda}{\sigma} \sum_{i=1}^3 \sum_{k=1}^3 \sum_{l=1}^n \frac{\phi(\lambda z_{ijkl})}{\Phi(\lambda z_{ijkl})} = 0,$$

$$\frac{\partial \ln L}{\partial \delta_k} = \frac{1}{\sigma} \sum_{i=1}^3 \sum_{j=1}^3 \sum_{l=1}^n z_{ijkl} - \frac{\lambda}{\sigma} \sum_{i=1}^3 \sum_{j=1}^3 \sum_{l=1}^n \frac{\phi(\lambda z_{ijkl})}{\Phi(\lambda z_{ijkl})} = 0,$$

$$\frac{\partial \ln L}{\partial (\tau\gamma)_{ij}} = \frac{1}{\sigma} \sum_{k=1}^3 \sum_{l=1}^n z_{ijkl} - \frac{\lambda}{\sigma} \sum_{k=1}^3 \sum_{l=1}^n \frac{\phi(\lambda z_{ijkl})}{\Phi(\lambda z_{ijkl})} = 0,$$

$$\frac{\partial \ln L}{\partial (\tau\delta)_{ik}} = \frac{1}{\sigma} \sum_{j=1}^3 \sum_{l=1}^n z_{ijkl} - \frac{\lambda}{\sigma} \sum_{j=1}^3 \sum_{l=1}^n \frac{\phi(\lambda z_{ijkl})}{\Phi(\lambda z_{ijkl})} = 0,$$

$$\frac{\partial \ln L}{\partial (\gamma\delta)_{jk}} = \frac{1}{\sigma} \sum_{i=1}^3 \sum_{l=1}^n z_{ijkl} - \frac{\lambda}{\sigma} \sum_{i=1}^3 \sum_{l=1}^n \frac{\phi(\lambda z_{ijkl})}{\Phi(\lambda z_{ijkl})} = 0,$$

$$\frac{\partial \ln L}{\partial (\tau\gamma\delta)_{ijk}} = \frac{1}{\sigma} \sum_{l=1}^n z_{ijkl} - \frac{\lambda}{\sigma} \sum_{l=1}^n \frac{\phi(\lambda z_{ijkl})}{\Phi(\lambda z_{ijkl})} = 0$$

and

$$\frac{\partial \ln L}{\partial \sigma} = -\frac{N}{\sigma} + \frac{1}{\sigma} \sum_{i=1}^3 \sum_{j=1}^3 \sum_{k=1}^3 \sum_{l=1}^n z_{ijkl}^2 - \frac{\lambda}{\sigma} \sum_{i=1}^3 \sum_{j=1}^3 \sum_{k=1}^3 \sum_{l=1}^n z_{ijkl} \frac{\phi(\lambda z_{ijkl})}{\Phi(\lambda z_{ijkl})} = 0.$$

Maximum likelihood (ML) estimators of the unknown model parameters are obtained by solving these equations simultaneously. However, explicit solutions for the parameters cannot be obtained since the likelihood equations have nonlinear function of the parameters defined as $\frac{\phi(\lambda z_{ijkl})}{\Phi(\lambda z_{ijkl})}$.

As a result, numerical methods are necessary to handle the complexities of these functions. However, such methods can lead to convergence problems. To address these problems, we use MML methodology proposed by Tiku (1967), which offers explicit solutions for the likelihood equations. It should be noted that MML estimators maintain the same asymptotic properties with the corresponding ML estimators, for detail see for example Bhattacharya (1985) and Vaughan and Tiku (2000). The following steps are used for deriving MML estimators of the model parameters.

Firstly, observations are sorted in ascending order as $y_{ijk(1)} \leq y_{ijk(2)} \leq \dots \leq y_{ijk(n)}$ and likelihood equations are rewritten in terms of ordered observations as follows

$$\frac{\partial \ln L}{\partial \mu} = \frac{1}{\sigma} \sum_{i=1}^3 \sum_{j=1}^3 \sum_{k=1}^3 \sum_{l=1}^n z_{ijk(l)} - \frac{\lambda}{\sigma} \sum_{i=1}^3 \sum_{j=1}^3 \sum_{k=1}^3 \sum_{l=1}^n w(z_{ijk(l)}) = 0, \quad (5)$$

$$\frac{\partial \ln L}{\partial \tau_i} = \frac{1}{\sigma} \sum_{j=1}^3 \sum_{k=1}^3 \sum_{l=1}^n z_{ijk(l)} - \frac{\lambda}{\sigma} \sum_{j=1}^3 \sum_{k=1}^3 \sum_{l=1}^n w(z_{ijk(l)}) = 0, \quad (6)$$

$$\frac{\partial \ln L}{\partial \gamma_j} = \frac{1}{\sigma} \sum_{i=1}^3 \sum_{k=1}^3 \sum_{l=1}^n z_{ijk(l)} - \frac{\lambda}{\sigma} \sum_{i=1}^3 \sum_{k=1}^3 \sum_{l=1}^n w(z_{ijk(l)}) = 0, \quad (7)$$

$$\frac{\partial \ln L}{\partial \delta_k} = \frac{1}{\sigma} \sum_{i=1}^3 \sum_{j=1}^3 \sum_{l=1}^n z_{ijk(l)} - \frac{\lambda}{\sigma} \sum_{i=1}^3 \sum_{j=1}^3 \sum_{l=1}^n w(z_{ijk(l)}) = 0, \quad (8)$$

$$\frac{\partial \ln L}{\partial (\tau\gamma)_{ij}} = \frac{1}{\sigma} \sum_{k=1}^3 \sum_{l=1}^n z_{ijk(l)} - \frac{\lambda}{\sigma} \sum_{k=1}^3 \sum_{l=1}^n w(z_{ijk(l)}) = 0, \quad (9)$$

$$\frac{\partial \ln L}{\partial (\tau\delta)_{ik}} = \frac{1}{\sigma} \sum_{j=1}^3 \sum_{l=1}^n z_{ijk(l)} - \frac{\lambda}{\sigma} \sum_{j=1}^3 \sum_{l=1}^n w(z_{ijk(l)}) = 0, \quad (10)$$

$$\frac{\partial \ln L}{\partial (\gamma\delta)_{jk}} = \frac{1}{\sigma} \sum_{i=1}^3 \sum_{l=1}^n z_{ijk(l)} - \frac{\lambda}{\sigma} \sum_{i=1}^3 \sum_{l=1}^n w(z_{ijk(l)}) = 0, \quad (11)$$

$$\frac{\partial \ln L}{\partial (\tau\gamma\delta)_{ijk}} = \frac{1}{\sigma} \sum_{l=1}^n z_{ijk(l)} - \frac{\lambda}{\sigma} \sum_{l=1}^n w(z_{ijk(l)}) = 0, \quad (12)$$

and

$$\begin{aligned} \frac{\partial \ln L}{\partial \sigma} = & -\frac{N}{\sigma} + \frac{1}{\sigma} \sum_{i=1}^3 \sum_{j=1}^3 \sum_{k=1}^3 \sum_{l=1}^n z_{ijk(l)}^2 \\ & - \frac{\lambda}{\sigma} \sum_{i=1}^3 \sum_{j=1}^3 \sum_{k=1}^3 \sum_{l=1}^n z_{ijk(l)} w(z_{ijk(l)}) = 0 \end{aligned} \quad (13)$$

$$\text{where } w(z) = \frac{\phi(\lambda z)}{\Phi(\lambda z)}.$$

Note that summation is invariant to ordering, in other words, $\sum_{i=1}^3 \sum_{j=1}^3 \sum_{k=1}^3 \sum_{l=1}^n z_{ijkl} = \sum_{i=1}^3 \sum_{j=1}^3 \sum_{k=1}^3 \sum_{l=1}^n z_{ijk(l)}$.

Secondly, the function $w(z_{ijk(l)})$ is linearized by using the first two terms of the Taylor series expansion as follows

$$\begin{aligned} w(z_{ijk(l)}) & \cong w(t_{(l)}) + [z_{ijk(l)} - t_{(l)}] \left\{ \frac{d}{dz} w(z) \right\}_{z=t_{(l)}}, \\ & \cong \alpha_l - \beta_l z_{ijk(l)}. \quad i, j, k = 1, 2, 3; \quad l = 1, \dots, n \end{aligned}$$

$$\begin{aligned} \text{where } t_{(l)} &= E(z_{ijk(l)}), \quad \alpha_l = \frac{\phi(\lambda t_{(l)})}{\Phi(\lambda t_{(l)})} + t_{(l)} \beta_l \text{ and} \\ \beta_l &= \frac{\phi(\lambda t_{(l)})}{\Phi(\lambda t_{(l)})} \left(\frac{\lambda^2 t_{(l)} \Phi(\lambda t_{(l)}) + \lambda \phi(\lambda t_{(l)})}{\Phi(\lambda t_{(l)})} \right). \end{aligned}$$

Note that $t_{ijk(l)} = t_{(l)}$, $\alpha_{ijk(l)} = \alpha_l$ and $\beta_{ijk(l)} = \beta_l$ since the number of replicates in each cell are equivalent to n .

Approximate values of $t_{(l)}$ are obtained by using the following equality

$$\int_{-\infty}^{t_{(l)}} f(z) dz = \frac{l}{n+1}, \quad l = 1, 2, \dots, n,$$

where $f(z)$ denotes the pdf of standard SN distribution.

By substituting $w(z_{ijk(l)}) \cong \alpha_l - \beta_l z_{ijk(l)}$ into the likelihood equations given in (5)-(13), modified likelihood equations are obtained as follows

$$\frac{\partial \ln L^*}{\partial \mu} = \frac{1}{\sigma} \sum_{i=1}^3 \sum_{j=1}^3 \sum_{k=1}^3 \sum_{l=1}^n z_{ijk(l)} - \frac{\lambda}{\sigma} \sum_{i=1}^3 \sum_{j=1}^3 \sum_{k=1}^3 \sum_{l=1}^n (\alpha_l - \beta_l z_{ijk(l)}) = 0,$$

$$\frac{\partial \ln L^*}{\partial \tau_i} = \frac{1}{\sigma} \sum_{j=1}^3 \sum_{k=1}^3 \sum_{l=1}^n z_{ijk(l)} - \frac{\lambda}{\sigma} \sum_{j=1}^3 \sum_{k=1}^3 \sum_{l=1}^n (\alpha_l - \beta_l z_{ijk(l)}) = 0,$$

$$\frac{\partial \ln L^*}{\partial \gamma_j} = \frac{1}{\sigma} \sum_{i=1}^3 \sum_{k=1}^3 \sum_{l=1}^n z_{ijk(l)} - \frac{\lambda}{\sigma} \sum_{i=1}^3 \sum_{k=1}^3 \sum_{l=1}^n (\alpha_l - \beta_l z_{ijk(l)}) = 0,$$

$$\frac{\partial \ln L^*}{\partial \delta_k} = \frac{1}{\sigma} \sum_{i=1}^3 \sum_{j=1}^3 \sum_{l=1}^n z_{ijk(l)} - \frac{\lambda}{\sigma} \sum_{i=1}^3 \sum_{j=1}^3 \sum_{l=1}^n (\alpha_l - \beta_l z_{ijk(l)}) = 0,$$

$$\frac{\partial \ln L^*}{\partial (\tau\gamma)_{ij}} = \frac{1}{\sigma} \sum_{k=1}^3 \sum_{l=1}^n z_{ijk(l)} - \frac{\lambda}{\sigma} \sum_{k=1}^3 \sum_{l=1}^n (\alpha_l - \beta_l z_{ijk(l)}) = 0,$$

$$\frac{\partial \ln L^*}{\partial (\tau\delta)_{ik}} = \frac{1}{\sigma} \sum_{j=1}^3 \sum_{l=1}^n z_{ijk(l)} - \frac{\lambda}{\sigma} \sum_{j=1}^3 \sum_{l=1}^n (\alpha_l - \beta_l z_{ijk(l)}) = 0,$$

$$\frac{\partial \ln L^*}{\partial (\gamma\delta)_{jk}} = \frac{1}{\sigma} \sum_{i=1}^3 \sum_{l=1}^n z_{ijk(l)} - \frac{\lambda}{\sigma} \sum_{i=1}^3 \sum_{l=1}^n (\alpha_l - \beta_l z_{ijk(l)}) = 0,$$

$$\frac{\partial \ln L^*}{\partial (\tau\gamma\delta)_{ijk}} = \frac{1}{\sigma} \sum_{l=1}^n z_{ijk(l)} - \frac{\lambda}{\sigma} \sum_{l=1}^n (\alpha_l - \beta_l z_{ijk(l)}) = 0$$

and

$$\begin{aligned} \frac{\partial \ln L^*}{\partial \sigma} &= -\frac{N}{\sigma} + \frac{1}{\sigma} \sum_{i=1}^3 \sum_{j=1}^3 \sum_{k=1}^3 \sum_{l=1}^n z_{ijk(l)}^2 \\ &\quad - \frac{\lambda}{\sigma} \sum_{i=1}^3 \sum_{j=1}^3 \sum_{k=1}^3 \sum_{l=1}^n z_{ijk(l)} (\alpha_l - \beta_l z_{ijk(l)}) = 0. \end{aligned}$$

Solutions of these modified likelihood equations give the following MML estimators

$$\hat{\mu} = \hat{\mu}_{....} - \left(\frac{\lambda\Delta}{m}\right) \hat{\sigma}, \quad \hat{\tau}_i = \hat{\mu}_{i...} - \hat{\mu}_{....}, \quad \hat{\gamma}_j = \hat{\mu}_{.j..} - \hat{\mu}_{....}, \quad \hat{\delta}_k = \hat{\mu}_{..k.} - \hat{\mu}_{....},$$

$$(\widehat{\tau\gamma})_{ij} = \hat{\mu}_{ij..} - \hat{\mu}_{i...} - \hat{\mu}_{.j..} + \hat{\mu}_{....}, \quad (\widehat{\tau\delta})_{ik} = \hat{\mu}_{i.k.} - \hat{\mu}_{i...} - \hat{\mu}_{..k.} + \hat{\mu}_{....},$$

$$(\widehat{\gamma\delta})_{jk} = \hat{\mu}_{.jk.} - \hat{\mu}_{.j..} - \hat{\mu}_{..k.} + \hat{\mu}_{....},$$

$$(\widehat{\tau\gamma\delta})_{ijk} = \hat{\mu}_{ijk.} - \hat{\mu}_{ij..} - \hat{\mu}_{i.k.} - \hat{\mu}_{.jk.} + \hat{\mu}_{i...} + \hat{\mu}_{.j..} + \hat{\mu}_{..k.} - \hat{\mu}_{....} \text{ and}$$

$$\hat{\sigma} = \frac{-B + \sqrt{B^2 + 4NC}}{2\sqrt{N(N-3^3)}}.$$

Here,

$$\hat{\mu}_{....} = \frac{\sum_{i=1}^3 \sum_{j=1}^3 \sum_{k=1}^3 \sum_{l=1}^n \theta_l y_{ijk(l)}}{3^3 m}, \quad \hat{\mu}_{i...} = \frac{\sum_{j=1}^3 \sum_{k=1}^3 \sum_{l=1}^n \theta_l y_{ijk(l)}}{3^2 m},$$

$$\hat{\mu}_{.j..} = \frac{\sum_{i=1}^3 \sum_{k=1}^3 \sum_{l=1}^n \theta_l y_{ijk(l)}}{3^2 m},$$

$$\hat{\mu}_{..k.} = \frac{\sum_{i=1}^3 \sum_{j=1}^3 \sum_{l=1}^n \theta_l y_{ijk(l)}}{3^2 m}, \quad \hat{\mu}_{ij..} = \frac{\sum_{k=1}^3 \sum_{l=1}^n \theta_l y_{ijk(l)}}{3m}, \quad \hat{\mu}_{i.k.} = \frac{\sum_{j=1}^3 \sum_{l=1}^n \theta_l y_{ijk(l)}}{3m},$$

$$\hat{\mu}_{.jk.} = \frac{\sum_{i=1}^3 \sum_{l=1}^n \theta_l y_{ijk(l)}}{3m}, \quad \hat{\mu}_{ijk.} = \frac{\sum_{l=1}^n \theta_l y_{ijk(l)}}{m},$$

$$m = \sum_{l=1}^n \theta_l, \quad \theta_l = 1 + \lambda\beta_l, \quad \Delta = \sum_{l=1}^n \alpha_l, \quad N = 3^3 n,$$

$$B = \lambda \sum_{i=1}^3 \sum_{j=1}^3 \sum_{k=1}^3 \sum_{l=1}^n \alpha_l \{y_{ijk(l)} - \hat{\mu}_{ijk}\} \text{ and}$$

$$C = \sum_{i=1}^3 \sum_{j=1}^3 \sum_{k=1}^3 \sum_{l=1}^n \theta_l \{y_{ijk(l)} - \hat{\mu}_{ijk}\}^2.$$

4 Hypothesis Testing

The null hypotheses for testing the main effects and interactions are defined as follows

$$H_{01}: \tau_i = 0, H_{02}: \gamma_j = 0, H_{03}: \delta_k = 0,$$

$$H_{04}: (\tau\gamma)_{ij} = 0, H_{05}: (\tau\delta)_{ik} = 0, H_{06}: (\gamma\delta)_{jk} = 0,$$

and

$$H_{07}: (\tau\gamma\delta)_{ijk} = 0,$$

where $i, j, k = 1, 2, 3$.

For testing the above null hypotheses following test statistics based on MML estimators are proposed

$$F_A^* = \frac{3^2 m \sum_{i=1}^3 \hat{\tau}_i^2}{2\hat{\sigma}^2}, F_B^* = \frac{3^2 m \sum_{j=1}^3 \hat{\gamma}_j^2}{2\hat{\sigma}^2}, F_C^* = \frac{3^2 m \sum_{k=1}^3 \hat{\delta}_k^2}{2\hat{\sigma}^2},$$

$$F_{AB}^* = \frac{3m \sum_{i=1}^3 \sum_{j=1}^3 (\hat{\tau}\hat{\gamma})_{ij}^2}{4\hat{\sigma}^2}, F_{AC}^* = \frac{3m \sum_{i=1}^3 \sum_{k=1}^3 (\hat{\tau}\hat{\delta})_{ik}^2}{4\hat{\sigma}^2}, F_{BC}^* = \frac{3m \sum_{j=1}^3 \sum_{k=1}^3 (\hat{\gamma}\hat{\delta})_{jk}^2}{4\hat{\sigma}^2},$$

and

$$F_{ABC}^* = \frac{m \sum_{i=1}^3 \sum_{j=1}^3 \sum_{k=1}^3 (\hat{\tau}\hat{\gamma}\hat{\delta})_{ijk}^2}{8\hat{\sigma}^2}.$$

Asymptotically, the null distributions of the proposed test statistics follow F distribution with degrees of freedoms $(\nu_1, \nu_8), (\nu_2, \nu_8), (\nu_3, \nu_8), (\nu_4, \nu_8), (\nu_5, \nu_8), (\nu_6, \nu_8)$ and (ν_7, ν_8) , respectively,

$$\nu_1 = \nu_2 = \nu_3 = 2, \nu_4 = \nu_5 = \nu_6 = 4, \nu_7 = 8 \text{ and } \nu_8 = 3^3(n-1)$$

see Lemmas given in Karatepe (2025) and see also Çelik et al. (2015) and Çelik and Şenoğlu (2018) in the context of one-way ANOVA.

To gain insight into how accurate these central F approximations to the percentage points for small sample sizes, the simulated Type I error rates

of these tests are computed via Monte Carlo simulation study using the following equalities

$$P_1 = Prob\{F_A^* \geq F_\alpha(v_1, v_8)|H_{01}\}, P_2 = Prob\{F_B^* \geq F_\alpha(v_2, v_8)|H_{02}\},$$

$$P_3 = Prob\{F_C^* \geq F_\alpha(v_3, v_8)|H_{03}\}, P_4 = Prob\{F_{AB}^* \geq F_\alpha(v_4, v_8)|H_{04}\},$$

$$P_5 = Prob\{F_{AC}^* \geq F_\alpha(v_5, v_8)|H_{05}\}, P_6 = Prob\{F_{BC}^* \geq F_\alpha(v_6, v_8)|H_{06}\}$$

$$\text{and } P_7 = Prob\{F_{ABC}^* \geq F_\alpha(v_7, v_8)|H_{07}\}.$$

The simulated Type I error rates for the proposed tests and their counterparts based on LS estimates, in other words,

$$F_A = \frac{3^2 n \sum_{l=1}^3 \bar{\tau}_l^2}{2\bar{\sigma}^2}, F_B = \frac{3^2 n \sum_{j=1}^3 \bar{\gamma}_j^2}{2\bar{\sigma}^2}, F_C = \frac{3^2 n \sum_{k=1}^3 \bar{\delta}_k^2}{2\bar{\sigma}^2},$$

$$F_{AB} = \frac{3n \sum_{i=1}^3 \sum_{j=1}^3 (\bar{\tau}\bar{\gamma})_{ij}^2}{4\bar{\sigma}^2}, F_{AC} = \frac{3n \sum_{i=1}^3 \sum_{k=1}^3 (\bar{\tau}\bar{\delta})_{ik}^2}{4\bar{\sigma}^2}, F_{BC} = \frac{3n \sum_{j=1}^3 \sum_{k=1}^3 (\bar{\gamma}\bar{\delta})_{jk}^2}{4\bar{\sigma}^2}$$

and

$$F_{ABC} = \frac{n \sum_{l=1}^3 \sum_{j=1}^3 \sum_{k=1}^3 (\bar{\tau}\bar{\gamma}\bar{\delta})_{ljk}^2}{8\bar{\sigma}^2}$$

are presented in Section 5, Table 4. Here, note that we just produce the simulation results for the main effect A and interaction effects AB and ABC . The results for the remaining tests were similar therefore we did not reproduce them for the sake of brevity, however they can be provided upon request from the author. Monte Carlo simulation results show that the simulated Type I error rates of the proposed tests are very close to the nominal level $\alpha = 0.050$. This indicates that the proposed test statistics have an approximate F distribution even for small sample sizes.

5 Monte Carlo Simulation Study

In this section, performances of the proposed tests and their LS based counterparts are compared via Monte Carlo simulation study.

In this study,

- Without loss of generality μ and σ are taken as 0 and 1, respectively.
- The number of replicates is determined as $n = 6, 8, 10$.
- λ is taken to be 0, 1, 3 and 5.
- All simulations are performed using 10,000 Monte Carlo runs.

Before comparing the performances of the test statistics, the efficiencies of the MML estimators of the model parameters are compared with the corresponding LS estimators in the following subsection to ensure the integrity of the study.

5.1 Efficiencies of the Estimators

In this subsection, MML and LS estimators for the parameters of 3^3 factorial design model are compared in terms of bias, mean squares error (MSE), relative efficiency (RE) and deficiency (DEF) criteria defined below

$$Bias(\hat{\theta}) = E(\hat{\theta} - \theta), MSE(\hat{\theta}) = Bias^2(\hat{\theta}) + Var(\hat{\theta}),$$

$$RE = \frac{MSE(\hat{\theta}_{MML})}{MSE(\hat{\theta}_{LS})} \times 100$$

$$\text{and } DEF(\hat{\theta}_1, \hat{\theta}_2, \dots, \hat{\theta}_k) = MSE(\hat{\theta}_1) + MSE(\hat{\theta}_2) + \dots + MSE(\hat{\theta}_k).$$

Here, DEF is defined as the joint efficiency of the estimators $\hat{\theta}_1, \hat{\theta}_2, \dots, \hat{\theta}_k$. Simulated Bias, MSE, RE and DEF values for the LS and MML estimators are given in Tables 2 and 3.

Table 2. Simulated Bias values for the LS and MML estimators.

$\lambda = 0$										
n		μ	τ_1	γ_1	δ_1	$\tau\gamma_{11}$	$\tau\delta_{11}$	$\gamma\delta_{11}$	$\tau\gamma\delta_{111}$	σ
6	LS	0.0016	-0.0000	0.0032	-0.0000	-0.0000	-0.0021	0.0016	0.0016	-0.0000
	MML	0.0016	-0.0000	0.0032	-0.0000	-0.0000	-0.0021	0.0016	0.0016	-0.0000
8	LS	-0.0000	-0.0016	-0.0000	0.0000	0.0000	0.0018	0.0013	-0.0018	-0.0012
	MML	-0.0000	-0.0016	-0.0000	0.0000	0.0000	0.0018	0.0013	-0.0018	-0.0012
10	LS	0.0000	-0.0010	0.0000	-0.0021	0.0003	0.0013	0.0016	-0.0018	-0.0000
	MML	0.0000	-0.0010	0.0000	-0.0021	0.0003	0.0013	0.0016	-0.0018	-0.0000
$\lambda = 1$										
n		μ	τ_1	γ_1	δ_1	$\tau\gamma_{11}$	$\tau\delta_{11}$	$\gamma\delta_{11}$	$\tau\gamma\delta_{111}$	σ
6	LS	0.0018	0.0011	0.0017	0.0000	-0.0011	0.0000	-0.0026	-0.0027	-0.0018
	MML	0.0174	0.0010	0.0017	0.0000	-0.0012	0.0000	-0.0024	-0.0026	0.0023
8	LS	0.0006	-0.0000	-0.0000	-0.0000	0.0000	0.0000	0.0015	-0.0000	-0.0011
	MML	0.0129	-0.0000	-0.0000	-0.0000	-0.0000	0.0000	0.0015	-0.0000	0.0021
10	LS	0.0001	-0.0000	0.0000	-0.0000	-0.0000	0.0000	0.0000	0.0012	-0.0018
	MML	0.0102	-0.0000	0.0000	-0.0000	-0.0000	0.0000	0.0000	0.0012	0.0008
$\lambda = 3$										
n		μ	τ_1	γ_1	δ_1	$\tau\gamma_{11}$	$\tau\delta_{11}$	$\gamma\delta_{11}$	$\tau\gamma\delta_{111}$	σ
6	LS	0.0023	0.0000	-0.0000	-0.0000	-0.0000	-0.0000	0.0000	-0.0034	-0.0024
	MML	0.0668	0.0000	-0.0000	-0.0000	-0.0000	-0.0000	0.0000	-0.0019	-0.0121
8	LS	0.0007	0.0000	0.0000	0.0000	-0.0009	0.0000	0.0000	0.0029	-0.0011
	MML	0.0492	0.0000	0.0000	-0.0000	-0.0011	0.0000	0.0000	0.0020	-0.0076
10	LS	0.0010	-0.0000	-0.0000	0.0000	0.0019	0.0000	0.0009	0.0000	-0.0020
	MML	0.0399	0.0000	-0.0000	0.0000	0.0014	0.0000	0.0011	0.0000	-0.0069
$\lambda = 5$										
n		μ	τ_1	γ_1	δ_1	$\tau\gamma_{11}$	$\tau\delta_{11}$	$\gamma\delta_{11}$	$\tau\gamma\delta_{111}$	σ
6	LS	0.0017	-0.0016	-0.0000	0.0000	-0.0000	0.0000	0.0013	-0.0014	-0.0024
	MML	0.0970	-0.0008	-0.0000	0.0000	0.0000	0.0000	0.0005	-0.0018	-0.0278
8	LS	0.0021	-0.0000	0.0000	-0.0000	-0.0000	-0.0000	0.0014	0.0019	-0.0160
	MML	0.0711	-0.0000	-0.0000	-0.0000	-0.0000	-0.0000	0.0004	0.0014	-0.0174
10	LS	0.0009	-0.0000	0.0017	0.0000	0.0000	0.0000	0.0011	0.0000	-0.0020
	MML	0.0553	-0.0000	0.0008	0.0000	0.0000	0.0000	0.0010	0.0000	-0.0134

Table 3: Simulated MSE, RE and DEF values for the LS and MML estimators

$\lambda = 0$										
MSE										
n		μ	τ_1	γ_1	δ_1	$(\tau\gamma)_{11}$	$(\tau\delta)_{11}$	$(\gamma\delta)_{11}$	$(\tau\gamma\delta)_{111}$	DEF
6	LS	0.0062	0.0125	0.0124	0.0122	0.0247	0.0248	0.0248	0.0483	0.1697
	MML	0.0062	0.0125	0.0124	0.0122	0.0247	0.0248	0.0248	0.0483	0.1697
	RE =	100	100	100	100	100	100	100	100	100
8	LS	0.0047	0.0091	0.0090	0.0094	0.0189	0.0185	0.0186	0.0369	0.1277
	MML	0.0047	0.0091	0.0090	0.0094	0.0189	0.0185	0.0186	0.0369	0.1277
	RE =	100	100	100	100	100	100	100	100	100
10	LS	0.0037	0.0075	0.0075	0.0072	0.0148	0.0148	0.0146	0.0301	0.1022
	MML	0.0037	0.0075	0.0075	0.0072	0.0148	0.0148	0.0146	0.0301	0.1022
	RE =	100	100	100	100	100	100	100	100	100
$\lambda = 1$										
MSE										
n		μ	τ_1	γ_1	δ_1	$(\tau\gamma)_{11}$	$(\tau\delta)_{11}$	$(\gamma\delta)_{11}$	$(\tau\gamma\delta)_{111}$	DEF
6	LS	0.0050	0.0085	0.0084	0.0086	0.0171	0.0173	0.0170	0.0328	0.1185
	MML	0.0052	0.0084	0.0083	0.0085	0.0170	0.0172	0.0169	0.0326	0.1179
	RE =	104	99	99	99	99	99	99	99	100
8	LS	0.0037	0.0063	0.0062	0.0063	0.0125	0.0128	0.0126	0.0251	0.0882
	MML	0.0039	0.0062	0.0062	0.0063	0.0124	0.0127	0.0125	0.0249	0.0878
	RE =	105	98	100	100	99	99	99	99	100
10	LS	0.0030	0.0050	0.0049	0.0050	0.0102	0.0102	0.0100	0.0202	0.0706
	MML	0.0031	0.0049	0.0049	0.0050	0.0102	0.0101	0.0099	0.0200	0.0702
	RE =	103	98	100	100	100	100	99	99	100
$\lambda = 3$										
MSE										
n		μ	τ_1	γ_1	δ_1	$(\tau\gamma)_{11}$	$(\tau\delta)_{11}$	$(\gamma\delta)_{11}$	$(\tau\gamma\delta)_{111}$	DEF
6	LS	0.0031	0.0053	0.0052	0.0052	0.0106	0.0105	0.0107	0.0208	0.0758
	MML	0.0071	0.0043	0.0042	0.0042	0.0087	0.0085	0.0086	0.0171	0.0667
	RE =	229	81	81	81	82	81	80	82	91
8	LS	0.0022	0.0040	0.0040	0.0040	0.0079	0.0080	0.0080	0.0157	0.0570
	MML	0.0043	0.0032	0.0032	0.0033	0.0064	0.0065	0.0065	0.0127	0.0489
	RE =	195	80	80	82	81	81	81	81	88
10	LS	0.0018	0.0032	0.0032	0.0032	0.0062	0.0063	0.0065	0.0125	0.0454
	MML	0.0031	0.0026	0.0025	0.0026	0.0050	0.0051	0.0052	0.0101	0.0384
	RE =	172	81	78	81	81	81	80	81	88
$\lambda = 5$										
MSE										
n		μ	τ_1	γ_1	δ_1	$(\tau\gamma)_{11}$	$(\tau\delta)_{11}$	$(\gamma\delta)_{11}$	$(\tau\gamma\delta)_{111}$	DEF
6	LS	0.0027	0.0049	0.0048	0.0048	0.0099	0.0095	0.0095	0.0188	0.0696
	MML	0.0112	0.0033	0.0032	0.0032	0.0064	0.0064	0.0063	0.0127	0.0572
	RE =	415	67	67	67	65	65	66	68	96
8	LS	0.0020	0.0036	0.0036	0.0037	0.0071	0.0072	0.0072	0.0146	0.0525
	MML	0.0064	0.0023	0.0023	0.0023	0.0045	0.0047	0.0045	0.0094	0.0394
	RE =	320	64	64	62	63	63	62	64	86
10	LS	0.0016	0.0029	0.0029	0.0029	0.0058	0.0056	0.0058	0.0117	0.0419
	MML	0.0041	0.0018	0.0018	0.0018	0.0036	0.0036	0.0036	0.0072	0.0298
	RE =	256	62	62	62	62	62	62	62	85

Simulation results for parameters τ_1 , γ_1 , δ_1 $(\tau\gamma)_{11}$, $(\tau\delta)_{11}$, $(\gamma\delta)_{11}$, $(\tau\gamma\delta)_{111}$ are presented. Simulation results corresponding to the other parameters are similar, therefore they are not given here for the sake of brevity.

It can be seen from Tables 2 and 3 that biases for MML and LS estimators are negligible. Also, as λ increases, except for the LS estimator of the parameter μ , the other LS estimators lose their efficiencies. Therefore,

MML estimators outperform LS estimators according to DEF criteria. It should be noted that since the SN distribution reduces to the standard normal distribution for $\lambda = 0$, the efficiencies of the MML and LS estimators are found to be equal for this case as theory says.

5.2 Performances of the Tests

In this subsection, performances of the proposed tests F_A^* , F_{AB}^* and F_{ABC}^* are compared with the corresponding normal theory tests. Simulated Type I error rates for these tests are given in Table 4, while the simulated power values are presented in Table 5.

Table 4. Simulated Type I error rates of the tests.

n		$\lambda = 0$				$\lambda = 1$		
		A	AB	ABC		A	AB	ABC
6	F	0.053	0.050	0.049	F	0.048	0.044	0.053
	F^*	0.053	0.050	0.049	F^*	0.049	0.043	0.053
8	F	0.046	0.052	0.051	F	0.051	0.053	0.048
	F^*	0.046	0.052	0.051	F^*	0.049	0.052	0.048
10	F	0.051	0.046	0.048	F	0.046	0.049	0.050
	F^*	0.051	0.046	0.048	F^*	0.047	0.049	0.049

n		$\lambda = 3$				$\lambda = 5$		
		A	AB	ABC		A	AB	ABC
6	F	0.050	0.055	0.048	F	0.054	0.054	0.052
	F^*	0.048	0.054	0.046	F^*	0.045	0.048	0.049
8	F	0.051	0.047	0.050	F	0.051	0.051	0.052
	F^*	0.047	0.046	0.046	F^*	0.048	0.042	0.050
10	F	0.052	0.050	0.051	F	0.049	0.049	0.050
	F^*	0.054	0.049	0.050	F^*	0.046	0.046	0.044

Here, it is observed that the simulated Type I error rates of the proposed F_A^* , F_{AB}^* ve F_{ABC}^* tests based on MML estimators as well as those of the F_A , F_{AB} ve F_{ABC} tests based on LS estimators, are very close to the nominal level $\alpha = 0.050$.

It should be noted that to calculate the powers of the mentioned tests, the constant d is added to and subtracted from the observations in the appropriate cells. By "appropriate", we mean that, for instance, when obtaining the powers of the test statistics F_A and F_A^* , constant d is subtracted from the observations at the first level of factor A and added to the observations at the third level of factor A .

Table 5: Simulated power values for the $F_A, F_{AB}, F_{ABC}, F_A^*, F_{AB}^*$ and F_{ABC}^* tests. Table 5: Simulated power values for the $F_A, F_{AB}, F_{ABC}, F_A^*, F_{AB}^*$ and F_{ABC}^* tests.

<i>n</i>	$\lambda = 0$			$\lambda = 1$			$\lambda = 3$			$\lambda = 5$		
	<i>d</i>	F_A	F_A^*	<i>d</i>	F_A	F_A^*	<i>d</i>	F_A	F_A^*	<i>d</i>	F_A	F_A^*
6	0.00	0.056	0.056	0.00	0.048	0.049	0.00	0.050	0.048	0.00	0.054	0.045
	0.08	0.099	0.099	0.07	0.112	0.114	0.05	0.105	0.113	0.05	0.106	0.123
	0.16	0.298	0.298	0.14	0.326	0.327	0.10	0.274	0.318	0.10	0.299	0.405
	0.24	0.583	0.583	0.21	0.643	0.645	0.15	0.559	0.639	0.15	0.589	0.770
	0.32	0.844	0.844	0.28	0.886	0.888	0.20	0.812	0.885	0.20	0.848	0.952
	0.40	0.965	0.965	0.35	0.978	0.978	0.25	0.950	0.979	0.25	0.966	0.996
	0.48	0.995	0.995	0.42	0.998	0.999	0.30	0.992	0.998	0.30	0.996	0.999
8	0.00	0.046	0.046	0.00	0.051	0.049	0.00	0.051	0.047	0.00	0.051	0.048
	0.07	0.108	0.108	0.06	0.110	0.112	0.04	0.093	0.103	0.04	0.099	0.120
	0.14	0.293	0.293	0.12	0.318	0.319	0.08	0.239	0.279	0.08	0.267	0.371
	0.21	0.605	0.605	0.18	0.638	0.639	0.12	0.484	0.565	0.12	0.524	0.711
	0.28	0.853	0.853	0.24	0.878	0.882	0.16	0.743	0.829	0.16	0.787	0.932
	0.35	0.967	0.967	0.30	0.976	0.977	0.20	0.913	0.960	0.20	0.937	0.991
	0.42	0.997	0.997	0.36	0.997	0.997	0.24	0.981	0.994	0.24	0.989	0.999
10	0.00	0.051	0.051	0.00	0.046	0.047	0.00	0.052	0.054	0.00	0.049	0.045
	0.06	0.092	0.092	0.05	0.106	0.106	0.04	0.104	0.118	0.03	0.083	0.098
	0.12	0.279	0.279	0.10	0.285	0.290	0.08	0.290	0.344	0.06	0.190	0.269
	0.18	0.562	0.562	0.15	0.573	0.579	0.12	0.579	0.675	0.09	0.390	0.564
	0.24	0.815	0.815	0.20	0.835	0.837	0.16	0.842	0.911	0.12	0.629	0.825
	0.30	0.958	0.958	0.25	0.958	0.960	0.20	0.967	0.990	0.15	0.826	0.955
	0.36	0.994	0.994	0.30	0.995	0.995	0.24	0.994	0.999	0.18	0.940	0.993

n	$\lambda = 0$			$\lambda = 1$			$\lambda = 3$			$\lambda = 5$		
	d	F_{AB}	F_{AB}^*	d	F_{AB}	F_{AB}^*	d	F_{AB}	F_{AB}^*	d	F_{AB}	F_{AB}^*
6	0.00	0.050	0.050	0.00	0.044	0.043	0.00	0.055	0.054	0.00	0.054	0.054
	0.11	0.100	0.100	0.10	0.106	0.106	0.07	0.089	0.101	0.06	0.083	0.098
	0.22	0.275	0.275	0.20	0.328	0.329	0.14	0.256	0.304	0.12	0.218	0.287
	0.33	0.573	0.573	0.30	0.679	0.680	0.21	0.558	0.649	0.18	0.447	0.618
	0.44	0.850	0.850	0.40	0.916	0.919	0.28	0.832	0.903	0.24	0.728	0.889
	0.55	0.974	0.974	0.50	0.990	0.991	0.35	0.965	0.987	0.30	0.913	0.985
	0.66	0.998	0.998	0.60	0.999	0.999	0.42	0.994	0.999	0.36	0.982	0.999
8	0.00	0.052	0.052	0.00	0.053	0.052	0.00	0.047	0.046	0.00	0.051	0.042
	0.10	0.101	0.101	0.08	0.097	0.094	0.06	0.095	0.103	0.05	0.082	0.090
	0.20	0.301	0.301	0.16	0.285	0.289	0.12	0.256	0.308	0.10	0.198	0.279
	0.30	0.619	0.619	0.24	0.606	0.608	0.18	0.541	0.649	0.15	0.435	0.609
	0.40	0.890	0.890	0.32	0.869	0.872	0.24	0.821	0.899	0.20	0.691	0.881
	0.50	0.985	0.985	0.40	0.978	0.979	0.30	0.962	0.989	0.25	0.892	0.983
	0.60	0.999	0.999	0.48	0.998	0.998	0.36	0.995	0.999	0.30	0.976	0.999
10	0.00	0.046	0.046	0.00	0.049	0.049	0.00	0.049	0.049	0.00	0.049	0.046
	0.09	0.108	0.108	0.07	0.097	0.097	0.05	0.085	0.093	0.04	0.074	0.084
	0.18	0.311	0.311	0.14	0.279	0.282	0.10	0.228	0.267	0.08	0.168	0.229
	0.27	0.631	0.631	0.21	0.584	0.586	0.15	0.491	0.589	0.12	0.348	0.513
	0.36	0.893	0.893	0.28	0.847	0.851	0.20	0.756	0.856	0.16	0.592	0.800
	0.45	0.985	0.985	0.35	0.972	0.974	0.25	0.931	0.974	0.20	0.809	0.957
	0.54	0.999	0.999	0.42	0.997	0.998	0.30	0.989	0.998	0.24	0.936	0.996
n	$\lambda = 0$			$\lambda = 1$			$\lambda = 3$			$\lambda = 5$		
	d	F_{ABC}	F_{ABC}^*	d	F_{ABC}	F_{ABC}^*	d	F_{ABC}	F_{ABC}^*	d	F_{ABC}	F_{ABC}^*
6	0.00	0.049	0.049	0.00	0.053	0.053	0.00	0.048	0.046	0.00	0.052	0.049
	0.14	0.082	0.082	0.12	0.088	0.089	0.10	0.091	0.102	0.08	0.079	0.093
	0.28	0.213	0.213	0.24	0.235	0.234	0.20	0.249	0.296	0.16	0.184	0.240
	0.42	0.477	0.477	0.36	0.503	0.505	0.30	0.562	0.661	0.24	0.389	0.546
	0.56	0.774	0.774	0.48	0.806	0.810	0.40	0.853	0.920	0.32	0.682	0.853
	0.70	0.945	0.945	0.60	0.964	0.966	0.50	0.976	0.993	0.40	0.892	0.981
	0.84	0.993	0.993	0.72	0.996	0.996	0.60	0.999	0.999	0.48	0.980	0.998
8	0.00	0.051	0.051	0.00	0.048	0.048	0.00	0.049	0.046	0.00	0.052	0.049
	0.13	0.089	0.089	0.11	0.095	0.097	0.08	0.079	0.081	0.07	0.079	0.089
	0.26	0.246	0.246	0.22	0.259	0.257	0.16	0.223	0.261	0.14	0.185	0.265
	0.39	0.554	0.554	0.33	0.570	0.571	0.24	0.491	0.589	0.21	0.424	0.597
	0.52	0.848	0.848	0.44	0.878	0.879	0.32	0.795	0.876	0.28	0.699	0.890
	0.65	0.970	0.970	0.55	0.983	0.984	0.40	0.954	0.986	0.35	0.896	0.988
	0.78	0.998	0.998	0.66	0.999	0.999	0.48	0.994	0.999	0.42	0.983	0.999
10	0.00	0.048	0.048	0.00	0.049	0.049	0.00	0.051	0.049	0.00	0.049	0.044
	0.11	0.083	0.083	0.10	0.094	0.095	0.07	0.078	0.086	0.06	0.074	0.087
	0.22	0.224	0.224	0.20	0.277	0.276	0.14	0.213	0.251	0.12	0.170	0.253
	0.33	0.503	0.503	0.30	0.591	0.598	0.21	0.482	0.574	0.18	0.389	0.581
	0.44	0.797	0.797	0.40	0.887	0.893	0.28	0.785	0.873	0.24	0.653	0.873
	0.55	0.956	0.956	0.50	0.983	0.983	0.35	0.940	0.984	0.30	0.879	0.981
	0.66	0.997	0.997	0.60	0.999	0.999	0.42	0.991	0.999	0.36	0.972	0.999

According to the simulation results presented in Table 5, the proposed tests and the corresponding tests have the same power values when $\lambda = 0$, as expected. As the value of λ increases, the proposed tests have significantly higher power values than their competitors based on LS estimators for all n values.

6 Application

In this section, a simulated data set given below is used for illustrative purposes. The data set is generated from $SN(\mu = 0, \sigma = 1, \lambda = 5)$ distribution with $n = 8$. While generating the data set, 0.12 is subtracted from the observations at the first level of factor A and added to the observations at the third level of factor A to make the effect of factor A significant while making the effects of other factors insignificant. It is clear that we have $N = 3^3n = 27(8) = 216$ observations, see Karatepe (2025).

Table 6. The simulated data set.

$l =$	1	2	3	4	5	6	7	8
y_{111l}	0.94076	1.82402	0.45390	0.24360	0.29616	-0.00857	1.46299	1.60721
y_{112l}	-0.07159	1.09816	0.59008	1.63085	1.59823	1.07739	0.53433	0.86774
y_{113l}	0.52236	0.87596	0.77235	1.59143	-0.20259	0.90618	0.77860	-0.05715
y_{121l}	0.28586	0.26604	0.55518	0.45987	0.78339	-0.20301	0.08271	0.05091
y_{122l}	0.95039	0.87465	1.48920	0.51073	0.82210	0.45923	0.47247	-0.02006
y_{123l}	1.82958	-0.05787	0.18501	0.28566	0.71530	0.63942	0.15379	0.72078
y_{131l}	-0.05228	1.39888	0.71806	0.47995	0.30788	0.40931	1.28019	0.23577
y_{132l}	0.62483	-0.38798	0.25132	0.10739	-0.19233	0.81800	1.22529	0.50407
y_{133l}	-0.24190	-0.28843	-0.40937	0.55014	2.49693	0.58843	1.67332	0.42334
y_{211l}	0.07271	2.63804	0.13475	1.90027	0.93597	1.49261	1.30421	0.69792
y_{212l}	0.56769	2.01064	0.96159	0.15793	0.67074	0.72389	1.14254	1.12185
y_{213l}	0.81450	0.98101	0.73412	0.42813	1.53694	0.61090	1.44376	1.01052
y_{221l}	1.52959	0.88139	0.18416	0.51567	1.63791	1.20914	2.36629	1.17290
y_{222l}	0.41243	0.79394	0.71449	-0.08624	2.41717	0.95093	0.65285	1.43707
y_{223l}	0.34534	0.70502	0.51157	0.43643	-0.17207	0.41514	1.20468	-0.13557
y_{231l}	1.39708	0.67572	1.86775	0.75874	1.15505	1.82046	0.98899	2.08457
y_{232l}	0.50292	0.31110	0.11533	1.25228	0.59871	0.63260	0.71677	1.63705
y_{233l}	0.29561	1.70925	0.37797	0.45124	0.85836	2.01860	0.53359	0.14207
y_{311l}	0.90694	0.35210	0.43893	0.48337	0.09438	0.51308	3.77557	0.85741
y_{312l}	1.57982	0.73708	0.00780	0.62315	1.64448	0.08713	0.80877	0.84469
y_{313l}	0.81798	0.25558	3.51811	0.77340	0.19627	0.42258	1.23949	0.73270
y_{321l}	0.49955	0.41549	0.99641	0.61780	0.57192	1.51218	0.81318	1.66778
y_{322l}	0.73376	0.74204	0.93096	1.00208	1.02982	0.24257	1.54391	0.65501
y_{323l}	1.41587	0.19940	1.09771	1.33149	0.50863	2.10126	1.43958	1.65729
y_{331l}	1.81404	1.31595	0.52121	0.38060	1.99278	1.32515	1.13335	0.13158
y_{332l}	0.53306	0.24601	2.02633	0.74805	0.90721	-0.03169	0.21236	0.85262
y_{333l}	1.82766	0.67857	0.58327	0.63276	1.11446	0.36983	1.77726	0.26252

Then the LS and MML estimates of the model parameters $\tau_i, \gamma_j, \delta_k, (\tau\gamma)_{ij}, (\tau\delta)_{ik}, (\gamma\delta)_{jk}$ and $(\tau\gamma\delta)_{ijk}, (i, j, k = 1, 2, 3)$ are given in Table 7. In addition, LS and MML estimates of the parameters μ and σ are obtained as follows

	μ	σ
LS	-0.0025	1.0568
MML	0.0861	1.0237

Table 7. The LS and MML estimates of the model parameters.

	τ_1	τ_2	τ_3	γ_1	γ_2	γ_3	δ_1	δ_2	δ_3
LS	-0.21091	0.10757	0.10335	0.08036	-0.04463	-0.03573	0.09835	-0.06101	-0.03734
MML	-0.20589	0.10787	0.09802	0.03488	0.00232	-0.03720	0.07906	-0.03519	-0.04388
	$(\tau\gamma)_{11}$	$(\tau\gamma)_{12}$	$(\tau\gamma)_{13}$	$(\tau\gamma)_{21}$	$(\tau\gamma)_{22}$	$(\tau\gamma)_{23}$	$(\tau\gamma)_{31}$	$(\tau\gamma)_{32}$	$(\tau\gamma)_{33}$
LS	0.11176	-0.05580	-0.05596	-0.00836	-0.04974	0.05810	-0.10340	0.10554	-0.00214
MML	0.08677	0.01623	-0.10300	0.02199	-0.13861	0.11662	-0.10875	0.12238	-0.01363
	$(\tau\delta)_{11}$	$(\tau\delta)_{12}$	$(\tau\delta)_{13}$	$(\tau\delta)_{21}$	$(\tau\delta)_{22}$	$(\tau\delta)_{23}$	$(\tau\delta)_{31}$	$(\tau\delta)_{32}$	$(\tau\delta)_{33}$
LS	-0.13346	0.10738	0.02608	0.19569	-0.02019	-0.17549	-0.06222	-0.08719	0.14942
MML	-0.05142	0.08779	-0.03638	0.09804	-0.02653	-0.07151	-0.04662	-0.06126	0.10789
	$(\gamma\delta)_{11}$	$(\gamma\delta)_{12}$	$(\gamma\delta)_{13}$	$(\gamma\delta)_{21}$	$(\gamma\delta)_{22}$	$(\gamma\delta)_{23}$	$(\gamma\delta)_{31}$	$(\gamma\delta)_{32}$	$(\gamma\delta)_{33}$
LS	-0.02726	0.03196	-0.00470	-0.09169	0.10347	-0.01179	0.11894	-0.13543	0.01649
MML	-0.08955	0.03525	0.05431	-0.04601	0.08188	-0.03587	0.13557	-0.11713	-0.01843
	$(\tau\gamma\delta)_{111}$	$(\tau\gamma\delta)_{112}$	$(\tau\gamma\delta)_{113}$	$(\tau\gamma\delta)_{121}$	$(\tau\gamma\delta)_{122}$	$(\tau\gamma\delta)_{123}$	$(\tau\gamma\delta)_{131}$	$(\tau\gamma\delta)_{132}$	$(\tau\gamma\delta)_{133}$
LS	0.10936	0.03180	-0.14116	-0.10105	0.03202	0.06903	-0.00831	-0.06382	0.07212
MML	0.09590	0.02666	-0.12256	-0.13988	0.01633	0.12356	0.04398	-0.04299	-0.00099
	$(\tau\gamma\delta)_{211}$	$(\tau\gamma\delta)_{212}$	$(\tau\gamma\delta)_{213}$	$(\tau\gamma\delta)_{221}$	$(\tau\gamma\delta)_{222}$	$(\tau\gamma\delta)_{223}$	$(\tau\gamma\delta)_{231}$	$(\tau\gamma\delta)_{232}$	$(\tau\gamma\delta)_{233}$
LS	-0.12360	-0.03504	0.15864	0.14727	0.05180	-0.19907	-0.02367	-0.01677	0.04044
MML	-0.17691	0.00240	0.17451	0.13074	0.00696	-0.13769	0.04618	-0.00936	-0.03682
	$(\tau\gamma\delta)_{311}$	$(\tau\gamma\delta)_{312}$	$(\tau\gamma\delta)_{313}$	$(\tau\gamma\delta)_{321}$	$(\tau\gamma\delta)_{322}$	$(\tau\gamma\delta)_{323}$	$(\tau\gamma\delta)_{331}$	$(\tau\gamma\delta)_{332}$	$(\tau\gamma\delta)_{333}$
LS	0.01424	0.00324	-0.01748	-0.04622	-0.08382	0.13004	0.03198	0.08058	-0.11256
MML	0.08101	-0.02906	-0.05195	0.00915	-0.02328	0.01414	-0.09016	0.05234	0.03782

The values of the test statistics, corresponding p -values, critical values and degrees of freedoms for the test statistics based on LS and MML estimates are summarized in Table 8. Results of the analysis show that p -values for the F_A^* and F_A tests are smaller than the nominal level $\alpha = 0.050$, while p -values for the other tests are much larger than 0.050 as expected. Therefore, the null hypothesis H_{01} is rejected and the other null hypotheses cannot be rejected. In other words, there is a significant difference between the levels of factor A .

Table 8. Values of the test statistics, corresponding p -values, critical values and degrees of freedoms.

	<i>A</i>	<i>B</i>	<i>C</i>	<i>AB</i>	<i>AC</i>	<i>BC</i>	<i>ABC</i>
	Values of the test statistics						
<i>F</i>	5.546	0.808	1.229	0.644	1.847	0.745	0.492
<i>F*</i>	8.189	0.335	1.212	1.688	0.958	1.174	0.674
	<i>p</i>-values						
<i>F</i>	0.0046	0.4471	0.2949	0.6318	0.1216174	0.5623	0.8609
<i>F*</i>	0.0004	0.7155	0.3000	0.1545	0.4317284	0.3234	0.7143
	Critical values						
	3.044	3.044	3.044	2.419	2.419	2.419	1.988
	Degrees of freedoms						
	(v_1, v_8)	(v_2, v_8)	(v_3, v_8)	(v_4, v_8)	(v_5, v_8)	(v_6, v_8)	(v_7, v_8)
	(2,189)	(2,189)	(2,189)	(4,189)	(4,189)	(4,189)	(8,189)

7 Generalization to k -factors

The results obtained in the previous sections are generalized to the 3^k factorial design.

The mathematical model of 3^k factorial design with k factors, each having three levels, is given by

$$\begin{aligned}
 y_{abc\dots ijkl} = & \mu + \tau_a + \gamma_b + \delta_c + \dots + \phi_i + \psi_j + \nu_k + (\tau\gamma)_{ab} + \dots \\
 & + (\psi\nu)_{jk} + (\tau\gamma\delta)_{abc} + \dots + (\phi\psi\nu)_{ijk} + \dots \\
 & + (\tau\gamma\delta \dots \phi\psi\nu)_{abc\dots ijk} + \varepsilon_{abc\dots ijkl},
 \end{aligned}$$

$$a, b, c \dots i, j, k = 1, 2, 3; l = 1, \dots, n$$

where $\varepsilon_{abc\dots ijkl}$ are independent and identically distributed SN error terms.

The MML estimators for model parameters are obtained as follows

$$\hat{\mu} = \hat{\mu}_{\dots\dots\dots} - \left(\frac{\lambda\Delta}{m}\right) \hat{\sigma},$$

$$\hat{\tau}_a = \hat{\mu}_{a\dots\dots\dots} - \hat{\mu}_{\dots\dots\dots}, \dots, \hat{\nu}_k = \hat{\mu}_{\dots\dots k\dots} - \hat{\mu}_{\dots\dots\dots},$$

$$(\widehat{\tau\gamma})_{ab} = \hat{\mu}_{ab\dots\dots\dots} - \hat{\mu}_{a\dots\dots\dots} - \hat{\mu}_{b\dots\dots\dots} + \hat{\mu}_{\dots\dots\dots}, \dots,$$

$$(\widehat{\psi\nu})_{jk} = \hat{\mu}_{\dots\dots jk\dots} - \hat{\mu}_{\dots\dots j\dots} - \hat{\mu}_{\dots\dots k\dots} + \hat{\mu}_{\dots\dots\dots},$$

$$\begin{aligned}
 (\widehat{\tau\gamma\delta})_{abc} = & \hat{\mu}_{abc\dots\dots\dots} - \hat{\mu}_{ab\dots\dots\dots} - \hat{\mu}_{a.c\dots\dots\dots} - \hat{\mu}_{b.c\dots\dots\dots} + \hat{\mu}_{a\dots\dots\dots} + \hat{\mu}_{b\dots\dots\dots} + \hat{\mu}_{.c\dots\dots\dots} - \hat{\mu}_{\dots\dots\dots} \\
 & , \dots,
 \end{aligned}$$

$$(\widehat{\phi\psi\nu})_{ijk} = \hat{\mu}_{\dots ijk.} - \hat{\mu}_{\dots ij.} - \hat{\mu}_{\dots i.k.} - \hat{\mu}_{\dots .jk.} + \hat{\mu}_{\dots i.} + \hat{\mu}_{\dots .j.} + \hat{\mu}_{\dots .k.} - \hat{\mu}_{\dots},$$

⋮

$$(\tau\gamma\delta\ldots\widehat{\phi\psi\nu})_{abc\dots ijk} = \hat{\mu}_{abc\dots ijk.} - \cdots \pm \hat{\mu}_{\dots} \quad \text{and } \hat{\sigma} = \frac{-B + \sqrt{B^2 + 4NC}}{2\sqrt{N(N-3^k)}}.$$

Here,

$$B = \lambda \sum_{a=1}^3 \sum_{b=1}^3 \sum_{c=1}^3 \cdots \sum_{i=1}^3 \sum_{j=1}^3 \sum_{k=1}^3 \sum_{l=1}^n \alpha_l \{y_{abc\dots ijk(l)} - \hat{\mu}_{abc\dots ijk.}\},$$

$$C = \sum_{a=1}^3 \sum_{b=1}^3 \sum_{c=1}^3 \cdots \sum_{i=1}^3 \sum_{j=1}^3 \sum_{k=1}^3 \sum_{l=1}^n \theta_l \{y_{abc\dots ijk(l)} - \hat{\mu}_{abc\dots ijk.}\}^2$$

and $N = 3^k n$.

Also, it should be noted that the expressions $\hat{\mu}_{a\dots}$, $\hat{\mu}_{ab\dots}$, ..., $\hat{\mu}_{abc\dots}$ etc., are structurally analogous to those defined in earlier sections. Therefore, they are not given here to avoid redundancy. See Section 3 for the coefficients α_l and θ_l .

The null hypotheses for testing the main effects and interactions are defined as follows

$$H_{01}: \tau_a = 0, \dots, H_{0k}: \nu_k = 0,$$

$$H_{0(k+1)}: (\tau\gamma)_{ab} = 0, \dots, H_{0(k+d)}: (\psi\nu)_{jk} = 0,$$

$$H_{0(k+d+1)}: (\tau\gamma\delta)_{abc} = 0, \dots,$$

$$H_{0(k+d+s)}: (\phi\psi\nu)_{ijk} = 0$$

⋮

$$H_{0T}: (\tau\gamma\delta\ldots\phi\psi\nu)_{abc\dots ijk} = 0.$$

Here, k denotes the number of main effects, $d = \binom{k}{2}$, $s = \binom{k}{3}$ and $T = \sum_{r=1}^k \binom{k}{r}$

For testing the null hypotheses about the main and interaction effects following test statistics based on MML estimators are defined as follows

$$F_A^* = \frac{3^{k-1}m \sum_{a=1}^3 \hat{\tau}_a^2}{2\hat{\sigma}^2}, \dots, F_K^* = \frac{3^{k-1}m \sum_{k=1}^3 \hat{\nu}_k^2}{2\hat{\sigma}^2},$$

$$F_{AB}^* = \frac{3^{k-2}m \sum_{a=1}^3 \sum_{b=1}^3 (\widehat{\tau\gamma})_{ab}^2}{2^2\hat{\sigma}^2}, \dots, F_{JK}^* = \frac{3^{k-2}m \sum_{j=1}^3 \sum_{k=1}^3 (\widehat{\psi\nu})_{jk}^2}{2^2\hat{\sigma}^2},$$

$$F_{ABC}^* = \frac{3^{k-3}m \sum_{a=1}^3 \sum_{b=1}^3 \sum_{c=1}^3 (\widehat{\tau\gamma\delta})_{abc}^2}{2^3\hat{\sigma}^2}, \dots, F_{IJK}^* = \frac{3^{k-3}m \sum_{i=1}^3 \sum_{j=1}^3 \sum_{k=1}^3 (\widehat{\phi\psi\nu})_{ijk}^2}{2^3\hat{\sigma}^2}$$

:

$$F_{ABC\dots IJK}^* = \frac{m \sum_{a=1}^3 \sum_{b=1}^3 \sum_{c=1}^3 \dots \sum_{i=1}^3 \sum_{j=1}^3 \sum_{k=1}^3 (\widehat{\tau\gamma\delta\dots\phi\psi\nu})^2}{2^k\hat{\sigma}^2},$$

see Section 3 for the definition of m .

8 Concluding Remarks

In this study, MML estimators of 3^3 factorial design model parameters are obtained in detail under the assumption that the distribution of error terms is SN. Then, new tests have been proposed for testing the main and interaction effects. Efficiencies of the MML estimators and the performances of proposed tests are compared with the corresponding LS estimators and the tests based on LS estimators, respectively, via Monte Carlo simulation study. The results show that as the value of the skewness parameter increases, MML estimators become more efficient when compared to LS estimators. Consequently, it is observed that the proposed tests outperform their competitors as the degree of skewness increases. The results obtained in this study are generalized to 3^k factorial design by following exactly the similar steps in 3^3 factorial design.

References

- Azzalini, A. (1985). A class of distributions which includes the normal ones. *Scandinavian journal of statistics*, 12(2), 171-178.
- Bhattacharyya, G. K. (1985). The asymptotics of maximum likelihood and related estimators based on type II censored data. *Journal of the American Statistical Association*, 80(390), 398-404.
- Cox, D. R., & Reid, N. (2000). *The theory of the design of experiments*. Boca Raton, FL: Chapman and Hall/CRC.
- Çelik, N. (2012). *Robust statistical inference in Anova models using skew distributions and applications*, Ph. D. Thesis, Ankara University.
- Çelik, N., & Şenoğlu, B. (2018). Robust estimation and testing in one-way ANOVA for type II censored samples: Skew normal error terms. *Journal of Statistical Computation and Simulation*, 88(7), 1382-1393.
- Çelik, N., Şenoğlu, B., & Arslan, O. (2015). Estimation and testing in one-way ANOVA when the errors are skew-normal. *Revista Colombiana de Estadística*, 38(1), 75-91.
- Fisher, R. A. (1935). *The design of experiments*. Edinburgh: Oliver and Boyd.
- Hicks, C. R. (1982). *Fundamental concepts in the design of experiments*. New York: Holt, Rinehart and Winston.
- Karatepe, Ö. (2025). *Robust 3^k factorial designs*, Ph. D. Thesis (in progress), Ankara University.
- Kim, H. J. (2005). On a class of two-piece skew-normal distributions. *Statistics*, 39(6), 537-553.
- Kutner, M. H., Nachtsheim, C. J., Neter, J., & Li, W. (2005). *Applied linear statistical models*. McGraw-hill.
- Montgomery, D. C. (2001). *Design and analysis of experiments*. New York, NY: John Wiley & Sons.
- Onyiah, L. C. (2008). *Design and analysis of experiments: classical and regression approaches with SAS*. Boca Raton, FL: CRC Press.
- Şenoğlu, B. (2005). Robust 2^k factorial design with Weibull error distributions. *Journal of Applied Statistics*, 32(10), 1051-1066.
- Şenoğlu, B. (2007). Robust estimation and hypothesis testing in 2^k factorial design. *Communications Faculty of Sciences University of Ankara Series A1 Mathematics and Statistics*, 56(2), 39-50.

- Şenoğlu B., Acıtaş Ş. & Kasap P. (2012). Robust 2^k factorial designs: non-normal symmetric distributions. *Pakistan Journal of Statistics*, 28(1), 93-114.
- Şenoğlu, B., & Acıtaş, Ş. (2014). *İstatistiksel deney tasarımı: Sabit etkili modeller*. Ankara, Türkiye: Nobel Akademik Yayıncılık.
- Tabachnick, B. G., & Fidell, L. S. (2007). *Experimental designs using ANOVA*. Belmont, CA: Thomson/Brooks/Cole.
- Tiku, M. L. (1967). Estimating the mean and standard deviation from a censored normal sample. *Biometrika*, 54(1-2), 155-165.
- Vaughan, D. C., & Tiku, M. L. (2000). Estimation and hypothesis testing for a nonnormal bivariate distribution with applications. *Mathematical and Computer Modelling*, 32(1-2), 53-67.
- Wu, C. F. J., & Hamada, M. S. (2009). *Experiments: Planning, analysis, and optimization* (2nd ed.). Hoboken, NJ: Wiley.
- Yates, F. (1937). *Design and analysis of factorial experiments* (Technical Communication No. 35). London: Imperial Bureau of Soil Science.

Chapter 4

ESTIMATING THE PARAMETERS OF LONG-TAILED SYMMETRIC DISTRIBUTION USING METAHEURISTIC ALGORITHMS

Adil KILIÇ¹, Gamze GÜVEN², Birdal ŞENOĞLU³

1 Dr., Kırıkkale University, ORCID: 0000-0003-3114-9118, adilkilic@kku.edu.tr

2 Doç. Dr., Eskişehir Osmangazi University, ORCID: 0000-0002-8821-3179, gamze-guven@ogu.edu.tr

3 Prof. Dr., Ankara University, ORCID: 0000-0003-3707-2393, senoglu@science.ankara.edu.tr

1 INTRODUCTION

The long-tailed symmetric (LTS) distribution proposed by Tiku and Kumra (1985) is a plausible alternative to the well-known normal distribution for modeling datasets containing outliers and exhibiting heavy-tailed behavior. In the statistical literature, there are several studies considering general linear models such as one way analysis of variance (ANOVA), one-way analysis of covariance (ANCOVA), and regression analysis when the error terms follow an LTS distribution, see for example Kasap et al. (2016), Acitas and Senoglu (2018), Aydin and Senoglu (2018), and Guven et al. (2019) for details. It should be realized that the performance of the statistical tests used in these procedures depends on the accurate estimation of the underlying distribution parameters. In this context, this study focuses on the estimation of the location and scale parameters of the LTS distribution when the shape parameter is known. We therefore use maximum likelihood (ML) methodology because of its well-known theoretical properties. However, likelihood equations associated with the LTS distribution are nonlinear and do not admit closed form solutions. Traditionally, these equations are solved using numerical approaches. Despite their widespread use, numerical approaches may suffer from several drawbacks such as sensitivity to initial values, convergence to incorrect roots, slow convergence, or even failure to converge. To overcome these limitations, metaheuristic optimization algorithms as an alternative to traditional numerical approaches have recently attracted growing attention for the estimation of distribution parameters of interest. For example, Wang and Huang (2014) compared the use of particle swarm optimization (PSO) with the quasi-Newton method and the expectation-maximization (EM) algorithms for ML estimation of a two-component Weibull mixture model. Jha (2016) employed differential evolution (DE) algorithm to obtain ML estimates for censored three-parameter Weibull distribution. Jiang et al. (2017) compared PSO, bat algorithm, and cuckoo search to estimate the Weibull, Rayleigh, gamma, and log-normal parameters. Yalcinkaya et al. (2018) proposed a novel search space for genetic algorithm (GA) constructed from confidence intervals through modified ML (MML) estimators in estimating the unknown parameters of the skew normal distribution. Acitas et al. (2019) used the search space developed by Yalcinkaya et al. (2018) for PSO algorithm for estimating the parameters of Weibull

distribution. Lu et al. (2019) introduced a PSO-based nonlinear least squares method for estimating mixed Weibull distribution parameters. Yalcinkaya et al. (2021) employed the GA to obtain ML estimates of the model parameters for multiple linear regression. Kumar (2021) compared DE, GA, and simulated annealing algorithms to obtain the ML estimates of Weibull distribution parameters for modeling the wind speed. Yalcinkaya et al. (2024) utilized GA-based approach to compute ML estimates of generalized logistic distribution parameters. Kilic and Senoglu (2024) used GA method for ML estimation of the unknown parameters of beta distribution.

In estimating the parameters of LTS distribution, we prefer to use the well-known PSO and DE algorithms among the various metaheuristic optimization algorithms as parallel to their widespread usage in the literature. Since the determination of search space is one of the crucial components of the metaheuristic algorithms, PSO and DE algorithms are implemented under reduced search space (RSS) proposed by Yalçinkaya et al. (2018) as well as fixed search space (FSS), see also Acitas et al. (2019) and Kilic and Senoglu (2024) for the superiority of the RSS approach over FSS. Finally, an extensive Monte Carlo simulation study is performed to evaluate and compare the efficiencies of the PSO and DE algorithms in the R software environment. To maintain the integrity of the study and to compare the efficiencies of derivative-based numerical approaches with the metaheuristics algorithms considered, the Broyden–Fletcher–Goldfarb–Shanno (BFGS) algorithm (Broyden 1965) which is one of the derivative-based quasi-Newton methods is specifically used and incorporated into the study.

2 MATERIAL AND METHODS

This section provides a concise overview of the LTS distribution, ML estimation of its parameters, and the details of the metaheuristic algorithms (i.e., PSO and DE).

2.1 The LTS Distribution

Let Y be a random variable that follows the LTS distribution with the location parameter μ , scale parameter σ , and shape parameter p , denoted

by $Y \sim LTS(\mu, \sigma, p)$. The probability density function (pdf) of Y is defined as follows

$$f(y) = \frac{1}{\sigma \sqrt{k} B\left(\frac{1}{2}, p - \frac{1}{2}\right)} \left(1 + \frac{(y - \mu)^2}{k\sigma^2}\right)^{-p}, y \in \mathbb{R}, -\infty < \mu < \infty, \sigma > 0, p \geq 2 \#(1)$$

where $B(\cdot, \cdot)$ denotes the beta function and $k = 2p - 3$, see Tiku and Kumra (1985). The expected value, variance and kurtosis of the LTS distribution are given by

$$E(Y) = \mu, Var(Y) = \sigma^2, \text{ and } \beta_2 = 3(p - 3/2)/(p - 5/2),$$

respectively.

The kurtosis values of the LTS distribution corresponding to different p values are given in Table 1.

Table 1. Kurtosis values associated with selected p parameters

p	2.5	3	3.5	5	10	∞
β_2	∞	9.0	6.0	4.2	3.4	3.0

It is evident from Table 1 that LTS distribution approaches to the normal distribution when $p \rightarrow \infty$. Also,

$$T = \sqrt{\frac{v}{k}} \left(\frac{Y - \mu}{\sigma} \right) \sim t_v$$

where $v = 2p - 1$.

2.2 ML Estimation

Assume that y_1, y_2, \dots, y_n is a random sample from the $LTS(\mu, \sigma, p)$ distribution. The corresponding log-likelihood ($\ln L$) function is as follows

$$\ln L = -n \ln \left(\sigma \sqrt{k} B\left(\frac{1}{2}, p - \frac{1}{2}\right) \right) - p \sum_{i=1}^n \ln \left(1 + \frac{(y_i - \mu)^2}{k\sigma^2} \right). \#(2)$$

By taking the partial derivatives of the $\ln L$ with respect to μ and σ , the likelihood equations are obtained as follows:

$$\frac{\partial \ln L}{\partial \mu} = \frac{2p}{k\sigma} \sum_{i=1}^n \left(\frac{z_i}{1 + (1/k)z_i^2} \right) = 0 \#(3)$$

and

$$\frac{\partial \ln L}{\partial \sigma} = -\frac{n}{\sigma} + \frac{2p}{k\sigma} \sum_{i=1}^n z_i \left(\frac{z_i}{1 + (1/k)z_i^2} \right) = 0 \#(4)$$

where $z_i = (y_i - \mu)/\sigma$ for $i = 1, 2, \dots, n$.

Since Equations (3) and (4) involve nonlinear functions of the unknown parameters, the derivation of closed-form ML estimators is not feasible. We therefore resort to the PSO and DE algorithms to obtain ML estimates of μ and σ due to the drawbacks of the derivative-based numerical methods mentioned earlier.

2.3 Metaheuristic Algorithms

This section presents the details of PSO and DE algorithms and explains how to determine the search space having significant influence on the performances of the metaheuristic algorithms.

2.3.1 PSO Algorithm

PSO introduced by Kennedy and Eberhart (1995) is a metaheuristic optimization algorithm inspired by the collective behavior of bird flocks. It is classified as a swarm intelligence-based optimizer. In PSO, an individual candidate solution is described as a particle and a collection of particles constitutes a swarm. These particles collaboratively explore the search space by updating their positions based on their past experiences and other particles' experiences. Because of this ability, PSO tends to avoid local optima and instead converges to the global optimum by exploring different areas in the search space. It is widely used due to its advantages, including easy applicability and rapid convergence.

Let there be p particles in the d -dimensional search space. Then, the position and velocity of i th particle are denoted as $X_i = (x_{i,1}, x_{i,2}, \dots, x_{i,d})$ and $V_i = (v_{i,1}, v_{i,2}, \dots, v_{i,d})$, respectively. Also, $Pbest_i^{(k)}$ and $Gbest^{(k)}$ represent the best position of i th particle until the iteration k and the particle's position having the highest fitness value within the swarm at the iteration k , respectively. According to the fitness values of each particle in the swarm, $Pbest_i^{(k)}$ and $Gbest^{(k)}$ are defined as follows

$$Pbest_i^{(k)} = (P_{i,1}, P_{i,2}, \dots, P_{i,d}), i = 1, 2, \dots, p$$

and

$$Gbest^{(k)} = (P_{g,1}, P_{g,2}, \dots, P_{g,d}).$$

The velocity and position of i th particle are updated as given below

$$v_{i,j}^{(k+1)} = w \cdot v_{i,j}^{(k)} + c_1 \cdot r_1 \cdot (P_{i,j}^{(k)} - x_{i,j}^{(k)}) + c_2 \cdot r_2 \cdot (P_{g,j}^{(k)} - x_{i,j}^{(k)}), \quad j = 1, 2, \dots, d \#(5)$$

and

$$x_{i,j}^{(k+1)} = x_{i,j}^{(k)} + v_{i,j}^{(k+1)}, \#(6)$$

respectively. Here, w is the inertia weight, c_1 and c_2 are the acceleration coefficients, r_1 and r_2 are random numbers in $[0,1]$ interval. $c_1 \cdot r_1 \cdot (P_{i,j}^{(k)} - x_{i,j}^{(k)})$ is cognitive component or self-knowledge of the particle. $c_2 \cdot r_2 \cdot (P_{g,j}^{(k)} - x_{i,j}^{(k)})$ is teamwork component or social-knowledge. Each particle's velocity and position are updated until the stopping criterion is met, see also Marini and Walczak (2015) for further details of the PSO algorithm.

2.3.2 DE Algorithm

DE introduced by Storn and Price (1995) is a well-known metaheuristic algorithm inspired by the evolutionary process. It uses crossover and mutation operators similar to GA, but their implementation in DE differs from GA. DE algorithm iteratively searches for the global optimum by applying mutation, crossover, and selection operators to a population of candidate solutions. It is widely adopted for solving complex

optimization problems due to its simplicity and strong global search capability.

Let the population size be N in the d -dimensional search space. Then i th chromosome in the population is represented by $X_i = (x_{i,1}, x_{i,2}, \dots, x_{i,d})$, $i = 1, 2, \dots, N$. The initial population for the DE algorithm is generated as follows

$$x_{i,j}^{(0)} = lb_{i,j} + r \cdot (ub_{i,j} - lb_{i,j}), r \in [0,1], i = 1, 2, \dots, N, j = 1, 2, \dots, d \#(7)$$

where $lb_{i,j}$ and $ub_{i,j}$ are the predetermined lower and upper bounds of the j th gene of i th chromosome. After initialization, the mutation operator is applied to generate the donor chromosome $V_i^{(k)}$ to be used for the crossover operator as follows:

$$V_i^{(k)} = X_{r_1}^{(k)} + F \cdot (X_{r_2}^{(k)} - X_{r_3}^{(k)}), i = 1, 2, \dots, N, r_1 \neq r_2 \neq r_3 \#(8)$$

where, F is the scaling factor, k is the iteration number, and $X_{r_1}^{(k)}$, $X_{r_2}^{(k)}$, and $X_{r_3}^{(k)}$ represent the different chromosomes randomly selected from the population. To increase diversity within the population, the crossover operator is performed on the target chromosome X_i and the corresponding donor chromosome V_i as shown below:

$$u_{i,j}^{(k)} = \begin{cases} v_{i,j}^{(k)}, & \text{if } r_{i,j} < CR \text{ or } j = j_{rand} \\ x_{i,j}^{(k)}, & \text{otherwise} \end{cases} \#(9)$$

where, $r_{i,j} \in [0,1]$, CR is the crossover rate and j_{rand} is a randomly chosen index from $\{1, 2, \dots, d\}$. After the crossover, the trial chromosome U_i is obtained to be used for the selection operator. Which of the target chromosome X_i and the trial chromosome U_i is passed on to the next generation is determined as given below

$$X_i^{(k+1)} = \begin{cases} U_i^{(k)}, & \text{if } f(U_i^{(k)}) \geq f(X_i^{(k)}) \\ X_i^{(k)}, & \text{otherwise} \end{cases} \#(10)$$

where $f(\cdot)$ is the objective function.

2.3.3 Determining the Search Space

The performance of the metaheuristic optimization algorithms depends on their parameter settings such as the search space, initial values of the coefficients, and swarm (or population) size etc. In particular, the proper determination of the search space remarkably increases the convergence speed, computational efficiency and accuracy of the resulting estimates. In literature, a widely used approach in determining the search space is FSS which is a predefined interval. Since the FSS is typically determined based on user experience and the results of previous studies, it is prone to potential improper determination. Therefore, this study employs a data-based search space known as RSS, see Yalcinkaya et al. (2018). RSS is determined by using asymptotic confidence intervals based on the MML estimators of the unknown LTS distribution parameters. Asymptotic confidence intervals for μ and σ are given below

$$\hat{\mu}_{MML} - z_{\alpha/2} \sqrt{\widehat{Var}(\hat{\mu}_{MML})} < \mu < \hat{\mu}_{MML} + z_{\alpha/2} \sqrt{\widehat{Var}(\hat{\mu}_{MML})} \quad (11)$$

and

$$\hat{\sigma}_{MML} - z_{\alpha/2} \sqrt{\widehat{Var}(\hat{\sigma}_{MML})} < \sigma < \hat{\sigma}_{MML} + z_{\alpha/2} \sqrt{\widehat{Var}(\hat{\sigma}_{MML})}, \quad (12)$$

respectively. Here, $z_{\alpha/2}$ is the upper $\alpha/2$ quantile of the standard normal distribution and

$$\hat{\mu}_{MML} = \frac{\sum_{i=1}^n \beta_i y_{(i)}}{m} \text{ and } \hat{\sigma}_{MML} = \frac{B + \sqrt{B^2 + 4nC}}{2\sqrt{n(n-1)}} \quad (13)$$

are the MML estimators of the parameters μ and σ , respectively. Here, $y_{(i)}$ represents the i th ordered observation from the sample. Also,

$$B = \left(\frac{2p}{k}\right) \sum_{i=1}^n \alpha_i (y_{(i)} - \hat{\mu}_{MML}), \quad C = \left(\frac{2p}{k}\right) \sum_{i=1}^n \beta_i (y_{(i)} - \hat{\mu}_{MML})^2, \\ m = \sum_{i=1}^n \beta_i, \quad \alpha_i = \frac{(2/k)t_{(i)}^3}{(1+(1/k)t_{(i)}^2)^2}, \quad \beta_i = \frac{(1-(1/k)t_{(i)}^2)}{(1+(1/k)t_{(i)}^2)^2}$$

and $t_{(i)} = E(z_{(i)})$.

It can be seen from the Equation (13) that $\hat{\mu}_{MML}$ and $\hat{\sigma}_{MML}$ are explicit functions of the sample observations. See Tiku (1967, 1968) and Tiku and Kumra (1985) for details of the MML methodology and LTS distribution.

3 MONTE CARLO SIMULATION STUDY

This section presents a comprehensive Monte Carlo simulation study aimed at comparing the efficiencies of the ML estimators for the location μ and scale σ parameters of the LTS distribution, assuming a known shape parameter. The simulation study includes four optimization algorithms: DE based on RSS (DE-RSS), DE based on FSS (DE-FSS), PSO based on RSS (PSO-RSS), and PSO based on FSS (DE-FSS). It should be remembered that derivative-based BFGS algorithm is also included into the Monte Carlo simulation study because of the reasons mentioned above.

The shape parameter p takes the values 2, 2.5, 3, and 5. Without loss of generality, the values of μ and σ are set to 0 and 1, respectively and the sample sizes n are taken to be 20, 50, 100, and 250. The simulation is repeated $M = 10,000$ times for each scenario. R software environment is used for all computations in this section.

Throughout the simulation study, the settings for DE and PSO are specified as follows:

Settings	
DE	$N = 200, maxit = 200, CR = 0.5, F = 0.8$
PSO	$maxit = 100, s = 50, c_1 = c_2 = 5.3, w = 1.6$

Here, *maxit* and *s* are the number of maximum iteration and swarm size, respectively. Also, in both algorithms, the FSS for μ and σ is specified as $[-1, 1]$ and $(0, 2]$, respectively, to make a fair comparison with its counterpart RSS. As mentioned earlier, the RSS for the parameters μ and σ is defined by using the asymptotic confidence intervals given in Equations (11) and (12).

To evaluate and compare the efficiencies of the estimators, the simulated *Mean*, mean squared error (*MSE*) and deficiency (*DEF*) criteria are used. The simulated *Mean* and *MSE* are calculated as follows

$$Mean(\hat{\theta}) = \sum_{i=1}^M \hat{\theta}_i / M$$

$$MSE(\hat{\theta}) = Var(\hat{\theta}) + \left(Bias(\hat{\theta}) \right)^2$$

where $\hat{\theta}$ represents the estimator of the parameter θ . Also, mathematical definition of *DEF* criteria is defined as follows

$$DEF(\hat{\mu}, \hat{\sigma}) = MSE(\hat{\mu}) + MSE(\hat{\sigma}).$$

The simulated *Mean*, *MSE* and *DEF* values for the estimators of the parameters μ and σ are presented in Table 2. It is worth noting that the simulation results for the PSO-RSS and PSO-FSS methods are almost equivalent to those of the corresponding DE-RSS and DE-FSS methods for all scenarios. Therefore, the results for the PSO-RSS and PSO-FSS are not included into the table to maintain brevity and avoid redundancy.

		$\hat{\mu}$		$\hat{\sigma}$		
Sample Size	Method	Mean	MSE	Mean	MSE	DEF
$p = 2$						
$n = 20$	DE-RSS	-0.0018	0.0239	0.9727	0.0519	0.0758
	DE-FSS	-0.0016	0.0257	0.9725	0.0519	0.0776
	BFGS	-0.0057	0.0258	0.9817	0.0511	0.0769
$n = 50$	DE-RSS	-0.0005	0.0091	0.9900	0.0194	0.0286
	DE-FSS	-0.0004	0.0099	0.9898	0.0194	0.0293
	BFGS	-0.0055	0.0108	0.9976	0.0205	0.0314
$n = 100$	DE-RSS	-0.0007	0.0044	0.9900	0.0092	0.0136
	DE-FSS	-0.0011	0.0047	0.9895	0.0096	0.0144
	BFGS	0.0009	0.0051	0.9949	0.0095	0.0146
$n = 250$	DE-RSS	-0.0003	0.0017	1.0023	0.0040	0.0057
	DE-FSS	-0.0005	0.0019	1.0015	0.0043	0.0062
	BFGS	-0.0003	0.0019	1.0030	0.0044	0.0063
$p = 2.5$						
$n = 20$	DE-RSS	0.0013	0.0335	0.9758	0.0435	0.0770
	DE-FSS	0.0013	0.0360	0.9764	0.0449	0.0810
	BFGS	-0.0014	0.0351	0.9772	0.0441	0.0792
$n = 50$	DE-RSS	0.0026	0.0132	0.9847	0.0168	0.0301

	DE-FSS	0.0029	0.0143	0.9849	0.0176	0.0319
	BFGS	0.0019	0.0141	0.9946	0.0173	0.0315
<i>n</i> = 100	DE-RSS	0.0023	0.0062	0.9939	0.0081	0.0144
	DE-FSS	0.0021	0.0069	0.9938	0.0083	0.0153
	BFGS	-0.0025	0.0071	0.9958	0.0095	0.0166
<i>n</i> = 250	DE-RSS	0.0009	0.0023	0.9993	0.0033	0.0056
	DE-FSS	0.0009	0.0026	0.9999	0.0037	0.0063
	BFGS	0.0013	0.0030	1.0016	0.0037	0.0068
		$\hat{\mu}$		$\hat{\sigma}$		
Sample Size	Method	Mean	MSE	Mean	MSE	DEF
<i>p</i> = 3						
<i>n</i> = 20	DE-RSS	0.0006	0.0381	0.9794	0.0398	0.0779
	DE-FSS	0.0010	0.0409	0.9796	0.0415	0.0824
	BFGS	-0.0006	0.0396	0.9753	0.0409	0.0805
<i>n</i> = 50	DE-RSS	0.0054	0.0146	0.9889	0.0164	0.0310
	DE-FSS	0.0053	0.0161	0.9887	0.0174	0.0336
	BFGS	-0.0015	0.0168	0.9895	0.0162	0.0331
<i>n</i> = 100	DE-RSS	-0.0033	0.0080	0.9959	0.0077	0.0158
	DE-FSS	-0.0032	0.0085	0.9959	0.0083	0.0169
	BFGS	0.0027	0.0079	0.9955	0.0078	0.0157
<i>n</i> = 250	DE-RSS	0.0018	0.0030	0.9929	0.0028	0.0059
	DE-FSS	0.0019	0.0033	0.9935	0.0031	0.0065
	BFGS	-0.0035	0.0033	1.0011	0.0030	0.0063
<i>p</i> = 5						
<i>n</i> = 20	DE-RSS	-0.0037	0.0443	0.9689	0.0322	0.0766
	DE-FSS	-0.0037	0.0476	0.9688	0.0338	0.0815
	BFGS	0.0001	0.0458	0.9715	0.0337	0.0795
<i>n</i> = 50	DE-RSS	0.0067	0.0173	0.9853	0.0138	0.0327
	DE-FSS	0.0065	0.0188	0.9855	0.0138	0.0336
	BFGS	0.0007	0.0179	0.9860	0.0136	0.0315
<i>n</i> = 100	DE-RSS	0.0012	0.0090	0.9932	0.0060	0.0150
	DE-FSS	0.0015	0.0101	0.9936	0.0064	0.0165
	BFGS	0.0008	0.0091	0.9948	0.0069	0.0160
<i>n</i> = 250	DE-RSS	0.0002	0.0032	0.9953	0.0023	0.0056
	DE-FSS	0.0004	0.0035	0.9951	0.0025	0.0061
	BFGS	-0.0022	0.0036	1.0017	0.0029	0.0065

The findings obtained from Table 2 can be summarized as follows:

- The estimators for μ and σ exhibit negligible bias in general; however, for the case where the sample size is $n = 20$, the estimators of the scale parameter σ show a slight bias.
- As expected, the MSE values of all estimators decrease with increasing sample size n .
- According to the MSE and DEF criteria, the DE-RSS method demonstrates superior performance in estimating the μ and σ across the majority of the scenarios considered. A comparison between the DE-FSS and BFGS methods reveals that when $p = 2$, DE-FSS generally yields better performance; however, as the value of p increases, the BFGS method tends to outperform DE-FSS. Furthermore, in general, the performance of DE-FSS increases as compared to BFGS when the sample size n increases, see for example $n = 250$.

4 APPLICATION

A simulated data set consisting of randomly generated $n = 100$ observations from $LTS(\mu = 0, \sigma = 1, p = 2.5)$ distribution is used to illustrate the implementation of the DE-RSS method which outperformed competing methods. The descriptive statistics of the simulated data are provided in Table 3.

Table 3. The descriptive statistics for the simulated data

n	Min	Max	Mean	Median	Variance
100	-3.3892	3.8558	0.0673	-0.0200	1.2186

As a first step, the RSS is obtained as $(-0.1666, 0.1686)$ and $(0.7947, 1.2289)$ for μ and σ , respectively. By incorporating RSS into the DE algorithm, the ML estimates of the unknown parameters are obtained as -0.041 and 1.0046 , respectively. Then, the Kolmogorov–Smirnov (K-S) test is employed to assess whether the distribution of the data set follows an LTS distribution with parameters $\mu = -0.041$, $\sigma = 1.0046$, and $p = 2.5$. The p -value obtained from the K-S test is 0.9996 . Since this

value exceeds the predefined significance level of $\alpha = 0.05$, the null hypothesis

H_0 : Data set follows an LTS distribution with parameters $\mu = -0.041$, $\sigma = 1.0046$, and $p=2.5$

can not be rejected. It is concluded that the data set follows an LTS distribution with the specified parameter values. This is further supported by the LTS Q-Q plot (see Figure 2), which demonstrates that the observations are closely aligned along a straight line.

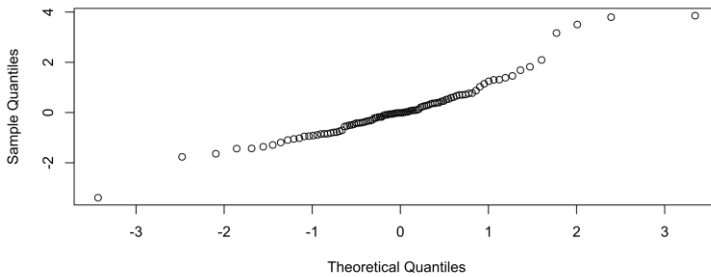


Figure 2. LTS Q-Q plot of the data.

Finally, $LTS(\mu = -0.041, \sigma = 1.0046, p = 2.5)$ is fitted to the histogram of the data set, see Figure 3.

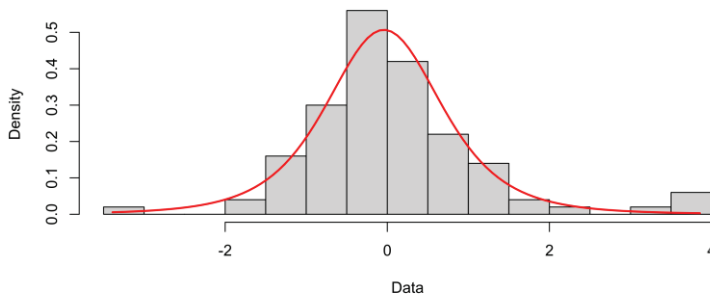


Figure 3. Histogram of the data and the fitted density.

It is apparent that $LTS(\mu = -0.041, \sigma = 1.0046, p = 2.5)$ models the data set accurately. This further demonstrates the strong modeling capability of the LTS distribution when its unknown parameters are estimated via ML using the DE-RSS approach.

5 CONCLUSION

This study focuses on obtaining the ML estimates of the location (μ) and scale (σ) parameters of the LTS distribution under the assumption that the shape parameter (p) is known. For the estimation of the unknown parameters, it is employed well-known metaheuristics algorithms DE and PSO, along with derivative-based BFGS method. Furthermore, the search spaces for the DE and PSO algorithms are determined using two different approaches, namely RSS and FSS. The performances of the metaheuristic algorithms and BFGS are compared through a simulation study. The simulation study results indicate that DE-RSS generally show better performance compared to its rivals. The implementation of the DE-RSS method which outperformed competing methods is illustrated using a simulated data set. As a result, it can be concluded that metaheuristic algorithms DE and PSO have superior performance than the derivative-based BFGS in the context of ML estimation for the unknown LTS parameters, especially when the search space is appropriately determined. In our case, RSS is used as a proper search space.

REFERENCES

- Acitas, S., & Senoglu, B. (2018). Robust factorial ANCOVA with LTS error distributions. *Hacettepe Journal of Mathematics and Statistics*, 47(2), 347-363.
- Acitas, S., Aladag, C. H., & Senoglu, B. (2019). A new approach for estimating the parameters of Weibull distribution via particle swarm optimization: an application to the strengths of glass fibre data. *Reliability Engineering & System Safety*, 183, 116-127.
- Aydın, D., & Şenoğlu, B. (2018). Estimating the missing value in one-way anova under long-tailed symmetric error distributions. *Sigma Journal of Engineering and Natural Sciences*, 36(2), 523-538.
- Broyden, C. G. (1965). A class of methods for solving nonlinear simultaneous equations. *Mathematics of Computation*, 19(92), 577-593.
- Güven, G., Güler, Ö., Şamkar, H., & Şenoğlu, B. (2019). A fiducial-based approach to the one-way ANOVA in the presence of nonnormality and heterogeneous error variances. *Journal of Statistical Computation and Simulation*, 89(9), 1715-1729.
- Jha, S. K. (2016). Computation of Maximum Likelihood Estimates in Three Parameter Weibull for Censored Data. In *Recent Advances in Mathematics, Statistics and Computer Science* (pp. 93-102).
- Jiang, H., Wang, J., Wu, J., & Geng, W. (2017). Comparison of numerical methods and metaheuristic optimization algorithms for estimating parameters for wind energy potential assessment in low wind regions. *Renewable and Sustainable Energy Reviews*, 69, 1199-1217.
- Kasap, P., Senoglu, B., & Arslan, O. (2016). Stochastic analysis of covariance when the error distribution is long-tailed symmetric. *Journal of Applied Statistics*, 43(11), 1977-1997.
- Kennedy, J., & Eberhart, R. (1995, November). Particle swarm optimization. In *Proceedings of ICNN'95 - International Conference on Neural Networks* (Vol. 4, pp. 1942-1948). IEEE.
- Kilic, A., & Senoglu, B. (2024). Point Estimation for the Beta Distribution Parameters Using Genetic Algorithm. In *International Studies and Evaluations In the Field of Science and Mathematics* (pp.149-170), Serüven Yayınevi.
- Kumar, R., & Kumar, A. (2021). Application of differential evolution for wind speed distribution parameters estimation. *Wind Engineering*, 45(6), 1544-1556.

- Lu, Z., Dong, L., & Zhou, J. (2019). Nonlinear least squares estimation for parameters of mixed Weibull distributions by using particle swarm optimization. *IEEE Access*, 7, 60545-60554.
- Marini, F., & Walczak, B. (2015). Particle swarm optimization (PSO). A tutorial. *Chemometrics and Intelligent Laboratory Systems*, 149, 153-165.
- Stron, R., & Price, K. (1995). Differential evolution – a simple and efficient adaptive scheme for global optimization over continuous spaces. *J Glob Optim*, 11, 341-59.
- Tiku, M. L. (1967). Estimating the mean and standard deviation from a censored normal sample. *Biometrika*, 54(1-2), 155-165.
- Tiku, M. L. (1968). Estimating The Parameters of Normal and Logistic Distributions from Censored Samples 1. *Australian Journal of Statistics*, 10(2), 64-74.
- Tiku, M. L., & Kumra, S. (1985). Expected values and variances and covariances of order statistics for a family of symmetric distributions (Student's t). *Selected Tables in Mathematical Statistics*, 8, 141-270.
- Wang, F. K., & Huang, P. R. (2014). Implementing particle swarm optimization algorithm to estimate the mixture of two Weibull parameters with censored data. *Journal of Statistical Computation and Simulation*, 84(9), 1975-1989.
- Yalçinkaya, A., Şenoğlu, B., & Yolcu, U. (2018). Maximum likelihood estimation for the parameters of skew normal distribution using genetic algorithm. *Swarm and Evolutionary Computation*, 38, 127-138.
- Yalçinkaya, A., Balay, İ. G., & Şenoğlu, B. (2021). A new approach using the genetic algorithm for parameter estimation in multiple linear regression with long-tailed symmetric distributed error terms: An application to the Covid-19 data. *Chemometrics and Intelligent Laboratory Systems*, 216, 104372.
- Yalçinkaya, A., Kılıç, A., & Şenoğlu, B. (2024). Estimating the Parameters of Generalized Logistic Distribution via Genetic Algorithm Based on Reduced Search Space. *Journal of Mathematical Sciences*, 1–17.

Chapter 5

TESTING BLOCKS FOR QUASI-METRIC VALIDATION IN FINITE TOPOLOGIES

Bünyamin YILDIZ¹

¹ Prof. Dr. , Hatay Mustafa Kemal Üniversitesi, ORCID ID: 0000-0002-0792-9520

Preface

Topology studies fundamental spatial properties preserved under continuous deformations—such as connectedness, compactness, and convergence—independent of precise distances or angles; this chapter explores the transformative combinatorial framework of binary quasimetrics, pioneered by Ercan and Vural, which encodes topological structures on finite sets into families of 0-1 matrices, enabling powerful enumeration techniques and revealing deep connections between continuous spaces and discrete combinatorics, while developing both theoretical foundations and practical counting methods illustrated through extensive examples that demonstrate how every topology corresponds to matrix patterns, continuous functions to matrix operations, and topological generation to combinatorial enumeration, ultimately providing new insights into the super-exponential growth of topological spaces and their applications across physics, computer science, and algebraic geometry.

1 Historical Development

The systematic enumeration of topological spaces represents one of combinatorics' most intricate challenges, blending set theory, lattice theory, and algebraic structures into a rich tapestry of mathematical discovery. This journey began in earnest during the mid-20th century when mathematicians first seriously considered the combinatorial complexity of topological structures.

The Foundational Period (1940s-1960s)

The quest originated not with topology itself, but with related combinatorial structures:

- **1942:** Garrett Birkhoff's lattice theory work first hinted at topological enumeration through his analysis of closure operators
- **1950:** Oystein Ore published the first connection between topologies and preorders, recognizing that every topology induces a specialization order
- **1960:** Richard Stanley established the fundamental relationship between topologies and quasi-orders, proving they share the same enumeration sequence

The true breakthrough came in 1966 when V. Krishnamurthy published his seminal paper *On the Number of Topologies on a Finite Set* in the *American Mathematical Monthly*. Krishnamurthy's approach was revolutionary for its time.

Krishnamurthy achieved this by:

1. Observing that topologies correspond to families of closed sets
2. Noticing that closed sets must be closed under arbitrary intersections and finite unions
3. Developing a matrix representation where each column indicates set containment

Despite this breakthrough, actual enumeration remained computationally infeasible beyond $n = 4$. The 29 topologies for $n = 3$ were known, but confirming the 355 topologies for $n = 4$ required extensive hand calculation and was errorprone.

Yet fundamental challenges persisted:

- No closed-form formula for $T(n)$ existed
- The best bounds $\left(O\left(2^{n^2/n!}\right)\right)$ remained imprecise
- Matrix representations were high-dimensional and inefficient

The Quasi-Metric Revolution (2010s-Present)

The field transformed dramatically in 2019 when Z. Ercan and M. Vural published their landmark paper All Topologies Come From a Family of 0-1-valued Quasimetrics. Their breakthrough consisted of three fundamental insights:

Theorem 1.1 (Ercan-Vural Representation). For any topology τ on X , there exists a family of binary quasi-metrics $\{d_U\}_{U \in \tau}$ where:

$$d_U(x, y) = \chi_U(x) \chi_{U^c}(y)$$

that generates exactly τ .

This representation had profound implications:

1. Topological generation reduced to matrix operations
2. Continuous functions corresponded to matrix homomorphisms
3. Topological products translated to tensor products

Vural's subsequent work established powerful combinatorial tools:

Theorem 1.2. For $n > 2$:

$$T(n) \leq 2^{n^2-n} - 2^{n^2-n-3}$$

The proof strategy featured innovative concepts:

- Testing matrices that validate triangle inequalities

- Pivot triplets detecting "unwelcome situations"
- Quasi-metric algebras with \diamond operations

The historical journey reveals a fascinating evolution: from Birkhoff's abstract lattices to Krishnamurthy's set-theoretic approach, through computational combinatorics, arriving at Ercan and Vural's elegant matrix representation. This progression demonstrates mathematics' characteristic interplay between abstract theory and concrete computation, where each advance illuminates previously hidden structures.

2 Foundations of Topology

Definition 2.1 (Topology). A topology on a set X is a collection $\tau \subseteq \mathcal{P}(X)$ satisfying:

1. $\emptyset, X \in \tau$
2. $\bigcup_{i \in I} U_i \in \tau$ for any $\{U_i\}_{i \in I} \subseteq \tau$
3. $\bigcap_{i=1}^n U_i \in \tau$ for any finite $\{U_i\}_{i=1}^n \subseteq \tau$

Elements of τ are called open sets.

Definition 2.2 (Continuous Function). A function $f: (X, \tau_X) \rightarrow (Y, \tau_Y)$ is continuous if $f^{-1}(V)$ is open in X for every open V in Y .

3 Bases and Subbases

Definition 3.1 (Base). A collection $\mathcal{B} \subseteq \mathcal{P}(X)$ is a base for topology τ if:

1. $\forall x \in X, \exists B \in \mathcal{B}: x \in B$
2. $\forall B_1, B_2 \in \mathcal{B}, \forall x \in B_1 \cap B_2, \exists B_3 \in \mathcal{B}: x \in B_3 \subseteq B_1 \cap B_2$

The topology τ consists of all unions of base elements.

Example 3.2 (Standard Topology on \mathbb{R}). The collection $\mathcal{B} = \{(a, b) \mid$

$a < b\}$ is a base. The open interval $(0,1)$ is a base element, while $[0,1)$ is not open.

Definition 3.3 (Subbase). A collection $\mathcal{S} \subseteq \mathcal{P}(X)$ is a subbase if $\bigcup_{S \in \mathcal{S}} S = X$. The generated topology is the smallest topology containing \mathcal{S} , with base formed by finite intersections of subbase elements.

Example 3.4 (Product Topology Subbase). For $X \times Y$, the subbase is $\{\pi_X^{-1}(U), \pi_Y^{-1}(V) \mid U \subseteq X, V \subseteq Y \text{ open}\}$.

4 Quasi-Metrics and Topological Structures

Definition 4.1 (Quasi-Metric). A quasi-metric on X is $d: X \times X \rightarrow [0, \infty)$ satisfying:

1. $d(x, x) = 0 \ \forall x \in X$
2. $d(x, z) \leq d(x, y) + d(y, z) \ \forall x, y, z \in X$

Remark 4.2. Quasi-metrics generalize metrics by relaxing symmetry and separation:

- May have $d(x, y) \neq d(y, x)$
- $d(x, y) = 0 \nRightarrow x = y$

Example 4.3 (Taxicab Geometry Variant). On \mathbb{R}^2 , define $d((x_1, y_1), (x_2, y_2)) = \max(|x_1 - x_2|, 0) + |y_1 - y_2|$. This is asymmetric in x -coordinate.

Theorem 4.4 (Quasi-Metric Topology). Every quasi-metric d induces a topology with base:

$$\mathcal{B} = \{B_d(x, \epsilon) \mid x \in X, \epsilon > 0\}$$

where $B_d(x, \epsilon) = \{y \in X \mid d(x, y) < \epsilon\}$.

5 Binary Quasi-Metrics and Topology

Definition 5.1 (0-1-Valued Generalized Quasi-Metric). A family $d: X \times X \rightarrow \{0,1\}^I$ where each $d_i(x, y) = d(x, y)(i)$ satisfies:

1. $d_i(x, x) = 0$
2. $d_i(x, z) \leq d_i(x, y) + d_i(y, z)$

The induced topology has $U \subseteq X$ open if:

$$\forall x \in U, \exists \text{ finite } J \subseteq I: \bigcap_{i \in J} \{y \mid d_i(x, y) = 0\} \subseteq U$$

Theorem 5.2 (Ercan-Vural Representation). For any topology τ on X , there exists $I = \tau$ and:

$$d_U(x, y) = \begin{cases} 0 & x \in U \Rightarrow y \in U \\ 1 & x \in U \text{ and } y \notin U \end{cases}$$

such that τ is exactly the topology generated by $(d_U)_{U \in \tau}$.

Example 5.3 (Discrete Topology Representation). For $X = \{a, b\}$ with discrete topology $\tau = \{\emptyset, \{a\}, \{b\}, X\}$:

$$d_{\{a\}} = \begin{pmatrix} 0 & 1 \\ 0 & 0 \end{pmatrix}$$

$$d_{\{b\}} = \begin{pmatrix} 0 & 0 \\ 1 & 0 \end{pmatrix}$$

The topology is generated by these two matrices.

6 Matrix Representation for Finite Topologies

Definition 6.1 (Related Matrix). For $U \in \tau$, the related matrix M^U has entries:

$$a_{ij} = d_U(x_i, x_j) = \chi_U(x_i) \cdot \chi_{U^c}(x_j)$$

Proposition 6.2 (Matrix Characterization). An $n \times n$ matrix $M = [a_{ij}]$ with $a_{ij} \in \{0,1\}$ represents a quasi-metric iff:

1. $a_{ii} = 0 \forall i$
2. $a_{ij} = 1$ and $a_{ik} = 0 \Rightarrow a_{kj} = 1$

Example 6.3 (Topology Matrices for $n = 3$). For $X = \{1,2,3\}$ with topology $\tau = \{\emptyset, \{1\}, \{1,2\}, X\}$:

$$M^{\{1\}} = \begin{pmatrix} 0 & 1 & 1 \\ 0 & 0 & 0 \\ 0 & 0 & 0 \end{pmatrix}$$

$$M^{\{1,2\}} = \begin{pmatrix} 0 & 0 & 1 \\ 0 & 0 & 1 \\ 0 & 0 & 0 \end{pmatrix}$$

The topology is generated by these matrices.

Theorem 6.4 (Uniqueness). Distinct non-trivial open sets produce distinct related matrices. Only \emptyset and X both map to the zero matrix.

7 Combinatorial Enumeration of Topologies

Theorem 7.1 (Krishnamurthy's Bound). The number $T(n)$ of topologies on n elements satisfies:

$$T(n) \leq 2^{n^2-n-1}$$

Theorem 7.2 (Vural's Improved Bound). For $n > 2$:

$$T(n) \leq 2^{n^2-n} - 2^{n^2-n-3}$$

Proof Strategy. 1. Total possible matrices: 2^{n^2-n} (zero diagonal)

2. Identify "unwelcome situations": Triples (i, j, k) where $a_{ij} = 1, a_{ik} = 0$, but $a_{kj} = 0$

3. For $n \geq 3$, show at least 2^{n^2-n-3} matrices contain unwelcome situations
4. Valid quasi-metrics are the remainder

Example 7.3. The enumeration of topologies on finite sets reveals a fascinating combinatorial landscape where theoretical bounds and actual counts diverge in instructive ways. The table below compares the exact number of topologies $T(n)$ with Vural's upper bound for small values of n :

n	$T(n)$	Vural's Bound	$\frac{\text{Bound}}{T(n)}$	$\log_2(\text{ Bound } /T(n))$
1	1	1	1.00	0
2	4	4	1.00	0
3	29	56	1.93	0.95
4	355	3,584	10.10	3.33
5	6,942	917,504	132.16	7.05
6	209,527	939,524,096	4,484.70	12.13
7	9,535,241	7,516,192,768	788.13	9.62

Vural's bound exactly equals $T(n)$ since all 2^{n^2-n} possible matrices satisfy the quasi-metric conditions at this scale. For $n = 2$, the 4 matrices correspond exactly to:

- Trivial topology: $\begin{pmatrix} 0 & 0 \\ 0 & 0 \end{pmatrix}$
- Two Sierpiński topologies: $\begin{pmatrix} 0 & 1 \\ 0 & 0 \end{pmatrix}, \begin{pmatrix} 0 & 0 \\ 1 & 0 \end{pmatrix}$

- Discrete topology: $\begin{pmatrix} 0 & 1 \\ 1 & 0 \end{pmatrix}$

At $n = 3$, the bound (56) is nearly double the actual count (29), revealing the impact of triangle inequality constraints. The 27 "missing" topologies correspond to matrices violating the quasi-metric condition $a_{ij} = 1 \wedge a_{ik} = 0 \Rightarrow a_{kj} = 1$.

While the absolute gap grows, the relative tightness improves compared to earlier bounds. Krishnamurthy's bound 2^{n^2-n-1} is twice as large as Vural's for $n > 2$:

n	Krishnamurthy/Vural	Vural / $T(n)$
3	2.00	1.93
4	2.00	10.10
5	2.00	132.16

Computational frontier: The exact enumeration becomes computationally infeasible beyond $n = 7$ (9.5 million topologies). For $n = 8$, estimates suggest approximately 1.5 billion topologies, while Vural's bound gives 7.86×10^{13} .

Why the gap grows: The bound counts valid quasi-metrics, while $T(n)$ counts distinct topologies. The discrepancy comes from:

- Redundancy: Multiple quasi-metrics can generate the same topology
- Topological constraints: Additional axioms (e.g., T_0 separation) reduce counts

- Symmetry: Automorphisms create equivalence classes

8 Testing Matrix Validity

Definition 8.1 (Pivot Triplet). For matrix $[a_{ij}]$ and indices i, j, k , the pivot triplet is:

$$p_{i,j,k} = [a_{ij}, a_{ik}, a_{kj}]$$

The triangle inequality requires:

$$a_{ij} \leq a_{ik} + a_{kj} \Leftrightarrow \neg(a_{ij} = 1 \wedge a_{ik} = 0 \wedge a_{kj} = 0)$$

Definition 8.2 (Testing Matrix). The i -th testing matrix T_i has entries:

$$T_i[j, k] = p_{i,j,k} = [a_{ij}, a_{ik}, a_{kj}]$$

Example 8.3 (Testing Matrix for $n = 2$). Consider matrix $\begin{pmatrix} 0 & 1 \\ 0 & 0 \end{pmatrix}$:

$$T_1 = \begin{bmatrix} [0,0,0] & [0,1,0] \\ [1,0,1] & [1,1,0] \end{bmatrix}, T_2 = \begin{bmatrix} [0,0,0] & [0,0,1] \\ [0,0,0] & [0,0,0] \end{bmatrix}$$

Check triangle inequalities:

- $T_1[2,1] : [1,0,1]$ requires $1 \leq 0 + 1$ (true)
- $T_1[2,2] : [1,1,0]$ requires $1 \leq 1 + 0$ (true)

Valid quasi-metric.

Example 8.4 (Testing Matrix for Symmetric Case). Consider the symmetric matrix $A = \begin{pmatrix} 0 & 1 \\ 1 & 0 \end{pmatrix}$ representing a metric. The testing matrices are:

$$T_1 = \begin{bmatrix} [0,0,0] & [0,1,1] \\ [1,0,1] & [1,1,0] \end{bmatrix}, T_2 = \begin{bmatrix} [1,1,0] & [1,0,1] \\ [0,1,1] & [0,0,0] \end{bmatrix}$$

Verification of triangle inequalities:

- $T_1[1,2] : [0,1,1]$ requires $0 \leq 1 + 1$ (true)
- $T_1[2,1] : [1,0,1]$ requires $1 \leq 0 + 1$ (true)
- $T_2[1,1] : [1,1,0]$ requires $1 \leq 1 + 0$ (true)
- $T_2[1,2] : [1,0,1]$ requires $1 \leq 0 + 1$ (true)

All conditions satisfied - valid metric space.

Example 8.5 (Testing Matrix for $n = 3$ with Violation). Consider matrix

$B = \begin{pmatrix} 0 & 1 & 0 \\ 0 & 0 & 1 \\ 1 & 0 & 0 \end{pmatrix}$. The first testing matrix T_1 is:

$$T_1 = \begin{bmatrix} [0,0,0] & [0,1,0] & [0,0,1] \\ [1,0,0] & [1,1,0] & [1,0,0] \\ [0,0,1] & [0,1,0] & [0,0,0] \end{bmatrix}$$

Critical checks:

- $T_1[2,1] : [1,0,0]$ requires $1 \leq 0 + 0$? False (violation)
- $T_1[2,3] : [1,0,0]$ requires $1 \leq 0 + 0$? False (violation)

The pivot triplet $[1,0,0]$ appears at positions $(2,1)$ and $(2,3)$, violating the triangle inequality $d(x_1, x_2) \leq d(x_1, x_k) + d(x_k, x_2)$ for $k = 1, 3$.

This matrix fails the quasi-metric test.

9 Algorithms for Generating Topologies

Proposition 9.1 (Matrix Generation). All topologies on n elements can be generated by:

1. Generate all 2^{n^2-n} binary matrices with zero diagonal
2. Filter matrices satisfying $\forall i, j, k: (a_{ij} = 1 \wedge a_{ik} = 0) \Rightarrow a_{kj} = 1$

3. Group matrices by the topology they generate

Remark 9.2. This naive approach has complexity $O(2^{n^2})$, feasible only for $n \leq 4$. More efficient algorithms use lattice generation or preorder enumeration.

Example 9.3 (Algorithm for $n = 3$). There are $2^{9-3} = 64$ candidate matrices. After filtering:

- 29 valid quasi-metrics
- 19 distinct topologies (some matrices generate same topology)
- 10 topologies correspond to T0 spaces

10 Applications

10.1 Computational Topology

Binary quasi-metric representations enable efficient topology computation in:

- Point cloud data analysis
- Persistent homology calculations
- Topological data structures

10.2 Logic and Computer Science

Applications include:

- Domain theory in programming language semantics models for concurrency
- Knowledge representation systems

Conclusion

The representation of topological structures through binary quasi-metrics has fundamentally transformed our understanding of finite topological spaces, establishing a powerful combinatorial framework that bridges continuous mathematics and discrete computation. By translating topological axioms into matrix operations—where open sets correspond to specific 0-1 patterns, continuous functions to matrix homomorphisms, and topological generation to combinatorial enumeration—this approach has enabled unprecedented insights into the structural complexity of topological spaces. The quasi-metric paradigm demonstrates that topology is inherently combinatorial at its core, with the super-exponential growth $T(n)$ reflecting profound combinatorial richness rather than geometric complexity. Vural's bound $T(n) \leq 2^{n^2-n} - 2^{n^2-n-3}$ for $n > 2$ represents a landmark achievement in this field, significantly improving Krishnamurthy's classical result by systematically excluding invalid matrices through the identification of "unwelcome situations" in testing matrices, while also revealing the intricate constraints imposed by the triangle inequality in quasi-metric spaces.

Despite these advances, fundamental challenges remain unresolved. The exact enumeration problem for $n \geq 5$ continues to defy complete classification, with $T(10)$ estimated to exceed 10^{30} and no closed-form formula yet discovered. The tension between combinatorial expressiveness and computational feasibility persists, as current algorithms still face exponential complexity barriers. Moreover, deeper structural questions await investigation: the precise relationship between quasi-metric algebras and topology lattices remains incompletely characterized, the categorical foundations of this correspondence warrant further exploration, and potential connections to sheaf theory and topos

theory suggest rich avenues for generalization. Looking forward, three promising frontiers emerge: quantum computational approaches that could potentially crack $n \geq 10$ through superposition and entanglement; machine learning methods that might discover novel topology patterns in high-dimensional spaces; and physical applications in topological quantum computing where quasi-metric representations could optimize qubit arrangements. Ultimately, this combinatorial reframing of topology has not only provided powerful new enumeration techniques but has fundamentally reshaped our conception of topological structure itself—revealing that continuity, when viewed through the discrete lens of binary relations, becomes a combinatorial phenomenon of remarkable depth and beauty.

Exercises

1. Verify the 4 topologies for $n = 2$ and their matrix representations
2. Show that the discrete topology on n elements requires n generating matrices
3. Prove that $d_U \diamond d_V = d_{U \cap V}$
4. For $X = \{a, b, c\}$, construct matrices for the topology $\{\emptyset, \{a, b\}, X\}$
5. Calculate Vural's bound for $n = 4$ and compare to actual $T(4) = 355$

References

1. Benoumhani, M. (2006). The number of topologies on a finite set. *Journal of Integer Sequences*, 9.
2. Ercan, Z., & Vural, M. (2019). All topologies come from a family of 0-1-valued quasimetrics. *Bulletin of Iranian Mathematical Society*, 45, 835.
3. Goubault-Larrecq, J. (2013). *Non-Hausdorff topology and domain theory*. Cambridge University Press.
4. Krishnamurthy, V. (1966). On the number of topologies on a finite set. *American Mathematical Monthly*, 73, 154-157.
5. Munkres, J. (2000). *Topology* (2nd ed.). Pearson.
6. Stanley, R. (2011). *Enumerative combinatorics* (Vol. 1). Cambridge University Press.
7. Steiner, A. (1966). The lattice of topologies: Structure and complementation. *Transactions of the American Mathematical Society*.
8. Vural, M., & Daldalı, A. H. (2023). The relation between the number of related-matrices and the number of topologies on a finite set. *Journal of Contemporary Applied Mathematics*, 13.

Chapter 6

TYPES OF CONVERGENCE IN LATTICES AND THEIR INTERRELATIONSHIPS

Büşra Zümre DOĞRU¹

¹ Hatay Mustafa Kemal Üniversitesi, ORCID ID: 0009-0003-1390-835X

Types of Convergence in Lattices and Their Interrelationships

The theory of convergence in lattices represents a fundamental intersection between order theory, functional analysis, and topology. This chapter provides a comprehensive examination of various types of convergence defined on lattices, with particular emphasis on their interrelationships and hierarchical structure. We explore classical order convergence and its unbounded variants, star convergence and its recent generalizations, as well as various hybrid forms that have emerged in the modern theory of Riesz spaces. Our treatment encompasses both the historical development of these concepts and their current state-of-the-art applications, providing a unified framework for understanding how different modes of convergence interact within the lattice-theoretic setting.

1.1 Introduction and Historical Development

The concept of convergence stands as one of the cornerstones of mathematical analysis, with its roots extending deep into the 19th century. Initially formulated for sequences in metric spaces, the notion of convergence underwent a fundamental transformation with the introduction of directed sets and nets by Moore and Smith in 1922. This generalization proved particularly fruitful in the context of topological spaces, where the limitations of sequential convergence became apparent.

The emergence of Riesz space theory in the late 1920s created a natural setting for developing convergence concepts that respect both the algebraic and order structures present in these spaces. Unlike topological convergence, which relies on open sets and neighborhoods, convergence in lattices exploits the partial order to define various modes of convergence that are intrinsic to the ordered structure.

1. TYPES OF CONVERGENCE IN LATTICES AND THEIR INTERRELATIONSHIPS

1.1.1 Order Convergence

The first and perhaps most fundamental type of convergence in lattices is order convergence, introduced by Birkhoff in his seminal 1937 paper [6]. This concept arose naturally from the study of lattice-ordered groups and vector lattices, where the order structure provides a natural way to measure the "closeness" of elements.

Definition 1.1.1 (Order Convergence). Let X be a Riesz space, $(x_\alpha)_{\alpha \in \Lambda} \subset X$ be a net, and $x \in X$. The net (x_α) is said to order converge to x (denoted $x_\alpha \xrightarrow{o} x$) if there exists a net $(y_\beta)_{\beta \in \Omega}$ in X such that:

1. $y_\beta \downarrow 0$ (i.e., (y_β) is decreasing and $\inf_{\beta} y_\beta = 0$)
2. For each $\beta \in \Omega$, there exists $\alpha_0 \in \Lambda$ such that $|x_\alpha - x| \leq y_\beta$ for all $\alpha \geq \alpha_0$

The element x is called the order limit of the net (x_α) . A crucial property of order convergence is its uniqueness: in a Riesz space, if a net has an order limit, this limit is unique. This fact, combined with the compatibility of order convergence with the lattice operations, makes it a natural tool for studying the structure of Riesz spaces. The theory of order convergence has been extensively developed and applied in various contexts [1,2,3,21].

1.1.2 Individual Convergence and Unbounded Order Convergence

The year 1948 marked a significant development in the theory of convergence in ordered spaces with Nakano's introduction of individual convergence in continuous semi-ordered linear spaces [12]. Nakano's

motivation stemmed from the desire to capture the notion of "almost everywhere convergence" in measure theory using only lattice operations, without explicit reference to measures.

Definition 1.1.2 (Nakano's Individual Convergence). Let \mathcal{M} be a continuous semiordered linear space and $(x_\alpha)_{\alpha \in \Lambda}$ be a net in \mathcal{M} . For any $c_1, c_2 \in \mathcal{M}$ with $c_1 \geq c_2$, if:

1. $\limsup_{\alpha \rightarrow \infty} (x_\alpha \wedge c_1) \vee c_2 = \bar{x}$ exists,
2. $\liminf_{\alpha \rightarrow \infty} (x_\alpha \wedge c_1) \vee c_2 = \underline{x}$ exists,
3. $\bar{x} = \underline{x} = x$,

then the net $(x_\alpha)_{\alpha \in \Lambda}$ is said to converge individually to x in \mathcal{M} .

This concept was later reformulated and generalized by DeMarr in 1964 [8], who introduced what is now known as unbounded order convergence:

Definition 1.1.3 (Unbounded Order Convergence). A net $(x_\alpha)_{\alpha \in \Lambda}$ in a Riesz space X unboundedly order converges to an element $x \in X$ (denoted by $x_\alpha \xrightarrow{\text{uo}} x$) if for every $y \in X_+$, we have $|x_\alpha - x| \wedge y \xrightarrow{o} 0$.

The relationship between unbounded order convergence and weak convergence was thoroughly investigated by Wickstead in 1977 [22], revealing deep connections between order-theoretic and topological modes of convergence. Kaplan [10] provided several important characterizations of unbounded order convergence, establishing its role as a fundamental tool in the study of Riesz spaces.

1.1.3 Modern Developments in Unbounded Convergence

The success of unbounded order convergence inspired researchers to explore similar "unbounded" versions of other convergence types. This

led to a proliferation of new convergence concepts in the early 21st century.

Taylor introduced unbounded topological convergence in 2019 [16], providing a framework that unifies topological and order-theoretic approaches:

Definition 1.1.4 (Unbounded Topological Convergence). Let (X, τ) be a locally solid vector lattice and $A \subseteq X$ an ideal. A net (x_α) in X unboundedly τ -converges to $x \in X$ with respect to A if $|x_\alpha - x| \wedge |a| \xrightarrow{\tau} 0$ for all $a \in A$, or equivalently, if $|x_\alpha - x| \wedge a \xrightarrow{\tau} 0$ for all $a \in A_+$.

In the context of Banach lattices, Troitsky introduced d-convergence in 2004 [17], which was later renamed unbounded norm convergence by O'Brien [13]:

Definition 1.1.5 (Unbounded Norm Convergence). A net $(x_\alpha) \subset X$ in a Banach lattice X is said to unboundedly norm converge to $x \in X$ (denoted $x_\alpha \xrightarrow{un} x$) if for every $y \in X_+$, we have $\| |x_\alpha - x| \wedge y \| \rightarrow 0$.

Zabeti's 2018 contribution [23] introduced unbounded absolute weak convergence, further enriching the landscape of convergence concepts:

Definition 1.1.6 (Unbounded Absolute Weak Convergence). A net $(x_\alpha) \subset X$ in a Banach lattice X is said to unboundedly absolute weak converge to $x \in X$ (denoted $x_\alpha \xrightarrow{uaw} x$) if for every $y \in X_+$ and every $f \in X^*$, we have $|f|(|x_\alpha - x| \wedge y) \rightarrow 0$.

Remark. For comprehensive examination of these convergence theories and their applications, readers are encouraged to consult the extensive literature on unbounded convergence, with particular attention to Vural's

foundational work on unbounded locally solid Riesz spaces [21], which provides essential theoretical groundwork for understanding these advanced convergence concepts. Additional fundamental references include Abramovich and Aliprantis's comprehensive treatment of operator theory in vector lattices [1], Aliprantis and Burkinshaw's classical work on positive operators [3], and Schaefer's authoritative text on Banach lattices [15].

1.1.4 Star Convergence and Its Generalizations

Star convergence represents another fundamental approach to convergence in lattices, discovered independently by Urysohn [18], Kantorovich [9], and Von Neumann [19]. Birkhoff's comprehensive study [7] established star convergence as a central concept in lattice theory.

Definition 1.1.7 (Star Convergence). Let (L, \leq) be a lattice and $(x_\alpha)_{\alpha \in \Lambda}$ be a net in L . The net (x_α) is said to star converge to $x \in L$ (denoted $x_\alpha \xrightarrow{s} x$) if every subnet (x_β) of (x_α) has a subnet (x_γ) such that $x_\gamma \xrightarrow{o} x$.

4CHAPTER 1. TYPES OF CONVERGENCE IN LATTICES AND THEIR INTERRELATIONSHIPS

Star convergence satisfies the Urysohn property: if every subnet of a net has a further subnet converging to x , then the original net star converges to x . This property makes star convergence particularly useful in compactness arguments.

The most recent addition to this family of convergence concepts is unbounded star convergence, introduced by Vural in 2024 [20]:

Definition 1.1.8 (Unbounded Star Convergence). Let (L, \leq) be a lattice, (x_α) be a net in L and $x \in L$. The net (x_α) is said to unboundedly star converge to x (denoted $x_\alpha \xrightarrow{us} x$) if for every subnet (x_β) of (x_α) , there exists a subnet (x_ζ) of (x_β) such that $(x_\zeta \wedge b) \vee a \xrightarrow{o} (x \wedge b) \vee a$ for every $a, b \in L$ with $a \leq b$.

1.2 Relationships Between Types of Convergence

Understanding the relationships between different types of convergence is crucial for applying these concepts effectively. This section provides a comprehensive analysis of how these convergence types relate to one another.

1.2.1 Fundamental Implications

The following theorem summarizes the basic relationships between the convergence types we have introduced:

Theorem 1.2.1 (Fundamental Convergence Relationships). Let X be a Riesz space and (x_α) be a net in X . The following implications hold:

1. Order convergence \Rightarrow Star convergence
2. Order convergence \Rightarrow Unbounded order convergence
3. Star convergence \Rightarrow Unbounded star convergence
4. Unbounded order convergence \Rightarrow Unbounded star convergence
5. Unbounded norm convergence \Rightarrow Unbounded absolute weak convergence (in Banach lattices)
6. Unbounded topological convergence \Rightarrow Unbounded order convergence (in locally solid vector lattices)

Proof. We provide a sketch of the key ideas:

(1) If $x_\alpha \xrightarrow{o} x$, then for any subnet (x_β) , we still have $x_\beta \xrightarrow{o} x$, which immediately gives star convergence.

(2) If $|x_\alpha - x| \leq y_\beta$ with $y_\beta \downarrow 0$, then for any $z \in X_+$, we have $|x_\alpha - x| \wedge z \leq y_\beta \wedge z \downarrow 0$.

(3) and (4) follow from combining the definitions with (1) and (2).

(5) and (6) follow from the properties of the norm and topology in the respective spaces.

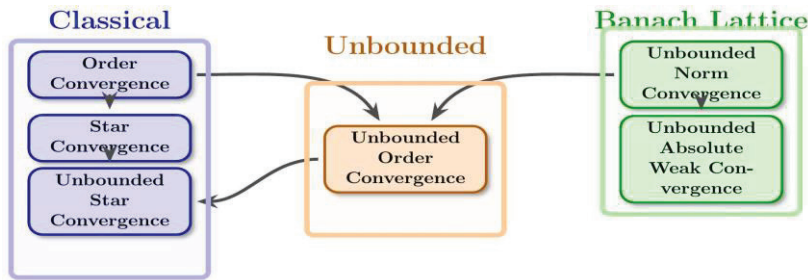
1.2.2 Non-Implications and Counterexamples

Equally important are the relationships that do not hold in general: Theorem 1.2.2 (Non-Implications). The following implications do not hold in general:

1. Star convergence \nRightarrow Order convergence
2. Unbounded order convergence \nRightarrow Order convergence
3. Unbounded star convergence \nRightarrow Star convergence
4. Unbounded star convergence \nRightarrow Unbounded order convergence
5. Unbounded absolute weak convergence \nRightarrow Unbounded norm convergence

1.2.3 Relationship Diagram

The complete hierarchy of convergence types can be visualized in the following diagram:



Convergence Hierarchy

\rightarrow : implies

1.3 Examples and Applications

This section provides concrete examples illustrating the relationships and distinctions between different types of convergence.

Example 1.3.1 (Standard Unit Vectors in c_0). Consider the sequence of standard unit vectors (e_n) in the Riesz space c_0 of sequences converging to zero. We have:

- $e_n \xrightarrow{uo} 0$ (unbounded order converges to 0)

6CHAPTER 1. TYPES OF CONVERGENCE IN LATTICES AND THEIR INTERRELATIONSHIPS

- $e_n \xrightarrow{q} 0$ (does not order converge to 0)
- $e_n \xrightarrow{us} 0$ (unbounded star converges to 0)
- $e_n \xrightarrow{s} p$ (does not star converge to 0)
- $e_n \xrightarrow{un} 0$ (unbounded norm converges to 0 in the supremum norm)

- $e_n \xrightarrow{\text{uaw}} 0$ (unbounded absolute weak converges to 0)

To see why $e_n \xrightarrow{9} 0$, note that if there were a sequence (y_k) with $y_k \downarrow 0$ and $e_n \leq y_k$ for all large n , then each coordinate of y_k would need to be at least 1 , contradicting $y_k \downarrow 0$ in c_0 .

For unbounded order convergence, observe that for any $y \in c_0^+$, we have $e_n \wedge y = (0, \dots, 0, \min(1, y_n), 0, \dots) \xrightarrow{0} 0$ since $y_n \rightarrow 0$.

Example 1.3.2 (Borel Sets and Star Convergence). In the lattice of Borel subsets of the unit interval $[0,1]$, Birkhoff [7] and Rennie [14] constructed sequences that star converge but do not order converge.

Consider the sequence of sets defined by:

$$A_n = \bigcup_{k=2^n}^{2^{n+1}-1} \left[\frac{k}{2^{n+1}}, \frac{k+1}{2^{n+1}} \right)$$

This sequence consists of alternating intervals that become finer with each n . One can verify that:

- (A_n) star converges to \emptyset
- (A_n) does not order converge to \emptyset

The failure of order convergence occurs because there is no decreasing sequence of sets (B_k) with $B_k \downarrow \emptyset$ such that $A_n \subseteq B_k$ for all sufficiently large n .

Example 1.3.3 (Function Spaces). Let $X = L^p[0,1]$ for $1 \leq p < \infty$. Consider the sequence of functions $f_n(t) = n^{1/p} \chi_{[0,1/n]}(t)$, where χ_A denotes the characteristic function of set A .

- $f_n \xrightarrow{9} 0$ (does not order converge)
- $f_n \xrightarrow{uo} 0$ (unbounded order converges)
- $\|f_n\|_p = 1$ for all n , so $f_n \not\rightarrow 0$ in norm
- For any $g \in L^p[0,1]^+$, we have $|f_n| \wedge g \xrightarrow{o} 0$

This example shows that unbounded order convergence can occur even when norm convergence fails.

1.4 Special Cases and Characterizations

Understanding when different types of convergence coincide provides valuable insights into the structure of specific spaces.

Theorem 1.4.1 (Convergence in Order Continuous Banach Lattices). Let X be an order continuous Banach lattice. Then:

1. Unbounded norm convergence implies unbounded order convergence
2. If X has order continuous norm, then $x_\alpha \xrightarrow{uo} x$ and (x_α) is norm bounded implies $x_\alpha \xrightarrow{\|\cdot\|} x$

Theorem 1.4.2 (Convergence in Dedekind Complete Spaces). In a Dedekind complete Riesz space:

1. A net (x_α) unboundedly order converges to x if and only if $(x_\alpha - x)^+ \wedge y \xrightarrow{o} 0$ and $(x_\alpha - x)^- \wedge y \xrightarrow{o} 0$ for all $y \in X_+$
2. Star convergence can be characterized using order convergence of appropriate subnets

1.5 Applications to Functional Analysis

The various types of convergence in lattices have found numerous applications in functional analysis and related fields.

1.5.1 Operator Theory

Unbounded order convergence plays a crucial role in the study of order continuous operators between Riesz spaces. An operator $T: X \rightarrow Y$ between Riesz spaces is unbounded order continuous if $x_\alpha \xrightarrow{uo} 0$ in X implies $Tx_\alpha \xrightarrow{uo} 0$ in Y .

Theorem 1.5.1. Let X and Y be Riesz spaces with Y Dedekind complete. An order bounded operator $T: X \rightarrow Y$ is unbounded order continuous if and only if T maps unbounded order null nets to unbounded order null nets.

1.5.2 Measure Theory

In spaces of measurable functions, unbounded order convergence often corresponds to convergence in measure, while order convergence corresponds to dominated convergence.

Theorem 1.5.2 (Convergence in L^0). Let $(\Omega, \mathcal{F}, \mu)$ be a measure space and $L^0(\mu)$ be the space of measurable functions. Then:

8CHAPTER 1. TYPES OF CONVERGENCE IN LATTICES AND THEIR INTERRELATIONSHIPS

1. A sequence (f_n) in $L^0(\mu)$ unboundedly order converges to f if and only if $f_n \rightarrow f$ in measure on every set of finite measure
2. Order convergence in $L^0(\mu)$ is equivalent to dominated convergence in measure

1.6 Recent Developments and Open Problems

The theory of convergence in lattices continues to be an active area of research. Recent developments include:

1.6.1 Convergence Structures

Researchers have begun studying abstract convergence structures on lattices that generalize the specific types of convergence discussed here. These structures provide a unified framework for understanding convergence phenomena.

1.6.2 Applications to Vector Optimization

Unbounded convergence concepts have found applications in vector optimization problems, where the order structure provides a natural way to compare vector-valued objectives.

1.6.3 Open Problems

Several important questions remain open:

1. **Characterization Problem:** For which classes of lattices does unbounded star convergence coincide with unbounded order convergence?
2. **Compactness Problem:** Develop appropriate notions of compactness for each type of convergence and characterize the spaces in which these compactness notions are equivalent.
3. **Duality Theory:** Extend the theory of convergence to dual spaces and characterize when convergence in a space corresponds to convergence in its dual.
4. **Topological Characterization:** Find topological characterizations of spaces where different types of convergence coincide.

5. Applications to PDEs: Explore applications of unbounded convergence concepts to the theory of partial differential equations in function spaces.

1.7 Conclusion

The theory of convergence in lattices provides a rich framework for understanding limiting processes in ordered structures. From the classical order convergence introduced by Birkhoff to the recent unbounded star convergence of Vural, each type of convergence captures different aspects of how nets behave in lattices.

The hierarchy of convergence types reveals a delicate interplay between ordertheoretic and topological properties. While order convergence provides the strongest form of convergence, its unbounded variants offer greater flexibility and wider applicability, particularly in spaces of unbounded functions and operators.

As the theory continues to develop, new applications emerge in areas ranging from functional analysis and measure theory to optimization and mathematical economics. The open problems presented here suggest that the field remains vibrant, with many fundamental questions yet to be resolved.

Understanding these convergence concepts and their relationships is essential for anyone working with ordered structures in analysis, providing both theoretical insights and practical tools for tackling complex problems in modern mathematics.

References

1. Abramovich, Y. A., & Aliprantis, C. D. (2002). *An invitation to operator theory*. American Mathematical Society.
2. Abramovich, Y., & Sirotkin, G. (2005). On order convergence of nets. *Positivity*, 9(3), 287-298.
3. Aliprantis, C. D., & Burkinshaw, O. (1985). *Positive operators*. Academic Press.
4. Anguelov, R., & van der Walt, J. H. (2005). Order convergence structure on $C(X)$. *Quaestiones Mathematicae*, 28(4), 425-457.
5. Birkhoff, G. (1935). On the structure of abstract algebras. *Mathematical Proceedings of the Cambridge Philosophical Society*, 31(4), 433-454.
6. Birkhoff, G. (1937). Moore-Smith convergence in general topology. *Annals of Mathematics*, 38(1), 39-56.
7. Birkhoff, G. (1940). *Lattice theory* (Vol. 25). American Mathematical Society.
8. DeMarr, R. (1964). Partially ordered linear spaces and locally convex linear topological spaces. *Illinois Journal of Mathematics*, 8(4), 601-606.
9. Kantorovitch, L. V. (1937). Lineare halbgeordnete Räume. *Matematicheskii Sbornik*, 2(1), 121-168.
10. Kaplan, S. (1997). On unbounded order convergence. *Real Analysis Exchange*, 23(2), 175-184.
11. Lowig, H. (1941). Intrinsic topology and completion of Boolean rings. *Annals of Mathematics*, 42(4), 1138-1196.
12. Nakano, H. (1948). Ergodic theorems in semi-ordered linear spaces. *Annals of Mathematics*, 49(2), 538-556.
13. O'Brien, M. J. (2016). *Unbounded norm convergence in Banach lattices* (Doctoral dissertation). University of Mississippi.
14. Rennie, B. C. (1950). Lattices. *Proceedings of the London Mathematical Society*, 52(1), 386-400.
15. Schaefer, H. H. (1974). *Banach lattices and positive operators*. Springer-Verlag.

16. Taylor, M. A. (2019). Unbounded topologies and uo-convergence in locally solid vector lattices. *Journal of Mathematical Analysis and Applications*, 472(1), 981-1000.
17. Troitsky, V. G. (2004). Measures of non-compactness of operators on Banach lattices. *Positivity*, 8, 165-178.
18. Urysohn, P. (1926). Sur les classes (L) de M. Fréchet. *L'Enseignement Mathématique*, 25, 77-83.
19. Von Neumann, J. (1935). On complete topological spaces. *Transactions of the American Mathematical Society*, 37(1), 1-20.
20. Vural, M. (2024). Unbounded star convergence in lattices. *OKU Journal of The Institute of Science and Technology*, 7(4), 1775-1782.
21. Vural, M. (2019). Towards a theory of unbounded locally solid Riesz spaces. *Journal of New Theory*, 20-27.
22. Wickstead, A. W. (1977). Weak and unbounded order convergence in Banach lattices. *Journal of the Australian Mathematical Society*, 24(3), 312-319.
23. Zabeti, O. (2018). Unbounded absolute weak convergence in Banach lattices. *Positivity*, 22, 501-505.

Chapter 7

ON POINTWISE CONVERGENCE OF M-SINGULAR INTEGRAL OPERATORS INVOLVING FINITE SUM

GÜMRAH UYSAL¹

¹ Assoc. Prof. Dr., Faculty of Science, Department of Mathematics, Karabük University, fgumrahuysal@gmail.com, ORCID: 0000-0001-7747-1706.

1. INTRODUCTION

In the realm of approximation theory, the accurate estimation of the derivatives of a function holds equal significance to that of the function itself. A foundational contribution in this area was made by Mamedov (1963), who introduced a novel class of summation-integral operators aimed at achieving enhanced precision in the approximation of higher-order derivatives. Historically, finite difference schemes have long served as the primary tools for such approximations; however, Mamedov's operators represent a more refined alternative, offering increased sensitivity and accuracy relative to these traditional methods. The operators proposed by Mamedov can be interpreted as natural extensions of classical integral operators characterized by linear and convolution-type kernels. Within the framework of his study, these are referred to as m -singular integral operators, encapsulating a broad spectrum of generalizations. Notably, when the parameter $m = 1$, these operators reduce to the well-established classical integral forms. Such generalizations are frequently categorized under the umbrella of Jackson-type or Jackson-Stechkin-type operators in the contemporary literature (see, for instance, (Rydzewska, 1978; Yılmaz, 2014)). A salient feature of Mamedov's approach lies in the abstraction of the kernel function through a general symbolic representation. This formulation enables the incorporation of a wide variety of classical approximate identities, such as the Picard, Gauss-Weierstrass and Abel-Poisson kernels, which are prominent in smoothing and regularization procedures. In several subsequent investigations, the general kernel framework has been concretely specified, thereby facilitating the detailed analytical treatment and numerical implementation of the associated operators (see, for example, (Butzer & Nessel, 1971; Aydın & Aral, 2013; Aydın-Arı & Yılmaz, 2021)).

Musielak (1983) undertook a detailed study on the approximation behavior of nonlinear integral operators, wherein the primary analytical obstacle—nonlinearity—was effectively addressed by employing a generalized Lipschitz-type condition. This methodological innovation enabled the control of nonlinearity within the approximation framework, thereby extending the scope of classical operator theory. In a subsequent and more advanced contribution, Musielak (1991) expanded upon the analytical groundwork established in (Musielak, 1983) by formulating the problem within the structure of generalized Orlicz spaces, thus facilitating a more flexible and comprehensive functional setting for analyzing the approximation properties of the aforementioned operators.

Later, Świdorski and Wachnicki (2000) investigated the pointwise convergence of the nonlinear integral operator family by taking into account the influence of two distinct parameters. Their analysis focused on the behavior of these operators at Lebesgue points of functions belonging to the Lebesgue space L_p with $p \geq 1$ providing deeper insight into the local convergence phenomena. For a broader context and further related developments in this area, we refer the interested reader to the works cited in (Bardaro et al., 2003; Bardaro et al., 2013; Karşlı, 2014; Esen-Almalı & Gadjiev, 2016; Uysal, 2018).

Let R, R_0^+ and Z^+ stand for the set of all real numbers, all non-negative real numbers and all positive integers, respectively. Mamedov (1963) constructed the following m –singular integral operators:

$$I_r^{[m]}(u; z) = (-1)^{m+1} \int_{-\infty}^{+\infty} \left(\sum_{j=1}^m (-1)^{m-j} \binom{m}{j} u(z + js) \right) K_r(s) ds, \quad (1.1)$$

where $z, s \in R$. In equation (1.1), m is a certain positive integer and the (kernel) function $K_r, K_r: R \rightarrow R_0^+$, where r denotes a positive parameter which belongs to the index set I , is possessing some specific properties as the approximate identities (see (Butzer & Nessel, (1971)). Some studies related to m –singular integral operators were presented by Rydzewska (1978), Bardaro et al. (2013), Karşlı (2014), Yılmaz (2014) and Uysal (2018).

Esen-Almalı (2017) considered the following nonlinear integral operators:

$$W_r^{[N]}(u; z) = \int_e^f \sum_{n=1}^N u^n(s) G_{r,n}(z, s) ds, \quad (1.2)$$

where $z, s \in (e, f)$, (e, f) is a bounded interval of R or R itself. $G_{r,n}, G_{r,n}: R \times R \rightarrow R_0^+$, where r denotes a positive parameter which belongs to the index set I , is enriched with some specific properties. The source of nonlinearity stems from the expression $u^n(s)$, characterizing a power-type nonlinearity. Some related studies are given by Esen-Almalı et al. (2017), Uysal (2018) and Serin (2020).

Incorporating the operators in equations (1.1) and (1.2), we get

$$W_k^{[m,N]}(u; z) = \int_{-\infty}^{+\infty} \sum_{j=1}^m (-1)^{j-1} \binom{m}{j} \sum_{n=1}^N u^n(js) G_{k,n}(z, s) ds, \quad (1.3)$$

where $z, s \in R$, $k \in Z^+$ and $G_{k,n}, G_{k,n}: R \times R \rightarrow R_0^+$.

Lebesgue space $L_p(R)$ with $1 \leq p < \infty$ is consisting of all functions $u: R \rightarrow R$ which are measurable on R in the sense of Lebesgue such that $\int_{-\infty}^{+\infty} |u(s)|^p ds < \infty$. The norm of the function in $L_p(R)$ is stated as follows:

$$\|u\|_p = \left(\int_{-\infty}^{+\infty} |u(s)|^p ds \right)^{1/p}, \quad 1 \leq p < \infty.$$

The current study is a continuation and a generalization of (Esen-Almalı et al., 2017; Serin, 2020) for $L_p(R)$. The chapter is organized as follows: In Section 2, we present preliminary concepts and prove main results. In Section 3, we give conclusions.

2. PRINCIPAL CONTRIBUTIONS

Definition 2.1. (Esen-Almalı, 2017; Esen-Almalı et al., 2017) Let $k \in Z^+$ and $N \in Z^+$ be fixed. The sequence of kernel functions $\{G_{k,n}\}_{k \in Z^+}$ consisting of the functions $G_{k,n}: R \times R \rightarrow R_0^+$ for each $n = 1, 2, \dots, N$ satisfies the following conditions:

(a) $\lim_{k \rightarrow +\infty} \left| \int_{-\infty}^{+\infty} G_{k,n}(z, s) ds - C_n \right| = 0$, where C_n are certain positive constants, for any fixed $z \in R$ and $n = 1, 2, \dots, N$.

(b) $\lim_{k \rightarrow +\infty} \sup_{|z-s| \geq \gamma} G_{k,n}(z, s) = 0$ for every $\gamma > 0$, for any fixed $z \in R$ and $n = 1, 2, \dots, N$.

(c) $\lim_{k \rightarrow +\infty} \int_{|z-s| \geq \gamma} G_{k,n}(z, s) ds = 0$ for every $\gamma > 0$, for any fixed $z \in R$ and $n = 1, 2, \dots, N$.

(d) $G_{k,n}$ is non-decreasing for $s < z$ and non-increasing for $s > z$ with respect to s on R , for any fixed $z \in R$, $k \in Z^+$ and $n = 1, 2, \dots, N$.

This class of kernel functions is called G ; see also (Butzer & Nessel, 1971; Esen-Almalı & Gadjiev, 2016; Karşı, 2014; Uysal, 2018).

Definition 2.2. Let $1 \leq p < +\infty$ and $n \in Z^+$ be a fixed. The point $z_0 \in R$ at which

$$\lim_{h \rightarrow 0^+} \frac{1}{\mu(h)} \int_{z_0}^{z_0+h} \left| \sum_{j=1}^m (-1)^{j-1} \binom{m}{j} [u^n(js) - u^n(z_0)] \right|^p ds = 0$$

and

$$\lim_{h \rightarrow 0^+} \frac{1}{\mu(h)} \int_{z_0-h}^{z_0} \left| \sum_{j=1}^m (-1)^{j-1} \binom{m}{j} [u^n(js) - u^n(z_0)] \right|^p ds = 0$$

hold, is called $m - \mu - p$ -generalized Lebesgue point of a globally bounded function $u \in L_p(R)$. Here, where $\mu: R \rightarrow R$ is an increasing and absolutely continuous function on $[0, \alpha]$ with $0 < h \leq \alpha$ and $\mu(0) = 0$ (cf. (Mamedov, 1963) for $\mu(s) = s$; (Gadjiev, 1968) for $m = 1$)).

For similar definitions and their variants, we advice the interested reader to see also (Gadjiev, 1968; Karshi, 2014; Esen-Almalı et al., 2017).

Now, we prove two pointwise convergence theorems. These theorems are of type Fatou (see (Fatou, 1906)). Similar theorems can be found in (Taberski, 1962; Karshi, 2014; Esen-Almalı et al., 2017; Uysal, 2018).

Theorem 2.1. Let $\{G_{k,n}\}_{k \in \mathbb{Z}^+} \subset G$. If $z_0 \in R$ is a $m - \mu$ -generalized Lebesgue point ($p = 1$) of function $u \in L_1(R)$ and u is bounded on R , then

$$\lim_{k \rightarrow +\infty} W_k^{[m,N]}(u; z_0) = \sum_{n=1}^N C_n u^n(z_0),$$

on any set Q_1 consisting of (δ, k) on which the function

$$\sum_{n=1}^N \int_{z_0-\delta}^{z_0+\delta} G_{k,n}(z_0, s) |\{\mu(|z_0 - s|)\}'_s| ds,$$

where $0 < \delta < \delta^*$ with certain $\delta^* > 0$, is bounded as k tends to $+\infty$.

Proof. Denote

$$A_k := \left| W_k^{[m,N]}(u; z_0) - \sum_{n=1}^N C_n u^n(z_0) \right|.$$

Therefore, the following inequality holds:

$$|A_k| \leq \left| \int_{-\infty}^{+\infty} \sum_{j=1}^m (-1)^{j-1} \binom{m}{j} \sum_{n=1}^N [u^n(js) - u^n(z_0)] G_{k,n}(z_0, s) ds \right| \\ + \sum_{n=1}^N |u^n(z_0)| \left| \int_{-\infty}^{\infty} G_{k,n}(z_0, s) ds - C_n \right|.$$

By condition (a), one has

$$\lim_{k \rightarrow +\infty} \sum_{n=1}^N |u^n(z_0)| \left| \int_{-\infty}^{\infty} G_{k,n}(z_0, s) ds - C_n \right| = 0.$$

Denote

$$|A_{1,k}| = \left| \int_{-\infty}^{+\infty} \sum_{j=1}^m (-1)^{j-1} \binom{m}{j} \sum_{n=1}^N [u^n(js) - u^n(z_0)] G_{k,n}(z_0, s) ds \right|.$$

Moreover, one has

$$|A_{1,k}| \leq \sum_{n=1}^N \int_{-\infty}^{+\infty} \left| \sum_{j=1}^m (-1)^{j-1} \binom{m}{j} [u^n(js) - u^n(z_0)] \right| G_{k,n}(z_0, s) ds \\ =: \sum_{n=1}^N A_{2,n,k},$$

where

$$A_{2,n,k} = \int_{-\infty}^{+\infty} \left| \sum_{j=1}^m (-1)^{j-1} \binom{m}{j} [u^n(js) - u^n(z_0)] \right| G_{k,n}(z_0, s) ds.$$

Since z_0 is a $m - \mu$ -generalized Lebesgue point of function $u \in L_1(R)$, for every given $\varepsilon > 0$ there exists a number $\delta > 0$ such that

$$\int_{z_0}^{z_0+h} \left| \sum_{j=1}^m (-1)^{j-1} \binom{m}{j} [u^n(js) - u^n(z_0)] \right| ds < \varepsilon \mu(h) \quad (2.1)$$

and

$$\int_{z_0-h}^{z_0} \left| \sum_{j=1}^m (-1)^{j-1} \binom{m}{j} [u^n(js) - u^n(z_0)] \right| ds < \varepsilon \mu(h) \quad (2.2)$$

hold for every h satisfying $0 < h \leq \delta$.

We split the integral $A_{2,n,k}$ with respect to this $\delta > 0$ as follows:

$$\begin{aligned} A_{2,n,k} &= \int_{z_0}^{z_0+\delta} \left| \sum_{j=1}^m (-1)^{j-1} \binom{m}{j} [u^n(js) - u^n(z_0)] \right| G_{k,n}(z_0, s) ds \\ &\quad + \int_{z_0-\delta}^{z_0} \left| \sum_{j=1}^m (-1)^{j-1} \binom{m}{j} [u^n(js) - u^n(z_0)] \right| G_{k,n}(z_0, s) ds \\ &\quad + \int_{-\infty}^{z_0-\delta} \left| \sum_{j=1}^m (-1)^{j-1} \binom{m}{j} [u^n(js) - u^n(z_0)] \right| G_{k,n}(z_0, s) ds \\ &\quad + \int_{z_0+\delta}^{+\infty} \left| \sum_{j=1}^m (-1)^{j-1} \binom{m}{j} [u^n(js) - u^n(z_0)] \right| G_{k,n}(z_0, s) ds \\ &=: A_{2,n,k}[1] + A_{2,n,k}[2] + A_{2,n,k}[3] + A_{2,n,k}[4]. \end{aligned}$$

We know that u is bounded on R . Using condition (d), there holds that

$$\begin{aligned} A_{2,n,k}[3] &\leq 2^m |u^n(z_0)| \int_{-\infty}^{z_0-\delta} G_{k,n}(z_0, s) ds \\ &\quad + \left\| \sum_{j=1}^m \binom{m}{j} u^n(j *) \right\|_1 G_{k,n}(z_0, z_0 - \delta). \end{aligned}$$

Similarly, we obtain

$$\begin{aligned} A_{2,n,k}[4] &\leq 2^m |u^n(z_0)| \int_{z_0+\delta}^{+\infty} G_{k,n}(z_0, s) ds \\ &\quad + \left\| \sum_{j=1}^m \binom{m}{j} u^n(j *) \right\|_1 G_{k,n}(z_0, z_0 + \delta). \end{aligned}$$

In view of conditions (c) and (b),

$$\lim_{k \rightarrow +\infty} A_{2,n,k}[3] = 0$$

and

$$\lim_{k \rightarrow +\infty} A_{2,n,k}[4] = 0.$$

In view of equation (2.1) and making standard operations as in, for example, (Esen-Almalı, 2017; Esen-Almalı et al., 2017), we get

$$A_{2,n,k}[1] \leq \varepsilon \int_{z_0}^{z_0+\delta} G_{k,n}(z_0, s) |\{\mu(s - z_0)\}'_s| ds.$$

Similarly, In view of equation (2.2), we get

$$A_{2,n,k}[2] \leq \varepsilon \int_{z_0-\delta}^{z_0} G_{k,n}(z_0, s) |\{\mu(z_0 - s)\}'_s| ds.$$

Hence, we have

$$A_{2,n,k}[1] + A_{2,n,k}[2] \leq \varepsilon \int_{z_0-\delta}^{z_0+\delta} G_{k,n}(z_0, s) |\{\mu(|s - z_0|)\}'_s| ds.$$

Since $\varepsilon > 0$ is arbitrary, the proof is completed.

Theorem 2.2. Let $\{G_{k,n}\}_{k \in \mathbb{Z}^+} \subset G$. If $z_0 \in R$ is a $m - \mu - p$ -generalized Lebesgue point of function $u \in L_p(R)$ with $1 < p < +\infty$ and u is bounded on R , then

$$\lim_{k \rightarrow +\infty} W_k^{[m,N]}(u; z_0) = \sum_{n=1}^N C_n u^n(z_0),$$

on any set Q_2 consisting of (δ, k) on which the function

$$\sum_{n=1}^N \int_{z_0-\delta}^{z_0+\delta} G_{k,n}(z_0, s) |\{\mu(|z_0 - s|)\}'_s| ds,$$

where $0 < \delta < \delta_*$ with certain $\delta_* > 0$, is bounded as k tends to $+\infty$.

Proof. Set

$$B_k := \left| W_k^{[m,N]}(u; z_0) - \sum_{n=1}^N C_n u^n(z_0) \right|.$$

Therefore, we can write

$$|B_k| \leq \left| \int_{-\infty}^{+\infty} \sum_{j=1}^m (-1)^{j-1} \binom{m}{j} \sum_{n=1}^N [u^n(js) - u^n(z_0)] G_{k,n}(z_0, s) ds \right| \\ + \sum_{n=1}^N |u^n(z_0)| \left| \int_{-\infty}^{\infty} G_{k,n}(z_0, s) ds - C_n \right|.$$

By condition (a), one has

$$\lim_{k \rightarrow +\infty} \sum_{n=1}^N |u^n(z_0)| \left| \int_{-\infty}^{\infty} G_{k,n}(z_0, s) ds - C_n \right| = 0.$$

Set

$$|B_{1,k}| = \left| \int_{-\infty}^{+\infty} \sum_{j=1}^m (-1)^{j-1} \binom{m}{j} \sum_{n=1}^N [u^n(js) - u^n(z_0)] G_{k,n}(z_0, s) ds \right|.$$

The following inequality holds:

$$|B_{1,k}| \leq \sum_{n=1}^N \int_{-\infty}^{+\infty} \left| \sum_{j=1}^m (-1)^{j-1} \binom{m}{j} [u^n(js) - u^n(z_0)] \right| G_{k,n}(z_0, s) ds \\ =: \sum_{n=1}^N B_{2,n,k},$$

where

$$B_{2,n,k} = \int_{-\infty}^{+\infty} \left| \sum_{j=1}^m (-1)^{j-1} \binom{m}{j} [u^n(js) - u^n(z_0)] \right| G_{k,n}(z_0, s) ds$$

We see that

$$(B_{2,n,k})^p = \left(\int_{-\infty}^{+\infty} \left| \sum_{j=1}^m (-1)^{j-1} \binom{m}{j} [u^n(js) - u^n(z_0)] \right| G_{k,n}(z_0, s) ds \right)^p.$$

Applying Hölder's inequality with $\frac{1}{p} + \frac{1}{q} = 1$ for $1 < p, q < +\infty$ (see, for example, (Rudin, 1987)), we get

$$\begin{aligned} (B_{2,n,k})^p &\leq \int_{-\infty}^{+\infty} \left| \sum_{j=1}^m (-1)^{j-1} \binom{m}{j} [u^n(js) - u^n(z_0)] \right|^p G_{k,n}(z_0, s) ds \\ &\quad \times \left(\int_{-\infty}^{+\infty} G_{k,n}(z_0, s) ds \right)^{\frac{p}{q}} \\ &=: B_{3,n,k} \times \left(\int_{-\infty}^{+\infty} G_{k,n}(z_0, s) ds \right)^{\frac{p}{q}}. \end{aligned}$$

Here, the term $\left(\int_{-\infty}^{+\infty} G_{k,n}(z_0, s) ds \right)^{\frac{p}{q}}$ is bounded by condition (a).

Since z_0 is a $m - \mu - p$ -generalized Lebesgue point of function $u \in L_p(R)$, for every given $\varepsilon > 0$ there exists a number $\delta > 0$ such that

$$\int_{z_0}^{z_0+h} \left| \sum_{j=1}^m (-1)^{j-1} \binom{m}{j} [u^n(js) - u^n(z_0)] \right|^p ds < \varepsilon \mu(h) \quad (2.3)$$

and

$$\int_{z_0-h}^{z_0} \left| \sum_{j=1}^m (-1)^{j-1} \binom{m}{j} [u^n(js) - u^n(z_0)] \right|^p ds < \varepsilon \mu(h) \quad (2.4)$$

hold for every h satisfying $0 < h \leq \delta$.

We split the integral $B_{3,n,k}$ with respect to this $\delta > 0$ as follows:

$$\begin{aligned} B_{3,n,k} &= \int_{z_0}^{z_0+\delta} \left| \sum_{j=1}^m (-1)^{j-1} \binom{m}{j} [u^n(js) - u^n(z_0)] \right|^p G_{k,n}(z_0, s) ds \\ &\quad + \int_{z_0-\delta}^{z_0} \left| \sum_{j=1}^m (-1)^{j-1} \binom{m}{j} [u^n(js) - u^n(z_0)] \right|^p G_{k,n}(z_0, s) ds \end{aligned}$$

$$\begin{aligned}
& + \int_{-\infty}^{z_0-\delta} \left| \sum_{j=1}^m (-1)^{j-1} \binom{m}{j} [u^n(js) - u^n(z_0)] \right|^p G_{k,n}(z_0, s) ds \\
& + \int_{z_0+\delta}^{+\infty} \left| \sum_{j=1}^m (-1)^{j-1} \binom{m}{j} [u^n(js) - u^n(z_0)] \right|^p G_{k,n}(z_0, s) ds \\
& =: B_{3,n,k}[1] + B_{3,n,k}[2] + B_{3,n,k}[3] + B_{3,n,k}[4].
\end{aligned}$$

Using condition (d), there holds that

$$\begin{aligned}
B_{3,n,k}[3] & \leq 2^{(m+1)p} |u^n(z_0)|^p \int_{-\infty}^{z_0-\delta} G_{k,n}(z_0, s) ds \\
& + 2^p \left(\left\| \sum_{j=1}^m \binom{m}{j} u^n(j*) \right\|_p \right)^p G_{k,n}(z_0, z_0 - \delta).
\end{aligned}$$

Similarly, we obtain

$$\begin{aligned}
B_{3,n,k}[4] & \leq 2^{(m+1)p} |u^n(z_0)|^p \int_{z_0+\delta}^{+\infty} G_{k,n}(z_0, s) ds \\
& + 2^p \left(\left\| \sum_{j=1}^m \binom{m}{j} u^n(j*) \right\|_p \right)^p G_{k,n}(z_0, z_0 + \delta).
\end{aligned}$$

We know that u is bounded on R . In view of conditions (c) and (b),

$$\lim_{k \rightarrow +\infty} B_{3,n,k}[3] = 0$$

and

$$\lim_{k \rightarrow +\infty} B_{3,n,k}[4] = 0.$$

In view of equation (2.3) and making standard operations as in, for example, (Esen-Almalı, 2017; Esen-Almalı et al., 2017), we obtain

$$B_{3,n,k}[1] \leq \varepsilon \int_{z_0}^{z_0+\delta} G_{k,n}(z_0, s) |\{\mu(s - z_0)\}'_s| ds.$$

Similarly, In view of equation (2.4), we get

$$B_{3,n,k}[2] \leq \varepsilon \int_{z_0-\delta}^{z_0} G_{k,n}(z_0, s) |\{\mu(z_0 - s)\}'_s| ds.$$

Hence, we have

$$B_{3,n,k}[1] + B_{3,n,k}[2] \leq \varepsilon \int_{z_0-\delta}^{z_0+\delta} G_{k,n}(z_0, s) |\{\mu(|s - z_0|)\}'_s| ds.$$

Since $\varepsilon > 0$ is arbitrary, the proof is completed.

3. CONCLUSION

This study is devoted to the rigorous analysis of the m – singular modifications of the operators defined in equation (1.2), with particular attention given to establishing a pointwise approximation theorem. The modified operators serve as a natural extension of classical integral constructs and are of significant interest due to their enhanced approximation capabilities, particularly in handling higher-order behaviors of functions. Furthermore, the class of operators introduced in equation (1.3) opens up several avenues for future research, especially within the framework of nonlinear approximation theory. Their structural flexibility and potential to accommodate various kernel functions make them a promising tool for addressing complex approximation problems, including those involving irregular data or non-standard functional spaces.

REFERENCES

- Aydın, D., & Aral A. (2013). Some Approximation properties of Complex q -Gauss-Weierstrass type integral operators in the unit disk. *Annals of Oradea University, Fasc. Matematica*, Tom XX (1) 155–168.
- Bardaro, C., Musielak, J., & Vinti, G. (2003). *Nonlinear Integral Operators and Applications*. De Gruyter Series in Nonlinear Analysis and Applications. Vol. 9. Walter de Gruyter & Co., Berlin.
- Bardaro, C., Karlı, H., & Vinti, G. (2013). On pointwise convergence of Mellin type nonlinear m –singular integral operators. *Comm. Appl. Nonl. Anal.*, 20(2), 25–39.
- Butzer, P. L., & Nessel, R. J. (1971). *Fourier Analysis and Approximation*. Volume 1: One-dimensional Theory. Pure and Applied Mathematics, Vol. 40. Academic Press, New York, London.
- Esen-Almalı, S., & Gadjev, A. D. (2016). On approximation properties of certain multidimensional nonlinear integrals. *J. Nonlinear Sci. Appl.*, 9(5), 3090–3097.
- Esen-Almalı, S., Uysal, G., Mishra, V. N., & Özalp-Güller, Ö. (2017). On singular integral operators involving power nonlinearity. *Korean J. Math.*, 25(4), 483–494.
- Esen-Almalı, S., (2017). On approximation properties for non-linear integral operators. *New Trends Math. Sci.*, 5(4), 123–129.
- Fatou, P. (1906). Series trigonometriques et series de Taylor. *Acta Math.*, 30(1), 335–400.
- Karlı, H. (2014). Fatou type convergence of nonlinear m -singular integral operators. *Appl. Math. Comput.*, 246, 221–228.
- Mamedov, R. G. (1963). On the order of convergence of m –singular integrals at generalized Lebesgue points and in the space $L_p(-\infty, \infty)$. (Russian) *Izv. Akad. Nauk SSSR Ser. Mat.*, 27, 287–304.
- Musielak, J. (1983). On some approximation problems in modular spaces. In: *Constructive Function Theory, Proceedings of International Conference Varna, 1–5 June, 1981*. Publication House of Bulgarian Academic of Sciences, Sofia, 455–461.
- Musielak, J. (1991). Approximation by nonlinear singular integral operators in generalized Orlicz spaces. *Comment. Math. Prace Mat.*, 31, 79–88.
- Rudin, W. (1987). *Real and Complex Analysis*. (Third Ed.) McGraw-Hill Book Company, New York.

- Rydzewska, B. (1978). Point-approximation des fonctions par des certaines intégrales singulières. (French) Fasc. Math., 10, 13–24.
- Serin, G. (2020). Pointwise convergence of the non-linear integral operator family. M. Sc. Thesis, Kırıkkale University, Graduate School of Natural and Applied Sciences, Kırıkkale.
- Swiderski, T., & Wachnicki, E. (2000). Nonlinear singular integrals depending on two parameters. Comment. Math. (Prace Mat.), 40, 181–189.
- Taberski, R. (1962). Singular integrals depending on two parameters. Prace Mat., 7, 173–179.
- Uysal, G. (2018). Nonlinear m –singular integral operators in the framework of Fatou type weighted convergence. Commun. Fac. Sci. Univ. Ank. Sér. A1 Math. Stat., 67(1), 262–276.
- Yılmaz, B. (2014). Jackson type generalization of nonlinear integral operators. J. Comput. Anal. Appl., 17(1), 77–83.
- Yılmaz, B., & Aydın-Arı, D. (2021). A note on the modified Picard integral operators. Math. Meth. Appl. Sci., 44(9), 7571-7576.

Chapter 8

EFFECT OF METAL OXIDE TYPE AND PARTICLE SIZE ON OPTICAL AND STRUCTURAL BEHAVIOR OF PS/METAL OXIDE NANOCOMPOSITE FILMS

M. Selin SUNAY¹, Abdelhamid ELAISSARI²

1 Mimar Sinan Fine Arts University, School of Cultural Heritage Conservation and Restoration, Department of Conservation, İstanbul, Türkiye, selin.sunay@msgsu.edu.tr ORCID ID: 0000-0002-4054-6302

2 CNRS- Claude Bernard University Lyon, Lyon, France, elaissari@lagep.univ-lyon1.fr ORCID ID: 0000-0002-2151-9894

INTRODUCTION

Polymer latexes, equivalently termed colloidal polymer dispersions, are extensively employed across diverse technological domains, including coatings, adhesives, biomedical applications, information technology, and microelectronics. A notable characteristic of these materials is their remarkable optical clarity, which persists even when incorporated with reinforcing nanofillers [1]. Latex films are generally formed by coalescence of submicrometer polymer particles in the form of a colloidal dispersion, usually in water. The term “latex film” normally refers to a film formed from soft latex particles (T_g below room temperature) where the forces accompanying the evaporation of water are sufficient to compress and deform the particles into a transparent, void-free film. Latex films are typically fabricated through the coalescence of submicrometer polymer particles, initially present within a colloidal dispersion, most commonly an aqueous medium. The designation ‘latex film’ conventionally refers to a film derived from compliant (low glass transition temperature, $T_g < 25^\circ\text{C}$) latex particles, where capillary forces generated during solvent evaporation induce sufficient particle compression and deformation to yield a transparent, void-free monodisperse structure. Conversely, latex films can also be produced through compression molding of films fabricated from dried latex powder. These powders are composed of relatively rigid polymers, such as polystyrene (PS) or poly(methyl methacrylate) (PMMA), characterized by a glass transition temperature (T_g) exceeding ambient temperature. Aqueous dispersions comprising compliant latex particles are conventionally termed ‘low- T_g ’ dispersions, while non-aqueous dispersions of rigid polymer particles are generally referred to as ‘high- T_g ’ dispersions.

During the drying process, high- T_g latex particles largely maintain their discrete morphology and remain undeformed. The mechanical properties of films derived from such particles are subsequently enhanced post-solvent evaporation through an annealing process. This thermal treatment initially facilitates void closure, followed by the interdiffusion of polymer chains across particle–particle boundaries, contributing to the macroscopic integrity and mechanical performance of the film [2].

The diverse applications of polymer nanocomposites are directly attributable to their tunable optical, electrical, and mechanical properties [3–7]. In this study, polystyrene (PS), a polymer with a high glass transition temperature ($T_g = 105^\circ\text{C}$), was utilized. The high T_g of PS signifies its rigid, glassy state at ambient conditions, which is crucial for achieving the desired mechanical and optical properties in the resulting films. Polystyrene (PS), a polymer characterized by a high glass transition temperature ($T_g = 105^\circ\text{C}$), exhibits a combination of properties that make it highly va-

luable for various industrial applications [8,9]. These properties include exceptional durability, high optical transparency, a notable refractive index (approximately 1.60), excellent electrical insulation, and minimal water absorption, coupled with efficient processing characteristics. Furthermore, PS demonstrates superior optical qualities, encompassing inherent clarity and a high refractive index, and while typically achiral, its optical behavior is well-defined [10]. Due to this confluence of advantageous properties, PS is frequently selected as the primary matrix material for investigating the optical characteristics of polymer nanocomposites[11].-

Considerable research efforts have recently focused on the development of organic/inorganic composite materials with tailored compositions. The intrinsic self-assembly capabilities of colloidal latex particles enable their utilization as sacrificial templates for the fabrication of porous nanoparticle films. Porous materials have garnered significant scientific and industrial interest due to their versatile applications, including their deployment as heterogeneous catalysts [12-15], scaffolds for directed nanomaterial synthesis [16-20], substrates for cell culture [21-23], advanced separation media [24-26], and anti-reflective coatings [27-29]. The synthesis of nano- and meso-sized spheres yields highly valuable materials that can serve diverse functions, including hollow particles, drug delivery vehicles, confined nano- and meso-scale reaction vessels, and protective encapsulation shells [30]. Furthermore, the tailored utilization of these structured particles facilitates the production of various innovative functional products, such as photonic crystals [31] and porous inorganic architectures [32]. Recent research has extensively documented the fabrication of ordered polymer arrays (e.g., polystyrene) or silica nanospheres specifically for advanced photonic crystal applications [23, 25]. Macroporous films exhibit pronounced photonic band gaps, which can be precisely tuned by manipulating the periodicity and diameter of the templating structures. Photonic crystals, defined as spatially periodic dielectric materials with varying refractive indices, have been a subject of extensive investigation in the scientific literature. Analogous to semiconductors that regulate electron emission, these materials are capable of controlling photon emission, provided their lattice constant is commensurate with visible or infrared wavelengths. To fully realize their potential across a broad spectrum of optical applications, considerable research efforts have been dedicated to the theoretical prediction and experimental fabrication of three-dimensional (3D) complete photonic band gap structures [33]. Recent advancements have reinvigorated research interest in these structures, shifting focus from complex semiconductor nanolithography techniques towards the fabrication of 3D photonic crystals active within the optical wavelength range. This shift is driven by the inherent

advantages of these novel approaches, including enhanced simplicity, improved time efficiency, and significant financial benefits [34-36].

For this reason, we examined the polymer/metal oxide nanocomposite films obtained by coating the polymers we used with TiO_2 and ZnO inorganic materials according to different parameters. For this purpose, TiO_2 , one of the inorganic particles we used, is the most popular substance among photocatalysts due to its non-toxicity, reliability, high stability, cost-effectiveness and abundance properties. In experiments with lethal or growth inhibitory bacteria, this compound was mainly used due to its physicochemical stability, non-toxicity, biocompatibility and low costs [37-39].

Its photocatalytic activity enables the degradation or complete mineralization of a broad spectrum of atmospheric contaminants. These include, but are not limited to, nitrogenous and sulfurous compounds, volatile organic compounds (VOCs) emitted from construction materials, various greenhouse gases, components of cigarette smoke, and ubiquitous atmospheric pollutants such as chlorofluorocarbons (CFCs) [40-41]. Among the myriad of inorganic materials, zinc oxide (ZnO) stands out as a highly compelling semiconductor. The incorporation of ZnO as a filler into polymer matrices has been shown to effectively modulate their optical, electrical, and mechanical properties [44-48]. Specifically, ZnO /polystyrene (PS) nanocomposites have demonstrated utility in applications such as anti-reflective coatings, ultraviolet (UV) protective films, and materials exhibiting enhanced thermal stability. Notably, their efficacy in UV shielding applications has been well-documented [49].

Our aim in this study is to characterize the optical properties, film formation behaviors and surface morphologies of both the films obtained by coating two different types of polymers on glass surfaces with certain thicknesses and the nanocomposite films obtained by coating these polymer films with different types and particle sizes of metal oxides in different layer numbers, depending on different parameters, and to obtain regular periodic structures at the nanoscale. The progressive formation of latex films from polystyrene (PS) particles was investigated as a function of temperature and time using the photon transmission method, with measurements conducted via UV-visible (UV-Vis) spectroscopy. For this purpose, the film formation behaviors of thin latex films obtained from polystyrene (PS) particles and nanocomposite systems obtained by coating them with metal oxides of different types and sizes were investigated as a function of temperature and time using the UV-visible (UVV) technique. The evolution of polystyrene (PS) latex film formation was systematically investigated using the photon transmission method, specifically employing UV-Visible (UV-Vis) spectroscopy. Samples were subjected to incremen-

tal annealing steps, with temperatures ranging from 100°C to 250°C in 10°C increments, ensuring all treatments were performed above the glass transition temperature (T_g) of the polymers under study. Following each annealing cycle, the optical transmission of the films was monitored at a wavelength of 550 nm. A bare glass plate served as the reference standard for all UV-Vis experiments, and all measurements were conducted at ambient temperature after the annealing process. In addition, the changes in the morphological structures of the films were followed by SEM.

EXPERIMENTAL

Fabrication of Pure Polystyrene (PS) Latex Films

Latex-based, Pyrene(P) labeled PS latex particles were synthesized by A. Elaissari in France by surfactant-free emulsion polymerization. Pyrene-(P) was used as a fluorescent molecule and was covalently labeled to the polymer chains during polymerization. The particle size distribution of PS polymer was measured in the Malvern Zetasizer Nano ZS-3600 device operating with laser technique and the average particle size was determined as **475nm** for PS. The glass transition temperature of the PS polymer is 105°C, its density is 1.05 g/cm³ and its average molecular weight is $M_w \sim 2.779 \cdot 10^5$ g.mol⁻¹. In order to ensure homogeneous distribution, polymer latexes were mixed for a certain period of time at room temperature in a magnetic stirrer, then applied to glass surfaces of 2.5x2.5 cm² that had been cleaned with alcohol, via the drop-casting method at ambient temperature, in equal numbers of drops to give films of the same thickness ($d = 3.5 - 4 \mu\text{m}$), and finally left to dry at room temperature for 24 hours to obtain pure polymer latex films. A schematic illustration of these steps is provided in Figure 1.

Dispersion of PS and PMMA latexes
in suspension

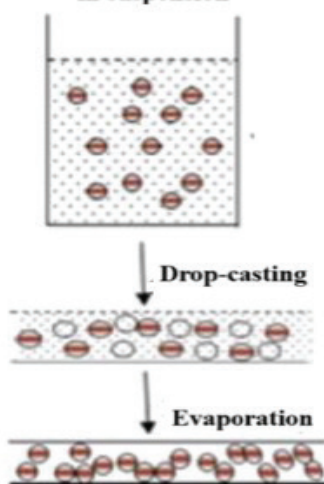


Figure 1: Preparation of pure polymer films.

The PS films left to dry at room temperature formed an opaque coating. To find the thickness of the films, the glass plates were weighed before and after coating.

Preparation of PS/Metal Oxide Nanocomposite Films

Nanoparticles in metal oxide suspensions of ZnO (15nm and 40nm) and TiO_2 (15nm and 40nm) with different particle sizes have a strong tendency to agglomerate due to their large surface areas. In order to prevent this and ensure the stabilization of metal oxide nanoparticles and to obtain a homogeneous distribution, a certain amount of the surfactant Pluronic F127 was incorporated into the metal oxide suspensions. The resulting mixture was subjected to continuous agitation using a magnetic stirrer for 3 hours at ambient temperature, followed by a quiescent period of 24 hours, also at ambient temperature. In the last stage, pure PS polymer films were coated with 5 layers, 10 and 15 layers of 15nm sized (TiO_2 and ZnO) and 40nm sized (TiO_2 and ZnO) metal oxides using the spin coating method to produce polymer-metal oxide nanocomposite films with different nanoparticle sizes, types and layer numbers and metal oxide contents. Then, these samples were annealed above the glass transition temperature of PS at temperatures between 100 °C and 250 °C for ten minutes. The temperature was maintained at 2°C with a fluctuation of $\pm 2^\circ\text{C}$ throughout the annealing period. These steps are shown schematically in Figure 2.

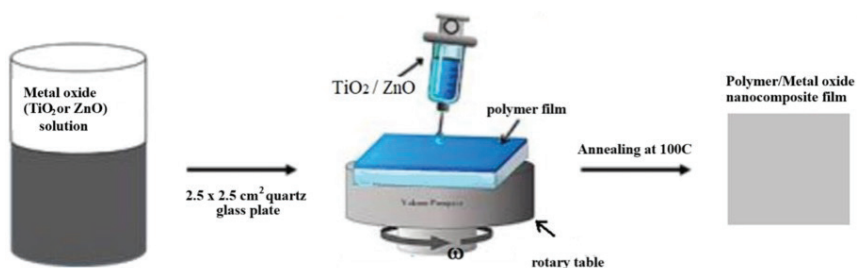


Figure 2: Preparation of PS/Metal Oxide Nanocomposite films.

METHODS

UVV Measurements

The optical transmittance intensity (I_{tr}) of the films was monitored at 550 nm. In these measurements, an empty glass surface was used as a reference and the base correction was made with this glass plate. The measurements after each annealing process were carried out at room tem-

perature. The positions of the samples used in UVV measurements are shown in Figure 3, respectively.

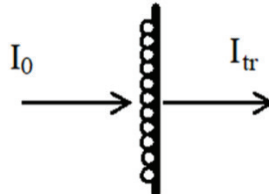


Figure 3: Incident Light (I_0) and light intensity passing through the film surface (I_{tr})

Field Emission Gun Scanning Electron Microscope (FEGSEM-E-DS) Measurements

Morphological images of polymer and nanocomposite thin films were taken on a FEI QUANTA 450 FEG ESEM SEM microscope at 10–20 kV. A thin gold film (10 nm) was sputtered onto the surface of the samples using a Hummer-600 sputtering system to aid in imaging the metal oxide containing films against the glass background.

THEORETICAL ASSUPTIONS

Viscous flow and void closure mechanism

Latex film formation involves the deformation of polymer particles and the subsequent elimination of interstitial voids. This process is primarily driven by the shear stress originating from the polymer's surface tension (specifically, the polymer-air interfacial tension). The kinetics governing this void closure phenomenon directly dictate the ultimate optical transparency and the overall time required for the latex film to fully form [50]. To quantitatively describe the shrinkage of a spherical void with initial radius r within a medium of viscosity η , a fundamental expression has been derived, which establishes the following relationship [51].

$$\frac{dr}{dt} = - \frac{\gamma}{2\eta} \left(\frac{1}{\rho(r)} \right) \quad (4.1)$$

Here, γ represents the surface energy, t denotes time, and $\rho(r)$ is a term reflecting the relative density. The surface energy drives the reduction in void size. The $\rho(r)$ term itself is a function of several microstructural

parameters, including the number of voids within the material, the initial particle size, and the packing characteristics of the microstructure. Equation (4.1) exhibits a strong analogy to expressions describing the time dependence of the minimum film formation temperature during latex film formation [52, 53]. Assuming that the viscosity, η , remains constant with respect to time, the integrated form of Equation (4.1) is given by:

$$t = - \frac{2\eta}{\gamma} \int_{r_0}^r \rho(r) dr \quad (4.2)$$

Here r_0 corresponds to the void radius at the initial time, t_0 . The influence of temperature on polymer fluidity is affected by the overcoming of the macromolecular forces that cause the polymer chain to jump from one equilibrium state to another. This stage occurs at temperatures where the free volume is sufficiently large and the potential barrier is overcome. The Frenkel-Eyring theory gives the temperature dependence of the fluidity as the following equation [54]

$$\eta = \frac{N_0 h}{V} \exp \left(\frac{\Delta G}{kT} \right) \quad (4.3)$$

N_0 is Avogadro's number, h is Planck's constant, V is the molar volume and k is the Boltzmann constant. Since $\Delta G = \Delta H - T\Delta S$, equation (4.3) can be written as follows.

$$\eta = A \exp \left(\frac{\Delta H}{kT} \right) \quad (4.4)$$

ΔH is the activation energy for a viscous fluid. For example, it is the amount of heat that must be given to one mole of substance to make it jump during viscous flow. ΔS is the activation entropy of a viscous fluid. Here A is a constant related to parameters that do not change with temperature. The combination of equation (4.2) and equation (4.4) gives us a useful relationship.

$$t = - \frac{2A}{\gamma} \exp \left(\frac{\Delta H}{kT} \right) \int_{r_0}^r \rho(r) dr \quad (4.5)$$

Assuming that the interparticle voids are of equal diameter and the number of voids remains constant during film formation (i.e. $\rho(r) \approx r^3$), we can use equation (4.5) to examine the above results. Integration of equation (4.5) gives the following relation.

$$t = \frac{2AC}{\gamma} \exp\left(\frac{\Delta H}{kT}\right) \left(\frac{1}{r^2} - \frac{1}{r_0^2}\right) \quad (4.6)$$

C is a constant that depends on the relative density $\rho(r)$. A decrease in the gap size (r) causes an increase in the I_{tr} intensities. Since the scattering intensity (I_{sc}) is proportional to the square of the volume (V) of the scattering body ($I_{sc} \sim V^2$) [55], I can be assumed to be inversely proportional to the sixth power of the gap radius (r) ($I \sim r^6$), so equation (4.6) can be written as:

$$t = \frac{2AC}{\gamma} \exp\left(\frac{\Delta H}{kT}\right) (I_p)^{1/3} \quad (4.7)$$

Here r_0^{-2} is ignored because it is very small compared to the r^2 values after the void closure process has started. Equation (4.7) can be arranged algebraically to facilitate the interpretation of the experimental data, especially the transmitted light intensity (I_{tr}) as a function of the annealing temperature ($T^\circ C$) for all investigated systems;

$$I_p = \left[S(t) \exp\left(-\frac{3\Delta H}{kT}\right) \right] \quad (4.8)$$

where $S(t) = (\lambda t / 2 AC)^3$. For a certain time, equation (4.8) can be written in logarithmic form.

$$\ln I = \ln S(t) - \left(\frac{3\Delta H}{k_b T}\right) \quad (4.9)$$

This equation gives us the activation energy (ΔH) of the viscous flow by using the intensity of the transmitted light (I_{tr}).

RESULTS AND DISCUSSIONS

Optical behavior of pure PS and PMMA films

To monitor the progression of film formation and the concomitant development of optical transparency, the transmitted light intensity (I_{tr}) was quantified following each annealing step. Figure 4 presents the I_{tr} curves for the pure polystyrene (PS) film, annealed at various temperatures.

The transmitted light intensity (I_{tr}) exhibits a notable increase above a critical temperature, conventionally termed the minimum film formation temperature (T_0). Within the coatings industry, T_0 is a crucial parameter, serving as the primary indicator for the lowest effective temperature at which a latex dispersion can be successfully employed in various applications [56, 57, 58]. Fundamentally, T_0 signifies the lowest temperature at which sufficient particle deformation occurs, enabling the reduction of interstitial void diameters to dimensions significantly below the wavelength of visible light [59].

Below this critical temperature, the dried latex typically manifests as an opaque, powdery solid. Conversely, at or above T_0 , the cast latex film undergoes a transition to a continuous and optically transparent state [60]. Consequently, in this investigation, T_0 is empirically defined as the temperature at which the transmitted light intensity (I_{tr}) exhibits an observable increase. The observed increase in transmitted light intensity (I_{tr}) with rising annealing temperature is attributed to the closure of interparticle voids within the films, driven by viscous flow of the polymer. A higher I_{tr} directly correlates with enhanced optical clarity in the films. Therefore, this observed increase in transmitted light intensity unequivocally indicates a significant microstructural evolution within the films upon annealing, signifying an improvement in their overall optical transparency. Upon annealing, the polymer undergoes viscous flow, leading to the deformation of particles and the subsequent elimination of interparticle voids. Further thermal treatment at elevated temperatures promotes polymer chain healing and interdiffusion across former particle boundaries, ultimately yielding a film with enhanced optical transparency. The optical transmittance of these films is primarily governed by two main light scattering phenomena: surface scattering and scattering from internal interfaces (i.e., polymer-polymer and polymer-metal oxide boundaries). Prior to annealing, the film microstructure is characterized by a high density of voids (representing numerous polymer-air interfaces), resulting in significant light scattering predominantly from these air-polymer interfaces (surface scattering). Following the completion of the void closure process, light scattering is primarily attributable to refractive index mis-

matches at polymer-polymer and polymer-metal oxide interfaces within the consolidated film.

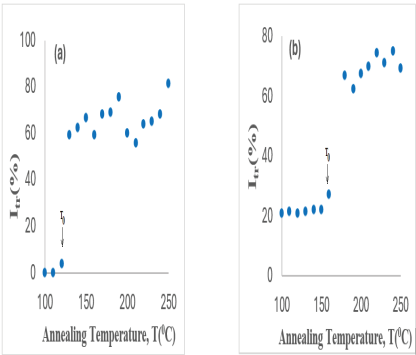


Figure 4: Transmitted light intensity (I_{tr}) of Pure Polystyrene (PS) film according to annealing temperature $T(^{\circ}\text{C})$.

In order to support the above explanations, SEM images of the latex film that have not yet undergone the annealing process in Figure 5 and those annealed at 250°C in Figure 6 were taken, respectively. It is seen in Figures 6 that after annealing at 250°C, the spherical microstructures of the latexes are completely destroyed. This situation shows that the polymer chains are viscous flowing into the interparticle voids and the film formation is completed through across chain diffusion from the particle boundaries and transparency is achieved.

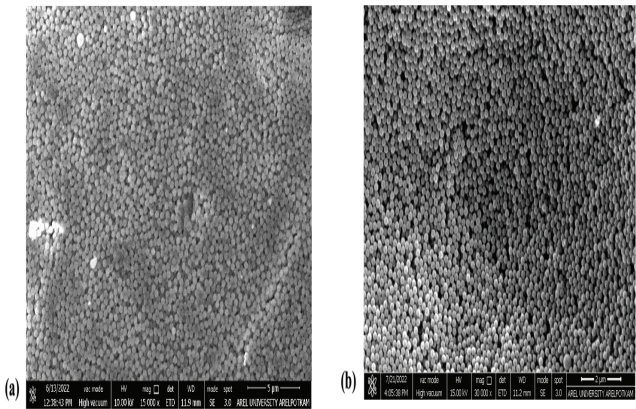
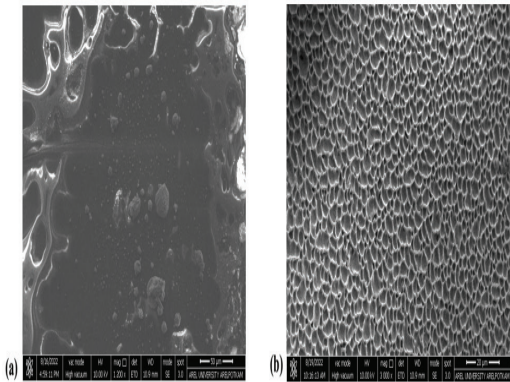


Figure 5: SEM micrographs of the as-prepared nano-sized polystyrene (PS) latex film at room temperature.



Şekil 6: SEM micrographs of the nano-sized polystyrene (PS) latex film following annealing at 250°C.

Equation (4.9) was applied to the region above the minimum film formation temperature (T_0) in all transmitted light intensity (I_{tr}) curves. The activation energy of viscous flow (ΔH_{tr}) was subsequently calculated from the slope of the linear fits obtained from the logarithmic transformation of these curves. The calculated values are tabulated in Table 1. The behavior of $\ln(I_{tr})$ versus $T^{-1} \times 10^{-3} (^{\circ}K)$ for PS is also seen in Figure 7.

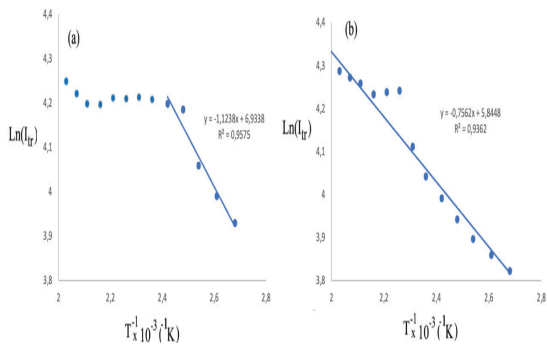


Figure 7: Change in the logarithmic form $\ln(I_{tr})$ of the curves of Polystyrene (PS) film in Figure 5 with T^{-1} . The slope line on the graph is the activation energy ΔH_{tr} .

Table 1: Calculated viscous flow (ΔH_{tr}) activation energy value for pure PS film.

Polymer	ΔH_{tr} (kcal/mol)
PS	4,59

After this section, we investigated the film formation behaviors of polymer/metal oxide nanocomposite films, which we obtained by coating pure polymers with two different types of metal oxides (TiO_2 and ZnO) having different particle sizes (15nm and 40nm) in varying layer numbers by the spin coating method, according to temperature, metal oxide layer number, metal oxide type and metal oxide size difference.

Optical Behavior of PS (polystyrene) / Metal Oxide (ZnO , TiO_2) Nanocomposite Films

In this section, we investigated the optical properties and surface structures of Polystyrene (PS) films by coating them with TiO_2 (15nm and 40nm) and ZnO (15nm and 40nm) particles with two different particle size distributions in increasing layer numbers.

Firstly, we investigated the transmitted light intensity (I_{tr}) by coating TiO_2 and ZnO metal oxides with 15nm and 40nm particle size distribution onto PS films with increasing layer numbers by spin coating method. The optical transmittance spectra of PS/ TiO_2 and PS/ ZnO nanocomposite films consisting of 5, 10, and 15 layers of 15-nm TiO_2 and 15-nm ZnO , respectively, are presented in Figures 8a and 8b. These films were subjected to thermal annealing at high temperatures for 10 min before spectral acquisition.

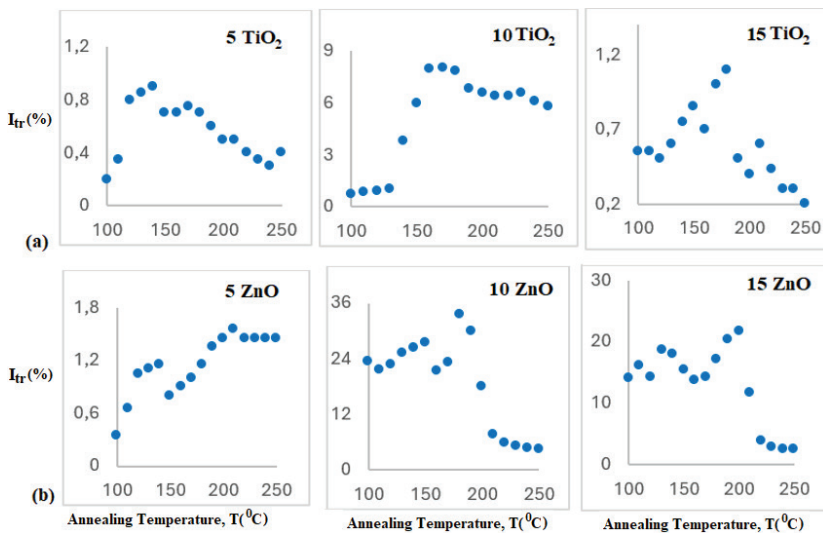


Figure 8: Plots of I_{tr} versus annealing temperatures for various number of (a) TiO_2 and (b) ZnO layers of PS/ TiO_2 and PS/ ZnO nanocomposite films. Numbers on each curve represent TiO_2 (15nm) and ZnO (15nm) content in the film.

When the $(I_{tr})_{max}$ value (~ 80) of the transmitted light intensity of the pure PS polymer film is compared, we see that the application of metal oxide to the PS films reduces the light transmittance in both series (a and b), and especially in the coatings made with TiO_2 , it reduces the transmitted light intensity values by 90%. This rate is around (65%-70%) in the films coated with ZnO. In other words, the transparency of the films coated with ZnO particles is slightly better than the films coated with TiO_2 . When we compare the composite films among themselves, it is seen that the films coated with 10 layers of TiO_2 and 10 layers of ZnO give higher transmittance than the films coated with 5 and 10 layers, i.e. they are more transparent.

Optical transmittance spectra of PS/ TiO_2 and PS/ZnO nanocomposite films containing 5, 10 and 15 layers of $TiO_2(40nm)$ and ZnO(40nm) annealed at elevated temperatures for 10 min are shown in Figures 9a and b, respectively.

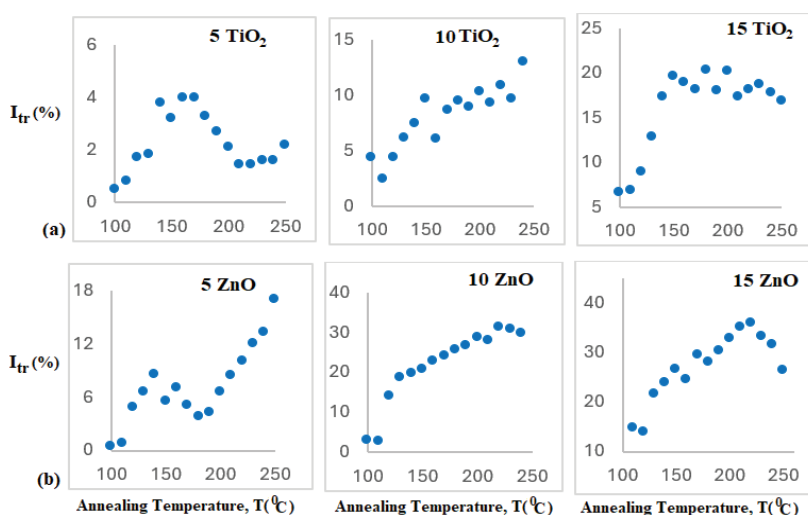


Figure 9: Plots of I_{tr} as a function of annealing temperature for various number of (a) TiO_2 and (b) ZnO layers of PS/ TiO_2 and PS/ZnO nanocomposites. The numerical labels on each curve indicate the TiO_2 (40 nm) and ZnO (40 nm) content in the films.

In this series prepared with metal oxides having large particle size distribution, it is observed that the optical transmittance (I_{tr}) of the films coated with ZnO is higher than the TiO_2 coated films. In both series, especially in the 10 and 15 layer coated films, the transmittance increased with increasing annealing temperature and after reaching a maximum value at

a certain temperature, it either saturated or started to decrease slightly. In the films containing TiO_2 , this maximum was reached at earlier temperatures, but they reached lower transmitted light intensities than the maximum transmitted light intensities of the films coated with ZnO. In the film containing 5 layers of TiO_2 , the optical transmittance intensity started to decrease significantly immediately after reaching the maximum. This shows that the film started to become opaque as the annealing continued after 160°C . In the film coated with 5 layer ZnO, after the increase started, it suddenly collapsed at early temperatures and then started to increase again. We can explain this situation as follows; when the voids are filled and the particle boundaries are in contact, that is, before the particle-particle interfaces disappear, most of the incoming light is scattered from these interfaces and I_{tr} becomes minimum due to this scattering. Later, with the annealing continuing at higher temperatures, the particle-particle interfaces disappear. This causes the film to become transparent, so I_{tr} increases again at high annealing temperatures. We can say that this behavior develops in this way in relation to the particle size of ZnO.

Figure 10 illustrates the dependence of the maximum transmitted light intensity ($I_{\text{tr,max}}$) on the number of metal oxide layers. A similar characteristic response of ($I_{\text{tr,max}}$) is observed in films fabricated with ZnO particles of different sizes, demonstrating a comparable behavior to that influenced by an increasing number of ZnO layers. We can see that the transparency in the films increases with the increase in the number of ZnO layers, but the light intensities in films prepared with ZnO with large particle size (40nm) are slightly higher than in films containing ZnO with 15nm particle size.

Similar behavior is observed more clearly and regularly especially in films prepared with large-sized (40nm) TiO_2 . As a result, the fact that ($I_{\text{tr,max}}$) intensities of light transmitted in films containing metal oxides (ZnO and TiO_2) with large-sized (40nm) particle distribution in composite systems prepared with two different metal oxide types gives higher values indicates that the development in the transparency of composite films is significantly affected by the particle size of the metal oxide.

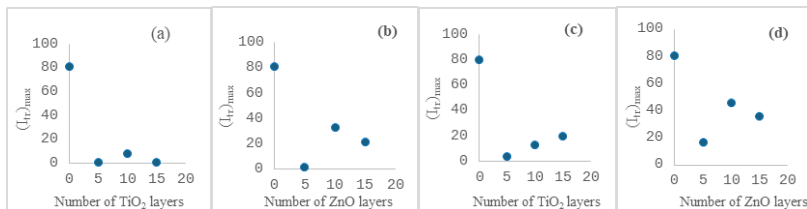


Figure 10: Variation of maximum transmitted light intensities ($I_{\text{tr,max}}$) of (a) PS/ TiO_2 (15nm), (b) PS/ZnO(15nm), (c) PS/ TiO_2 (40nm) and (d) PS/ZnO(40nm) composite films with the number of metal oxide layers.

The increase in I_{tr} originates because of the void closure process, then Eq. (4.9) was applied to I_{tr} above T_0 below maxima for all film samples in two series. Figures 11(a-b) and 12(a-b) present the present $\ln I_{tr}$ versus T^{-1} plots from which ΔH_{tr} activation energies were obtained. The measured ΔH_{tr} activation energies are listed in Table 2 for both series, where It is observed that the activation energies in PS films coated with 15nm particle size TiO_2 and ZnO do not change much, that is, the amount of heat required for one mole of polymeric material to perform a jump during viscous flow does not change by changing the mixture composition in the films.

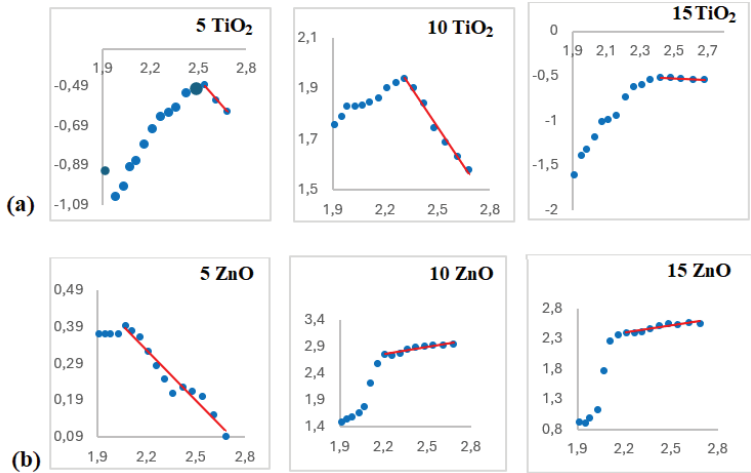


Figure 11: Figure 8 presents the $\ln(I_{tr})$ as a function of T^{-1} for (a) PS/ TiO_2 (15nm) and (b) PS/ZnO(15nm) composite films with 5, 10, and 15 layers of metal oxide. The ΔH_{tr} is derived from the slope of the linear fit to these plots.

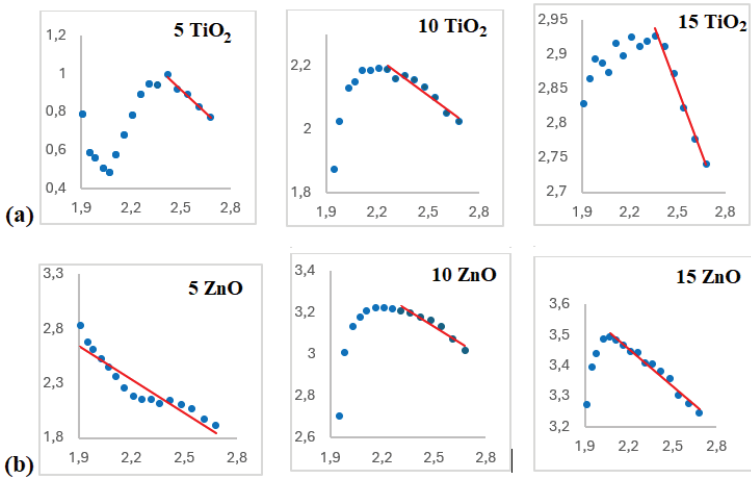


Figure 12: Figure 9 presents the $\ln(I_{tr})$ as a function of T^{-1} for (a) PS/ TiO_2 (40nm) and (b) PS/ZnO(40nm) composite films with 5, 10, and 15 layers of metal oxide. The ΔH_{tr} is derived from the slope of the linear fit to these plots.

However, in 40nm particle size TiO_2 and ZnO coated films, a completely opposite behavior is observed. In TiO_2 (40nm) coated films, as the number of layers increases, the activation energy required for viscous flow also increases, but in ZnO(40nm) coated films, the activation energy decreases with the increasing number of ZnO layers. A comparative analysis of the ΔH_{tr} values obtained in this study with that of the pure polystyrene (PS) latex system ($\Delta H_{tr} = 4.59 \text{ kcal}\cdot\text{mol}^{-1}$) reveals a significant reduction in the viscous flow activation energy upon the incorporation of TiO_2 and ZnO. This indicates that the presence of these metal oxides promotes the void closure process, consequently enabling latex film formation in the composite systems with substantially lower energy input compared to the pure latex system.

Table 2: Experimentally determined activation energies of both PS/ TiO_2 and PS/ZnO films for different metal oxide particle size and varying numbers of metal oxide layers.

Number of metal oxide layers	ΔH for TiO_2 (15nm)/PS nanocomposites (kcal/mol)	ΔH for TiO_2 (40nm)/PS nanocomposites (kcal/mol)	ΔH for ZnO (15nm)/PS nanocomposites (kcal/mol)	ΔH for ZnO (40nm)/PS nanocomposites (kcal/mol)
0	4,59	4,59	4,59	4,59
5	1,25	1,99	0,886	3,039
10	2,67	2,033	1,155	2,92
15	- 0,213	2,912	0,993	2,88

In addition, we observed that the activation energies of the composite films obtained by coating them 15 times with TiO_2 having both 15nm and 40nm particle sizes were very low. We can explain this as the fact that PS latexes were coated very densely with this level of TiO_2 content, almost completely preventing them from making viscous flow.

In Figure 13 and Figure 14, we examined the changes in the morphology of the films by taking SEM micrographs of the PS/ TiO_2 composite films containing 5 and 10 layers of TiO_2 (15 nm) after heat treatment at 100°C and 250°C , respectively, and finally after dissolving in a suitable solvent.

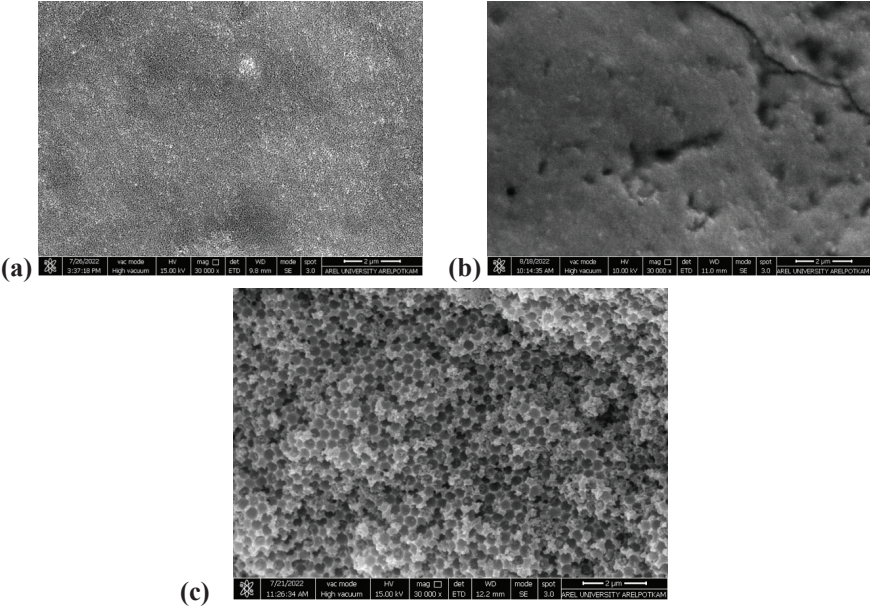


Figure 13: SEM images of the PS/ TiO_2 composite film containing 5 layers of TiO_2 (15 nm) after annealing at (a) 100°C (b) at 250°C for 10 min and (c) after dissolution.

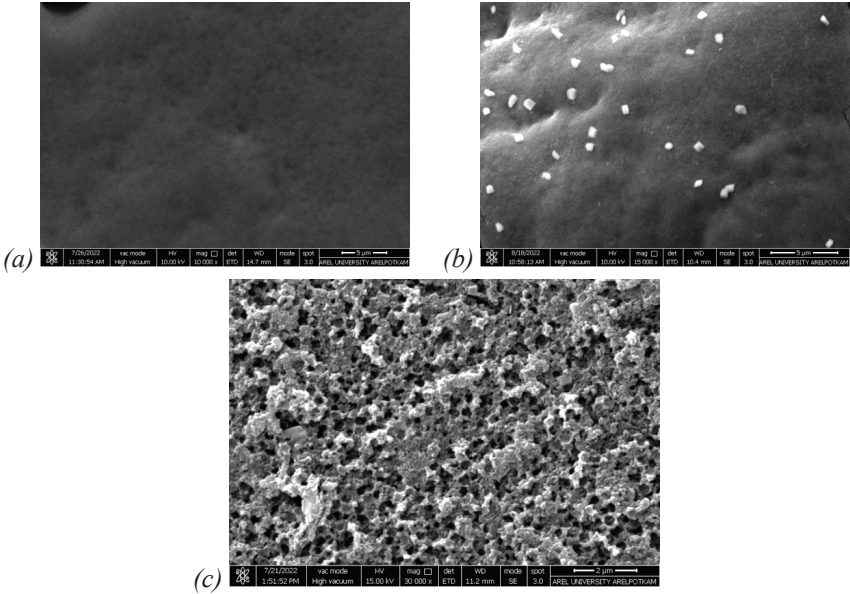


Figure 14: SEM images of the PS/ TiO_2 composite film containing 10 layers of TiO_2 (15 nm) after annealing at (a) 100°C (b) at 250°C for 10 min and (c) after dissolution.

When we look at the annealed states of the 5 and 10-layer TiO_2 coated films in Figures 13(a-b) and 14(a-b) at 100°C and 250°C , it is seen that the PS spheres in the film containing 5 layers of TiO_2 melted after the 250°C heat treatment and gave a flat structure, but voids locally formed in places. This may be due to phase separation of PS and TiO_2 at this stage. It is observed that the surface of the film coated with 10 layers of TiO_2 annealed at 100°C has a much flatter structure. We can explain this as the accumulation of TiO_2 particles on the surface as a result of the very dense coating of the PS latex film surface with TiO_2 and the formation of a flat structure on the upper surface of the film. In addition, although a smooth surface structure is obtained by the melting of the PS latex spheres after annealing at 250°C on the surface of the film containing 10 layers of TiO_2 , we also see clustered TiO_2 particles in some areas due to the density of the coating.

Figures 13c and 14c show the surface structures of the films with 5 and 10 layers of TiO_2 (15nm) after the dissolution process, respectively. The intended porosity was achieved in both films, but the most regular and dense porosity was achieved in the film coated with 5 layers of TiO_2 . In the 10-layer TiO_2 coated film, we see that the porosity is not as honeycomb-like as expected and its number decreases due to the dense accumulation of TiO_2 particles on the PS spheres.

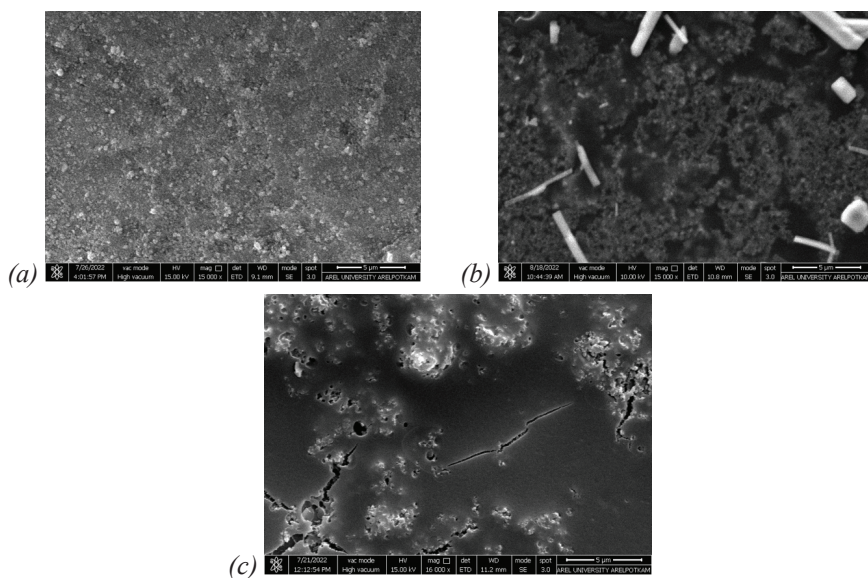


Figure 15: SEM images of the PS/ TiO_2 composite film containing 5 layers of TiO_2 (40nm) after annealing at (a) 100°C (b) at 250°C for 10 min and (c) after dissolution.

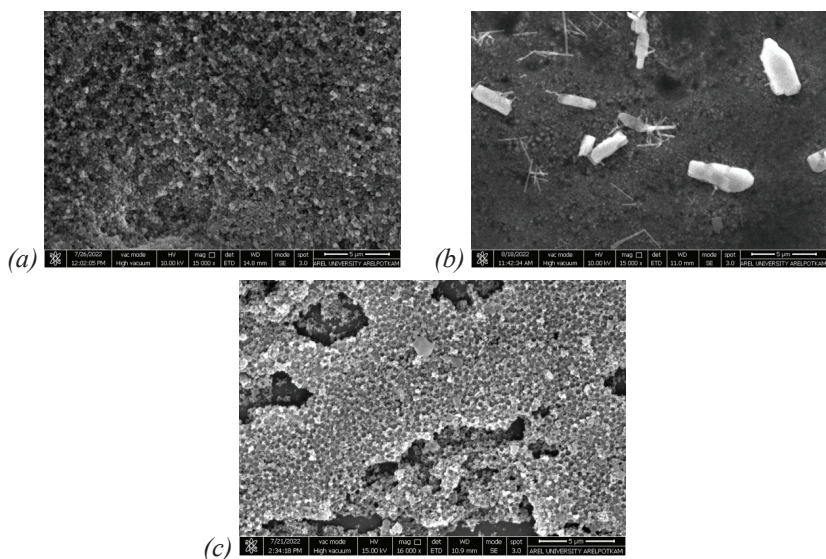


Figure 16: SEM images of the PS/ TiO₂ composite film containing 10 layers of TiO₂ (40nm) after annealing at (a) 100°C (b) at 250°C for 10 min and (c) after dissolution

Figures 15 and 16 show the surface morphologies of PS/TiO₂ composite films prepared by coating 5 and 10 layers with large-sized (40 nm) TiO₂ particles according to their annealing temperatures and post-dissolution states. Firstly, when we look at the annealed states at 100°C and 250°C, we cannot clearly see the spherical forms of PS latexes at 100°C in both 5-layer and 10-layer TiO₂ (40nm) containing films. This is because large particle size (40nm) TiO₂ particles accumulate and form a coating on the upper surface of PS latexes. After heat treatment at 250°C, we see that the film structures have turned into a flat form due to viscous flow and mutual chain diffusion of PS latex chains from intermediate boundaries, but TiO₂ particles have accumulated in some regions of the film and clustered on the surface with this melting.

In addition, when we compare these films with the surfaces of the films coated with small-sized TiO₂(15 nm) particles in Figures 13a and 14a, we see that the small-sized TiO₂(15 nm) particles penetrate better into the gaps between the PS latexes and accumulate more evenly in the gaps, resulting in a smoother surface compared to the films coated with 40 nm TiO₂.

Finally, it is observed that porous structures, although not very regular, were formed in the composite film coated with only 10 layers of TiO₂ after dissolution (Figure 16c).

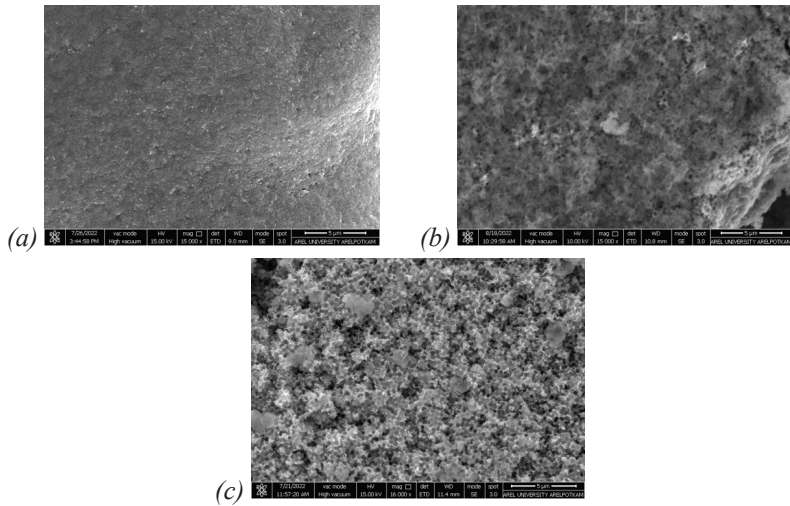


Figure 17: SEM images of the PS/ZnO composite film containing 5 layers of ZnO(15nm) after annealing at (a) 100°C (b) at 250°C for 10 min and (c) after dissolution.

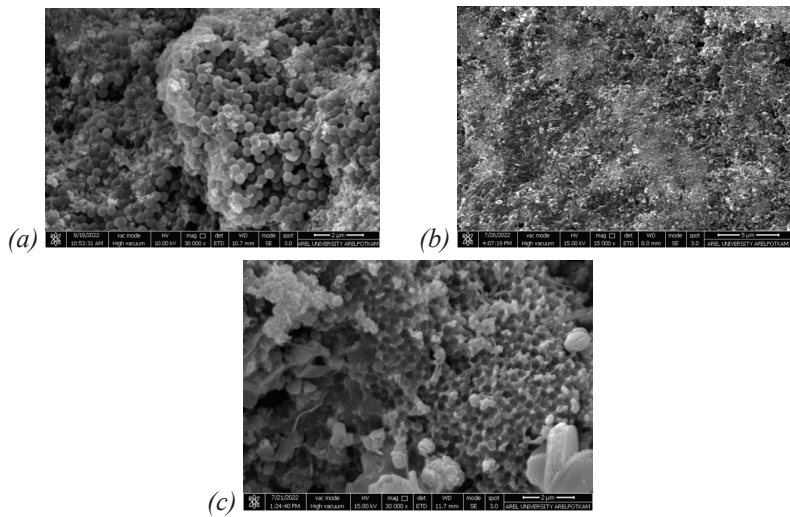


Figure 18: SEM images of the PS/ZnO composite film containing 5 layers of ZnO(40nm) after annealing at (a) 100°C (b) at 250°C for 10 min and (c) after dissolution.

When we look at the annealed states of the films in figures 17a and 18a at 100°C, the spherical structures of the PS latexes are clearly seen in the film coated with 5 layers of ZnO with small-sized (15nm) ZnO particles. When we compare the film surfaces annealed at 250°C, we see that porosity has started in the films coated with 5 layers of ZnO (15nm) in Figure

17b, but in the film prepared by coating with **5** layers of ZnO (**40nm**) in Figure **18b**, the PS spheres that have not yet melted are still seen.

It is understood that ZnO particles have a weak accumulation between PS latexes, that is, ZnO particles start from the lower parts of the film and cover the PS latexes through accumulation, and that the wall height is sufficient for pore formation in these areas of the film after dissolution, but in some areas of the film, ZnO particles do not accumulate from the lower parts of the film, but accumulate directly on the top surface of the film and form a layer there, completely covering the PS spheres, thus preventing pore formation after dissolution.

In conclusion, We observed that porosity was achieved in varying proportions and arrangements in PS/TiO₂ and PS/ZnO composite systems prepared by coating with almost both metal oxide types and metal oxide particle sizes. Thus, we found that the production of regular porosity with sufficient wall height can be completely controlled by changing two parameters (type of metal oxide and particle size of metal oxide). Tunable control over the dimensions of internal features such as wall thickness and pore size is crucial for certain applications. In the context of photonic crystals, this capability facilitates precise manipulation of the periodicity of the dielectric constant, thereby enabling the desired optical response. The structural changes were found to be consistent with the UUV data for each film series. In particular, we found that the particle size of the metal oxide had a significant effect on the viscous flow activation energies of the composite films. The activation energies of the films prepared with 30 nm sized metal oxides were found to be slightly larger than the activation energies of the composite films prepared with 15 nm sized metal oxides; this phenomenon was attributed to the particle size effect of the metal oxide.

Finally, the transmittance of the ZnO-coated films is 30-60% higher than that of the TiO₂ series, promising the use of ZnO-coated composite films in anti-reflective applications. In this study, we also found that the formation of monodisperse, submicron inorganic oxide pores depends on the type, size and number of layers of the metal oxide by spin-coating technique, which is the simplest and cheapest technique. These structures can potentially be used in applications of chromatographically supported materials, solid crystals, battery materials, thermal insulators, or photonic crystals.

Acknowledgments

This study was supported by the Scientific Research Projects (BAP) Coordination Office of Mimar Sinan Fine Arts University (MSGSU).

The authors would also like to thank the Physics Department for the optical analyses performed in the MSGSU Physics Department research laboratory and Istanbul Arel University Polymer Technologies and Composite Application and Research Center (POTKAM) for the SEM imaging analyses.

Finally, I would like to thank Prof. Dr. Şaziye Uğur, who has always supported and contributed to my academic development.

REFERENCES

- [1] Wicks, Z. L., Jones, F.N., Pappas, S.P. and Wicks, D.A. (2006). *Organic Coatings: Science and Technology*. John Wiley & Sons, Inc. USA.
- [2] Ugur, S., Elaissari, A. and Pekcan, O. (2003). Void closure and diffusion processes during latex film formation from surfactant-free polystyrene particles: a fluorescence study, *Journal of Colloid and Interface Science* 263, 674–683, [https://doi.org/10.1016/S0021-9797\(03\)00398-9](https://doi.org/10.1016/S0021-9797(03)00398-9)
- [3] Beecroft, L. L. and Ober, C. K. (1997). *Chem. Mater.* 9, 1302.
- [4] Vijaya Kumar, R., Elgamiel, R., Diamant, Y., Gedanken A., and Norwig, J. (2001). *Langmuir* 17, 1406.
- [5] Sadek, E. M., Mansour, N. A., Sahara, S. I. and Motawie, A. M. (2011). *J. Appl. Sci.* 7, 535.
- [6] Motawie, A. M., Madany, M. M., El-Dakrory, A. Z., Osman, H. M. Ismail, E. A., Badr, M. M. D., El-Komy, A. D. and Abulyazied, E. (2014). *Egypt. J. Pet.* 23, 331.
- [7] Ayeleru, O. O., Dlova, S., Ntuli, F., Kupolati, W. K. P., and Olubambi, A. (2019). *Procedia Manuf.* 30, 194.
- [8] Shaffer, M. S. P. and Koziol, K. (2002). *Chem. Commun.*, 2074.
- [9] Walker, J. P. and Asher, S. A. (2005). *Anal. Chem.* 77, 1596.
- [10] Sharma, D., Sharma, P. and Thakur, N. (2009). *Optoelectron. Adv. Mater.* 3, 145.
- [11] Jeeju, P. P., Jayalekshmi, S., Chandrasekharan, K. and Sudheesh, P. (2012). *Opt. Commun.* 285, 5433.
- [12] Tanev, P. T., Chibwe, M. and Pinnavaia, T. J. (1994). Titanium-containing mesoporous molecular sieves for catalytic oxidation of aromatic compounds, *Nature*, 368, 321–323, DOI: 10.1038/368321a0
- [13] Gin, D. L. and Gu, W. (2001). Nanoporous Catalytic Materials with Organic Frameworks, *Adv. Mater.*, 13, 1407-1410, DOI: 10.1002/1521-4095(200109)13:183.0.CO;2-0
- [14] Wang, X., Yu, J. C., Hou, Y.; and Fu, X. (2005). Three-Dimensionally Ordered Mesoporous Molecular- Sieve Films as Solid Superacid Photocatalysts, *Adv. Mater.*, 17, 99-102, DOI: 10.1002/adma.200400884.
- [15] Skrabalak, S. E. and Suslick, K. S. J. (2005). Porous MoS₂ Synthesized by Ultrasonic Spray Pyrolysis, *J. Am. Chem. Soc.*, 127, 9990-9991 DOI: 10.1021/ja051654g
- [16] Hobbs, K. L., Larson, P. R., Lian, G. D., Keay, J. C. and Johnson, M. B. (2004). Fabrication of nanoring arrays by sputter redeposition using porous alumina templates, *Nano Lett.*, 4, 167- 171, DOI: 10.1021/nl034835u
- [17] Kim, J. Y., Yoon, S. B., Kooli, F. and Yu, J. S. (2001). Synthesis of highly ordered mesoporous polymer networks, *J. Mater. Chem.*, 11, 2912-2914, DOI: 10.1039/b108207h
- [18] Melde, B. J., Burkett, S. L., Xu, T., Goldbach, J. T. and Russell, T. P. (2005).

- Hawker Silica nanostructures templated by oriented block copolymer thin films using pore-filling and selective-mineralization routes, *C. J. Chem. Mater.*, 17, 4743-4749, DOI: 0.1021/cm051407b
- [19] Xiong, L. M., Shi, J. L., Gu, J. L., Shen, W. H., Dong, X. P., Chen, H. R., Zhang, L. X., Gao J. H. and Ruan, M. L. (2005). Directed Growth of Well-Aligned Zinc Silicate Nanowires along the Channels of Surfactant-Assembled Mesoporous Silica, *Small*, 1, 672-682, DOI: 10.1002/smll.200500066.
- [20] Tian, S. J., Wang, J. J., Jonas, U. and Knoll, W.(2005). Porous networks through colloidal templates, *Chem. Mater.*, 17, 135-180, DOI: 10.1007/128_2008_3
- [21] Nishikawa, T., Nishida, J., Ookura, R., Nishimura, S. I., Wada, S., Karino, T.(1999). Shimomura M. Honeycomb-patterned thin films of amphiphilic polymers as cell culture substrates, *Mater. Sci. Eng. C.*, 8–9, 495-500, DOI: /10.1016/S0928-4931(99)00075-2
- [22] Li, Y., Neoh, K. G., Cen, L. and Kang, E. T.(2005). Porous and electrically conductive polypyrrole– poly (vinyl alcohol) composite and its applications as a biomaterial, *Langmuir*, 21, 10702-10709, DOI: 10.1021/la0514314
- [23] Kanungo, M., Collinson, M. M. (2004). Fabrication of two-dimensionally ordered macroporous silica materials with controllable dimensions, *Chem. Commun.*, 548-549, DOI: 0.1039/B314081B
- [24] Davis, M. E. (2002). Ordered porous materials for emerging applications, *Nature*, 417, 813-821 , DOI: 10.1038/nature00785
- [25] Zalusky, A. S., OlayoValles, R., Wolf, J. H. and Hillmeyer, M. A.(2002). Ordered nanoporous polymers from polystyrene– polylactide block copolymers, *J. Am. Chem. Soc.*, 43, 12761-12773, DOI: 10.1021/ja0278584
- [26] Lewandowski, K., Murer, P., Svec, F. and Fréchet, J. M. J.(1998). *Anal. Chem.*, 70, 1629-1698, DOI: 10.1021/ac971196x.
- [27] Walheim, S., Schäffer, E., Mlynek, J., and Steiner, U. (1999). Nanophase-separated polymer films as high-performance antireflection coatings, *Science*, 283, 520-522, DOI: 0.1126/science.283.5401.520
- [28] Ibn-Elhaj, M. and Schadt, M. (2001). Optical polymer thin films with isotropic and anisotropic nano-corrugated surface topologies, *Nature*, 410, 796–799, DOI: 10.1038/35071039
- [29] Hiller, J. A., Mendelsohn, J. D., and Rubner, M. F.(2002). Reversibly erasable nanoporous antireflection coatings from polyelectrolyte multilayers, *Nat. Mater.*, 1, 176-179, DOI: 10.1038/nphoton.2007.26
- [30] Xiangling, Xu, Asher, Sanford A.(2004). Synthesis and Utilization of Monodisperse Hollow Polymeric Particles in Photonic Crystals, *J. Am. Chem. Soc.*,126, 7940-7945, DOI:10.1021/ja049453k
- [31] Chomski, E. and Ozin, G. A. (2000). Panoscopic Silicon—A Material for “All” Length Scales, *Adv. Mater.*, 12, 1071-1078, DOI: 10.1002/1521-4095(200007)12:143.O.CO;2-J
- [32] Moon, J. H., Kim, S., Yi, G. R., Lee, Y. H. and Yang, S. M. (2004). Fabrication of Ordered Macroporous Cylinders by Colloidal Templating in Microcapillaries, *Langmuir*, 20, 2033-2035, DOI: 10.1021/la0358015

- [33] Joannopoulos, J. D., Meade, R. D. and Winn, N. (1995). *Photonic Crystals: Molding the Flow of Light*, Princeton University Press, Princeton, N.J., DOI: 10.2307/j.ctvc4gz9
- [34] Vlasov, Y. A., Bo, X. Z., Sturm, J. C. and Norris, D. J. (2001). On-chip Natural Assembly of Silicon Photonic Bandgap Crystals, *Nature*, 414, 289-93, DOI: 10.1038/35104529
- [35] Blanco, A., Chomski, A., Grubbs, S., Ibbett, M., John, S., Leonard, S. W., Lopez, C., Meseguer, F., Miguez, H., Mondia, J. P., Ozin, G. A., Toader, O. and van Driel H. M. (2000). Large-scale Synthesis of a Silicon Photonic Crystal With a Complete Three-Dimensional Bandgap Near 1.5 Micrometres, *Nature*, 405, 437-440, DOI: 10.1038/35013024
- [36] Wijnhoven, J. and Vos, W. L.(1998). Preparation of Photonic Crystals Made of Air Spheres in Titania, *Science*, 281, 802-804, DOI: 10.1126/science.281.5378.802
- [37] Sunada, K., Watanabe, T., and Hashimoto, K. (2003). Bactericidal Activity of Copper-Deposited TiO₂ Thin Film under Weak UV Light Illumination, *Environ. Sci. Technol.*, 37, 4785-4789, DOI: 10.1021/es034106g
- [38] Lin, H., Xu, Z., Wang, X., Long, J., Su, W., Fu, X. and Lin, Q.(2008). Photocatalytic and antibacterial properties of medical-grade PVC material coated with TiO₂ film, *J. Biomed. Mater. Res. B: Appl. Biomater.*, 87, 425-431, DOI: 10.1002/jbm.b.31120
- [39] Linkous, A. C., Carter, G. J., Locusek, D. B., Ouellette, A. J., Slatery, D. and Simitha, L. A.(2000). Photocatalytic Inhibition of Algae Growth Using TiO₂, WO₃, and Cocatalyst Modifications, *Environ. Sci. Technol.*, 34, 4754-58, DOI: 10.1021/es001080+
- [40] Herrmann, J. M.(1999) Heterogeneous photocatalysis: fundamentals and applications to the removal of various types of aqueous pollutants, *Catal. Today*, 53, 115–129, DOI: 10.1016/S0920-5861(99)00107-8
- [41] Schmid, C. M., Buchbinder, A. M., Weitz, E. and Geiger, F. M.(2007). Photochemistry of the indoor air pollutant Acetone on Degussa P25 TiO₂ studied by chemical ionization mass spectrometry, *J. Phys. Chem. A*, 111, 13023–13031, DOI: 10.1016/S0920- 5861(99)00107-8
- [42] Peral, J. and Ollis, D. F.(1992). Heterogeneous photocatalytic oxidation of gas-phase organics for air purification: acetone, 1-butanol, butyraldehyde, formaldehyde, and m-xylene oxidation, *J. Catal.*, 136, 554–565, DOI: 10.1016/0021-9517(92)90085-V
- [43] Daisey, J. M., Hodgson, A. T., Fisk, W. J., Mendell, M. J. and Tenbrinke, J. (1994). Volatile organic compounds in twelve California office buildings: classes, concentrations and sources, *Atmos. Environ.*, 28, 3557–3562, DOI: 10.1016/1352-2310(94)00200-5
- [44] Lee, J., Bhattacharyya, D., Eastaugh, A. J. and Metson, J. B. (2008). *Curr. Appl. Phys.* 8, 42.
- [45] Chae, D. W., and Kim, B. C. (2005). *Polym. Adv. Technol.* 16, 846.
- [46] Tang, E. and Dong, S. (2009). *Colloid Polym. Sci.* 287, 1025 .

- [47] Thapoung, J., Tasurin, K., Traiphol, N., and Pangpaiboon, N.(2018). J. Met. Mater. Miner. 28, 89.
- [48] Kiaei, M., Kord, B., Samariha, A., Moghdam, Y. R. and Farsi, M. (2017). BioResources 12, 6518.
- [49] W.-C. Shih, M.-S. Wu, J. Cryst. Growth 137, 319 (1994).
- [50] Pekcan, O. and Canpolat, M. (1996). J. Appl. Polym. Sci. 59, 277.
- [51] Keddie, J.L., Meredith, P., Jones, R.A.L., Donald, A.M., In Provder, T., Winnik, M.A.(1996). Urban MW, editors. Film formation in waterborne coatings, Proceedings off ACS Symposium Series 648. Washington, DC: American Chemical Society, P.332-48.
- [52] Sperry, P.R., Snyder, B.S., O'Dowd, M.L. and Lesko, P.M.(1994). Langmuir 10, 2619.
- [53] (a) Canpolat, M. and Pekcan, O. (1995). Polymer 36, 4433.
(b) Canpolat, M. and Pekcan, O. (1996). J. Polym. Sci. Part B: Polym. Phy. 34, 691-698.
- [54] Fulcher, G.S. (1925). J. Am. Ceram. Soc., 8, 339.
- [55] Voyutskii, S. S. (1978). Colloid Chemistry, MIR Publisher, Moscow.
- [56] Keddie, J.L. (1997). Mater. Sci. Eng., R21, 101.
- [57] Steward, P.A, Hearn, J., and Wilkinson, M.C. (2000). Adv. Colloid. Interface Sci., 86, 195.
- [58] Jensen, D.P. and Morgan, L.W. (1991). J. Appl. Polym. Sci., 42. 2845.
- [59] Keddie, J.L., Meredith, P., Jones, R.A.L. and. Donald, A.M.(1995). Macromolecules, 28, 2673.
- [60] Eckersley, S.T. and Rudin, A. (1990). J. Coat. Technol., 62, 89.

Chapter 9

AN INVESTIGATION OF TOTALLY UMBILICAL SEMI-INVARIANT SUBMANIFOLDS IN LOCALLY DECOMPOSABLE GOLDEN RIEMANNIAN MANIFOLDS¹

Mustafa GÖK²

¹ This book chapter is produced from the author's doctoral thesis.

² Associate Professor, National Defence University, Turkish Military Academy,
06420 Ankara, Turkey, Orcid: 0000-0001-6346-0758, mustafa.gok@email.com

Introduction

The basis for the concept of a golden structure on manifolds are polynomial structures defined by Goldberg and Yano (Goldberg & Yano, 1970) and it was introduced by Hreţcanu and Crâşmăreanu (Hreţcanu & Crâşmăreanu, 2007) with inspiration from the golden ratio. Golden structures were researched by the same authors (Crâşmăreanu & Hreţcanu, 2008) with the help of the properties of corresponding almost product structures. Complete and horizontal lifts of golden structures in tangent bundles were explored by Özkan (Özkan, 2014). The integrability conditions of golden Riemannian structures were discussed by Gezer, Cengiz and Salimov (Gezer, Cengiz, & Salimov, 2013). The fundamental features of the induced structures on submanifolds in golden Riemannian manifolds were given and invariant submanifolds were characterized by Hreţcanu and Crâşmăreanu (Hreţcanu & Crâşmăreanu, 2007; Hreţcanu & Crâşmăreanu, 2009). Anti-invariant submanifolds of golden Riemannian manifolds were examined by Gök, Kılıç and Keleş (Gök, Kılıç, & Keleş, 2020) in terms of the characterizations and the condition of being totally geodesic. Also, the stability problem of a particular class of anti-invariant submanifolds, i.e., Lagrangian-like submanifolds in golden Riemannian manifolds was investigated by Gök and Kılıç (Gök & Kılıç, 2023). As an ordinary generalization of invariant and anti-invariant submanifolds, the notion of a semi-invariant submanifold in golden Riemannian manifolds was introduced by Erdoğan and Yıldırım (Erdoğan & Yıldırım, 2018), who studied the geometry of distributions arose from its definition. Furthermore, the induced canonical structures and the associated distributions of semi-invariant submanifolds in golden Riemannian manifolds were analyzed by Gök, Keleş and Kılıç (Gök, Keleş, & Kılıç, 2019).

Motivated by the above investigations, in this paper, three classification theorems for totally umbilical semi-invariant submanifolds in locally decomposable golden Riemannian manifolds are given. It is also shown that there is no totally umbilical proper semi-invariant submanifolds in a positively or negatively curved locally decomposable golden Riemannian manifold.

Preliminaries

In this section, we give a short background on golden manifolds and their submanifolds.

A golden structure $\tilde{\Phi}$ on a differentiable manifold \tilde{M} is a polynomial structure of degree 2 yielding the equation

$$\tilde{\Phi}^2 = \tilde{\Phi} + I, \quad (1)$$

where I is the identity transformation on \tilde{M} . In this case, the pair $(\tilde{M}, \tilde{\Phi})$ is called a golden manifold. The k -th power of $\tilde{\Phi}$ is given by

$$\tilde{\Phi}^k = F_k \tilde{\Phi} + F_{k-1} I, \quad (2)$$

where (F_k) is the Fibonacci sequence generated by the rule $F_{k+1} = F_k + F_{k-1}$ with $F_0 = 0$ and $F_1 = 1$. The eigenvalues of $\tilde{\Phi}$ are the roots of the Fibonacci equation $x^2 = x + 1$, i.e., $\phi = \frac{1+\sqrt{5}}{2}$ and $1 - \phi = \frac{1-\sqrt{5}}{2}$. Also, denoting by $\tilde{\Phi}^{-1}$ the inverse of $\tilde{\Phi}$, it is given by

$$\tilde{\Phi}^{-1} = \tilde{\Phi} - I \quad (3)$$

and verifies the equation

$$\left(\tilde{\Phi}^{-1}\right)^2 = -\tilde{\Phi}^{-1} + I, \quad (4)$$

so it is not a golden structure.

A Riemannian manifold (\tilde{M}, \tilde{g}) endowed with a golden structure $\tilde{\Phi}$ is called a golden Riemannian manifold if

$$\tilde{g}(\tilde{\Phi} X, Y) = \tilde{g}(X, \tilde{\Phi} Y) \quad (5)$$

for all $X, Y \in \Gamma(T\tilde{M})$ and it is denoted by the triple $(\tilde{M}, \tilde{g}, \tilde{\Phi})$ (Hreţcanu & Crâşmăreanu, 2007; Crâşmăreanu & Hreţcanu, 2008; Hreţcanu & Crâşmăreanu, 2009). In particular, a golden Riemannian manifold $(\tilde{M}, \tilde{g}, \tilde{\Phi})$ is said to be a locally decomposable golden Riemannian manifold if $\tilde{\nabla} \tilde{\Phi} = 0$, where $\tilde{\nabla}$ stands for the Levi-Civita connection on \tilde{M} (Hreţcanu & Crâşmăreanu, 2007).

Let $(\tilde{M}, \tilde{g}, \tilde{\Phi})$ be a locally decomposable golden Riemannian manifold. In this case, the Riemannian curvature tensor \tilde{R} of \tilde{M} satisfies the following relations (Blaga & Hreţcanu, 2017):

$$\tilde{R}(X, Y) \tilde{\Phi} Z = \tilde{\Phi} \tilde{R}(X, Y) Z, \quad (6)$$

$$\tilde{R}(\tilde{\Phi} X, Y) = \tilde{R}(X, \tilde{\Phi} Y), \quad (7)$$

$$\tilde{R}(\tilde{\Phi} X, \tilde{\Phi} Y) = \tilde{R}(\tilde{\Phi} X, Y) + \tilde{R}(X, Y) \quad (8)$$

and

$$\tilde{R}(\tilde{\Phi}^{k+1} X, Y) = F_{k+1} \tilde{R}(\tilde{\Phi} X, Y) + F_k \tilde{R}(X, Y) \quad (9)$$

for all $X, Y \in \Gamma(T\tilde{M})$. In addition, from (5), (6) and (7), we have

$$\tilde{K}(\tilde{\Phi} X, Y, Z, W) = \tilde{K}(X, \tilde{\Phi} Y, Z, W) \quad (10)$$

and

$$\tilde{K}(X, Y, \tilde{\Phi} Z, W) = \tilde{K}(X, Y, Z, \tilde{\Phi} W) \quad (11)$$

for all $X, Y, Z, W \in \Gamma(T\tilde{M})$, where \tilde{K} denotes the Riemann-Christoffel curvature tensor of \tilde{M} .

We consider any isometrically immersed submanifold M of a golden Riemannian manifold $(\tilde{M}, \tilde{g}, \tilde{\Phi})$. Also, we denote by the same notation \tilde{g} the Riemannian metric on M . Then the formulas of Gauss and Weingarten of M in \tilde{M} are given, respectively, by

$$\tilde{\nabla}_X Y = \nabla_X Y + \sigma(X, Y) \quad (12)$$

and

$$\tilde{\nabla}_X U = -A_U X + \nabla_X^\perp U \quad (13)$$

for all $X, Y \in \Gamma(TM)$ and $U \in \Gamma(TM^\perp)$, where ∇ , σ , ∇^\perp and A_U are the induced connection, the second fundamental form, the Weingarten endomorphism associated with U and the normal connection, respectively. Moreover, the Codazzi equation of M in \tilde{M} is given by

$$(\tilde{R}(X, Y)Z)^\perp = (\nabla_X \sigma)(Y, Z) - (\nabla_Y \sigma)(X, Z) \quad (14)$$

for all $X, Y, Z \in \Gamma(TM)$.

On the other hand, if $\sigma = 0$, then M is said to be a totally geodesic submanifold; if $H = 0$, then M is called a minimal submanifold,

where H is the mean curvature vector of M ; if $\sigma(X, Y) = \tilde{g}(X, Y)H$ for all $X, Y \in \Gamma(TM)$, then M is termed a totally umbilical submanifold (Bejancu, 1986). Also, if M is a totally umbilical submanifold such that $\dim M \geq 2$ and has the non-zero parallel mean curvature vector H , i.e., $\nabla_X^\perp H = 0$ for all $X \in \Gamma(TM)$, then it is named an extrinsic sphere (Nomizu & Yano, 1974).

If M is a totally umbilical submanifold in \tilde{M} , then the formulas of Gauss and Weingarten are expressed as follows:

$$\tilde{\nabla}_X Y = \nabla_X Y + \tilde{g}(X, Y)H \quad (15)$$

and

$$\tilde{\nabla}_X U = -\tilde{g}(H, U)X + \nabla_X^\perp U \quad (16)$$

for all $X, Y \in \Gamma(TM)$ and $U \in \Gamma(TM^\perp)$, respectively. Furthermore, the Codazzi equation becomes the form

$$\tilde{R}(X, Y, Z, U) = \tilde{g}(Y, Z)\tilde{g}(\nabla_X^\perp H, U) - \tilde{g}(X, Z)\tilde{g}(\nabla_Y^\perp H, U) \quad (17)$$

for all $X, Y, Z \in \Gamma(TM)$ and $U \in \Gamma(TM^\perp)$ (Bejancu, 1986).

For any $X \in \Gamma(TM)$, we write

$$\tilde{\Phi} X = fX + hX, \quad (18)$$

where fX and hX are the tangential and normal components of $\tilde{\Phi} X$, respectively. Similarly, for any $U \in \Gamma(TM)$, we put

$$\tilde{\Phi} U = tU + sU, \quad (19)$$

where tU and sU are the tangential and normal components of $\tilde{\Phi} U$, respectively. Also, f, h, t and s hold the following relations:

$$\tilde{g}(fX, Y) = \tilde{g}(X, fY), \quad (20)$$

$$\tilde{g}(sU, V) = \tilde{g}(U, sV) \quad (21)$$

and

$$\tilde{g}(hX, U) = \tilde{g}(X, tU) \quad (22)$$

for all $X, Y \in \Gamma(TM)$ and $U, V \in \Gamma(TM^\perp)$. Considering (1), by means of (18) and (19), we have the following relations:

$$f + I = f^2 + th, \quad (23)$$

$$h = hf + sh, \quad (24)$$

$$t = ft + ts \quad (25)$$

and

$$s + I = s^2 + ht. \quad (26)$$

A Review on Semi-Invariant Submanifolds in Golden Riemannian Manifolds

This section provides a short review on semi-invariant submanifolds in golden Riemannian manifolds to clarify the main results of the paper.

Definition 1. (Erdoğan & Yıldırım, 2018) Any isometrically immersed submanifold M of a golden Riemannian manifold $(\tilde{M}, \tilde{g}, \tilde{\Phi})$ is said to be semi-invariant if there exist two orthogonal complementary distributions P and Q on M satisfying the following relations:

a) $\tilde{\Phi}(P_a) = P_a \subseteq T_a M$, i.e., P is a $\tilde{\Phi}$ -invariant distribution,

b) $\tilde{\Phi}(Q_a) \subseteq T_a M^\perp$, i.e., Q is a $\tilde{\Phi}$ -anti-invariant distribution

for each point $a \in M$. If neither $P = \{0\}$ nor $Q = \{0\}$, then M is called a proper semi-invariant submanifold.

Proposition 1. (Gök, Keleş, & Kılıç, 2019) Let M be any semi-invariant submanifold of a golden Riemannian manifold $(\tilde{M}, \tilde{g}, \tilde{\Phi})$. Then we have the following relations:

$$fQ = \{0\}, \quad (27)$$

$$hQ = \tilde{\Phi} Q, \quad (28)$$

$$hP = \{0\} \quad (29)$$

and

$$fP = P. \quad (30)$$

Proposition 2. (Gök, Keleş, & Kılıç, 2019) A necessary and sufficient condition for any isometrically immersed submanifold M of a golden Riemannian manifold $(\tilde{M}, \tilde{g}, \tilde{\Phi})$ to be semi-invariant that

$$hf = 0. \quad (31)$$

Remark 1. (Gök, Keleş, & Kılıç, 2019) Let us define a tensor field $\tilde{\Psi}$ of type (1,1) on a golden Riemannian manifold $(\tilde{M}, \tilde{g}, \tilde{\Phi})$ by

$$\tilde{\Psi} = -\tilde{\Phi}^{-1}. \quad (32)$$

In this situation, it follows that $\tilde{\Psi}$ is a golden structure and \tilde{g} is $\tilde{\Psi}$ -compatible, i.e.,

$$\tilde{g}(\tilde{\Psi}X, Y) = \tilde{g}(X, \tilde{\Psi}Y) \quad (33)$$

for all $X, Y \in \Gamma(T\tilde{M})$. Hence, $(\tilde{M}, \tilde{g}, \tilde{\Psi})$ is also a golden Riemannian manifold.

Remark 2. (Gök, Keleş, & Kılıç, 2019) Let M be any proper semi-invariant submanifold of a golden Riemannian manifold $(\tilde{M}, \tilde{g}, \tilde{\Phi})$. We put $Q = \tilde{\Phi}Q$ and denote by \mathcal{P} its orthogonal complement in the normal bundle TM^\perp . Then we have $TM^\perp = \mathcal{P} \oplus Q$.

Proposition 3. (Gök, Keleş, & Kılıç, 2019) Let M be any semi-invariant submanifold of a golden Riemannian manifold $(\tilde{M}, \tilde{g}, \tilde{\Phi})$. Then there is a pair of orthogonal complementary distributions (\mathcal{P}, Q) on the normal bundle TM^\perp such that \mathcal{P} is a $\tilde{\Psi}$ -invariant distribution and Q is a $\tilde{\Psi}$ -anti-invariant distribution.

Proposition 4. (Gök, Keleş, & Kılıç, 2019) Let M be any semi-invariant submanifold of a golden Riemannian manifold $(\tilde{M}, \tilde{g}, \tilde{\Phi})$. Then we have the following relations:

$$t\mathcal{P} = \{0\}, \quad (34)$$

$$s\mathcal{P} = (I - s)\mathcal{P} = \mathcal{P} \text{ or } \tilde{\Phi}\mathcal{P} = \mathcal{P}, \quad (35)$$

$$(I - s)Q = \{0\} \quad (36)$$

and

$$tQ = Q \text{ or } \tilde{\Psi}Q = Q. \quad (37)$$

Proposition 5. (Erdoğan & Yıldırım, 2018) Let M be any totally umbilical proper semi-invariant submanifold of a locally decomposable golden Riemannian manifold $(\tilde{M}, \tilde{g}, \tilde{\Phi})$. Then both of the invariant distribution \mathcal{P} and the anti-invariant distribution Q are integrable.

Main Results

This section is devoted to a study of totally umbilical semi-invariant submanifolds of a locally decomposable golden Riemannian manifold containing three classification theorems and one absence theorem.

Theorem 1. Let M be any totally umbilical proper semi-invariant submanifold of a locally decomposable golden Riemannian manifold $(\tilde{M}, \tilde{g}, \tilde{\Phi})$. Then we have

$$H \in \Gamma(\mathcal{P}). \quad (38)$$

Proof. From the assumption that M is a totally umbilical semi-invariant submanifold, Proposition 5 implies that Q is integrable, that is, $A_{\tilde{\Phi}X}Y = 0$ for all $X, Y \in \Gamma(Q)$, so we get

$$\tilde{g}(H, \tilde{\Phi}X)Y = 0 \quad (39)$$

for all $X, Y \in \Gamma(Q)$. Hence, it follows that

$$\tilde{g}(H, \tilde{\Phi}X) = 0, \quad (40)$$

which is the desired equality.

Proposition 6. Let M be any totally umbilical proper semi-invariant submanifold of a locally decomposable golden Riemannian manifold $(\tilde{M}, \tilde{g}, \tilde{\Phi})$. Then the covariant derivative of the endomorphism f vanishes identically, i.e., $\tilde{\nabla}f = 0$.

Proof. We recall from (Hreţcanu & Blaga, 2018) that the covariant derivative of f is defined by

$$(\tilde{\nabla}_X f)Y = A_{hY}X + t\sigma(X, Y) \quad (41)$$

for all $X, Y \in \Gamma(TM)$. Because M is a totally umbilical semi-invariant submanifold, (41) turns into the form

$$(\tilde{\nabla}_X f)Y = \tilde{g}(H, hY)X + \tilde{g}(X, Y)tH \quad (42)$$

for all $X, Y \in \Gamma(TM)$. If $H = 0$, then the proof is obvious. Now, we assume that $H \neq 0$. In this case, by means of (28), (29), (34) and (38), it is derived from (42) that $\tilde{\nabla}f = 0$.

Theorem 2. Let M be any totally umbilical semi-invariant submanifold of a locally decomposable golden Riemannian manifold $(\tilde{M}, \tilde{g}, \tilde{\Phi})$. If $\dim \tilde{M} = \dim M + \dim Q$, then M is totally geodesic.

Proof. If $\dim Q = 0$, then the proof is trivial. Now, we suppose that $\dim Q \neq 0$. In this case, from the assumption that $\dim \tilde{M} = \dim M + \dim Q$, we have

$$\dim Q = \dim TM^\perp. \quad (43)$$

Hence, since $\tilde{\Phi}$ is injective and Q is anti-invariant, we get

$$\tilde{\Phi} Q = TM^\perp. \quad (44)$$

In addition, we recall that Q is a subbundle of TM^\perp , so (44) means that $Q = \{0\}$. Thus, we conclude from Theorem 1 that

$$H = 0, \quad (45)$$

which ends the proof.

Theorem 3. Let M be any totally umbilical proper semi-invariant submanifold with the non-zero mean curvature vector H of a locally decomposable golden Riemannian manifold $(\tilde{M}, \tilde{g}, \tilde{\Phi})$. If $\dim P \geq 2$, then M is an extrinsic sphere.

Proof. Because of the fact that $\dim P \geq 2$, we have two non-zero vector fields $X, Y \in \Gamma(P)$ satisfying

$$\tilde{g}(X, Y) = 0. \quad (46)$$

Putting $Z = fY$ in (6), we get

$$\tilde{R}(X, Y) \tilde{\Phi} fY = \tilde{\Phi} \tilde{R}(X, Y) fY. \quad (47)$$

By means of (18), from Proposition 2, (47) is written as follows:

$$\tilde{R}(X, Y) f^2 Y = \tilde{\Phi} \tilde{R}(X, Y) fY. \quad (48)$$

On the other hand, from Proposition 6, we deduce

$$\tilde{R}(X, Y) fZ = f \tilde{R}(X, Y) Z. \quad (49)$$

In fact, (49) holds for all $X, Y, Z \in \Gamma(TM)$. Hence, considering (23), (27), (28) and (49), we obtain from (48) that

$$f \tilde{R}(X, Y) Y + \tilde{R}(X, Y) Y = \tilde{\Phi} f \tilde{R}(X, Y) Y. \quad (50)$$

Taking account of the fact that P is invariant, using (30) in (50), we get

$$\tilde{g}(\tilde{R}(X, Y)Y, U) = 0 \quad (51)$$

for all $U \in \Gamma(TM^\perp)$. Moreover, by virtue of (17) and (46), (51) turns into

$$\tilde{g}(Y, Y)\tilde{g}(\nabla_X^\perp H, U) = 0, \quad (52)$$

which means that $\nabla_X^\perp H = 0$ for all $X \in \Gamma(P)$. In a similar manner, it can be proven that $\nabla_X^\perp H = 0$ for all $X \in \Gamma(Q)$. Therefore, $\nabla_X^\perp H = 0$ for all $X \in \Gamma(TM)$, that is, M is an extrinsic sphere.

Theorem 4. There is no totally umbilical proper semi-invariant submanifolds in a positively or negatively curved locally decomposable golden Riemannian manifold $(\tilde{M}, \tilde{g}, \tilde{\Phi})$.

Proof. We suppose that M is a totally umbilical proper semi-invariant submanifold of a positively or negatively curved locally decomposable golden Riemannian manifold $(\tilde{M}, \tilde{g}, \tilde{\Phi})$. If $H = 0$, then the proof is trivial. Now, we evaluate the case $0 \neq H \in \Gamma(\mathcal{P})$. Let us take two vector fields X and U such that $X \in \Gamma(P)$ and $U \in \Gamma(\tilde{\Phi}Q)$. Then we get

$$\tilde{g}(U, H) = 0. \quad (53)$$

Differentiating (53) with respect to ∇^\perp , we obtain

$$\tilde{g}(\nabla_X^\perp U, H) = -\tilde{g}(U, \nabla_X^\perp H). \quad (54)$$

On the other hand, as is seen that the parallelism of $\tilde{\Phi}$ with respect to $\tilde{\nabla}$ is equivalent to that of $\tilde{\Psi}$ given by $\tilde{\Psi} = -\tilde{\Phi}^{-1}$ in (32). Thus, we have

$$\tilde{\nabla}_X \tilde{\Psi} U = \tilde{\Psi} \tilde{\nabla}_X U. \quad (55)$$

From (15) and (16), we have

$$\nabla_X \tilde{\Psi} U + \tilde{g}(X, \tilde{\Psi} U)H = -\tilde{g}(U, H)\tilde{\Psi} X + \tilde{\Psi} \nabla_X^\perp U. \quad (56)$$

Using (53) in (56), we obtain

$$\nabla_X \tilde{\Psi} U = \tilde{\Psi} \nabla_X^\perp U. \quad (57)$$

As Q is $\tilde{\Psi}$ -anti-invariant, we get

$$\nabla_X^\perp U \in \Gamma(Q). \quad (58)$$

Hence, we deduce from (54) and (58) that

$$\nabla_X^\perp H \in \Gamma(Q). \quad (59)$$

Besides, U has the form

$$U = \tilde{\Phi} Y, \quad (60)$$

where $Y \in \Gamma(Q)$. Meantime, by an analogous way used in the proof of Theorem 3, we derive

$$\tilde{g}(\nabla_Y^\perp H, \tilde{\Phi} Y) = 0. \quad (61)$$

On the other hand, it follows from (11) and (32) that

$$\tilde{K}(X, Y, X, Y) = -\tilde{K}(X, Y, \tilde{\Psi} X, \tilde{\Phi} Y). \quad (62)$$

Taking notice of (61), by means of (17), (59) and (60), we derive

$$\begin{aligned} \tilde{K}(X \wedge Y) &= \tilde{g}(Y, \tilde{\Psi} X) \tilde{g}(\nabla_X^\perp H, \tilde{\Phi} Y) \\ &\quad - \tilde{g}(X, \tilde{\Psi} X) \tilde{g}(\nabla_Y^\perp H, \tilde{\Phi} Y), \end{aligned} \quad (63)$$

where \tilde{K} is the sectional curvature of the plane section spanned by X and Y of \tilde{M} . Hence, applying (59) and (61) to (63), we obtain

$$\tilde{K}(X \wedge Y) = 0, \quad (64)$$

which is a contradiction. Ultimately, the proof has been shown.

Corollary 1. There is no totally geodesic proper semi-invariant submanifolds in a positively or negatively curved locally decomposable golden Riemannian manifold $(\tilde{M}, \tilde{g}, \tilde{\Phi})$.

Proof. As a consequence of Theorem 4, the proof follows from the fact that any totally geodesic submanifold is totally umbilical.

References

- Bejancu, A. (1986). *Geometry of CR-Submanifolds*. Dordrecht: D. Reidel Publishing Company.
- Blaga, A. M., & Hreţcanu, C. E. (2017). Golden warped product Riemannian manifolds. *Libertas Mathematica*, 37(1), 1-11.
- Crăşmăreanu, M. C., & Hreţcanu, C. E. (2008). Golden differential geometry. *Chaos, Solitons & Fractals*, 38(5), 1229-1238.
- Erdoğan, F. E., & Yıldırım, C. (2018). On a study of the totally umbilical semi-invariant submanifolds of golden Riemannian manifolds. *Journal of Polytechnic*, 21(4), 967-970.
- Gezer, A., Cengiz, N., & Salimov, A. (2013). On integrability of golden Riemannian structures. *Turkish Journal of Mathematics*, 37(4), 693-703.
- Goldberg, S. I., & Yano, K. (1970). Polynomial structures on manifolds. *Kodai Mathematical Seminar Reports*, 22(2), 199-218.
- Gök, M., & Kılıç, E. (2023). The stability problem of certain anti-invariant submanifolds in golden Riemannian manifolds. *International Electronic Journal of Geometry*, 16(1), 343-348.
- Gök, M., Keleş, S., & Kılıç, E. (2019). Some characterizations of semi-invariant submanifolds of golden Riemannian manifolds. *Mathematics*, 7(12), 1209.
- Gök, M., Kılıç, E., & Keleş, S. (2020). Anti-invariant submanifolds of locally decomposable golden Riemannian manifolds. *Balkan Journal of Geometry and its Applications*, 25, 47-60.
- Hreţcanu, C. E., & Blaga, A. M. (2018). Slant and semi-slant submanifolds in metallic Riemannian manifolds. *Journal of Function Spaces*, 2018, 2864263.
- Hreţcanu, C. E., & Crăşmăreanu, M. C. (2007). On some invariant submanifolds in a Riemannian manifold with golden structure. *Analele Stiintifice ale Universităţii "Alexandru Ioan Cuza" din Iaşi (Serie nouă). Matematică*, 53(supl. 1), 199-211.
- Hreţcanu, C. E., & Crăşmăreanu, M. C. (2009). Applications of the golden ratio on Riemannian manifolds. *Turkish Journal of Mathematics*, 33(2), 179-191.
- Nomizu, K., & Yano, K. (1974). On circles and spheres in Riemannian geometry. *Mathematische Annalen*, 210(2), 163-170.
- Özkan, M. (2014). Prolongations of golden structures to tangent bundles. *Differential Geometry- Dynamical Systems*, 16, 227-238.

Chapter 10

MATERIAL INNOVATIONS DRIVING THE FUTURE OF LIGHT-CHARGED SUPERCAPACITORS

*Melisa ÖĞRETİCİ¹, Kibar ARAS²,
Sinem ORTABOY SEZER³*

¹ Yüksek Lisans Öğrencisi, İstanbul Üniversitesi-Cerrahpaşa, Mühendislik Fakültesi, Kimya Bölümü, melisa.ogretici@ogr.iuc.edu.tr, 0009-0003-4141-10092

² Araştırma Görevlisi, Atatürk Üniversitesi, Fen Fakültesi, Kimya Bölümü, kibar-aras@atauni.edu.tr, 0000-0002-1736-958X

³ Profesör Doktor, İstanbul Üniversitesi-Cerrahpaşa, Mühendislik Fakültesi, Kimya Bölümü, ortaboy@iuc.edu.tr, 0000-0003-3152-1637

1. INTRODUCTION

The growing global demand for sustainable energy has caused an urgent shift towards clean and renewable energy solutions. Due to its abundance and low cost, solar power has become a highly sought-after energy source. Nonetheless, the variability of solar radiation poses considerable difficulties in maintaining a consistent and stable power supply. Therefore, combining efficient solar energy conversion with compact, high-performance energy storage (ES) systems is essential for developing the next generation of self-sustaining devices.

Photo-supercapacitors (PSCs) have gained attention as an innovative solution to this problem. These devices combine solar cells with supercapacitors, enabling them to generate and store energy simultaneously. Unlike traditional setups that require separate components, PSCs simplify the system by integrating everything into a single unit. This not only makes the devices smaller and cheaper but also helps reduce energy loss during transfer. Solar technologies, such as perovskite, dye-sensitized, organic, and quantum dot derivate cells, are particularly suitable for these systems due to their flexibility, ease of production, and good performance under various lighting conditions (Ng et al., 2018; Harankahawa et al., 2017; Zheng et al., 2022).

The performance of a PSC device is affected from several factors, including the efficacy of the power conversion of the photovoltaic (PV) unit, the charge storage capability of the supercapacitor (SC) unit, and the interfacial interactions between these components. Studies have shown that photoactive materials, new electrode designs, and interface engineering have increased the efficiency of energy conversion and storage (Ng et al., 2015; Namsheer & Rout, 2021; Jacob et al., 2024).

This review aims to provide an overview of recent developments in PSC technology, with a focus on photoactive electrodes and electrolytes, as well as future research directions for real-world applications.

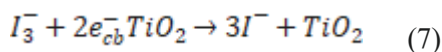
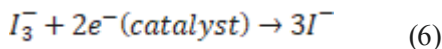
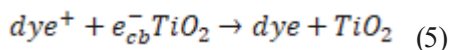
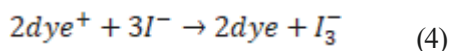
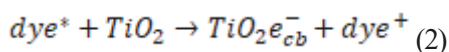
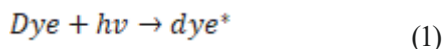
2. FUNDAMENTALS OF PHOTO-SUPERCAPACITORS

PSCs represent an innovative combination of two technologies that integrate the principles of energy storage and harvesting through the use of a shared electrode, facilitated by either an intermediate layer or a connecting wire. These devices harvest energy from solar cells, which is subsequently stored as electrochemical energy by supercapacitors. Notably, third-generation solar cells are preferred for PSC applications due to their simpler architecture compared to first and second generations. This compatibility allows for the combination of supercapacitors with various solar

cell types, including quantum dot (QD)-sensitized, organic, perovskite, dye-sensitized solar cells (DSSC) (Jacob et al., 2024).

In 2004, Miyasaka et al. introduced the groundbreaking concept of the first PSC, focusing on a photo-charging capacitor that associates a DSSC. A PSC comprises two principal components: the DSSC and a supercapacitor. The DSSC is characterized by a photoanode that is coated with a light-absorbing semiconductor material, typically titanium dioxide (TiO_2), affixed to a transparent glass substrate. The device also incorporates a liquid electrolyte, a counter electrode fabricated from materials such as porous activated carbon or platinum, and a dye serving as a sensitizer. In contrast to conventional supercapacitors, which derive their charge from an external electrical energy source, PSCs utilize solar energy for their charging mechanisms. Upon exposure to solar irradiation, the incident light excites electrons within the dye molecules, facilitating their promotion into the semiconductor material's conduction band (CB). Simultaneously, electron holes generated in the dye molecule migrate towards the counter electrode. The redox ions present in the electrolyte are fundamental in sustaining the equilibrium of the photo-induced electron flow; electrons residing in the electrolyte contribute to the regeneration of the dye, whereas electrons from the counter electrode occupy the vacant sites within the electrolyte. This complex interaction highlights the distinct operational dynamics of PSCs, setting them apart from conventional energy storage systems. (Vadivel et al., 2019).

The reaction mechanism of DSSC-based PSC is explained below (Namsheer et al., 2021).



PSCs can be categorized based on their electrode configuration into two distinct types: two-electrode and three-electrode systems. Fig. 1 illustrates the main components of PSC. In a two-electrode configuration,

one electrode functions as the photoelectrode, responsible for sunlight absorption, while the second electrode serves as the counter electrode, which stores charge. These electrodes create a heterojunction with activated carbon to enhance electrochemical properties. However, two-electrode systems frequently encounter challenges such as high internal resistance and discharging inefficiencies. To approach these issues, a three-electrode system has been introduced, incorporating a bifunctional electrode located between the photoelectrode and the charge storage parts. During the charging process, the photoelectrode connects to the counter electrode (CE), while the intermediate electrode remains disconnected. Conversely, during discharging, the CE interfaces with the intermediate electrode, and the photoelectrode remains isolated (Jacob et al., 2024).

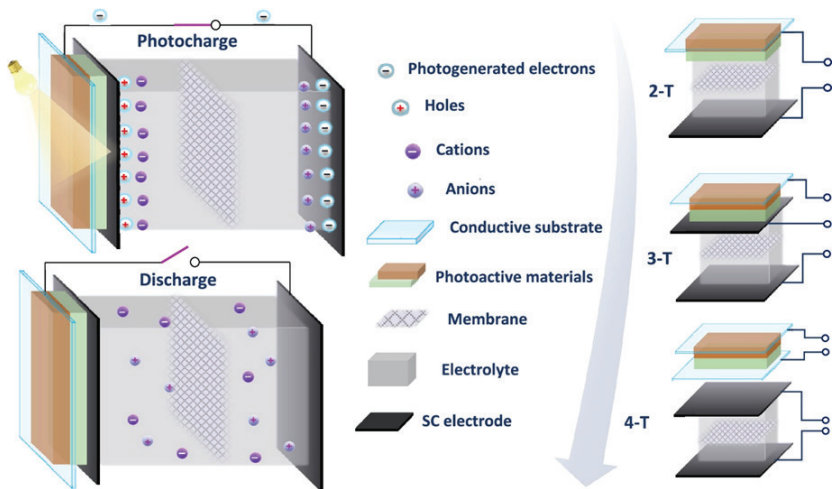


Fig. 1 Schematic illustration of the photocharging/discharging mechanisms in a PSC (Reproduced under the Creative Commons Attribution 4.0 International (CC BY 4.0) License) (Flores-Diaz et al., 2023).

3. ADVANCED MATERIALS FOR PHOTO-SUPERCAPACITORS

PSC is an integrated energy system that combines a PV unit for light energy conversion combined a supercapacitor (SC) unit for electrochemical energy storage. In this architecture, the PV component absorbs solar or artificial light and converts it into electrical energy, which is subsequently transferred to the SC unit, where it is stored at the electrode/electrolyte interface layer. The structural configuration of the PV unit is largely dependent on the photovoltaic technology employed. Although

first generation and second generation solar cells can be adapted for photo-supercapacitor integration, their limited architectural flexibility and fabrication constraints render them less suitable for advanced device design. In contrast, third-generation photovoltaic technologies—including perovskite solar cells, DSSCs, QDSCs, and OPVs—offer greater adaptability due to their facile fabrication methods, compatibility with diverse substrates and configurations, and cost-effectiveness. These emerging systems commonly incorporate photoactive materials such as metal chalcogenides, metal oxides, perovskites, and polymer-based electrodes or electrolytes, which enhance their overall efficiency and integration potential (Flores-Diaz et al., 2023).

3.1. Photoactive Electrodes

A photoanode with a nanocrystalline film serves as the primary electron donor and is essential for achieving high power conversion efficiency. The mesoporous nanocrystalline film's large surface area facilitates the dye loading process, enabling electron flow to the counter electrode (Ng et al., 2015). To enhance the performance of photoactive electrodes in PSCs, research has focused on investigating various functional materials. In particular, the incorporation of advanced nanostructured substances, such as metal oxides, metal chalcogenides, perovskites, metal-organic frameworks (MOFs), and conductive polymers, has garnered attention. These materials offer unique electronic, optical, and structural characteristics that can improve light absorption, charge separation, and overall energy storage performance. The following sections provide an in-depth exploration of these material categories and their specific roles in developing efficient, high-performance photoelectrodes for PSC system technologies.

3.1.1. Inorganic Semiconductor Materials

- **Metal Oxides**

A diverse range of transition metal oxides (MOs), such as molybdenum oxide (MoO_3), titanium dioxide (TiO_2), vanadium oxides (VO_x), and tungsten oxide (WO_3), have been extensively investigated as promising candidates for application in photo-supercapacitor systems. These materials possess tunable band gaps and demonstrate strong photoresponsivity from the visible region to the near-infrared regions of the electromagnetic spectrum, enabling efficient solar energy harvesting. Their intrinsic semiconducting properties, coupled with high chemical stability and favorable electronic structures, make them particularly advantageous for integrating light absorption and charge storage functionalities within a single device architecture.

Skunik-Nuckowska et al. (2013) reported that devices have led to the development of a novel photoelectrochemical capacitor that seamlessly combines energy harvesting and storage. Combination of a photo effective rechargeable RuO_2 -based (RuO_x) capacitor and a DSSC, utilizing a D35 dye-modified titanium oxide photoanode and a poly-(3-hexylthiophene-2,5-diyl) (P3HT) hole conductor. The incorporation of a bipolar silver electrode effectively separates the storage and photovoltaic components. Under full sun illumination (100 mW cm^{-2}), the integrated PSC demonstrated an energy density of 0.17 mWh cm^{-2} and a specific capacitance of 407 F g^{-1} . The device demonstrated a coulombic conversion efficiency of 88% and an energy conversion efficiency of 0.8%. Its ability to produce a photovoltage of 0.9 V while performing effectively even in low-light conditions ($10 \text{ et al., 2013. mW cm}^{-2}$) highlights its potential for various energy harvesting applications (Skunik-Nuckowska

Bagheri et al. (2014) have introduced a novel photorechargeable device combining a liquid-type DSSC with a Co(II)/Co(III) polypyridyl as electrolyte and an Ni(Co)O_x /activated carbon supercapacitor paired with (E)-3-(6-(4-(bis(2',4'-dibutoxy-[1,1'-biphenyl]-4-yl)amino)phenyl)-4,4-dihexyl-4H cyclopental [1,2-b:5,4-b']dithiophen-2-yl)-2-cyanoacrylic acid (LEG4) dye. This unique architecture, featuring an intermediate Ni foil electrode covered with poly(3,4-ethylenedioxythiophene) (PEDOT), enables coexistent energy generation and storage. The DSSC component generated an open-circuit potential (OCP) of 0.8 V and achieved an energy conversion efficiency of 4.6–4.9%. After integration, the specific capacitance of the photocapacitor reached 32 F g^{-1} , slightly reduced from 46 F g^{-1} of the standalone supercapacitor, likely due to parasitic resistance. Despite this, the integrated system demonstrated a commendable energy density of 2.3 Wh kg^{-1} and an overall efficiency of 0.6%, marking it as one of the most efficient photo-rechargeable systems reported to date (Bagheri et al., 2014).

A study by Safshekan et al. (2017) introduced a novel photo-capacitive device based on the bismuth vanadate-lead oxide ($\text{BiVO}_4\text{--PbO}_x$) heterostructure, where BiVO_4 serves as a photoactive core and PbO_x nanoparticles, derived from lead sulfide (PbS) quantum dots, act as a redox pseudocapacitive platform. The device achieves a areal capacitance of 6 mF cm^{-2} and a high OCP of 1.5 V vs. RHE. Additionally, it exhibits stable charge–discharge cycling over 100 cycles, offering a promising approach to integrating solar energy conversion and storage (Safshekan et al., 2017).

The latest developments in metal oxides for photo supercapacitors have advanced to enhance energy storage and harvesting. When employed as photoelectrodes, metal oxides facilitate the conversion of solar

energy into electrical energy while simultaneously enabling its storage in the form of capacitive charge. This multifunctional capability positions metal oxide-based PSCs as promising candidates for next-generation applications in flexible electronics, self-powered systems, and sustainable energy technologies.

In another study, Altaf et al. (2023) developed zinc oxide (ZnO)-based PSCs using hydrothermally synthesized nanowire (NW) and nanoflower (NF) morphologies, employing a simple drop-casting technique on glass and plastic substrates. The NW-based PSCs demonstrated superior photo-response and energy density under UV illumination, achieving 78.1 mWh kg^{-1} at 1.1 mA g^{-1} , which is attributed to fewer core defects compared to NF powders. Under UV light, the Coulombic efficiency (CE %) increased significantly, with NW-based PSCs reaching 102%, three times higher than in the dark. In comparison, NF-based PSCs achieved 64%, indicating the critical role of defect structures in photo-induced charge separation. Additionally, both devices demonstrated remarkable stability, with a capacitance retention exceeding 99% after 3000 cycles, underscoring the potential of defect-optimized ZnO nanomaterials for next-generation flexible and rigid PSC applications (Altaf et al., 2023).

A novel symmetrical supercapacitor was developed by Chauhan et al. (2023) using a stacked $\text{V}_2\text{O}_5/\text{ZnO}$ structure on fluorine-doped tin oxide (FTO) coated glass, leveraging the distinct band gaps and work functions of metal oxides to enhance photogenerated charge separation. Under UV illumination, the device exhibited a remarkable $\sim 178\%$ rise in specific capacitance, confirmed via galvanostatic charge–discharge (GCD) measurements, and maintained outstanding cyclic stability over 5000 cycles. The innovative layered structure not only facilitated efficient light-to-electrochemical energy conversion but also provided long-term stability, marking a promising step toward the development of self-chargeable energy storage systems for modern applications (Chauhan et al., 2023).

Momeni et al. (2024) developed photo-assisted asymmetric supercapacitors with cobalt manganese sulfide (CoMnS) on TiO_2 nanotubes (TNTs), demonstrating efficient simultaneous light harvesting and charge storage. Integrating CoMnS as an electrochemically active material onto photoactive TNTs greatly improved charge storage capabilities when exposed to light, resulting in an impressive capacitance of 71.7 mF cm^{-2} , compared to 42.2 mF cm^{-2} in darkness, showing a $\sim 70\%$ increase in capacity. The device showed remarkable cyclic stability, maintaining over 96% of its capacity after 5000 consecutive cycles under the light exposure (Momeni et al., 2024).

One significant advancement is described by Momeni et al. (2025), who presented lightweight flexible PSCs by photoelectrochemical deposition of tellurium (Te) on Ppy (polypyrrole) and V_2O_5 films. A notable study reported the fabrication of a flexible solid-state photo-supercapacitor (FSSPC) using $Te@PPy-V_2O_5/ITO$ electrodes, achieving remarkable areal-specific capacitances of 131 and 45 $mF\ cm^{-2}$ at current densities of 1.0 and 3.0 $mA\ cm^{-2}$, respectively. The device also exhibited exceptional stability, with a capacitance retention of 93% over 12000 cycles, and showed a significant enhancement under visible light illumination, achieving a 65% increase at 3.0 $mA\ cm^{-2}$. These findings underscore the potential of $Te@PPy-V_2O_5$ -based FSSPCs in flexible, photo-chargeable energy storage applications, especially given their superior bending endurance and temperature resilience (Momeni et al., 2025).

Liang et al. (2025) integrated liquid metal (LM) into transition metal oxides (TMOs) to form robust LM-TMO interfacial structures. These unique combination significantly enhance the electronic conductivity and bandgap modulation, resulting in high energy storage density and superior light absorption. Photo-assisted asymmetric micro-supercapacitors (PAMSCs) based on LM-MoO₃//LM-MnO₂ achieve a specific capacitance of 304.2 $mF\ cm^{-2}$ and an energy density of 107.3 $\mu Wh\ cm^{-2}$ at 1.2 $mA\ cm^{-2}$ under simulated solar illumination. The device also features recyclability by recovering valuable LMs from discarded PAMSCs, addressing both performance and environmental challenges (Liang et al., 2025).

To sum up, advancements in metal oxides for PSCs are characterized by innovative structural designs, effective doping methods, and the integration of novel material combinations that significantly enhance their performance. These encouraging advancements indicate a promising avenue for future investigation in energy conversion and storage technologies.

- **Metal Chalcogenides**

Metal chalcogenides are a group of inorganic compounds that comprise at least one chalcogen anion and one electropositive metal element. Metal chalcogenides have drawn significant attention for potential applications in PSC, which merge light energy harvesting with energy storage capabilities.

One of the primary leverages of these 2D materials is a high specific surface area, combined with distinct electronic characteristics. Transition metal chalcogenides like molybdenum sulfides (MoS₂) and tungsten disulfide (WS₂) stand out due to their remarkable photoconductivity and their ability to promote efficient charge separation and transfer when exposed to light. This enhances the electrochemical activity and charge

storage efficiency, which are critical for the development of high-performance PSCs.

Cui et al. (2019) emphasize the adaptability of 2D metal mono-, di-, and tri-chalcogenide nanosheets for optoelectronic applications. Integrating these materials into perovskite solar cell architectures enhances their excellent light absorption and electron mobility, resulting in improved energy conversion efficiency and increased charge storage capacity. Furthermore, their compatibility with silicon-based technologies provides practical benefits for manufacturing and scalability (Cui et al., 2019).

Madhusudanan et al. (2020) investigated the photoelectrochemical properties of quaternary chalcogenides, synthesizing $\text{Cu}_2\text{FeSnS}_4$ (CFTS) nanoparticles using a solvothermal method with varying polyethylene glycol (PEG) solvents and sulfurization. CFTS2 showed the best photore-sponse under light, outpacing CFTS1 and CFTS3. Its enhanced light sensitivity and capacitance were attributed to photo-induced charge carrier excitation and excess surface sulfur, which aid in defect-mediated charge storage. CFTS's dual role as a photovoltaic absorber and light-responsive electrode suggests strong potential for supercapacitor applications (Madhusudanan et al., 2020).

MoS_2 -based composites have been developed by Guo et al. (2022) as multifunctional materials that harvest both thermal and electrical energy from solar radiation. They provide efficient solar steam generation and energy output under sunlight, achieving a power output of 3.35 mW m^{-2} after 30 minutes, with a voltage of approximately 300 mV and a current of 6.7 μA . The power output drops to roughly 0.9 mW m^{-2} under ambient settings. These porous structures, enhanced with carbon dots for light absorption, demonstrate a solar evaporation rate of $1.9 \text{ kg m}^{-2} \text{ h}^{-1}$ under full sunlight. Furthermore, storing energy in capacitors allows for continuous operation, even in the absence of consistent light exposure (Guo et al., 2022).

A conductive photoelectrode developed using $\text{Yb}_2\text{S}_3:\text{Cu}_2\text{S}:\text{ZnS}$ was synthesized through spin-coating method from a single-source precursor and evaluated for its performance in photoelectrochemical cells. Electrochemical analysis, conducted through, linear sweep voltammetry (LSV), cyclic voltammetry (CV), chronoamperometry (CA), and electrochemical impedance spectroscopy (EIS), revealed improved performance under illumination. The electrode showed an increased photocurrent density in all evaluations, attaining a maximum specific capacitance of 789 F g^{-1} (compared to 745 F g^{-1} in the dark) and a peak photocurrent of 23.5 mA in the CA tests. The EIS analysis yielded a low series resistance (R_s) of 23.4Ω , indicating good conductivity (Gul et al., 2023).

Furthermore, hybrid structures that combine metal chalcogenides with other functional materials have emerged as an effective strategy to enhance PSC performance further. The synergistic effects of hybridizing metal chalcogenides with carbon-based materials or metal oxides contribute to enhanced stability and improved electrochemical properties (Du et al., 2023). This adaptability across various energy-related applications underscores the potential of metal chalcogenides in future energy technologies (Su et al., 2019).

Michalec et al. (2023) reported a comprehensive investigation to evaluate the effect of heterojunctions formed between $\text{SnO}_2/\text{SnS}_2$ photocatalysts and different substrate materials on the photoelectrochemical performance of photoanodes. SnS_2 , SnO_2 , and $\text{SnO}_2/\text{SnS}_2$ flower-like (3D-2D) structures were synthesized via chemical bath deposition onto three types of substrates: indium tin oxide-coated (ITO) glass, etched Ti, and Ti coated with a TiO_x layer. The results revealed that interfacial phases formed between the photocatalysts and the substrates significantly influenced charge transfer characteristics. This study highlights the critical role of substrate selection and heterojunction engineering in optimizing the performance of photoelectrodes for solar energy conversion systems (Michalec et al., 2023).

Additionally, significant efforts have focused on developing metal chalcogenide materials with optimized electrochemical performance through different synthesis methods. Tailoring the composition and size of metal chalcogenide nanoparticles enhances energy storage by improving charge transfer and maintaining structural integrity during repeated charge-discharge cycles (Eikey et al., 2020).

In the study by Gul et al. (2023), a high-performance transparent photoelectrode, $\text{Nd}_2\text{S}_3:\text{Ni}_9\text{S}_8:\text{Co}_9\text{S}_8$, was successfully synthesized using the spin coating deposition method with diethyl dithiocarbamate as the ligand. The photoelectrochemical behavior of the transparent electrode $\text{In}:\text{SnO}_2/\text{Nd}_2\text{S}_3:\text{Ni}_9\text{S}_8:\text{Co}_9\text{S}_8$ was studied using various electrochemical techniques. The electrode exhibited specific capacitance, reaching 946 F g^{-1} when exposed to light, and showed a significantly better photocurrent response in illuminated conditions than in the dark. These findings indicate that this material holds excellent potential for future applications in renewable energy storage systems powered by light (Gul et al., 2023).

Recent advancements in metal chalcogenides show great promise for PSCs. Their unique properties, along with innovative fabrication techniques, position them as key materials for next-generation energy storage. Ongoing research is essential to maximize their potential and integrate them into efficient energy systems.

● Perovskites and Their Derivatives

Perovskites are typically represented as AMX_3 , with A denoting an organic or inorganic cation, M representing a metal ion, and X indicating an anion. Perovskites are auspicious materials recognized for their extensive range of properties. These include dielectric, ferroelectric, thermoelectric, electro-optic, conducting, and superconducting capabilities, in addition to their potential to modify the optical band gap. Recent progress in perovskites and their derivatives has highlighted their potential as versatile materials for PSCS applications, enhancing energy conversion and storage.

A notable advancement is the incorporation of perovskite materials into hybrid devices that combine the functionalities of photovoltaic cells and supercapacitors. For example, Ng et al. (2018) showed that cesium lead halide perovskite—specifically methylammonium lead iodide ($MAPbI_3$)—can serve both as a light-absorbing layer and an energy storage medium. This dual role enhances light harvesting and delivers excellent charge storage capabilities, achieving an overall efficiency of 7.8% in their experiments (Ng et al., 2018).

A new three-terminal PSC has been developed by Song et al. (2022) to promote the sustainable use of solar energy. The obtained prototype integrates a perovskite solar cell with a symmetric supercapacitor (SSC), implementing concurrent energy harvesting and storage. Utilizing a function portfolio management strategy, the device enhances energy transfer between the perovskite solar cell and SSC units, thereby improving performance and decreasing energy losses. The device shows remarkable cycling stability, preserving efficiency with minimal degradation over 200 cycles. Research conducted by Song et al. indicates a promising approach for developing high-efficiency, low-loss integrated PV-storage systems for future solar applications (Song et al., 2022).

Notable advancements have been made in understanding the charge storage mechanisms at the interface between perovskite and electrolyte. Kumar et al. (2022) showcase the complexity of charge dynamics in perovskite supercapacitors, emphasizing that the fundamental principles remain unclear due to the complex processes occurring at the interface. The study highlights the crucial role of optimizing ion conductivity in achieving high diffusion capacitance, a key factor for efficient energy storage.

Kumar et al. (2022) present a halide derived perovskite-based photo-rechargeable SC that can store and harvest solar energy. They developed a porous perovskite-carbon composite electrode to enhance electronic conductivity and optimize photocapacitance. Under white light at

a power density of 20 mW cm^{-2} , the SC produced a photo-charging energy density of 160 mWh kg^{-1} and a specific capacitance of up to 85 F g^{-1} with 15% carbon content, which caused to a photo-conversion efficiency of approximately 0.02%. It achieved maximum chargeable energy and power densities of 30.71 Wh kg^{-1} and 1875 W kg^{-1} , subsequently, while maintaining 94% of its initial capacitance after 1000 cycles of charge and discharge in the dark. The study highlights the benefits and challenges of halide perovskite materials in next-generation photo-rechargeable supercapacitors (Kumar et al., 2022).

Kumar et al. (2023) investigated the photo-capacitive behavior of two perovskite-based photoelectrodes: a mixed-halide perovskite (MHP, $\text{CH}_3\text{NH}_3\text{PbBr}_2\text{I}$) and a mixed-phase blend of $\text{CH}_3\text{NH}_3\text{PbBr}_3$ and $\text{CH}_3\text{NH}_3\text{PbI}_3$ (BP) in a 2:1 ratio. While BP electrodes showed higher capacitance in the dark due to better ion diffusion, they suffered from poor photo-performance and stability caused by iodine loss and carrier trapping. In contrast, MHP electrodes exhibited more stable performance under illumination, achieving photo-energy densities of $\sim 0.655 \text{ Wh kg}^{-1}$ (1500 LUX) and $\sim 1.6 \text{ Wh kg}^{-1}$ (90 mW cm^{-2} , 405 nm) with a photo-conversion efficiency of 0.017%. BP electrodes yielded lower energy densities (~ 0.372 and $\sim 0.316 \text{ Wh kg}^{-1}$). These results highlight the importance of halide homogeneity and synthesis methods in optimizing the photo-capacitive properties of perovskite-based supercapacitors (Kumar et al., 2023).

Moreover, transition metal-doped perovskite oxides like SrFeO_3 illustrate the versatile potential of perovskites as electrode materials. Ahangari et al. (2022) reported that such perovskite oxides demonstrate excellent stability and specific capacitance, making them promising candidates for supercapacitor electrodes. Likewise, Diatta et al. (2024) explore BaCoO_3 , demonstrating that its mixed ionic and electronic conductivity can be utilized for energy storage and conversion applications.

Popoola's group (2022) showcased a SC system for an all-inorganic perovskite-based photo-rechargeable device in the three-electrode configuration for efficient everyday applications. In the study, a lead-free symmetric PSC based on methylammonium bismuth triiodide (MBI) photo-capacitive electrodes and a CPH-G gel electrolyte was assembled. Exceptionally, a $\sim 1275\%$ enhancement in energy density was observed under light conditions. The MBI:CPH-G PSC demonstrated excellent cycling stability, retaining 94.79% of its initial capacitance after 5000 cycles, with a final equivalent series resistance (ESR) of 55.61Ω . Overall, the study presents a stable, lead-free, bifunctional PSC device that efficiently harvests and captures solar energy, showcasing impressive durability and notable enhancements in performance from light exposure (Popoola et al., 2022).

Popoola et al. (2023) present a copper-halide perovskite-based (CHP) photo-induced electrochemical capacitor using lead-free copper antimony iodide (Cu_3SbI_6) rudorffite as symmetric electrodes. A polymer gel electrolyte that is non-aqueous was employed between the electrodes. Under illumination, the CHP EC achieved a capacitance enhancement of 462%, with a max energy density of $9.98 \mu\text{Wh cm}^{-2}$ and a power density of 3.18 mW cm^{-2} . The CHP EC exhibited excellent cyclic stability, retaining 93% of its initial capacitance after 10000 charge–discharge cycles. This study highlights a rudorffite-based CHP electrochemical capacitor that integrates energy harvesting and storage, suggesting further exploration of other perovskite types in photo-rechargeable devices based on current advancements in PSCs and photo-batteries (Popoola et al., 2023).

Samtham et al. (2024) synthesized BiFeO_3 (BFO) nanoparticles with rhombohedral crystal structure and an average particle size of $\approx 100 \text{ nm}$ via a sol–gel auto combustion method. They examined their potential as electrode materials for photo-assisted supercapacitor applications. In a 3 M KOH electrolyte exposed to visible light, BFO demonstrated a specific capacity of 21 C g^{-1} and a specific capacitance of 110.5 F g^{-1} at a rate of 2 A g^{-1} , achieving a photo-efficiency of 26.77%. EIS indicated that photo-excited particles enhanced redox kinetics and pseudocapacitive charge storage. Furthermore, BFO maintained 77.5% of its capacitance after undergoing 1000 charge discharge cycles under illumination. (Samtha et al., 2024).

Hosseini et al. (2025) developed p-type lanthanum ferrite (LaFeO_3 , LFO) perovskite photoelectrodes via electrodeposition onto FTO glass and $\text{WO}_3\text{--TiO}_2$ nanotubes (WT) for photo-rechargeable supercapacitors. The LFO@WT photoelectrode exhibited exceptional photoresponsivity, achieving a maximum areal capacity of 3.5 mAh cm^{-2} under illumination, corresponding to a sevenfold enhancement compared to dark conditions. The symmetric hybrid photo-supercapacitors (HPSC) showed a peak areal capacity of 0.06 mAh cm^{-2} and an energy density of 0.15 mWh cm^{-2} at 76.5 mW cm^{-2} , while the asymmetric device achieved 2.67 mAh cm^{-2} and 9.34 mWh cm^{-2} at 84.1 mW cm^{-2} . The asymmetric LFO@WT//LFO@FTO HPSC also delivered a power density of 215.8 mW cm^{-2} and maintained 89% capacity retention after 4000 cycles in the dark environment, with a 3% increase under illuminated environment (Hosseini et al., 2025). These results indicate that doping methods can significantly improve the electrochemical performance of perovskite materials.

The advancements in perovskites and their derivatives highlight their multifunctional properties and significant potential for practical applications in energy conversion and storage. Ongoing research uncovers new

features and optimization methods, positioning perovskites as vital to advancing future energy technologies.

3.1.2. Organic Photoactive Materials

Recent developments in conducting polymers (CPs) and organic photovoltaic materials, such as P3HT and PCBM, have shed important light on their roles in perovskite solar cells (PSCs), which integrate energy harvesting and storage functionalities. Those materials, renowned for their unique attributes such as high electrical conductivity, flexibility, and ease of processing, are being increasingly explored as electrodes for supercapacitors that also exhibit photoactive properties.

Chen et al. (2010) reported an innovative plastic photo-rechargeable capacitor utilizing a three-electrode system that combines a flexible DSSC and a supercapacitor, both of which feature a common Pt electrode. A thick TiO_2 film is created by treating TiO_2 nanocrystals with isopropyl alcohol through electrophoretic deposition, followed by mechanical compression to improve connectivity. The supercapacitor employs a thick film of PEDOT for energy storage. The DSSC features a $10.9 \mu\text{m}$ TiO_2 film and achieves an electric conversion efficiency of 4.37% under sun illumination. The combined device exhibits a specific capacitance of 0.52 F cm^{-2} . This work presents a promising approach for flexible PSC applications, highlighting the need to enhance photoelectrode efficiency for broader adoption in plastic devices (Chen et al., 2010).

Wee et al. (2011) pioneered the integration of organic photovoltaics in the creation of a PSC, marking a significant advancement in this field. This cutting-edge technology harnesses the benefits of organic solar cells to create a printable, all-solid-state device. The PSC incorporates a PEDOT:PSS layer that functions as the electron donor and a poly(3-hexylthiophene: phenyl- C_{61} -butyric acid methyl ester (P3HT: PCBM) layer that runs as the electron acceptor. Additionally, a carbon nanotube solution is applied to an aluminum cathode, which serves as the electrode for the supercapacitor (Wee et al., 2011).

Zhang et al. (2013) introduced a polymer solar cell combined with a SC in a wire composition, referred to as an energy fiber. The device consists of a titania nanotube-modified Ti wire and aligned multi-walled carbon nanotubes (MWCNT) as electrodes. When light strikes the heterojunction of P3HT:PCBM, excitons are generated, which split into electrons and holes; electrons travel through the nanotubes to the Ti wire, and the MWCNT sheets collect holes. The maximum efficiency achieved was 1.01% for a wire length of $1.8 \mu\text{m}$, with 90% of the power conversion efficiency remaining after 10 days. The solar cell is connected to the SC

during the photo-charging phase, while during the discharging phase they stay disconnected. Electrochemical testing via GCD reveals an energy density of $1.61 \times 10^{-7} \text{ Wh cm}^{-2}$ and an energy conversion efficiency of 65.6%. Cyclic voltammetry reveals strong capacitive characteristics, with a specific capacitance of 0.077 mF cm^{-2} . For MWCNT sheets thicker than $20 \mu\text{m}$, the efficiencies of photoelectric conversion and storage are determined as approximately 0.82% (Zhang et al., 2013).

Takshi et al. (2015) demonstrated that composite films combining a conductive polymer and a dye can serve being photoactive electrodes in electrochemical cells, enabling simultaneous solar energy conversion and charge storage. A device established with polyethylenedioxythiophene: polystyrene sulfonate (PEDOT:PSS) and a porphyrin dye achieved a capacitance of approximately 1.04 mF , charging to 430 mV under simulated sunlight and maintaining the charge for over 10 minutes in darkness. The findings indicated that the dye-to-conducting polymer ratio is vital for optimizing both photovoltage and capacitance. Furthermore, with a Ru-based dye, we recorded a photovoltage of 198 mV and charge stability exceeding 2 hours (Takshi et al., 2015).

Xu et al. (2016) presented an integration of perovskite solar cells into photo-supercapacitors (PSCs), employing MAPbI_3 for the active layer alongside a PEDOT carbon electrode to link the solar cell with the SC. The device configuration, structured as $\text{FTO/perovskite/TiO}_2/\text{ZrO}_2/\text{PEDOT carbon electrode}$, achieved an open-circuit voltage of 0.71 V , capacitance ranging from 10.8 to 12.8 mF cm^{-2} , an energy density of $7.83 \times 10^{-7} \text{ Wh cm}^{-2}$, and a power density of 7.4 mW cm^{-2} . This system adeptly merges solar energy conversion with supercapacitive storage; the photogenerated electrons and holes are stored in the PEDOT-carbon electrodes. It reached a peak efficiency of 4.70% and demonstrated a notable energy storage efficiency of 73.77%. Nonetheless, the overall efficiency is limited by both the performance of the perovskite solar cells and the traits of the PEDOT-carbon electrode (Xu et al., 2016).

The use of compact electronics which powered by solar cells is on the rise, but these devices often experience unstable power output due to variations in sunlight. PSCs, which seamlessly integrate solar cells for energy conversion with supercapacitors for energy storage, are designed to overcome this challenge. Organometal halide perovskite solar cells can acquire impressive power conversion efficiencies of up to 22.1%, while PANI/carbon nanotube (CNT) composite supercapacitors (PANI/CNT SCs) provide outstanding energy storage potential. Nonetheless, the combination of perovskite derived solar cells and PANI/CNT supercapacitors poses particular difficulties, notably the risk of water from the superca-

pacitor's electrolyte damaging the perovskite solar cell absorber.

Liu et al. (2017) developed a PSC that utilizes $\text{CH}_3\text{NH}_3\text{PbI}_3$ (MAPbI_3) as the absorber, combined with a PANI/CNT SC, incorporating a carbon nanotube bridge to connect the two components. This setup achieved a specific area capacitance of 422 mF cm^{-2} , a coulombic efficiency of 96%, and an overall energy storage efficiency of 70.9%. PANI/CNT SC displayed stable power output across various lighting conditions, making it a promising option for solar-powered portable devices.

In their study performed in 2018, Das et al. (2018) explored a novel solar cell that uses cadmium sulfide quantum dots and hibiscus (hb) dye co-sensitized TiO_2 as the photoanode, paired with a Poly(3,4-ethylenedioxyppyrrrole)@Manganese dioxide (PEDOP@MnO_2) counter electrode. The photo-charging of PEDOP@MnO_2 is displayed in Fig. 2. This design serves as both a solar cell and a supercapacitor, acquiring a short-circuit current of 17.3 mA cm^{-2} , an open-circuit voltage of 0.746 V, and an storage efficiency of 6.11%. The supercapacitor demonstrated a specific capacitance of 155 F g^{-1} , with energy and power densities of 13.7 Wh kg^{-1} and 397.7 W kg^{-1} , respectively. This innovative PSC design, which utilizes a single long electrode with PEDOP@MnO_2 coatings, effectively captures visible light while being a low-cost alternative to traditional photoanodes. The combination of PEDOP's high conductivity and MnO_2 's redox capacitance enhances both charge storage and power conversion efficiency, making it a approach for energy conversion and storage technologies (Das et al., 2018).

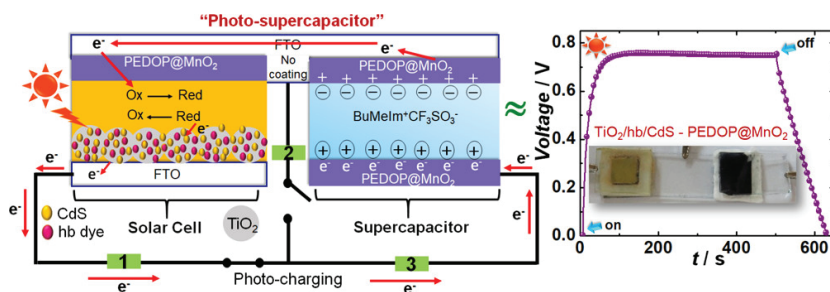


Fig. 2 Schematic of the PSC during photo-charging. Reprinted with permission from (Das et al., 2018). Copyright (2018) American Chemical Society.

Speranza et al. (2023) presented a PSC concept that employs laser-induced graphene (LIG) as a flexible counter electrode in DSSCs. By directly writing with a laser on a polyimide film, they developed electrodes

that perform effectively with both I^-/I_3^- and $Cu(II/I)$ redox couples. The assimilated device with a $Cu(II/I)$ redox mediator achieved a short-circuit current density of 1.2 mA cm^{-2} , an OCP of 0.94 V, and a fill factor of 0.75. Remarkably, the flexible LIG (F-LIG) electrodes demonstrated higher catalytic performance for the reduction of I_3^- compared to platinum-based electrodes and outperformed electrodeposited PEDOT for a copper bipyridyl complex electrolyte. The F-LIG-based DSSCs exhibited an open-circuit voltage of 0.94 V and a significant increase in photoconversion efficiency, improving from 3.08% to 4.96%. The one-step laser fabrication enabled the integration of the LIG-based DSSC with a supercapacitor, creating a flexible energy harvesting and storage system capable of self-charging under both solar and artificial light. This development holds promise for self-powered devices in the Internet of Things (IOT) (Speranza et al., 2023).

In conclusion, recent advancements in conducting polymers make them auspicious materials for future PSCs. By leveraging their unique properties, these polymers can significantly enhance the efficiency of energy storage devices, ultimately leading to the development of more sustainable and adaptable energy solutions.

3.1.3. Hybrid and Carbon-Based Photoactive Materials

MOFs are increasingly recognized as strong contenders for photo supercapacitors due to their distinct structural and chemical characteristics. Obtained of metal ions and connected by organic ligands, these materials exhibit high porosity, customizable pore sizes, and potential for conductivity, which makes them well-suited for energy storage applications.

The study by Li et al. (2014) introduced a model that illustrates the incorporation of MOF materials into dye-sensitized solar cells (DSSCs). For the first time, MOF-5 was successfully integrated into a ZnO film via screen printing, leading to the creation of hierarchical ZnO parallelepipeds after calcination, which acted as an efficient scattering layer. This innovative method utilized ZnO parallelepipeds with a dimension between 300 and 500 nm, derived from MOF-5 precursor, which greatly enhanced the performance of DSSCs. The results showcase the potential of MOFs in photovoltaic applications and suggest that further exploration of other MOFs could yield similar benefits (Li et al., 2014).

A series of zirconium(IV) coordination polymer thin films containing $Ru(II)L_2L'$ (with $L = 2,2'$ -bipyridyl and $L' = 2,2'$ -bipyridine-5,5'-dicarboxylic acid), known as RuDCBPY, were developed as sensitizers for solar cell applications. MOF-sensitized solar cells successfully generated photocurrent under simulated sun illumination, and emission lifetime mea-

measurements demonstrate over 90% efficiency in exciton quenching at the MOF–TiO₂ interface resulting from electron injection. While the efficiencies remained below 1%, these MOF-sensitized solar cells outperformed a monolayer of the same dye on TiO₂, underlined their potential for solar energy applications (Maza et al., 2016).

Furthermore, recent research highlights the importance of using MOFs in the development of composite materials that can improve photoactivity. A TiO₂ aerogel–MOF nanocomposite was synthesized by Alwin et al. (2018) using a sol–gel method and employed as a photoanode in quasi-solid DSSCs. The TiO₂ aerogel–MOF nanocomposite reached a power conversion efficiency of 2.34% and a short-circuit current density of 6.22 mA cm⁻². To enhance performance in DSSCs, controlling the density of electron-trapping sites by adjusting the MOF content in the composite is essential (Alwin et al., 2018).

In a different study, Dong et al. (2024) developed a composite electrode known as NiCo₂S₄@NiCo-LDH (NCS@NC-LDH) for an efficient asymmetric supercapacitor (ASC). This composite electrode maximizes the utilization of photo-induced charge carriers, yielding impressive performance metrics, including a specific capacitance of 3286.25 F g⁻¹ and a retention rate of 97%. The energy density of the ASC increased from 63.29 Wh kg⁻¹ to 83.2 Wh kg⁻¹, mainly due to chemical interactions that enhance charge storage. (Dong et al., 2024).

Ifraemov et al. (2019) demonstrate that a MOF-based electrode can switch its function from photo-anodic to photocathodic by altering the redox mediators in the electrolyte. The study also provides proof of concept for hydrogen production using a MOF-photocathode, highlighting new opportunities for solar fuel generation. The performance of MOF-based electrodes is determined by the charge transfer at the interface, not by the inherent properties of charge carriers (Ifraemov et al., 2019).

A significant development is the incorporation of conductive materials, such as MXenes, with TiO₂ to enhance charge transport properties. Lee et al. (2014) created a composite powder of TiO₂ nanoparticles and MWCNTs through a hydrothermal process. This powder was then transformed into a film using doctor blading and sensitized with copper-based MOFs through a layer-by-layer deposition method. The results indicated that the inclusion of carbon nanoenhancers boosts electron transfer, resulting in a nearly 60% improvement in power conversion efficiency. The integration of MWCNTs into the TiO₂ film decreases interfacial charge transfer resistance and speeds up electron transfer, greatly enhancing photovoltaic performance (Lee et al., 2014).

Colak et al. (2024) developed dual electrodes utilizing ZnO nano-flakes and $\text{Ti}_3\text{C}_2\text{T}_x$ -based MXene paper for a PSC device. The incorporation of MXene enhanced the capacitive contribution by nearly fourfold compared to using only ZnO PSC, thanks to enhanced surface oxidation and reduction reactions and electrical double layer formation. The maximum energy and power densities reached $57.3 \mu\text{Wh cm}^{-2}$ and 11.1 mW cm^{-2} , respectively, under UV irradiation at an operating voltage of 2.5 V, with an impressive areal capacitance of 151.5 mF cm^{-2} . The ZnO/MXene//MXene-PSC showed excellent stability, maintaining 100% coulombic efficiency and 98% capacitance retention over 10000 galvanostatic cycles. Although the ZnO/MXene//CP PSC retained 70% of its capacitance after 7 days, the ZnO/MXene//MXene/CP PSC experienced approximately an 85% loss, probably because of UV-induced aging of the MXene paper (Colak et al., 2024).

Carbon materials are intrinsically advantageous because of their elevated surface area, excellent conductivity, and customizable properties, which are vital for the effective functioning of supercapacitors. A significant trend involves creating hybrid carbon materials that merge the benefits of various carbon allotropes, including activated carbon, graphene, and CNTs.

Wang et al. (2022) presented a self-powered PSC with bulk micro-machined three-dimensional porous asymmetric electrodes, created using the deep reactive-ion etching technique, for detecting ultraviolet radiance (UV). The porous CNT@TiC/CNT@TiO_2 PSC achieves an areal capacitance of 2.69 mF cm^{-2} at 5 mV s^{-1} and 7.35 mF cm^{-2} at $20 \mu\text{A cm}^{-2}$ after the photo-charge process. Its optical response is linearly proportional to UV power intensity, with a photoresponsivity of 14.8 mA W^{-1} and a photocurrent density of $354 \mu\text{A cm}^{-2}$ under 15 mW cm^{-2} UV intensity, resulting in a photo-to-dark current ratio of 12. When integrated on-chip, the PSC can illuminate a white LED for more than 60 seconds at a UV intensity of 10 mW cm^{-2} , demonstrating practical applications in UV monitoring systems (Wang et al., 2022).

In photo supercapacitors, a lever to boost energy storage capacity, carbon materials are effectively combined with various components. For example, integrating graphitic carbon nitride with metal oxides enhances light-harvesting capabilities and improves electrochemical performance under light exposure. The study by Altaf et al. (2023) showcases the critical ratios for graphene oxide/zinc oxide (GO/ZnO) composites in the performance of PSC. The best-performing GO/ZnO composites achieved a specific capacitance of 6612 mF g^{-1} after UV illumination, reflecting a 2.7-fold increase. These devices achieved 99.6% capacitance retention

and 100% Coulombic efficiency across 30000 charge-discharge cycles. The maximum energy density reached 6.3 Wh kg^{-1} , alongside a power density of 625 W kg^{-1} at a 2.5 V operating voltage under UV light. The study highlights a critical ratio for GO/ZnO composites that enhances the performance of PSCs. Future research could aim at creating lightweight devices that effectively convert and store solar energy through various heterojunctions or composite materials (Altaf et al., 2023).

Zheng et al. (2022) developed a PSC device that integrates a CdS/CdSe quantum dot sensitized solar cell with an activated carbon-based supercapacitor, using a mutual electrode and aqueous electrolytes. The device achieved an overall efficiency of 2.66% during photo-charging and galvanostatic discharging at 1 mA cm^{-2} , along with an areal capacitance of $132.83 \text{ mF cm}^{-2}$ and an energy density of 23.9 mJ cm^{-2} . It maintained 76.7% of its initial efficiency after 100 cycles, demonstrating good stability. This integrated device effectively harvests, converts, stores, and releases solar energy. When exposed to solar irradiation, it quickly charges to 0.6 V in just seconds and can discharge in both light and dark settings, which makes it ideal for compact, self-powered electronic devices (Zheng et al., 2022).

3.2. Electrolytes for Enhanced Photoactivity

Research into photo-active electrolytes has contributed significantly to the advancement and efficiency of PSCs, which integrate energy harvesting and storage functionalities. These electrolytes are crucial for enhancing the electrochemical performance of PSCs by introducing additional Faradaic reaction pathways, thereby improving energy density and charge storage capabilities.

The majority of harvesting-supply (HS) devices discussed in the literature exhibit a maximum voltage of less than 1 V, mainly because they utilize a single solar cell. Scalia et al. (2018) report an exception, achieving a voltage just under 2.3 V with an HS device that contains eight organic solar cell modules and a graphene-based supercapacitor utilizing 1 M tetraethylammonium tetrafluoroborate in propylene carbonate (PC) as the electrolyte. They noted that the voltage is limited by the electrolyte's reaction with the electrode, which reduces the device's lifespan. Their attempt to connect two SCs in series also faced stability issues. In contrast, they present a new, highly stable HS device fabricated on a glass substrate. This design uses a W-type dye-sensitized solar module with four cells in series, paired with a supercapacitor utilizing activated carbon (AC) and the ionic liquid *N*-butyl-*N*-methylpyrrolidinium bis(trifluoromethanesulfonyl)imide ($\text{Pyr}_{14}\text{TFSI}$) as the electrolyte. This ionic

liquid exhibits better thermal stability than organic electrolytes, such as PC, which can cause voltage saturation above approximately 2.2 V, even with higher OCP, indicating instability and irreversible behavior (Scalia et al., 20158).

Gel polymer electrolytes (GPEs) represent a promising class of materials that successfully blend the advantages of solid and liquid electrolytes. Typically, these electrolytes consist of a polymer matrix completely immersed in a liquid electrolyte. This distinctive structure offers mechanical stability and high ionic conductivity, positioning GPEs as a desirable choice for numerous applications in batteries and energy storage technologies.

The study by Harankahawa et al. (2017) investigates redox capacitors as a potential energy storage option, focusing on the fabrication of a DSSC that enhances these capacitors. The DSSC was developed using a gel polymer electrolyte (GPE), which offers several advantages compared to traditional liquid electrolytes. GPEs mitigate common issues associated with liquid electrolytes, such as leakage and short lifespan, thereby enhancing the stability and durability of the DSSC. Initial results for the DSSC include an open circuit potential (VOC) of 0.68 V, short circuit current density (JSC) of 0.33 mA cm^{-2} , fill factor (FF) of 0.24, and efficiency (η) of 0.05%. The redox capacitor was charged for 722 seconds and fully discharged in 36 seconds, with satisfactory stability observed. The optimal GPE composition consisted of polyacrylonitrile (PAN), sodium iodide (NaI), ethylene carbonate (EC), and PC, resulting in a room temperature conductivity of $4.29 \times 10^{-3} \text{ S cm}^{-1}$. This research marks the first attempt in Sri Lanka to couple a DSSC with a redox capacitor. As interest in solar energy expands in the region, this study seeks to enhance research into effective energy storage solutions. Current efforts will concentrate on enhancing the performance and stability of both the DSSC and redox capacitor (Harankahawa et al., 2017).

A simple and low-cost method for preparing this composite gel electrolyte is described by Lai & Fan (2022). PANI-based gel material has shown excellent charge storage, photovoltaic, and electrochromic properties. A hybrid device for solar energy harvesting and charge storage was created by layering the gel between a TiO_2 -coated electrode and a carbon electrode, achieving an open-circuit voltage of 137 mV under light with only a 10 mV drop after 600 seconds of darkness. While these devices are traditionally electrochemical, the use of the composite gel enables a novel design with a single-layer material that is active throughout. Modifying the gel with various additives may result in cost-effective and efficient devices, necessitating additional research on how changes in materials

impact energy storage and photovoltaic characteristics (Lai & Fan, 2022).

In a separate study, Wang et al. (2020) created reversible ion-conducting switches via photoswitchable sol-gel transitions. The ion gel was produced by mixing azobenzene (Azo), poly(N-isopropylacrylamide) (PNIPAm), and 1-ethyl-3-methylimidazolium bis(trifluoromethylsulfonyl) imide ([C2mim][NTf₂]). The gel's structure was designed to mirror the principles of control theory, comprising sensor, amplification, and action. The light-induced isomerization of Azo initiates the macroscopic sol-gel transition of PNIPAm assemblies, which influences ionic movements and produces notable switching behavior. When exposed to UV light, the sol-like state of Azo/PNIPAm/[C2mim][NTf₂] exhibited increased ion conduction, while the gel state demonstrated reduced conduction. Fig. 3 shows the graphical illustrations of these mechanisms. This photoswitchable ion conductivity device was incorporated into a well-structured logic gate, enabling the switching of circuits on or off (Wang et al., 2020).

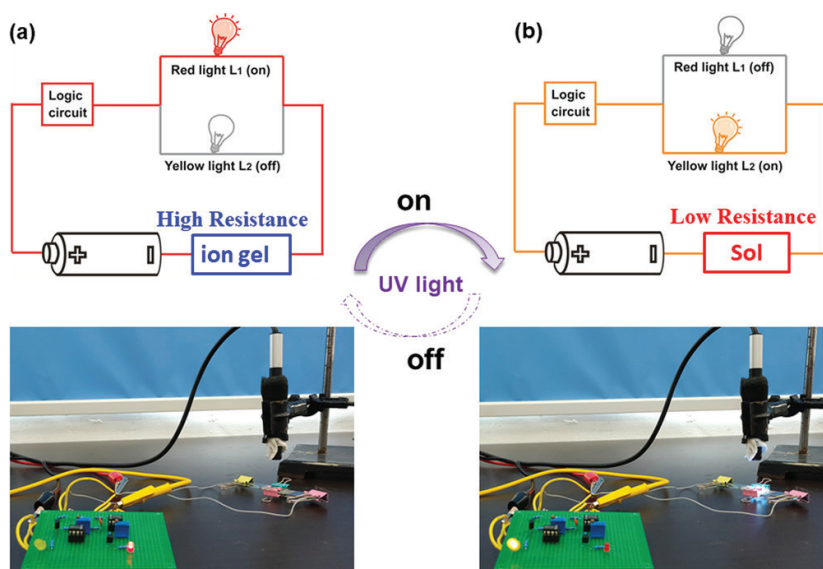


Fig. 3 Photoswitchable ionic circuits at 28 °C: (a) In the gel state, the red light is on while the yellow light is off in the absence of UV irradiation; (b) In the sol state, the yellow light is on and the red light is off when UV light is applied. Reprinted with permission from (Wang et al., 2020). Copyright (2020) American Chemical Society.

Nie et al. (2020) created a synthetic platform that highlights the reversible photoswitch properties of diarylethene-based polymeric ionic liquids

(DAE-based PILs). These solid PIL films enable tunable ionic conductivity, achieving a reduction of up to 70% upon irradiation. This light sensitive feature allows for effective in situ spatiotemporal patterning and local conductivity control. The copolymer (PEO-stat-PAGE-DAE-BF₄) is expected to advance research in PIL materials, offering promise for smart electrical circuits and wearable photodetectors. The non-invasive photo-modulation process eliminates the need for additional chemical agents, laying the groundwork for future mechanistic studies. Ongoing research aims to develop imidazolium-containing photoswitches with enhanced fatigue resistance and thermal stability, also to investigate how ion-polymer interactions influence ion transport (Nie et al., 2020).

The reliability of light-harvesting photovoltaic systems with charge storage components is essential for their effectiveness in fluctuating weather conditions. Skunik-Nuckowska et al. (2021) demonstrated a portable solar charger that combines a silicon solar cell with an advanced hybrid supercapacitor utilizing activated carbon electrodes and iodide-based aqueous electrolyte to stabilize power output during fluctuations. The optimized supercapacitor module has a capacitance of 60 F and a voltage of 3 V, achieved through specific series and parallel connections of the CR2032 coin cells. Their evaluation demonstrated its effectiveness for pulse electronic applications under various laboratory conditions (temperatures of 15 and 25 °C, and solar irradiance levels of 600 and 1000 W m⁻²). Redox Electrolyte Hybrid Energy Storage (REHES) was introduced for this solar charger, enabling enhanced capacitance, improved energy output, and optimized charge-discharge dynamics. The charger can fully charge the supercapacitor in approximately 2 hours, with minimal impact from temperature changes, ensuring reliable performance during cloudless days in European latitudes during the second and third quarters, from 8:00 to 16:00 (Skunik-Nuckowska et al., 2021).

Kim et al. (2025) presented reversible photo-switchable supercapacitors using azobenzene-containing polymer electrolytes that undergo a gel-to-sol transition when exposed to light, achieving a 3206% increase in ionic conductivity. These devices offer a capacitance modulation of 105% with a 4-minute response time and improved self-discharge under visible light, enhancing long-term energy storage potential. Photo-switchable supercapacitors achieve an areal capacitance of 1.84 mF cm⁻² with rapid modulation driven by light exposure, showcasing exciting possibilities for versatile energy management in future applications (Kim et al., 2025).

Bhaumik et al. (2025) have introduced an innovative design for a photo-rechargeable supercapacitor that employs an aqueous solution of 2-nitrobenzaldehyde as its electrolyte, complemented by activated char-

coal electrodes. This design leverages the photoinduced transformation of 2-nitrobenzaldehyde into labile benzoic acid derivatives, which generates redox-active ionic species and contributes to a substantial increase in capacitance. The device achieves a specific capacitance of $320 \text{ F g}^{-1} \text{ cm}^{-2}$ when configured in a three-electrode system and about $90 \text{ F g}^{-1} \text{ cm}^{-2}$ in a two-electrode system (Bhaumik et al., 2025).

4. FUTURE PERSPECTIVES AND OUTLOOKS

The future perspectives for PSCs appear immensely promising, especially as technological advancements significantly enhance energy conversion and storage capabilities. PSCs, which integrate photovoltaic elements with supercapacitors, are at the forefront of research aimed at developing sustainable energy solutions. Their capability to convert and store solar energy constitutes a pivotal advancement toward realizing energy efficiency and autonomy in portable and wearable devices.

A key aspect of the future development of PSCs is their integration with advanced materials that enhance performance. Recent studies highlight that using materials such as mesoporous carbon in monolithic structures can significantly improve energy conversion efficiency. Additionally, the performance of PSCs heavily relies on the active components used, including the photoanode, sensitizers, and electrolytes.

The increasing interest in flexible and lightweight applications for energy devices, particularly in wearables, highlights another trend in the development of PSCs. Jin et al. formulated the creation of all-printed PSC fibers designed for self-charging applications (Jin et al., 2020). This innovation addresses existing consumer demands for mobile energy solutions and aligns with the growing emphasis on integrating energy harvesting with practical consumer electronics. The investigation of halide perovskites as energy storage materials, as noted by Zhang et al., further signifies a robust future direction for lightweight photo-rechargeable systems capable of seamless integration into daily applications (Zhang et al., 2020).

In considering the future of energy storage, the technology roadmap for photovoltaics outlines a comprehensive strategy to tackle the challenges related to energy delivery and storage systems. There is a growing demand for systems that can efficiently balance the variability of renewable energy sources. This need is highlighted in several reviews that explore how integrated renewable systems can improve energy stability (Sinsel et al., 2020; Chirapongsananurak & Santoso, 2018). This understanding arises from the necessity for advanced energy storage solutions to ensure grid reliability and reduce system costs, especially with the increasing

global capacity for photovoltaics.

In conclusion, the prospects for PSCs will likely include innovations in material science, optimization of efficiency, integration with wearable technologies, and the development of integrated systems that harmonize energy generation and storage. Ongoing advancements in these domains are essential for realizing the full potential of PSCs and enhancing their role in fulfilling future energy requirements.

REFERENCES

- Ahangari, M., Mahmoodi, E., Delibas, N., Mostafaei, J., Asghari, E., & Niaei, A. (2022). Application of SrFeO₃ perovskite as electrode material for supercapacitor and investigation of co-doping effect on the b-site. *Turkish Journal of Chemistry*, 46(5), 1723-1732. <https://doi.org/10.55730/1300-0527.3475>
- Altaf, C. T., Colak, T. O., Rostas, A. M., Mihet, M., Lazar, M. D., Iatsunskyi, I., Coy, E., Yildirim, I. D., Misirlioglu, F. B., Erdem, E., Sankir, M., & Sankir, N. D. (2023). GO/ZnO-based all-solid-state photo-supercapacitors: Effect of GO:ZnO ratio on composite properties and device performance. *Journal of Energy Storage*, 68, 107694. <https://doi.org/10.1016/J.EST.2023.107694>
- Altaf, C. T., Coskun, O., Kumtepe, A., Rostas, A. M., Iatsunskyi, I., Coy, E., Erdem, E., Sankir, M., & Sankir, N. D. (2023). Photo-supercapacitors based on nanoscaled ZnO. *Scientific Reports*, 13(1), 1–1. <https://doi.org/10.1038/s41598-022-15180-z>
- Altaf, T. C., Rostas, A. M., Popa, A., Toloman, D., Stefan, M., Demirci Sankir, N., & Sankir, M. (2023). Recent Advances in Photochargeable Integrated and All-in-One Supercapacitor Devices. *ACS Omega*, 8(50), 47393–47411. <https://doi.org/10.1021/ACSOMEGA.3C07464>
- Alwin, S., Ramasubbu, V., & Sahaya Shajan, X. (2018). TiO₂ aerogel–metal organic framework nanocomposite: A new class of photoanode material for dye-sensitized solar cell applications. *Bulletin of Materials Science*, 41(1), 1–8. <https://doi.org/10.1007/s12034-017-1532-8>
- Bagheri, N., Aghaei, A., Ghotbi, M. Y., Marzbanrad, E., Vlachopoulos, N., Häggman, L., Wang, M., Boschloo, G., Hagfeldt, A., Skunik-Nuckowska, M., & Kulesza, P. J. (2014). Combination of Asymmetric Supercapacitor Utilizing Activated Carbon and Nickel Oxide with Cobalt Polypyridyl-Based Dye-Sensitized Solar Cell. *Electrochimica Acta*, 143, 390–397. <https://doi.org/10.1016/J.ELECTACTA.2014.07.125>
- Bhaumik, S.K., Biswas, S., Shauloff, N., Morag, A., & Jelinek, R. (2025). Photo-Rechargeable Organic Supercapacitor via Light-Activated Electrolytes. *Advanced Science*, 2500978. <https://doi.org/10.1002/advs.202500978>
- Chauhan, P. S., Kumar, S., Mondal, A., Sharma, P., Parekh, M. N., Panwar, V., Rao, A. M., & Misra, A. (2023). Stacked vanadium pentoxide–zinc oxide interface for optically-chargeable supercapacitors. *Journal of Materials Chemistry A*, 11(1), 95–107. <https://doi.org/10.1039/D2TA06790K>
- Chen, H. W., Hsu, C. Y., Chen, J. G., Lee, K. M., Wang, C. C., Huang, K. C., & Ho, K. C. (2010). Plastic dye-sensitized photo-supercapacitor using electrophoretic deposition and compression methods. *Journal of Power Sources*, 195(18), 6225–6231. <https://doi.org/10.1016/J.JPOWSOUR.2010.01.009>
- Chirapongsananurak, P. & Santoso, S. (2018). Inventions and innovation in integration of renewable energy systems. *Inventions*, 3(2), 28. <https://doi.org/10.3390/inventions3020028>
- Colak, T. O., Altaf, C. T., Yesilbag, F. N. T., Yesilbag, Y. O., Yildirim, I. D.,

- Erdem, E., Misirlioglu, F. B., Sankir, N. D., & Sankir, M. (2024). Photo-supercapacitors based on zinc oxide/MXene paper dual acting electrodes. *Journal of Energy Storage*, 86, 111274. <https://doi.org/10.1016/J.EST.2024.111274>
- Cui, Y., Zhou, Z., Li, T., Wang, K., Li, J., & Wei, Z. (2019). Versatile crystal structures and (opto)electronic applications of the 2d metal mono-, di-, and tri-chalcogenide nanosheets. *Advanced Functional Materials*, 29(24). <https://doi.org/10.1002/adfm.201900040>
- Das, A., Deshagani, S., Kumar, R., & Deepa, M. (2018). Bifunctional Photo-Supercapacitor with a New Architecture Converts and Stores Solar Energy as Charge. *ACS Applied Materials and Interfaces*, 10(42), 35932–35945. <https://doi.org/10.1021/acsami.8b11399>
- Das, A., Ojha, M., Subramanyam, P., & Deepa, M. (2020). A poly(3,4-propylenedioxythiophene)/carbon micro-sphere-bismuth nanoflake composite and multifunctional Co-doped graphene for a benchmark photo-supercapacitor. *Nanoscale Advances*, 2(7), 2925–2942. <https://doi.org/10.1039/D0NA00103A>
- Diatta, A., Colin, C., Viennois, R., Beaudhuin, M., Haines, J., Hermet, P., Lee, A. v. d., Konczewicz, L., Armand, P., & Rouquette, J. (2024). Bacoo2 with tetrahedral cobalt coordination: the missing element to understand energy storage and conversion applications in bacoo3– δ -based materials. *Journal of the American Chemical Society*, 146(22), 15027-15035. <https://doi.org/10.1021/jacs.3c14047>
- Dong, Z., Zhang, Q., Shu, X., Hu, J., & Han, S. (2024). Photo-assisted charging of heterostructured NiCo2S4@NiCo-LDH composite electrode with remarkable photoelectronic memory effect for high-performance asymmetric supercapacitor. *Energy Conversion and Management*, 315, 118769. <https://doi.org/10.1016/J.ENCONMAN.2024.118769>
- Du, J., Zhang, B., Jiang, M., Zhang, Q., Zhang, K., Liu, Y., Wang, L., & Jiang, W. (2023). Inkjet printing flexible thermoelectric devices using metal chalcogenide nanowires. *Advanced Functional Materials*, 33(26). <https://doi.org/10.1002/adfm.202213564>
- Eikey, E., Gan, X., Kaseman, D., Murphey, C., Crawford, S., Johnston, K., Yazdi, S., & Millstone, J. (2020). Efficient control of atom arrangement in ternary metal chalcogenide nanoparticles using precursor oxidation state. *Chemistry of Materials*, 32(3), 1322-1331. <https://doi.org/10.1021/acs.chemmater.9b05261>
- Flores-Diaz, N., de Rossi, F., Das, A., Deepa, M., Brunetti, F., & Freitag, M. (2023). Progress of Photocapacitors. *Chemical Reviews*, 123(15), 9327–9355. <https://doi.org/10.1021/acs.chemrev.2c00773>
- Gul, M. M., Ahmad, K. S., Thomas, A. G., & Alarifi, S. (2023). Supercapacitor with highly efficient rare earth metal conjugated transition metal chalcogenide photoactive electrode In:SnO2/Nd2S3:Ni9S8:Co9S8. *Materials Science and Engineering: B*, 294, 116544. <https://doi.org/10.1016/J.MSEB.2023.116544>

- Gul, M. M., Ahmad, K. S., Thomas, A. G., & Ali, D. (2023). In:SnO₂/Yb₂S₃:Cu₂S:ZnS: A Rare Earth Metal Sulfide-Conjugated Transition Metal Sulfide Photoactive Electrode. *Energy Technology*, 11(7), 2300062. <https://doi.org/10.1002/ENTE.202300062>
- Guo, Z., Wang, J., Wang, Y., Wang, J., Li, J., Mei, T., Qian, J., & Wang, X. (2022). Achieving steam and electrical power from solar energy by MoS₂-based composites. *Chemical Engineering Journal*, 427, 131008. <https://doi.org/10.1016/J.CEJ.2021.131008>
- Harankahawa, N., Perera, K., & Vidanapathirana, K. (2017). Use of gel polymer electrolytes to integrate photoelectric conversion and energy storage. *Journal of Energy Storage*, 13, 96–102. <https://doi.org/10.1016/J.EST.2017.07.006>
- Hosseini, Z., Momeni, M. M., Lee, B. K., & Maijenburg, A. W. (2025). Light-Enhanced capacitive performance in LaFeO₃-Based photo-supercapacitors Employing p-n heterojunction Architecture. *Chemical Engineering Journal*, 515, 163566. <https://doi.org/10.1016/J.CEJ.2025.163566>
- Ifraemov, R., Shimoni, R., He, W., Peng, G., & Hod, I. (2019). A metal–organic framework film with a switchable anodic and cathodic behaviour in a photo-electrochemical cell. *Journal of Materials Chemistry A*, 7(7), 3046–3053. <https://doi.org/10.1039/C8TA10483B>
- Jacob, S., George, J., & Balachandran, M. (2024). Polymer photosupercapacitors: combined nanoarchitectonics with polymer solar cell and supercapacitor for emerging powerpacks in next-generation energy applications. *Journal of Materials Science* 2024 59:47, 59(47), 21649–21683. <https://doi.org/10.1007/S10853-024-10477-Y>
- Jin, W., Ovhal, M., Lee, H., Tyagi, B., & Kang, J. (2020). Scalable, all-printed photocapacitor fibers and modules based on metal-embedded flexible transparent conductive electrodes for self-charging wearable applications. *Advanced Energy Materials*, 11(4). <https://doi.org/10.1002/aenm.202003509>
- Kim, Y., Bark, H., Gupta, A., Zhang, Y., Lee, J., & Lee, P. S. (2025). Photo-Switchable Supercapacitors based on Photo-Responsive Azopolymers: Enabling Dual-Functionality in Tunable High Capacitance and Low Self-Discharge. *Advanced Energy Materials*, 15(13), 2405480. <https://doi.org/10.1002/AENM.202405480>
- Kumar, R., Kumar, A., Shukla, P. S., Varma, G. das, Venkataraman, D., & Bag, M. (2022). Photorechargeable Hybrid Halide Perovskite Supercapacitors. *ACS Applied Materials and Interfaces*, 14(31), 35592–35599. <https://doi.org/10.1021/ACSAMI.2C07440>
- Kumar, T., Kumar, A., Beniwal, S., Kumar, R., & Bag, M. (2023). Photo-generated Charge Trapping in Phase Segregated Halide Perovskites – A Comprehensive Approach towards Efficient Photo-Rechargeable Ion Capacitors. *Batteries and Supercaps*, 6(10), e202300213. <https://doi.org/10.1002/BATT.202300213>
- Lee, D. Y., Shin, C. Y., Yoon, S. J., Lee, H. Y., Lee, W., Shrestha, N. K., Lee, J. K., &

- Han, S. H. (2014). Enhanced photovoltaic performance of Cu-based metal-organic frameworks sensitized solar cell by addition of carbon nanotubes. *Scientific Reports*, 4(1), 1–5. <https://doi.org/10.1038/SREP03930>
- Lai, W. C., & Fan, R. W. (2022). A simple low-cost method to prepare gel electrolytes incorporating graphene oxide with increased ionic conductivity and electrochemical stability. *Journal of Electroanalytical Chemistry*, 907, 115889. <https://doi.org/10.1002/celec.201901850>
- Li, Y., Che, Z., Sun, X., Dou, J., & Wei, M. (2014). Metal–organic framework derived hierarchical ZnO parallelepipeds as an efficient scattering layer in dye-sensitized solar cells. *Chemical Communications*, 50(68), 9769–9772. <https://doi.org/10.1039/C4CC03352C>
- Liang, Y., Gao, J., Shen, T., Lu, N., Mu, T. S., Zhang, Y. C., & Zhu, X. D. (2025). Liquid metal-transition metal oxide photoactive electrode with interfacial interlocking structure for photo-enhanced asymmetric micro-supercapacitor. *Chemical Engineering Journal*, 515, 163698. <https://doi.org/10.1016/J.CEJ.2025.163698>
- Liu, R., Liu, C., & Fan, S. (2017). A photocapacitor based on organometal halide perovskite and PANI/CNT composites integrated using a CNT bridge. *Journal of Materials Chemistry A*, 5(44), 23078–23084. <https://doi.org/10.1039/C7TA06297D>
- Lu, H., Zhang, Y., Lin, X., & Gao, H. (2021). Novel two-dimensional transition metal chalcogenides created by epitaxial growth. *Science China Physics Mechanics and Astronomy*, 64(10). <https://doi.org/10.1007/s11433-021-1746-5>
- Madhusudanan, S. P., Suresh Kumar, M., Yamini Yasoda, K., Santhanagopalan, D., & Batabyal, S. K. (2020). Photo-enhanced supercapacitive behaviour of photoactive Cu₂FeSnS₄ (CFTS) nanoparticles. *Journal of Materials Science: Materials in Electronics*, 31(1), 752–761. <https://doi.org/10.1007/S10854-019-02582-5>
- Maza, W. A., Haring, A. J., Ahrenholtz, S. R., Epley, C. C., Lin, S. Y., & Morris, A. J. (2016). Ruthenium(ii)-polypyridyl zirconium(iv) metal–organic frameworks as a new class of sensitized solar cells. *Chemical Science*, 7(1), 719–727. <https://doi.org/10.1039/C5SC01565K>
- Michalec, K., Kusior, A., & Radecka, M. (2023). Photoelectrochemical activity of the nanostructured electrodes based on the SnO₂/SnS₂ – Heterojunction type II vs S-scheme mechanism. *Applied Surface Science*, 608, 155201. <https://doi.org/10.1016/J.APSUSC.2022.155201>
- Miyasaka, T., & Murakami, T. N. (2004). The photocapacitor: An efficient self-charging capacitor for direct storage of solar energy. *Applied Physics Letters*, 85(17), 3932–3934. <https://doi.org/10.1063/1.1810630>
- Momeni, M. M., Aydisheh, H. M., Lee, B. K., & Naderi, A. (2025). Lightweight flexible self-powered photo-supercapacitors with good stability through photoelectrochemical deposition of tellurium on PPy–V₂O₅ films as a new visible light active dual photoelectrode. *Journal of Materials Chemistry C*, 13(1), 430–444. <https://doi.org/10.1039/D4TC03090G>

- Momeni, M. M., Najafi, M., Farrokhpour, H., & Lee, B. K. (2024). Fabrication and photo/electrochemical properties of cobalt-manganese binary metal sulfides deposited on titania nanotubes: Efficient and stable photoelectrodes for photo-assisted charging supercapacitors. *Journal of Energy Storage*, 79, 109666. <https://doi.org/10.1016/J.EST.2023.109666>
- Namsheer, K., & Rout, C. S. (2021). Photo-powered integrated supercapacitors: a review on recent developments, challenges and future perspectives. *Journal of Materials Chemistry A*, 9(13), 8248-8278. <https://doi.org/10.1039/D1TA00444A>
- Ng, C. H., Lim, H. N., Hayase, S., Harrison, I., Pandikumar, A., & Huang, N. M. (2015). Potential active materials for photo-supercapacitor: A review. *Journal of Power Sources*, 296, 169–185. <https://doi.org/10.1016/J.JPOWSOUR.2015.07.006>
- Ng, C. H., Lim, H. N., Hayase, S., Zainal, Z., Shafie, S., Lee, H. W., & Huang, N. M. (2018). Cesium Lead Halide Inorganic-Based Perovskite-Sensitized Solar Cell for Photo-Supercapacitor Application under High Humidity Condition. *ACS Applied Energy Materials*, 1(2), 692–699. <https://doi.org/10.1021/ACSAEM.7B00103>
- Nie, H., Schausser, N. S., Dolinski, N. D., Hu, J., Hawker, C. J., Segalman, R. A., & Alaniz, J. R. de. (2020). Light-Controllable Ionic Conductivity in a Polymeric Ionic Liquid. *Angewandte Chemie*, 132(13), 5161–5166. <https://doi.org/10.1002/ANGE.201912921>
- Jacob, S., George, J. & Balachandran, M. Polymer photosupercapacitors: combined nanoarchitectonics with polymer solar cell and supercapacitor for emerging powerpacks in next-generation energy applications. *J Mater Sci* 59, 21649–21683 (2024). <https://doi.org/10.1007/s10853-024-10477-y>
- Popoola, I. K., Gondal, M. A., Oloore, L. E., & Popoola, A. J. (2023). Inorganic antimony-based rudorffite photo-responsive electrochemical capacitor utilizing non-aqueous polyvinylpyrrolidone polymer gel electrolyte for hybrid energy harvesting and storage applications. *Materials Science and Engineering: B*, 291, 116373. <https://doi.org/10.1016/J.MSEB.2023.116373>
- Popoola, I. K., Gondal, M. A., Popoola, A. J., & Oloore, L. E. (2022). Bismuth-based organometallic-halide perovskite photo-supercapacitor utilizing novel polymer gel electrolyte for hybrid energy harvesting and storage applications. *Journal of Energy Storage*, 53, 105167. <https://doi.org/10.1016/J.EST.2022.105167>
- Safshekan, S., Herraiz-Cardona, I., Cardenas-Morcoso, D., Ojani, R., Haro, M., & Gimenez, S. (2017). Solar Energy Storage by a Heterostructured BiVO4-PbOx Photocapacitive Device. *ACS Energy Letters*, 2(2), 469–475. <https://doi.org/10.1021/ACSENERGYLETT.6B00728>
- Scalia, A., Varzi, A., Lamberti, A., Tresso, E., Jeong, S., Jacob, T., & Passerini, S. (2018). High energy and high voltage integrated photo-electrochemical double layer capacitor. *Sustainable Energy & Fuels*, 2(5), 968–977. <https://doi.org/10.1039/C8SE00003D>
- Samtham, M., Patil, A., Choudhary, E., Srivastava, H., Jangir, R., Choudhary, R. J.,

- & Devan, R. S. (2024). Probing Photo-Assisted Charge Storage Mechanism Using Bi-Fe Perovskite Oxide Electrode for Solar Supercapacitor. *Small Methods*, 9(4), 2401441. <https://doi.org/10.1002/SMTD.202401441>
- Sinsel, S., Riemke, R., & Hoffmann, V. (2020). Challenges and solution technologies for the integration of variable renewable energy sources—a review. *Renewable Energy*, 145, 2271–2285. <https://doi.org/10.1016/j.renene.2019.06.147>
- Skunik-Nuckowska, M., Grzejszczyk, K., Kulesza, P. J., Yang, L., Vlachopoulos, N., Häggman, L., Johansson, E., & Hagfeldt, A. (2013). Integration of solid-state dye-sensitized solar cell with metal oxide charge storage material into photoelectrochemical capacitor. *Journal of Power Sources*, 234, 91–99. <https://doi.org/10.1016/J.JPOWSOUR.2013.01.101>
- Skunik-Nuckowska, M., Rączka, P., Lubera, J., Mroziejcz, A. A., Dyjak, S., Kulesza, P. J., Plebankiewicz, I., Bogdanowicz, K. A., & Iwan, A. (2021). Iodide electrolyte-based hybrid supercapacitor for compact photo-rechargeable energy storage system utilising silicon solar cells. *Energies*, 14(9), 2708. <https://doi.org/10.3390/EN14092708/S1>
- Song, Z., Wu, J., Sun, L., Zhu, T., Deng, C., Wang, X., Li, G., Du, Y., Chen, Q., Sun, W., Fan, L., Chen, H., Lin, J., & Lan, Z. (2022). Photocapacitor integrating perovskite solar cell and symmetrical supercapacitor generating a conversion storage efficiency over 20 %. *Nano Energy*, 100, 107501. <https://doi.org/10.1016/J.NANOEN.2022.107501>
- Speranza, R., Reina, M., Zaccagnini, P., Pedico, A., & Lamberti, A. (2023). Laser-induced graphene as a sustainable counter electrode for DSSC enabling flexible self-powered integrated harvesting and storage device for indoor application. *Electrochimica Acta*, 460, 142614. <https://doi.org/10.1016/J.ELECTACTA.2023.142614>
- Su, J., Liu, K., Wang, F., Jin, B., Guo, Y., Liu, G., Li, H., & Zhai, T. (2019). Van der waals 2d transition metal tellurides. *Advanced Materials Interfaces*, 6(19). <https://doi.org/10.1002/admi.201900741>
- Takshi, A., Yaghoubi, H., Tevi, T., & Bakhshi, S. (2015). Photoactive supercapacitors for solar energy harvesting and storage. *Journal of Power Sources*, 275, 621–626. <https://doi.org/10.1016/J.JPOWSOUR.2014.10.110>
- Vadivel, S., Hariganesh, S., Ramykrishna, P., & Boddula, R. (2019). Photo-Supercapacitor. *Supercapacitor Technology*, 61, 223–232. <https://doi.org/10.21741/9781644900499-9>
- Wang, C., Dong, W., Li, P., Wang, Y., Tu, H., Tan, S., Wu, Y., & Watanabe, M. (2020). Reversible Ion-Conducting Switch by Azobenzene Molecule with Light-Controlled Sol-Gel Transitions of the PNIPAm Ion Gel. *ACS Applied Materials and Interfaces*, 12(37), 42202–42209. <https://doi.org/10.1021/ACSAMI.0C12910>
- Wang, Y., Du, H., Xiao, D., Zhang, Y., Wang, W., Zhang, J., Liu, X., Geng, J., Hu, F., & Sun, L. (2022). A carbon nanotube@silicon-based three-dimensional porous photo-supercapacitor for self-powered UV detection. *Materials Today Energy*, 28, 101054. <https://doi.org/10.1016/J.MTENER.2022.101054>

- Wang, Z., Cheng, J., Huang, H., & Wang, B. (2020). Flexible self-powered fiber-shaped photocapacitors with ultralong cyclelife and total energy efficiency of 5.1%. *Energy Storage Materials*, 24, 255–264. <https://doi.org/10.1016/J.ENSME.2019.08.011>
- Wee, G., Salim, T., Lam, Y. M., Mhaisalkar, S. G., & Srinivasan, M. (2011). Printable photo-supercapacitor using single-walled carbon nanotubes. *Energy & Environmental Science*, 4(2), 413–416. <https://doi.org/10.1039/C0EE00296H>
- Xu, J., Ku, Z., Zhang, Y., Chao, D., & Fan, H. J. (2016). Integrated Photo-Supercapacitor Based on PEDOT Modified Printable Perovskite Solar Cell. *Advanced Materials Technologies*, 1(5), 1600074. <https://doi.org/10.1002/ADMT.201600074>
- Zhang, L., Miao, J., Li, J., & Li, Q. (2020). Halide perovskite materials for energy storage applications. *Advanced Functional Materials*, 30(40). <https://doi.org/10.1002/adfm.202003653>
- Zhang, Z., Chen, X., Chen, P., Guan, G., Qiu, L., Lin, H., Yang, Z., Bai, W., Luo, Y., & Peng, H. (2013). Integrated polymer solar cell and electrochemical supercapacitor in a flexible and stable fiber format. *Advanced Materials*, 26(3), 466–470. <https://doi.org/10.1002/ADMA.201302951>
- Zheng, R., Li, H., Hu, Z., Wang, L., Lü, W., & Li, F. (2022). Photo-supercapacitor based on quantum dot-sensitized solar cells and active carbon supercapacitors. *Journal of Materials Science: Materials in Electronics*, 33(28), 22309–22318. <https://doi.org/10.1007/S10854-022-09010-1>

Chapter 11

GENETICS OF *Drosophila melanogaster*

*Aylin YILMAZ ÇETINKAYA*¹

¹ Trakya University, Keşan Hakkı Yörük School of Health, Edirne, Turkey <https://orcid.org/0000-0001-6807-9016> aylincetinkaya@trakya.edu.tr

Drosophila melanogaster

Drosophila melanogaster is a eukaryotic organism in the family Drosophilidae of the order Diptera of the class Insecta of the animal kingdom. *Drosophila melanogaster* larvae are also called fruit flies because they develop on spoiled fruits.

Phylum : Arthropoda (arthropods)

Subphylum : Mandibulata-Antennata

Class : Insecta-Hexapoda (insects-six-leggeds)

Subclass : Pterygota (winged)

Superordo : Mecopteroidea (long-winged)

Order : Diptera (double-winged)

Suborder : Brachycera (short-antennaed)

Family : Drosophilidae (vinegar flies)

Genus : *Drosophila*

Species : *Drosophila melanogaster* (Wheeler, 1981)

Drosophila melanogaster has spread from its ancestors in Africa to all parts of the world except Antarctica (Lachaise et al., 1988), and has been one of the most widely used model organism in genetic studies for over 100 years (Haudry, Laurent, & Kapun, 2020).

Researches on *Drosophila* genetics has led to numerous discoveries in the fields of cell biology, developmental biology, neurobiology and behavior, molecular biology, evolutionary genetics, and population genetics (Jennings, 2011; Tolwinski, 2017).

Genetic studies on *D. melanogaster* began in 1901, when William Castle's team used it in the laboratory at Harvard University, and is still continuing (Ong, Yung, Cai, Bay, & Baeg, 2015; Tolwinski, 2017).

Drosophila is the first eukaryotic organism has its genome, which is approximately 180 Mb, completely sequenced (Haudry et al., 2020). There are known mutations of approximately 14,000 genes thought to be present in *Drosophila*, as well as many uncharacterized genes with no orthologs (Ong et al., 2015; Tolwinski, 2017).

In the 1920s, Hermann Muller discovered that X-rays greatly increased the mutation rate in *Drosophila* genes and could break chromosomes (Ong et al., 2015; Tolwinski, 2017). Thomas Hunt Morgan (1866–1945) discovered sex-linked inheritance, the existence of linked genes, and ionizing radiation caused mutations in genes in *Drosophila* to prove and expand the hypotheses of Mendelian genetics (Kohler, 1994).

Drosophila is so superior to other model organisms, with more tissue types and a greater variety of observable behaviors, and the extensive genome data available for many species within the genus, that it has made it possible to study the principles of genetics and understand modes of inheritance in many organisms (Jennings, 2011; Tolwinski, 2017).

The use of *D. melanogaster* as a model organism in laboratory studies is due to the advantages it provides thanks to its features. These are; *Drosophila* cultures provide ease of examination in laboratories due to their small size (they are large enough for rapid demonstration of mutant phenotypes), they can be stored as bee offspring, they have 4 pairs of chromosomes, they produce a large number of embryos or flies (offspring) rapidly at a time (they are easily cultured, they reproduce rapidly), they have short and traceable life cycles and life spans), they can be anesthetized quickly and easily and can be easily distinguished morphologically, they show great similarity with mammals in terms of genetic mechanisms, they are easy to maintain and have low usage costs, they can be stored as a large number of stocks in the laboratory, they are easy to work with, and there are generally very few restrictions on work (Jennings, 2011; Tolwinski, 2017).

Culture of *Drosophila melanogaster*

Drosophila cultures should be stored in a clean place at 20 to 25 °C (68 to 77 °F). When *Drosophila* is kept in culture at around 21 °C (70 °F), adult flies emerge in 14 days. The optimum living conditions of *Drosophila* is $25 \pm 1^\circ\text{C}$ and 40-60% relative humidity, and the average development time from egg to adult is 9-11 days (Bernards & Hariharan, 2001). If the flies cultured at 18°C, adults flies become in approximately 19 days. (Flatt, 2020; Koyama, Texada, Halberg, & Rewitz, 2020)

Drosophila is generally cultured in a standard nutrient medium in an incubator set to provide the optimum living conditions and a 12-hour light and 12-hour dark period. *Drosophila* medium contains 104 g of corn flour, 94 g of sugar, 19 g of yeast, 5 g of agar, 6 ml of weak acid and 1020 ml of distilled water. After the mixture of corn flour, sugar and water in the specified amounts is mixed and boiled over low heat, agar is added to the mixture and left to boil for a short time. The mixture is taken off the

heat and the *Drosophila* medium, which is prepared by adding weak acid due to its antifungal effect, is poured into 250 ml sterile bottles with a thickness of 2 cm. Then, the mouths of the bottles are closed with lids prepared with gauze and cotton and left to dry. In addition to standard food, *Drosophila* instant food is also used for *Drosophila* nutrition. *Drosophila* eggs/larvae are placed in falcons 50/100 ml tubes containing 1.5/4.5 g of *Drosophila* ready-made food moistened with 5/9 ml of distilled water and the mouth of the tubes are closed with sponge plugs.

The materials needed to grow *Drosophila* and perform experimental crosses include culture dishes, stoppers, medium, anesthetic (ether), a fine brush, a pen for labeling, and a magnifying glass or microscope (Lefevre, Ashburner, & Novitski, 1976).

Life Cycle of *Drosophila melanogaster*

Drosophila is an insect that undergoes complete metamorphosis with four different stages in its life cycle. These stages are, in order: egg (embryonic), larva, pupa and adult (Gui & Grant, 2008). The life cycle and longevity of *Drosophila* are affected in different ways by external factors such as temperature, nutrition, population density, radiation and humidity, as well as internal factors such as mating, maternal age, egg production, sex and genetic structure At 21°C (72°F), the embryonic and larval stages of *D. melanogaster* are completed in eight days, which the pupal stage is completed in six days (Osaba, Rey, Aguirre, Alonso, & Graf, 2002).

Development of *Drosophila* occurs in two stages: the embryonic period and the postembryonic period. The embryonic period begins with the fertilization of the egg and continues until the larva hatches. The postembryonic period includes all the changes from a larva until an adult (Bate, 1993).

In the *Drosophila* life cycle, the development of the embryo takes one day, the first and second larva take one day each, the third larva take two days, the prepupa takes 4 hours and the pupa takes 4-4.5 days (Wurgler, 1986). The survival time of the adult fly is about 40-50 days (Mitchell & Combes, 1984).

Eggs are 0.5 mm long, oval shaped and transparent in appearance. The outer side of the egg is covered with a membrane called chorion. A pair of filaments extending dorsally from the anterior end prevents the egg from sinking into the soft nutrient medium (McMillan, Fitz-Earle, Butler, & Robson, 1970). During embryogenesis, the body outline is determined along the anterior-posterior and dorsal-ventral axes by maternally derived determinant genes. Following hatching, the white and segmented

worm-like larvae that continuously feed and move through the medium, showing food-seeking behavior, and at the end of the larval stage, they reach a weight of 0.05 mg to 0.20 mg and a length of 4-4.5 mm (Mitchell & Combes, 1984).

The renewal of the cuticle layer twice, called molting, during larval development for reasons of adaptation to body size increase and food storage for use in metamorphosis, divides larval life into three stages. The period between two molts is called instar. Structures called imaginal discs are observed during development of embryo. Imaginal disc cells develop by mitosis during the larval period until the pupal stage, and they form the different organs of the adult, most of which are in a mature structure, at the pupal stages (Lefevre et al., 1976).

Towards the end of the third instar, the larvae leave the medium and climb the walls of the bottles, and with the hardening of the cuticle, they stabilize their location and develop into yellow-brown, protective chitin-based pupae. During the pupal stage, some larval organs that are not needed in the adult stage are eliminated, the larval body shortens, and metamorphosis process in which it undergoes detailed changes to complete its final body outline at 4-5 days begin for the fly. During this transformation process, *Drosophila* cannot feed from the external environment and converts stored nutrients into the energy it needs to survive. Upon completion of development, adult flies emerge by piercing the anterior part of the pupal case (M Ashburner, 1978; Mitchell & Combes, 1984).

Newly emerged adults are initially light-colored and have elongated bodies, but within a few hours their colors darken, their initially wrinkled wings open, and they attain the normal adult appearance (Lefevre et al., 1976).

Adults are 2-3 mm long and females are slightly longer than males. The body segments are head, thorax and abdomen. The head and thorax are covered with hairs that serve as sensory organ. The head, which consists of six segments, has honeycomb eyes on both sides, three simple eyes on top and two antennae. The thorax consists of three segments and each segment has a pair of legs. The second segment has a pair of wings, while the wings on the third segment are vestigial and have turned into a halter organ (Olgun & Yurtsever, 2003). The females have a 7-segment abdomen that is evenly colored with melanin, while the males have 5 abdominal segments that are fused, and the tip of the abdomen is dark. In addition, the tip of the abdomen is pointed in females and blunt in males. Since the coloration of the abdomen is not complete in adult males, the

dark rows of hairs on their forelegs, called sex combs, are decisive. All of the above-mentioned characteristics are used to determine sex (Mitchell & Combes, 1984; Olgun & Yurtsever, 2003).

Virgin females can reach sexual maturity 3.5-4 hours after emerging from the pupa and can lay eggs 12 hours later. Males can mate a few hours after emerging from the pupa (Houk, 1992).

Virgin Flies

Virgin females should be selected for genetic crosses because a female fly can store sperm from a single insemination and use it for most of her fertility. However, male flies do not have to be virgin.

Adult flies mature in about 8-12 hours and they are fertile for as long as they live. Adult flies are removed from the culture medium 8-12 hours before and mature virgin females are selected before 12 hours. When female flies are kept alone in culture bottles for 3-4 days, larvae should not appear. Afterwards, female flies are kept in crossbreeding bottles with male flies to perform fertilization and embryogenesis and lay fertilized eggs (Bernards & Hariharan, 2001; Houk, 1992).

In order to select the flies to be used in the crossbreeding, they are anesthetized for 5-10 minutes by inhaling ether in the culture medium. Excessive ether treatment can sterilize and even kill the flies. For this reason, pale flies that have just emerged from the pupa and whose wings have not yet fully opened should not be selected as they may become sterile. Flies whose wings and legs extend at right angles to their bodies should be considered dead (Lindsley, 1968).

Sorting

Adult flies are collected by inhaling ether until sufficient are obtained, then counted. Anesthetized flies are placed on white paper and moved with a fine brush. If *Drosophila* strains do not carry special sex markers, they can be examined under a microscope at a magnification of at least x12 - x15 to distinguish species and sex is distinguished as male and female. Dead or discarded flies are left in a morgue consisting of water and detergent in a bottle (Demerec, 1994).

Sex Determination

The sex of *Drosophila* can be determined with attached X inheritance, in which sex-linked phenotypes as sex markers. While daughters inherit any sex-linked character from their mothers, sons inherit it from their fathers in attached X strains (Strickberger, 1962).

In *Drosophila*, the diploid cells have four pairs of chromosomes ($2n:8$), including the first pair of sex chromosomes and three pairs of autosomes (Houk, 1992).

Female flies have two X chromosomes, while male flies have one X and one Y chromosome (Mitchell & Combes, 1984). X chromosomes are rearranged between sexes in generations, while the presence of the Y chromosome is unimportant in determining the sex of *Drosophila*. In *Drosophila*, the sex is determined by ratio of X chromosomes to number of chromosome sets of chromosomes. While a value is less than or equal to $\frac{1}{2}$, the sex of *Drosophila* is male, a value is equal to or greater than 1, it is female. Additionally, if the flies have a value between $\frac{1}{2}$ and 1, they are intersex.

Female flies in the attached X strain have one pair of attached X chromosomes and one Y chromosome, while male flies have an X chromosome and a Y chromosome. Attached X chromosomes do not separate during meiosis. While daughters are made of attached X eggs cross with Y-carrying sperm, sons are formed from fertilization of Y-carrying eggs by X-carrying sperm.

Y chromosomes, which are formed from the union of egg and sperm, do not continue development after the early embryonic stage, while rarely three X chromosomes survive as a superfemale 25 (Solomon, Berg, & Martin, 2004).

Experimental Mating

The first cross between *Drosophila* strains belongs to the parental generation P₁. Offspring of the first cross, first daughter or son generation, is called F₁, and the next generation is F₂.

For crossbreeding, equal numbers of 6 pairs of male and virgin female flies belongs to two different strains are placed in the same culture bottle. After 7-10 days, F₁ flies are removed from the culture and counted under anesthesia for 10 days.

Similarly, for producing the F₂ generation, 6 pairs of male and female flies that do not need to be virgin are selected from the F₁ generation and placed in a culture bottle and kept for 7-10 days, then removed from the medium and the F₂ offsprings begin to emerge after 12-14 days at 21 °C. The new generation when begin to appear is counted every other day for 10 days. While more female flies develop than males in the culture on the first day, production of male flies increase in the following days to balance the sex ratio. Since there may be flies that develop slowly due to sex and

mutants, counting shorter or longer than 10 days are not appropriate. In addition, the counted flies should not be added back to the culture medium.

When additional cultures should set up for reciprocal crosses, the opposite sex of each strain for crossover should be selected (Solomon et al., 2004).

Genetic Nomenclature, Symbols and Phenotypes

There is a standard name and abbreviation for the representation of each mutation. While lowercase letters are used for the name and the abbreviation of a recessive gene, the name and the abbreviation of a dominant gene start with a capital letter.

The location of a mutation, which is on the chromosome at position on genetic linkage map of *Drosophila* is indicated numerically in parentheses following the gene name or abbreviation.

Eyes: Phenotypes of different stocks with different eye color, shape and size (e.g.: wild type, Homozygous aristapedia, Recessive sex-linked white, Recessive autosomal eyeless, Recessive autosomal sepia, Dominant sex-linked Bar, Dominant autosomal Lobe).

Antennae: wild type (+) and mutant Homozygous aristapedia (spineless-aristapedia).

Bristles: wild (+), singed (1-21.0), forked (1-56.7), Stubble (3-58.2), spineless (3-58.5), shaven (4-3.0).

Body Color: wild type (+), yellow (1-0.0), mutant ebony (3-70.7)

Wings: Wing venation (e.g.: wild (+), crossveinless (1-13.7), radius incompletus), wing shape (e.g.: wild (+), Curly (3-50.0), scalloped (1-51.5), apterous (2-55.2), vestigial (2-67.0), dumpy (2-13.0), Dichaete (3-41.0), curved (2-75.5) and wing size.

Except in cases of sex linkage or dominance, all F_1 generation flies have wild phenotypes and are heterozygous. In first son generation, the phenotypic character will emerge only if the female parent carry a homozygous sex-linked mutation (Lindsley, 1968).

EXPERIMENTAL CROSSES

Monohybrid Crosses

For monohybrid inheritance, two *Drosophila* cultures are used, one

winged (wild type) and the other wingless (apterous) (2-55.2). In both fruit fly strains, the marker specifics are sex-dependent, with females have red eyes and yellow bodies, while males have white eyes and gray bodies. The wild type strain has normal wings and is indicated by the gene (+). The mutant wing specific is winglessness, in the apterous (2-55.2) strain is caused by the apterous (abbreviated as ap) gene. When winged female flies (+/+) are crossed with wingless (ap/ap) male flies at P₁, all flies have the genotype (+/ap) and are winged in the F₁ generation. Because the wild wing gene (+) is dominant, while the mutant wing gene ap is recessive.

When F₁ females crossed with F₁ males to produce the F₂ generation, the expected ratio is 3 wild type: 1 apterous (Campbell, 2006; Fairbanks & Rytting, 2001; Pierce, 2015).

Recessive Gene: For the inheritance of autosomal recessive genes that are not linked to sex, reciprocal crosses between wild (red eyes, normal wings) males and apterous (no wings) females are made. When F₁ female cross with F₁ male, the expected ratio for the F₂ generation is 3 wild type: 1 apterous.

Also, dumpy (2-13.0) (truncated wings), vestigial (2-67.0) (reduced wings and halteres) or sepia (3-26.0) (eyes change from brownish red to black with age) or ebony (3-70.7) (Body gradually turns black in adults. Allow flies to age several hours or a day before classifying) strains can cross with the wild type strain.

In addition, brown, vestigial, vestigial brown, dumpy, sepia strains can be used for the inheritance of the recessive gene (Campbell, 2006; Fairbanks & Rytting, 2001; Pierce, 2015)

Testcross: When any of the F₁ flies are backcrossed with the mutant parent, the expected ratio for the offspring is 1 apterous:1 wild type. The offspring have wingless and winged phenotype and reflect the heterozygous genotype (+/ap) of the wild type F₁ flies (Ahluwalia, 2009).

Dominant Gene: Reciprocal crosses between the wild type flies and Lobe (2-72.0) (reduced eye) flies are made for dominant gene inheritance. The expected ratio for the F₂ generation is 3 Lobe:1 wild. Also, Wrinkled (3-46.0) (wrinkled wings) strain can also cross with the wild type strain (Campbell, 2006; Fairbanks & Rytting, 2001; Pierce, 2015).

Sex Linkage on Recessive Gene: Sex-linked inheritance in *Drosophila* was first discovered by Thomas Hunt Morgan in 1910. After finding a white-eyed male fly, Morgan developed breeding strains for white eyes and showed that the white-eye gene was linked to the X chromosome.

Reciprocal crosses are made between wild type and white (1-1.5) (white eyes) strains for inheritance of the sex linkage on recessive gene. If a wild female fly cross with a white male fly with a recessive sex-linked mutation, only half of the males show phenotypic results of the mutation in F_2 generation, which is the only difference from a cross of a recessive autosomal mutation.

If a white female fly cross with a wild type male fly with a recessive sex-linked mutation, white-eyed males flies and red-eyed females reproduce in F_1 generation. Expected ratio for the F_2 generation is 1 wild type: 1 white, with half of each sex have white eyes (Campbell, 2006; Fairbanks & Rytting, 2001; Pierce, 2015).

Sex Linkage on Dominant Gene: Reciprocal crosses are made between wild type and Bar(1-57.0) (the smallest eye in males and homozygous females, kidney shaped eyes in heterozygous females) strains for sex linkage inheritance on dominant gene. If a wild female cross with a Bar-eyed male with a sex-linked mutation, all F_1 females are Bar and all F_1 males are wild. The expected ratio for the F_2 generation is 1 wild:1 Bar, with half of each sex have Bar eyes.

If a homozygous Bar female cross with a wild type male with the sex-linked mutation, all F_1 flies have Bar eyes. The expected F_2 ratio is 3 Bar:1 wild, with half the males are wild type (Campbell, 2006; Fairbanks & Rytting, 2001; Pierce, 2015).

Dihybrid Crosses

Autosomal Genes: Vestigial strain cross with sepia strain for autosomal gene inheritance. If a vestigial-winged (2-67.0) (reduced wings and halteres) and red-eyed female cross with a winged and sepia-eyed (3-26.0) (eyes change from brownish red to black with age) male, all genotypes in the F_1 generation are wild heterozygotes (+/vg, +/-se), winged and red-eyed. The expected F_2 ratio is 9 wild type: 3 vestigial: 3 sepia: 1 vestigial; sepia.

Also; vestigial and ebony strains or apterus and sepia strains can cross for autosomal gene inheritance (Klug, Cummings, Spencer, Palladino, & Killian, 2003).

Gene Interaction: When crosses are made between brown (2-104.5) (eye pale red-brown, darkening with age) and scarlet (3-44.0) (eyes bright red; ocelli colorless) strains for gene interactions, all flies homozygous for both brown and scarlet will have white eyes. The expected F_2 ratio is 9 wild: 3 brown: 3 scarlet: 1 white (brown; scarlet). The ratio may not

be achieved because of reduced survival rate of white-eyed flies (Klug et al., 2003).

Sex Linkage on Autosomal Genes: If white; vestigial (1-1.5; 2-67.0) (white eyes; reduced wings and halteres) females cross with wild type males, wild females and white males reproduce equally in F_2 generation. The expected F_2 ratio is 3 white: 3 wild: 1 white; vestigial: 1 vestigial (Klug et al., 2003).

Linkage Group

Linkage Between Two Autosomal Genes: The inheritance of autosomal genes is achieved by crosses between wild and a chromosome strain with two non-sex linked recessive mutations, such as sepia; spineless (3-26.0; 3-58.5) (eyes change from brownish red to black with age; spineless bristles) or sepia; ebony (3-26.0; 3-70.7) (eyes change from brownish red to black with age; Body gradually turns black in adults. Allow flies to age several hours or a day before classifying) or black; vestigial (2-48.5; 2-67.0) (black body; reduced wings and halteres) or vestigial; brown (2-67.0; 2-104.5 (reduced wings and halteres; eye pale red-brown, darkening with age). The F_1 females are backcrossed with mutant strains. Parental and recombinant types are seen in the strain (M. Ashburner, 1989; Strickberger, 1962).

Two Sex-Linked Genes: Yellow miniature (1-00; 1-36.1) (yellow body and scute bristles; miniature wings) or white miniature (1-1.5; 1-36.1) (white eyes; miniature wings) or white-eosin forked (eosin eyes; forked bristles) females cross with wild type males for the inheritance of two sex-linked genes. Also, yellow white (chromosome 1) females can be selected for tight linkage (M. Ashburner, 1989; Strickberger, 1962).

Three Sex-Linked Genes: White miniature forked (1-00; 1-36.1; 1-56.7), (white eyes; miniature wings; forked bristles), yellow white miniature (1-00; 1-1.5; 1-36.1) yellow body and scute bristles; white eyes; miniature wings), black vestigial brown (2-48.5; 2-67.0; 2-104.5) (black body; wings and halteres reduced; brown eyes), spineless-aristapedia (3-58.5) (spineless bristles-ends of antennae enlarged and leg-like) strains cross for the inheritance of three sex-linked genes.

In addition; for double crossovers; yellow crossveinless vermilion forked (1-00; 1-13.7; 1-33.0; 1-56.7) (yellow body and scute bristles; crossveinless wings; vermilion eyes; forked bristles) strain can select (M. Ashburner, 1989; Strickberger, 1962).

Determination of Linkage Group

For determination which of the four linkage groups of *Drosophila* a given mutant belongs to females of the mutant strain cross with *Curly/Plum* (chromosome 2); *Dichaete/Stubble* (chromosome 3) (curled wings; resembling brown eyes with darker spots; hairless bristles; short and thick bristles) males.

If only F1 males show the mutation, it is a sex-linked recessive.

If all the F1 flies show the mutation, it is dominant. If wild-type females cross with F1 males of one of the four phenotypes: *Curly;Dichaete*, *Curly;Stubble*, *Plum;Dichaete* or *Plum;Stubble*, a sex-linked dominant will appear only in females. The type with the two dominant mutant genes that will least interfere with classification of the mutant (other than dumpy and black) should be selected as parents. While *Curly/Plum* (chromosome 2) and *Dichaete/Stubble* (chromosome 3) do not appear as dominant, chromosome 4 with two dominant genes show independent variety as dominant.

If the mutation is an autosomal recessive, females of the mutant strain cross with F1 males of one of the four phenotypes: *Curly;Dichaete*, *Curly;Stubble*, *Plum; Dichaete* or *Plum; Stubble*. The type with the two dominant mutant genes that will least interfere with classification of the mutant (other than dumpy and black) should be selected as parents. While *Curly/Plum* (chromosome 2) and *Dichaete/Stubble* (chromosome 3) do not appear as recessive, chromosome 4 with two dominant genes show independent variety as recessive.

In addition, *Hairless/Stubble* (3-69.5; 3-58.2) (hairless bristless; short and thick bristles) can be used instead of *Dichaete/Stubble* (M. Ashburner, 1989; Strickberger, 1962).

Statistical Analysis

The evaluation of the agreement between the number of individuals (actual count) and the expected number in the records is done by the chi-square method. The calculated probability of 0.05 or less indicates that the experimental data significantly deviates from the theoretical expectation. The degrees of freedom and the calculated chi-square value indicate that difference between actual number and the expected number will happen by random chance more than X times (Strickberger, 1962).

REFERENCES

- Ahluwalia, K. B. (2009). *Genetics*: New Age International (P) Limited, Publishers.
- Ashburner, M. (1978). The laboratory culture of *Drosophila*. *The genetics and biology of Drosophila*, 2, 1-109.
- Ashburner, M. (1989). *Drosophila: A Laboratory Manual*. . In (pp. 434): Cold Spring Harbor, New York: Cold Spring Harbor Laboratory Press.
- Bate, M., Martinez Arias A. (1993). *The Development of Drosophila Melanogaster* (Vol. (2 Volume Set)): Cold Spring Harbor Laboratory Pr.
- Bernards, A., & Hariharan, I. K. (2001). Of flies and men—studying human disease in *Drosophila*. *Current opinion in genetics & development*, 11(3), 274-278.
- Campbell, N. A. (2006). *Biology concepts & connections*.
- Demerec, M. (1994). *Biology of Drosophila*: Cold Spring Harbor Laboratory Press.
- Fairbanks, D. J., & Rytting, B. (2001). Mendelian controversies: a botanical and historical review. *American Journal of Botany*, 88(5), 737-752.
- Flatt, T. (2020). Life-history evolution and the genetics of fitness components in *Drosophila melanogaster*. *Genetics*, 214(1), 3-48.
- Gui, Y., & Grant, A. (2008). Joint effects of density dependence and toxicant exposure on *Drosophila melanogaster* populations. *Ecotoxicology and Environmental Safety*, 70(2), 236-243.
- Haudry, A., Laurent, S., & Kapun, M. (2020). Population genomics on the fly: recent advances in *Drosophila*. *Statistical population genomics*, 357-396.
- Houk, V. S. (1992). The genotoxicity of industrial wastes and effluents: a review. *Mutation Research/Reviews in Genetic Toxicology*, 277(2), 91-138.
- Jennings, B. H. (2011). *Drosophila—a versatile model in biology & medicine*. *Materials today*, 14(5), 190-195.
- Klug, W. S., Cummings, M. R., Spencer, C. A., Palladino, M. A., & Killian, D. (2003). *Concepts of genetics*: Prentice Hall Upper Saddle River, NJ.

Kohler, R. E. (1994). *Lords of the fly: Drosophila genetics and the experimental life*: University of Chicago Press.

Koyama, T., Texada, M. J., Halberg, K. A., & Rewitz, K. (2020). Metabolism and growth adaptation to environmental conditions in *Drosophila*. *Cellular and Molecular Life Sciences*, 77(22), 4523-4551.

Lachaise, D., Cariou, M.-L., David, J. R., Lemeunier, F., Tsacas, L., & Ashburner, M. (1988). Historical biogeography of the *Drosophila melanogaster* species subgroup. *Evolutionary biology*, 159-225.

Lefevre, G., Ashburner, M., & Novitski, E. (1976). The genetics and biology of *Drosophila*. Vol. 1a, M. Ashburner and E* NovltBki (eds.)* Academic, New York.

Lindsley, D. L. (1968). Genetic variations of *Drosophila melanogaster*. *Carnegie Inst.*, 627.

McMillan, I., Fitz-Earle, M., Butler, L., & Robson, D. S. (1970). QUANTITATIVE GENETICS OF FERTILITY II. LIFETIME EGG PRODUCTION OF *DROSOPHILA MELANOGASTER*—EXPERIMENTAL. *Genetics*, 65(2), 355-369. doi:10.1093/genetics/65.2.355

Mitchell, I. d. G., & Combes, R. (1984). Mutation tests with the fruit fly *Drosophila melanogaster*. *Mutagenicity testing: A practical approach*. IRL Press, Oxford, 149-186.

Olgun, G., & Yurtsever, S. (2003). *Genetik laboratuvar kılavuzu*: Trakya Üniversitesi.

Ong, C., Yung, L.-Y. L., Cai, Y., Bay, B.-H., & Baeg, G.-H. (2015). *Drosophila melanogaster* as a model organism to study nanotoxicity. *Nanotoxicology*, 9(3), 396-403.

Osaba, L., Rey, M. a. J., Aguirre, A., Alonso, A., & Graf, U. (2002). Evaluation of genotoxicity of captan, maneb and zineb in the wing spot test of *Drosophila melanogaster*: role of nitrosation. *Mutation Research/ Genetic Toxicology and Environmental Mutagenesis*, 518(1), 95-106.

Pierce, B. A. (2015). *Genetics: A Conceptual Approach*: Macmillan Learning.

Solomon, E., Berg, L., & Martin, D. W. (2004). *Biology*: Cengage Learning.

Strickberger, M. W. (1962). Experiments in genetics with *Drosophila*.

Tolwinski, N. S. (2017). Introduction: *Drosophila*—A model system for developmental biology. In (Vol. 5, pp. 9): MDPI.

Wheeler, M. R. (1981). The Drosophilidae: a taxonomic overview. *The genetics and biology of Drosophila*, 3, 1-97.

Wurgler, F. E. (1986). In vivo mutagenicity testing using somatic cells of *Drosophila melanogaster*. *Chemical Mutagens*, 10, 1-72.